Understanding Microstructural Phase Evolution, Compositional Partitioning, Passivation, and Corrosion Resistance of Multi-Phase Complex Concentrated Alloys

---

A
Dissertation
Presented to
the faculty of the School of Engineering and Applied Science
University of Virginia

---

in partial fulfillment
of the requirements for the degree

Doctor of Philosophy

by

Samuel Boyd Inman

May 2024

APPROVAL SHEET

This
Dissertation
is submitted in partial fulfillment of the requirements
for the degree of
Doctor of Philosophy

Author: Samuel Boyd Inman

This Dissertation has been read and approved by the examing committee:

Advisor: John R. Scully

Advisor:

Committee Member: Elizabeth J. Opila

Committee Member: Stephen J. McDonnell

Committee Member: Sean R. Agnew

Committee Member: S. Joseph Poon

Committee Member:

Committee Member:

Accepted for the School of Engineering and Applied Science:

Jennifer L. West, School of Engineering and Applied Science

May 2024

Dissertation Abstract

Complex Concentrated Alloys (CCAs), alloys which contain four or more elements at concentrations above 5 at. % are evaluated for their possible contributions to corrosion-resistant alloy design. Possible benefits of the alloy class including unique distributions of passivating elements in protective oxides as well as exploiting elemental synergies in protective passivating oxides not necessarily available in conventional alloys. Such oxides regulate corrosion processes. However, the formation of additional phases in CCAs may cause passivating elements to partition within the microstructure changing their impact on passivation, and create interfaces limiting their benefit on corrosion resistance. In this work, the passivity and overall corrosion resistance of CCAs within the multi-phase Al-Cr-Fe-Mn-Mo-Ni-Ti system were evaluated. Compositions were targeted to reduce density to the range of 7-7.75 $g.cm^{-3}$, below those of conventional stainless steels, while also ensuring mechanical ductility due to the presence of an FCC matrix. Phases were synthesized and/or dual and three phase structures were interrogated with high resolution methods to evaluate the contributions of individual phases to corrosion behavior. Corrosion resistance was evaluated with combinations of AC and DC methods which determined attributes and marker of oxide protectiveness in dilute chloride solution at neutral or slight acidic pH. Additionally, corrosion behavior was evaluated across a range of pH, chloride concentrations, and in sulfate environments. Combinations of X-ray photoelectron spectroscopy and atomic emission spectroelectrochemistry were used to determine the roles or fates (e.g. passivation in an oxide film, dissolution into the electrolyte) of individual elements during the passivation process. The findings are used in an iterative design process to inform new optimal compositions. Optimal CCA compositions showed corrosion resistance comparable to, and in the case of best-performing compositions such as $Al_{0.3}Cr_{0.5}Fe_2Mn_{0.25}Mo_{0.15}Ni_{1.5}Ti_{0.3}$, superior to conventional corrosion resistant alloys such as 316L.

Increasing both Al and Ti content in CCA series promoted the formation of an $L2_1$ secondary phase enriched in Al, Ni, and Ti along with a third phase enriched in Cr, Fe, and Mo. All the evaluated CCAs demonstrated passivity, with Al, Cr, and Ti generally all suggested to promote passive film formation and stability in a variety of relative compositions. Increasing Al concentrations has minimal effect on parameters representative of passive film strength (e.g., passive current density, polarization resistance) while increasing Ti concentrations are shown to improve such parameters. However, high concentrations of both Al and Ti harm resistance to localized corrosion as evidenced by decreasing pitting and repassivation potentials. The effects of Mn and Mo on the microstructure and corrosion

behavior are also considered. Mn decreases the degree of microstructural partitioning for Al and Ti, allowing for improved corrosion resistance when added at low concentration despite the instability of Mn passive species itself. Decreasing Mo concentrations were similarly shown to decrease the degree of microstructural partitioning and potentially improve passivity, but also significantly decreased the resistance to localized corrosion.

Finally, to elucidate the relationships between the microstructure, passivity, and corrosion resistance for each individual phase, the passive film composition of a dual-phase FCC+L2_1 CCA was characterized with high-resolution techniques capable of differentiating the composition over individual phases in the bulk microstructure. Two distinct phases within the passive film were observed, with the interface acting as a preferential pitting site. The passive film formed over the FCC phase had comparatively higher concentrations of Fe, Cr, and Mo while the film formed over the L2_1 phase had higher concentrations of Al, Ni, and Ti, mirroring concentrations in the bulk microstructure. Thus, the passive film, and therefore the corrosion behavior, of the dual-phase was suggested to be representative of a mixture of each constituent phase. The application of composite theory to corrosion was evaluated by synthesizing single-phase CCAs representative of the constituent phase compositions. Passivity of the dual-phase CCA was attributed to the ability of both constituent phases to passivate. The dual-phase CCA showed similar corrosion resistance to each constituent phase, but the resistance to localized breakdown was suggested to be lower for both the dual-phase and single-phase L2_1 CCA than for the isolated FCC CCA phase. The findings indicate the importance of ensuring the ability of all individual phases within a multi-phase CCA microstructure to passivate for overall corrosion resistance. Furthermore, strategies to utilize CCA composition to affect phase structure, composition, and ability to passivate are addressed within the context of corrosion resistant alloy design.

Acknowledgements

Nearly six years ago, I committed to join the University of Virginia Department of Materials Science. What set this department apart from others was the support, care, and value that is demonstrated upon its people. As my time here has now come to an end, that continues to be as true as it was my first day here. I would like to thank everyone both within and beyond the department who gone out of their way to make that the case for me.

This work could not have been done without the support of my advisor, John Scully. Thank you for being active in my work from day one until departure. His contributions both to this work as well as my development as a researcher have been both valuable and steadfast. Likewise, I am beyond appreciative for the fantastic research group I have been blessed to join. Thank you to Junsoo Han, Angela Yu Gerard, and Carol Glover, who played active roles in training me and helping me navigate the electrochemistry field. Thank you to Debashish Sur and Alen Korjenic and my honorary third office-mate Katie Anderson for the consistent collaboration. I will sorely miss the many great memories in the sardine can that we shared together.

This work would be ultimately fruitless without the rest of UVA LW-LC-CCA team. They have been fundamental both in providing support for this work as well as enabling the work to have a home in the broad field of alloy design. The financial and technical support from the Office of Naval Research and Dave Shifler is appreciated. I specifically want to thank Peter Connors, whose contributions are spread all across this work. I am so fortunate to have gotten to work with him as closely as I did and trust that I am leaving this project in good hands. Thank you to Jie Qi and Diego Ibarra Hoyos for the countless samples prepared as well as Mark Wischhusen for the close collaboration and continued selfless support. I am grateful to have Sean Agnew and Joseph Poon helping to lead the team and for their role as committee members and frequent coauthors.

I would like to thank the many others in the department who have extended the same support, nearly always with nothing to gain for themselves. Stephen McDonnell and Beth Opila have both been valued members of my committee and constructive research contributors. They continue exemplify the many faculty members and staff at UVA who have selflessly made time to support me in my work. This work could not have been done without the help of the UVA NMCF staff, particularly Cathy Dukes who provided extensive training, even though she never anticipated the responsibilities to include digging dropped samples out of ultra-high vacuum. I would like to also specifically thank David Green for allowing me to co-instruct with him as well as for the personal mentorship on navigating faculty careers that has extended beyond the teaching semester. Such an opportunity could not have been possible without the UVA CTE and SEAS teaching fellowship, from whom I appreciate both the funding and continued support. Lastly, I would like to thank the many students of the class for granting me a fulfilling and unforgettable experience.

This program has introduced me to many people who are now some of my closest friends. Thank you for making me genuinely excited to come into lab every morning. I am beyond grateful to have lived with Alejandro Salanova, Lee Kendall, Mack Kinkaede, Victor Kontopanos, Loki, and Walter. Thank you for the constant support, keeping me in a healthy headspace throughout the difficulties of graduate school. They have helped to put out many fires in my life, and I wish I could say they were all metaphorical. In addition to many listed above, I would also like to thank Johnathan Skelton, Clark Luckhardt, Gaby Abad, Mike Roach, TJ Montoya, Keithen Orson, Rachael Guariello, and many more for their continued friendship, assistance in navigating the graduate program, and being the best SEM support group that I could ever ask for.

Finally, the support I have received in Charlottesville has extended well beyond the department. Thank you to my family who has loved and supported me every step of the way, to my parents, who have given more than I could count to get me to the place I am today, to Grandpa Wally, who gave me my first connection to metallurgy, and to Grandpa Sorensen, who laid the groundwork for me to pursue my education in it. Thank you to my CUDO friends, who no matter what is happening, continue to ensure I enjoy life, and to my church community, who have truly been my family away from home. You have been a constant reminder to me of presence and continued providence of the Lord in my life.

Soli Deo Gloria

Table of Contents

List of Figures

Chapter 1

Chapter 2

Chapter 3

Chapter 4

Chapter 5

Chapter 6

List of Tables

Chapter 1

Chapter 2

Chapter 3

Chapter 4

Chapter 5

Chapter 6

List of Symbols and Abbreviations

A	Exposure Area
AC	Alternating Current
AES	Auger Electron Spectroscopy
AESEC	Atomic Emission Spectroelectrochemistry
at. %	Atomic percent
BCC	Body Centered Cubic
BSE	Backscattered Electron
B_W	Warburg bound length
C	Cost
CALPHAD	Calculation of Phase Diagrams
CCA	Complex Concentrated Alloy
CPE	Constant Phase Element
E	Potential
E_{corr}	Corrosion potential
EDS	Energy Dispersive Spectroscopy
EIS	Electrochemical Impedance Spectroscopy
E_{pit}	Pitting potential
E_{rep}	Repassivation potential
f	Flow rate
f	Frequency
F	Faraday's constant (96485 C.mol^{-1})
f	Enrichment factor
FCC	Face Centered Cubic
FIB	Focused Ion Beam
GB	Grain Boundary
HAADF	High-angle annular dark-field
HEA	High Entropy Alloy
HI	Heterophase Interface
H_V	Vickers Hardness
i	Current density
I	Intensity
i_{crit}	Critical current density
i_{pass}	Passive current density
j	Equivalent dissolution current density
j_e	Electron current density
$L2_1$	Heusler Phase
l_{ox}	Oxide thickness
M	Molar mass
ML	Machine Learning
MPEA	Multi-Principal Element Alloy

OCP	Open Circuit Potential
Q	Total mass loss rate
R	Ideal gas constant (8.14 J.mol^{-1}K^{-1})
r	Atomic radius
R	Relative sensitivity factor
R_{CT}	Charge transfer resistance
RMS	Root Mean Squared
R_p	Polarization resistance
R_s	Solution resistance
S	Surface cation fraction
SCE	Saturated Calomel Electrode
SE	Secondary Electron
SEM	Scanning Electron Microscopy
SHE	Standard Hydrogen Electrode
STEM	Scanning Transition Electron Microscopy
t	Time
T_M	Melting temperature
ToF-SIMS	Time of Flight Secondary Ion Mass Spectrometry
x	Composition
X_B	Bulk composition
XPS	X-ray Photoelectron Spectroscopy
XRD	X-ray Diffraction
X_S	Surface cation fraction
Y_o	Admittance constant
Y_W	Warburg admittance
Z	Impedance
z	Charge of dissolved species at stable valence
Z"	Imaginary component of impedance
Z_{img}	Imaginary component of impedance
Z_{mod}	Impedance modulus
ZRA	Zero-Resistance Ammetery
α	Constant phase element coefficient
δ	Mean squared radius mismatch
ΔG^0	Gibbs free energy of formation
ΔG_f^0	Gibbs free energy of formation
ΔG_{mix}	Gibbs free energy of mixing
ΔH_{mix}	Enthalpy of mixing
$\Delta H_{mix,i,j}$	Enthalpy of mixing for element pair i,j

ΔH_{mix}^{IM}	Enthalpy of formation for most stable compound in alloy system
ΔS_{mix}	Entropy of mixing
ε_0	Vacuum permittivity
Θ	Mass of metal enriched at surface
κ	Dielectric constant
ν	Dissolution rate
ρ	Density
ρ_δ	Passive film boundary permittivity
Φ	King thermodynamic phase stability indicator
Φ	Phase angle
Ω	Zhang thermodynamic phase stability indicator

List of Publications

1. J.R. Scully, **S.B. Inman**, A.Y. Gerard, C.D. Taylor, W. Windl, D.K. Schreiber, P. Lu, J.E. Saal, G.S. Frankel, Controlling the corrosion resistance of multi-principal element alloys, Scripta Materialia, 188 (2020) 96-101.
2. **S.B. Inman**, J. Han, A.Y. Gerard, J. Qi, M.A. Wischhusen, S.R. Agnew, S.J. Poon, K. Ogle, J.R. Scully, Effect of Mn Content on the Passivation and Corrosion of Al0.3Cr0.5Fe2MnxMo0.15Ni1.5Ti0.3 Compositionally Complex Face-Centered Cubic Alloys, Corrosion, 78 (2021) 32-48.
3. J.J. Bhattacharyya, **S.B. Inman**, M.A. Wischhusen, J. Qi, J. Poon, J.R. Scully, S.R. Agnew, Light Weight, Low Cost, and Compositionally Complex Multiphase Alloys with Optimized Strength, Ductility and Corrosion Resistance: Discovery, Design and Mechanistic Understandings, Materials & Design, 228 (2023).
4. **S.B. Inman**, D. Sur, J. Han, K. Ogle, J.R. Scully, Corrosion Behavior of a Compositionally Complex Alloy Utilizing Simultaneous Al, Cr, and Ti Passivation, Corrosion Science, 217 (2023) 111138.
5. **S.B. Inman**, J. Han, M.A. Wischhusen, J. Qi, S.R. Agnew, K. Ogle, J.R. Scully, Passivation and Localized Corrosion Resistance of Al0.3Cr0.5Fe2MoxNi1.5Ti0.3 Compositionally Complex Alloys: Effect of Mo Content, Corrosion Science, 227 (2024) 111692.
6. **S.B. Inman**, J.R. Scully, Design and Discovery of Compositionally Complex Alloys (CCA) that Include High Corrosion Resistance, Corrosion, 80 (2024) 250-258.
7. **S.B. Inman**, M.A. Wischhusen, J. Qi, J. Poon, S.R. Agnew, J.R. Scully, Variation of the Passive Film on Compositionally Concentrated Dual-phase Al0.3Cr0.5Fe2Mn0.25Mo0.15Ni1.5Ti0.3 and Implications for Corrosion, Submitted to Metallurgical and Materials Transactions A, (2024).
8. D. Sur, **S.B. Inman**, K.L. Anderson, J. Qi, M. Barbiari, J.R. Scully, Passivation behavior of Fe-Cr-Al-Ti alloys in sulfate containing aqueous environments, In progress
9. **S.B. Inman**, J. Han, M.A. Wischhusen, J. Qi, S.R. Agnew, K. Ogle, J.R. Scully, Effect of Ti on the corrosion resistance of Al-Cr-Fe-Mn-Mo-Ni Dual Phase CCA, In progress from Chapter 3
10. **S.B. Inman**, J. Han, M.A. Wischhusen, J. Qi, S.R. Agnew, K. Ogle, J.R. Scully, Effect of Al on the corrosion resistance of Al-Cr-Fe-Mn-Mo-Ni Dual Phase CCA, In progress from Chapter 2

Chapter 1: Introduction

1.0 Background

High entropy alloys (HEAs), an alloy class utilizing multiple elements at equimolar or near-equimolar concentrations, have recently grown in popularity since their theorization and inception by Cantor et al. [1] and Yeh et al. [2]. Early reports indicated single-phase HEAs might be capable of possessing strong corrosion resistance due in part to their entropy-promoted homogenous distribution of passivating elements at concentrated levels [3, 4]. Additional strategies have since emerged such as targeting beneficial clustering of certain elements following heat treatment. Additionally, selection of combinations of elements that work together to enable multiple elemental functions including synergies which promote improve corrosion resistance, including some not seen in conventional alloys [5].

The complex concentrated alloy (CCA) design space, a broader field of which HEAs may be considered a subset, utilizes non-equimolar single-phase solid solution or multi-phase alloys. CCA compositions often contain four or more elements at concentrations between 5 and 35 at. % [6]. Given the vast compositional design space in comparison to the equimolar HEAs, high-throughput design methodologies or targeted approaches proven to identify key attributes traceable to key elements and their functions are necessary to filter and sort proposed compositions. Computational methods, in particular machine learning, exhibit viability in filtering CCA compositions for cost, density, and microstructure [7-9]. Many initial strategies to ensure corrosion resistance of CCAs rely on simply ensuring presence of popular passivator elements at adequate concentrations based on intuition and existing knowledge of critical concentrations required for passivation taken from binary alloys [5, 10]. Additionally well-known synergies such as the Al-Cr third element effect or the Cr-Mo synergy assumed to operate in CCAs may be incorporated [11, 12].

Moreover, although limited computational modeling [13, 14] and high-throughput experimental studies [11, 15, 16] have been introduced that could uncover second and third element effects (e.g. microstructural refinement [17, 18], multi-cation passivation [19, 20], inhibitor-assisted passivation [21]), the integration of predictive metrics for more complex passivation and corrosion phenomena in CCA design generally remains uncommon. Thus, comparatively unguided high-fidelity, low-throughput experimentation is often necessary, limiting the range of compositions that may be evaluated. Incorporation of synergistic behavior between elements, either through coexistence in the passive film or other second element effects (e.g. clustering assisted passivation [22], pit inhibition [23], etc.), provides opportunity to improve the corrosion resistance beyond the contribution of either element alone.

Materials with reinforcing phases operating as composites (i.e., dual phases strengthening) offer great benefits towards mechanical properties [24]. However, adverse consequences are often encountered with respect to corrosion resistance [5, 10]. Second phase, intermetallic compound or inclusion formation in the microstructure may deplete key passivating elements at interphase interfaces or may cause partitioning of beneficial alloys or passivating elements towards one phase, leading to depletion from the other. Such changes may create preferential sites for localized corrosion at the interface. Adverse effects of second phase formation have been observed in CCAs with FCC structures in combination with BCC [18, 25, 26], B2 [27-29], sigma [23, 30-32], and Laves [33] phases. Furthermore, two dissimilar phases may form microgalvanic couples, further enhancing localized corrosion if the galvanic couple potential is, for instance, is above the pitting potential [27, 28, 34, 35]. As corrosion resistance is affected by combinations of overall alloy composition, microstructural morphology, and element partitioning, all influences must then also be evaluated to ascertain their effect on corrosion, particularly in cases where corrosion must balance with other design goals. Challenges still exist with regards to isolating microstructural effects between structure, phase volume fractions (i.e., comparing multi-phase CCAs with different volume fractions of phases of similar compositions) or phase compositions (i.e., comparing multi-phase CCAs with similar volume fractions of phases with differing compositions). This work evaluates the design of corrosion-resistant CCAs in the of the newly reported Al-Cr-Fe-Mn-Mo-Ni-Ti system [12, 17, 19, 24].The effects of individual elements and multi-element interactions including passive film co-existence and microstructural partitioning are studied.

2.0 Motivation and Evaluation of Design Goals

This work summarizes the overarching conclusions for the corrosion resistance of multi-phase CCAs obtained from a broad project targeting multiple interdisciplinary design goals. While the primary findings summarized address the effects of CCA composition and microstructure on aqueous corrosion resistance, the conclusions must be addressed within the context of additional design goals. A brief summary of the motivation for each individual design goal targeted in this work is listed below.

2.1 Density

First, CCA compositions are targeted to reduce density relative to traditionally-established corrosion resistant alloys such as 316L (8.0 g/cm^3 [36]) as well as transition metal based CCAs such as

CoCrFeMnNi (8.0 g/cm^3 [37]). Decreased alloy density has long been established as a design strategy to reduce fuel consumption and overall cost for marine applications [38], with comparatively newer interest acquired in efforts to minimize adverse environmental effects of fuel emissions [39].

Experimental evaluation of CCA density is often time-consuming and limits high-throughput assessment of the broad alloys spaces that are characteristic of the CCA design space [6]. Thus, crude predictions of alloy density that may be efficiently predicted computationally often provide significant value. In this work, CCA densities (ρ) are predicted as an average of the densities of room temperature allotropes for each constituent element (ρ_i) [40] weighed by the alloy composition (x_i).

$$\rho = \sum \rho_i x_i \tag{1}$$

The method has been validated by comparison of weighted average predictions to experimentally observed densities for selected alloys from Chapter 2. Good agreement with the predictive values validates the technique. The strictly composition-based methodology suggests that the density may be decreased by increasing the concentration of lightweight elements. This strategy informs efforts to maximize concentrations of Al and Ti that are discussed further in Chapters 2 and 3 without adversely affecting other design criteria.

Table I: Predicted densities of selected CCAs utilized in Chapter 2 compared to densities obtained of alloys arc-melted and homogenized (6 hours, 1070 ˚C) using the Archimedes method [41]. Experimental densities were averaged across at least three measurements

Alloy Name	Alloy Composition (at. %)	Predicted Density (g.cm^{-3})	Experimental Density (g.cm^{-3})
Al-0	$Cr_{0.5}Fe_2Mn_{0.25}Mo_{0.15}Ni_{1.5}Ti_{0.3}$	7.95	7.98
Al-6.0	$Al_{0.3}Cr_{0.5}Fe_2Mn_{0.25}Mo_{0.15}Ni_{1.5}Ti_{0.3}$	7.64	7.78
Al-13.0	$Al_{0.7}Cr_{0.5}Fe_2Mn_{0.25}Mo_{0.15}Ni_{1.5}Ti_{0.3}$	7.28	7.16

2.2 Cost

Second, the alloy cost is evaluated. As in the case of density, the cost (C) is predicted as a weighted average of pure element costs (C_i) [42]. In the case of Mn, the pure element cost of Mn is replaced by that of a ferromanganese compound given the high production costs of pure Mn that would not be relevant to industrial alloy synthesis [42]. The Fe composition in such alloys is adjusted accordingly. While the cost of producing pure metals from natural states are incorporated into this method are neglected, any processing costs beyond pure metal production that may differ between alloy compositions. However, as in the case of density, the simplified nature of the metric allows for improved efficiency in the high-throughput evaluation of multiple CCA compositions. Cost calculations may inform the selected elements included in an evaluated compositional space. For example, despite use in the initial high entropy alloys [1], Co is eschewed from the compositional space due to the high costs and marginal contribution to passivity [24, 43].

$$C = \sum C_i x_i \tag{1}$$

In addition to the direct alloy costs, indirect (e.g. volatility of individual elements, geopolitical concentration) costs may affect the viability of individual compositions for industrial applications [44]. While such effects provide opportunities to improve cost analysis of selected CCA compositions and are recommended prior to industrial application of selected alloys, they are not expected to significantly affect comparative costs between individual alloys and are thus not considered in this work.

2.3 Corrosion Resistance

Third, CCAs are targeted to have good aqueous corrosions resistance. Corrosion limits the overall lifespan of components in marine conditions. Therefore, improved corrosion resistance may reduce both direct and indirect costs (e.g. maintenance, decreased production) of upkeep. CCAs provide opportunities to integrate multiple passivating elements into protection strategies. Namely, microstructural homogeneity, passive film stability, the viability of forming multi-cation or complex oxides, and control of local ion solubility affecting localized corrosion provide opportunities for the development of CCAs with improved corrosion resistance relative to conventual alloys [45].

This work mainly targets CCAs resistant to corrosion in marine conditions. Thus, in addition to the formation of a stable protective oxide film, the resistance of such films to localized corrosion such as pitting remains paramount given the tendency of Cl^- ions present in ocean water to initiate such localized corrosion. While ocean conditions may be replicated with concentrated sodium chloride solution among other constituent species [46], such aggressive conditions often limit the ability to evaluate the ability of CCAs to form stable passive films prior to breakdown using techniques such as potentiodynamic polarization. Thus, a dilute NaCl electrolyte is often utilized to establish initial comparisons between the passivity and corrosion resistance of CCAs. Additionally, to evaluate the ability of the alloys to passivate in the absence of Cl^-- induced localized corrosion, electrochemical experiments are often evaluated in sulfate solutions. Well-performing alloys are then evaluated in more aggressive solutions and/or solutions varying in pH that more closely replicate marine conditions and provide a wider scope of alloy viability. Precise techniques used to evaluate the corrosion resistance of CCA series are provided for each chapter.

2.4 Mechanical Strength and Ductility

Finally, the CCAs are targeted for combinations of mechanical strength and ductility. While HEAs were originally proposed to have mechanical strength arising from high degrees of lattice strain [6]. However, more recent work has challenged the degree to which strictly solid-solution effects may strengthen CCAs [47, 48]. For this reasons, second phase regions in multi-phase CCAs are targeted to further improve mechanical strength. In this work, CCAs with an FCC matrix were selected to improve mechanical ductility to avoid the characteristic brittle behavior of BCC-like matrix phases, particularly below the ductile to brittle transition temperature [6]. Second phases targeted for mechanical strengthening are generally of the $L2_1$ structure and Ni_2AlTi stoichiometry, owing to the combinations of Al and Ti utilized to decrease alloy density along with high concentrations of Ni targeted to stabilize the FCC phase.

The volume fraction of strengthening phase may be utilized to predict both the strength and ductility of the overall alloy utilizing crystal plasticity modeling developed by Bhattacharyya et al. [24]. Generally, the yield strength and hardness values are suggested to increase with increasing $L2_1$ volume fraction, with hardness increasing in a nearly proportional manner to $L2_1$ volume fraction following composite theory as shown in Figure 1. Alternatively, ductility is expected to decrease with $L2_1$ volume fraction. Efforts have been made to optimize the microstructure for mechanical toughness [24]. However, such methods have not incorporated other factors such as cost, density, and corrosion resistance. Thus, a more comprehensive overview of the effects of microstructures on corrosion resistance is necessary to evaluate the tradeoffs between mechanical and corrosion effects on specific microstructures that may be targeted during the alloy design process. While this work does not go into detail into the mechanical properties of this alloy class, the effects of second phase structure and volume fraction on mechanical properties may be integrated with corrosion conclusions to optimize alloy compositions for a combination of all of the aforementioned design goals.

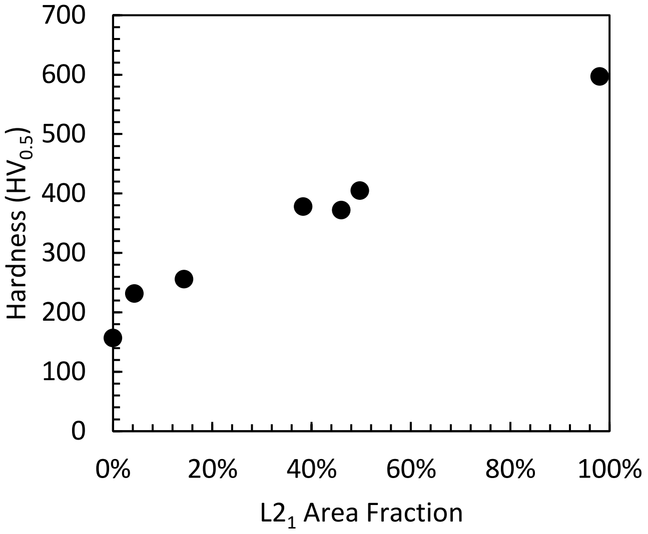

Figure 1: Vickers microhardness values (0.5 kg, 15 s) obtained from by Bhattacharyya et al. [24] for a series of selected CCAs in the Al-Cr-Fe-Mn-Mo-Ni-Ti system relative to $L2_1$ area fractions identified via ImageJ threshold analysis of back scattered electron scanning electron microscopy micrographs.

2.5 High-throughput Design and Integration of Alloy Design Goals

For a given CCA system, there is a wide compositional range over which any constituent element may be tuned, leading to many possible compositions for a given alloy system. Thus, the CCA alloy space has been historically characterized as broad and often has more possible compositions than may be practically evaluated with traditional experimental techniques. High-throughput experimental methods have shown great promise for evaluation of environmental degradation of CCAs [49, 50]. However, even with high-throughput methods, the vast alloy space cannot be surveyed in its entirety. Thus, computational work is often integrated into the development of CCAs prior to synthesis and characterization. The two methods informing compositions selected for this work are elaborated on further below.

Machine learning (ML) techniques have become valuable tools in identifying CCAs with targeted properties from broad compositional spaces [51-53]. In particular, ML techniques are often utilized to predict phase stability, either through targeting single phase alloys or specific desired multi-phase microstructures [7, 51, 52, 54]. This work utilized a methodology developed by Qi et al. [7] that uses binary phase diagrams of constituent element pairs to predict phase stability for given CCA compositions. An alloy space defined by selected elements and acceptable composition ranges may then be filtered to selected alloys which may be capable of desired microstructure following homogenization. However, the model is limited in identifying ideal temperatures for heat treatment, necessitating other methods.

Computational thermodynamic techniques such as CALPHAD integrate thermodynamic data to predict the phase stability for a given CCA composition and homogenization temperature. While high-throughput techniques dependent on CALPHAD techniques have been incorporated for the screening of candidate CCA compositions [55, 56], they often are comparatively lower throughput than ML methods nor do they account for experimentally observed metastable phases. Thus, this work utilized CALPHAD based techniques for a given CCA system varying only in the composition of one element for each series. In addition to identifying the effect of composition, CALPHAD techniques are beneficial in selection of processing temperatures. While processing techniques in this work are generally limited to high-temperature homogenization treatments intended to remove undesirable phases from the microstructure, evaluation of additional processing techniques on corrosion behavior and overall CCA properties remains an opportunity for future work.

Computational techniques are integrated into the cyclic design process illustrated in Figure 2. The ML model is incorporated over a range of proposed compositions to identify which may have a desirable microstructure. Additionally, the high-throughput computational loop may easily incorporate calculations for CCA cost and density using the equations above. Although there are no defined thresholds for CCAs cost and density as in the case of targeted microstructures, CCA compositions with low costs and/or densities are generally targeted for experimental synthesis. Additionally, low-throughput CALPHAD is also integrated to confirm the presence of a targeted microstructure as well as evaluate the composition and volume fraction of each phase. Mechanical modeling described elsewhere [24] may be used to predict yield strength as a function of second phase structure and volume fraction. Additionally, the compositions of each phase suggested by CALPHAD may be vetted prior to synthesis to ensure each phase has an adequate concentration of passivating elements [43]. Following synthesis, CCA series are experimentally characterized. The effects of both the presence and concentration of constituent elements are used to inform the selected elements and evaluated composition range for future sweeps of the design process.

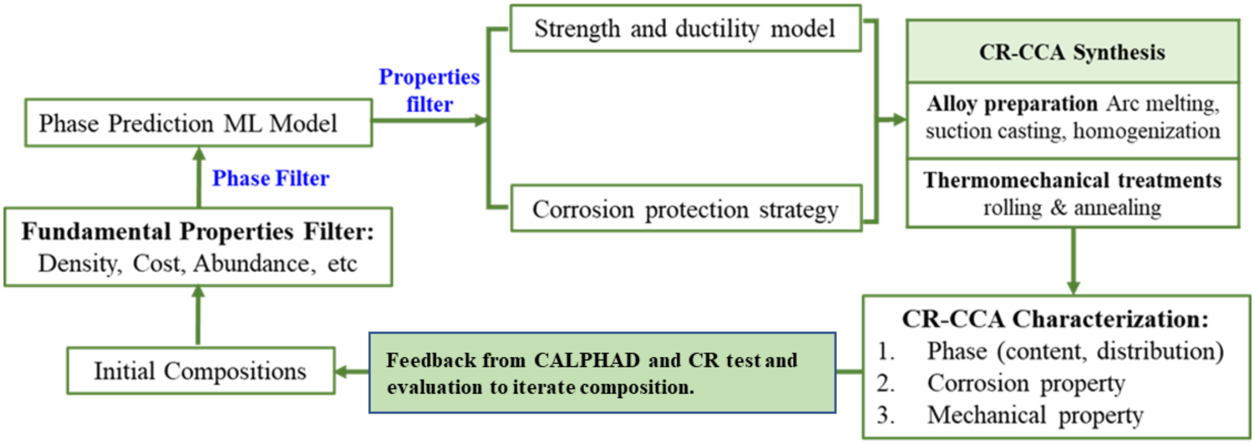

Figure 2: Schematic representation of design process utilized in this work

2.6 Properties of Evaluated CCAs

The density and cost of the CCAs evaluated in this work is summarized in Figure 3 below. The evaluated CCAs generally range in cost between 4.8 and 6.0 \$/kg, with densities between 7.0 and 8.0 g/cm^3. The CCAs offer marginal density decreases relative to 316L, but have significantly higher costs. Generally, the single-phase CCAs are suggested to be more dense than the two- or three-phase CCAs. This generally results from changes in the concentrations of Al and Ti, two lightweight elements which are shown to increase the likelihood of second and third phase formation. The low cost of Al relative to the targeted alloy space indicates that increasing Al concentrations will decrease the alloy cost, whereas the high cost of Ti relative to the alloy space indicates increasing Ti concentration generally increases the overall alloy cost when the ratios between other elements are held constant. The effects of Al and Ti on CCA microstructure and corrosion behavior are discussed further in Chapters 2 and 3, respectively. Mn has a similar density as the evaluated CCAs. Therefore, while increasing Mn concentrations can decrease alloy cost, it does not significantly affect density. Mo, while having a significantly higher cost and density than the alloy class, is only evaluated at concentrations up to 3 at. %, and thus, does not affect density to the same degree of other elements which were added at higher concentrations. Studies probing the effect of Mn and Mo concentration on corrosion behavior are described in Chapters 4 and 5, respectively.

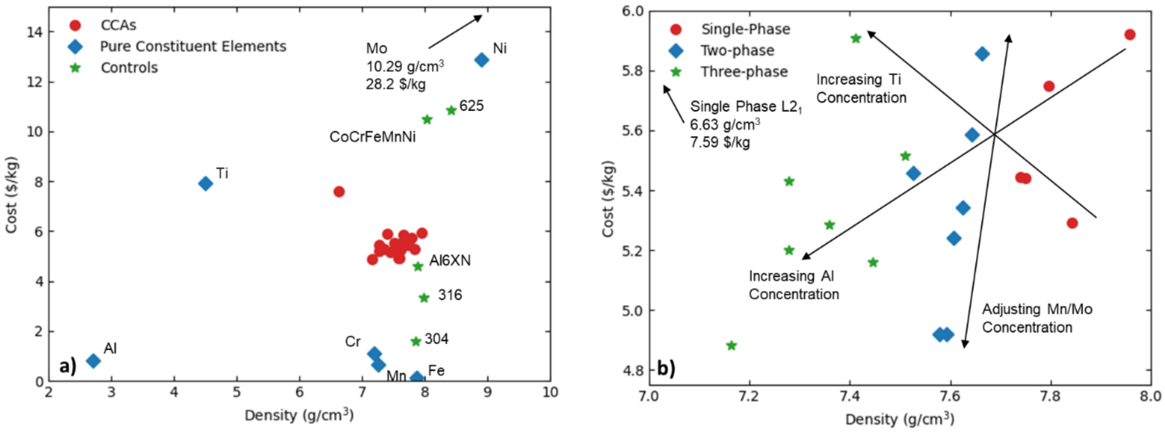

Figure 3: Cost and density calculations for the alloy series evaluated in this work **a)** compared to pure constituent elements and common corrosion resistant alloys and **b)** shown relative to alloy microstructures.

3.0 Summary

This work evaluates four series of CCAs selected to isolate the effects of individual elements on microstructure and corrosion behavior of CCAs. Al and Ti have been identified as two elements capable of both decreasing CCA density and improving passivity due to the presence of thermodynamically stable oxides. However, at high concentrations, each element can promote the formation of additional phases in the microstructure which may limit corrosion resistance. Thus, for each element, a tradeoff between beneficial and adverse contributions to both corrosion resistance and overall fulfillment of design goals. Therefore, individual alloy series are developed and synthesized to evaluate such effects as described below.

Chapter 2 probes the effect of Al concentration on the microstructure and corrosion resistance of a synthesized CCA series. Increasing Al concentrations are shown to decrease CCA density and cost for the system. The thermodynamic stability of Al passive species suggests Al will be a significant constituent element in the passive film when added at high concentration, and could possibly improve overall alloy passivity. Passivity is evaluated with combinations of electrochemical impedance spectroscopy (EIS) and potentiodynamic polarization with the chemical species in the protective oxide film identified with X-ray photoelectron spectroscopy (XPS). In addition to its contributions to passivity, Al is also expected to promote the formation of additional phases in the microstructure, which could increase susceptibility to localized corrosion. Localized corrosion is evaluated with breakdown characterization during and following potentiodynamic polarization. Thus, this chapter seeks to both confirm the existence of a microstructure-passivity tradeoff with increasing Al concentration as well as optimize such a trade-off to identify an optimal Al concentration for the evaluated alloy series.

As in the case of Al, the microstructure-passivity tradeoff is explored for the effect of Ti concentration in a CCA series described in Chapter 3. Like Al, Ti has a thermodynamically stable passive film in neutral environments that is expected to contribute to, and likely improve, corrosion resistance [57]. However, like the case of Al, Ti is also expected to stabilize additional phases in the microstructure which could act initiation sites for localized corrosion. Thus, similar to the case of Chapter 2, Chapter 3 seeks to use combinations of microstructural analysis, potentiodynamic polarization, EIS, and XPS to verify the existence of a microstructure-passivity tradeoff with increasing Ti concentration for overall corrosion resistance as well as to provide guidelines for optimization of Ti content for corrosion resistance in CCA systems.

Both Chapters 2 and 3 explore possible microstructural consequences of the addition of lightweight elements. However, such microstructural effects are dependent on the entirety of the alloy system. Given the benefits of increasing Al and Ti concentrations on lightweighting and possibly corrosion resistance, it is of interest to evaluate the effects of other elements on the microstructure as well as overall corrosion resistance. Thus, Chapters 4 and 5 probe the effect of other elements which are not expected to significantly alter alloy density, but may still affect the corrosion resistance and/or composition of individual phases. In both cases, CCA series with all alloys having two phases are developed to isolate effects strictly to those of individual elements and not to adverse effects of second and/or third phase formation.

In Chapter 4, the microstructure and corrosion resistance of a series of CCAs with varying Mn concentrations is evaluated based on observations of decreased partitioning of passivating species, specifically Al and Ti, relative to Mn-free CCAs. It is proposed that a trade-off exists between possible decreases in microstructural partitioning, which would allow all passivating elements to locally coexist and possibly have beneficial effects from their coexistence, with the well-established adverse effects of Mn on corrosion resistance. Traditional microstructural analysis techniques are paired with potentiodynamic polarization and EIS to evaluate the effects of Mn on microstructure and overall corrosion resistance. Additionally, to evaluate the elemental fates, XPS is used to characterize the passive film and individual elemental dissolution rates are tracked with atomic emission spectroelectrochemisry (AESEC) in efforts to identify evaluate the possibility of improvement in corrosion resistance with the addition of Mn.

Unlike the case of Mn, Mo has well established effects on corrosion resistance, mainly through improving resistance to localized corrosion. However, many third-phase regions formed in the evaluated alloy series are enriched in Mo. Therefore, decreasing Mo concentration may be of interest in order to allow for increased Al and/or Ti concentrations without adverse third-phase formation. However, to decrease Mo concentration, the effects on corrosion behavior must first be evaluated. Chapter 5 describes a series of CCAs with varying Mo concentration that is evaluated for corrosion resistance using combinations of potentiodynamic polarization, EIS, and AESEC. Additionally, the morphology of localized corrosion is addressed with regards to microstructural features to evaluate the degree to which removing or decreasing the concentration of Mo harms resistance to localized corrosion.

The initial four body chapters explore tradeoffs between alloy microstructure and corrosion behavior. However, evaluated microstructural features include second phase regions that vary in both volume fraction and composition, rendering it difficult to identify which of the two factors is responsible for the change in corrosion behavior. Thus, in Chapter 6, two single-phase CCAs with compositions selected to represent the compositions of each individual phase in a selected dual-phase CCA are synthesized. Corrosion behavior is evaluated using combinations of potentiodynamic polarization and EIS before comparison to the dual-phase CCA. Additionally, the morphology of the passive film is characterized with combinations of XPS, Auger electron microscopy, and transmission electron microscopy. The selected CCAs are utilized to determine to what degree may composite theory be applied to the corrosion behavior of multi-phase CCAs to predict both passivity and resistance to localized breakdown. These findings, in combination with those made in Chapters 2-5, are utilized to improve to inform the overall design of multi-phase corrosion-resistant CCAs.

References

[1] B. Cantor, I.T.H. Chang, P. Knight, A.J.B. Vincent, Microstructural development in equiatomic multicomponent alloys, Materials Science and Engineering: A, 375-377 (2004) 213-218.

[2] J.W. Yeh, S.K. Chen, S.J. Lin, J.Y. Gan, T.S. Chin, T.T. Shun, C.H. Tsau, S.Y. Chang, Nanostructured High-Entropy Alloys with Multiple Principal Elements: Novel Alloy Design Concepts and Outcomes, Advanced Engineering Materials, 6 (2004) 299-303.

[3] Y.Y. Chen, U.T. Hong, H.C. Shih, J.W. Yeh, T. Duval, Electrochemical kinetics of the high entropy alloys in aqueous environments—a comparison with type 304 stainless steel, Corrosion Science, 47 (2005) 2679-2699.

[4] Y.-J. Hsu, W.-C. Chiang, J.-K. Wu, Corrosion behavior of FeCoNiCrCux high-entropy alloys in 3.5% sodium chloride solution, Materials Chemistry and Physics, 92 (2005) 112-117.

[5] Y. Qiu, S. Thomas, M.A. Gibson, H.L. Fraser, N. Birbilis, Corrosion of high entropy alloys, npj Materials Degradation, 1 (2017) 15.

[6] D.B. Miracle, O.N. Senkov, A critical review of high entropy alloys and related concepts, Acta Materialia, 122 (2017) 448-511.

[7] J. Qi, A.M. Cheung, S.J. Poon, High Entropy Alloys Mined From Binary Phase Diagrams, Scientific Reports, 9 (2019) 15501.

[8] K.N. Sasidhar, N.H. Siboni, J.R. Mianroodi, M. Rohwerder, J. Neugebauer, D. Raabe, Enhancing corrosion-resistant alloy design through natural language processing and deep learning, Science Advances, 9 (2023) eadg7992.

[9] C. Wen, Y. Zhang, C. Wang, D. Xue, Y. Bai, S. Antonov, L. Dai, T. Lookman, Y. Su, Machine learning assisted design of high entropy alloys with desired property, Acta Materialia, 170 (2019) 109-117.

[10] Y. Shi, B. Yang, P.K. Liaw, Corrosion-Resistant High-Entropy Alloys: A Review, in: Metals, 2017.

[11] D. Sur, E.F. Holcombe, W.H. Blades, E.A. Anber, D.L. Foley, B.L. DeCost, J. Liu, J. Hattrick-Simpers, K. Sieradzki, H. Joress, J.R. Scully, M.L. Taheri, An Experimental High-Throughput to High-Fidelity Study Towards Discovering Al–Cr Containing Corrosion-Resistant Compositionally Complex Alloys, High Entropy Alloys & Materials, (2023) 1-18.

[12] S.B. Inman, J. Han, M.A. Wischhusen, J. Qi, S.R. Agnew, K. Ogle, J.R. Scully, Passivation and localized corrosion resistance of Al0.3Cr0.5Fe2MoxNi1.5Ti0.3 compositionally complex alloys: Effect of Mo content, Corrosion Science, 227 (2024) 111692.

[13] C.D. Taylor, P. Lu, J. Saal, G.S. Frankel, J.R. Scully, Integrated computational materials engineering of corrosion resistant alloys, npj Materials Degradation, 2 (2018) 6.

[14] K. Wang, J. Han, A.Y. Gerard, J.R. Scully, B.-C. Zhou, Potential-pH diagrams considering complex oxide solution phases for understanding aqueous corrosion of multi-principal element alloys, npj Materials Degradation, 4 (2020) 35.

[15] T.H. Muster, A. Trinchi, T.A. Markley, D. Lau, P. Martin, A. Bradbury, A. Bendavid, S. Dligatch, A review of high throughput and combinatorial electrochemistry, Electrochimica Acta, 56 (2011) 9679-9699.

[16] D. Sur, H. Joress, J. Hattrick-Simpers, J.R. Scully, A High Throughput Aqueous Passivation Testing Methodology for Compositionally Complex Alloys Using a Scanning Droplet Cell, Journal of The Electrochemical Society, 170 (2023) 081507.

[17] S.B. Inman, J. Han, A.Y. Gerard, J. Qi, M.A. Wischhusen, S.R. Agnew, S.J. Poon, K. Ogle, J.R. Scully, Effect of Mn Content on the Passivation and Corrosion of Al0.3Cr0.5Fe2MnxMo0.15Ni1.5Ti0.3 Compositionally Complex Face-Centered Cubic Alloys, Corrosion, 78 (2021) 32-48.

[18] Y. Shi, L. Collins, N. Balke, P.K. Liaw, B. Yang, In-situ electrochemical-AFM study of localized corrosion of AlxCoCrFeNi high-entropy alloys in chloride solution, Applied Surface Science, 439 (2018) 533-544.

[19] S.B. Inman, D. Sur, J. Han, K. Ogle, J.R. Scully, Corrosion Behavior of a Compositionally Complex Alloy Utilizing Simultaneous Al, Cr, and Ti Passivation, Corroison Science, 217 (2023) 111138.
[20] S. Choudhary, Y. Qiu, S. Thomas, N. Birbilis, Element-resolved electrochemical analysis of transpassive dissolution and repassivation behavior of the multi-principal element alloy AlTiVCr, Electrochimica Acta, 362 (2020) 137104.
[21] T. Li, O.J. Swanson, G.S. Frankel, A.Y. Gerard, P. Lu, J.E. Saal, J.R. Scully, Localized corrosion behavior of a single-phase non-equimolar high entropy alloy, Electrochimica Acta, 306 (2019) 71-84.
[22] W.H. Blades, B.W.Y. Redemann, N. Smith, D. Sur, M.S. Barbieri, Y. Xie, S. Lech, E. Anber, M.L. Teheri, C. Wolverton, T.M. McQueen, J.R. Scully, K. Seradzki, Tuning Chemical Short-range Order for Stainless Behavior at Reduced Chromium Concentrations in Multi-principal Element Alloys, (2023).
[23] Y.L. Chou, J.W. Yeh, H.C. Shih, The effect of molybdenum on the corrosion behaviour of the high-entropy alloys Co1.5CrFeNi1.5Ti0.5Mox in aqueous environments, Corrosion Science, 52 (2010) 2571-2581.
[24] J.J. Bhattacharyya, S.B. Inman, M.A. Wischhusen, J. Qi, J. Poon, J.R. Scully, S.R. Agnew, Light Weight, Low Cost, and Compositionally Complex Multiphase Alloys with Optimized Strength, Ductility and Corrosion Resistance: Discovery, Design and Mechanistic Understandings, Materials & Design, 228 (2023).
[25] W. Guo, J. Li, M. Qi, Y. Xu, H.R. Ezatpour, Effects of heat treatment on the microstructure, mechanical properties and corrosion resistance of AlCoCrFeNiTi0.5 high-entropy alloy, Journal of Alloys and Compounds, 884 (2021) 161026.
[26] X.-W. Qiu, Y.-P. Zhang, L. He, C.-g. Liu, Microstructure and corrosion resistance of AlCrFeCuCo high entropy alloy, Journal of Alloys and Compounds, 549 (2013) 195-199.
[27] Q. Zhao, Z. Pan, X. Wang, H. Luo, Y. Liu, X. Li, Corrosion and passive behavior of AlxCrFeNi3−x (x = 0.6, 0.8, 1.0) eutectic high entropy alloys in chloride environment, Corrosion Science, 208 (2022) 110666.
[28] R. Wang, K. Zhang, C. Davies, X. Wu, Evolution of microstructure, mechanical and corrosion properties of AlCoCrFeNi high-entropy alloy prepared by direct laser fabrication, Journal of Alloys and Compounds, 694 (2016).
[29] C.-C. Yen, H.-N. Lu, M.-H. Tsai, B.-W. Wu, Y.-C. Lo, C.-C. Wang, S.-Y. Chang, S.-K. Yen, Corrosion mechanism of annealed equiatomic AlCoCrFeNi tri-phase high-entropy alloy in 0.5 M H2SO4 aerated aqueous solution, Corrosion Science, 157 (2019) 462-471.
[30] X.-L. Shang, Z.-J. Wang, Q.-F. Wu, J.-C. Wang, J.-J. Li, J.-K. Yu, Effect of Mo Addition on Corrosion Behavior of High-Entropy Alloys CoCrFeNiMox in Aqueous Environments, Acta Metallurgica Sinica (English Letters), 32 (2019) 41-51.
[31] Z. Niu, Y. Wang, C. Geng, J. Xu, Y. Wang, Microstructural evolution, mechanical and corrosion behaviors of as-annealed CoCrFeNiMox (x = 0, 0.2, 0.5, 0.8, 1) high entropy alloys, Journal of Alloys and Compounds, 820 (2020) 153273.
[32] Y. Qiu, S. Thomas, D. Fabijanic, A.J. Barlow, H.L. Fraser, N. Birbilis, Microstructural evolution, electrochemical and corrosion properties of AlxCoCrFeNiTiy high entropy alloys, Materials & Design, 170 (2019) 107698.
[33] S. Shuang, Q. Yu, X. Gao, Q.F. He, J.Y. Zhang, S.Q. Shi, Y. Yang, Tuning the microstructure for superb corrosion resistance in eutectic high entropy alloy, Journal of Materials Science & Technology, 109 (2022) 197-208.
[34] X.-W. Qiu, C.-G. Liu, Microstructure and properties of Al2CrFeCoCuTiNix high-entropy alloys prepared by laser cladding, Journal of Alloys and Compounds, 553 (2013) 216-220.
[35] Y. Fu, J. Li, H. Luo, C. Du, X. Li, Recent advances on environmental corrosion behavior and mechanism of high-entropy alloys, Journal of Materials Science & Technology, 80 (2021) 217-233.

[36] A.S.M.I.H. Committee, ASM handbook. Volume 1, Properties and selection: irons, steels, and high-performance alloys, in, ASM International Materials Park, OH, Materials Park, OH, 1990.
[37] M.A. Melia, J.D. Carroll, S.R. Whetten, S.N. Esmaeely, J. Locke, E. White, I. Anderson, M. Chandross, J.R. Michael, N. Argibay, E.J. Schindelholz, A.B. Kustas, Mechanical and Corrosion Properties of Additively Manufactured CoCrFeMnNi High Entropy Alloy, Additive Manufacturing, 29 (2019) 100833.
[38] A. Murphy, Light Alloys for Marine Engines, Transactions, 57 (1945).
[39] B. Hayman, M. Dogliani, I. Kvale, A.M. Fet, Technologies for reduced environmental impact from ships-Ship building, maintenance and dismantling aspects, ENSUS-2000, Newcastle upon Tyne, UK, (2000).
[40] Density of Metals and Alloys, in: Corrosion: Materials, ASM International, 2005, pp. 0.
[41] Archimedes, On Floating Bodies (in Greek), 1 (c. 246 B.C.).
[42] Mineral commodity summaries 2023, in: Mineral Commodity Summaries, Reston, VA, 2023, pp. 210.
[43] S.B. Inman, J.R. Scully, Design and Discovery of Compositionally Complex Alloys (CCA) that Include High Corrosion Resistance, Corrosion, 80 (2024) 250-258.
[44] X. Fu, C.A. Schuh, E.A. Olivetti, Materials selection considerations for high entropy alloys, Scripta Materialia, 138 (2017) 145-150.
[45] J.R. Scully, S.B. Inman, A.Y. Gerard, C.D. Taylor, W. Windl, D.K. Schreiber, P. Lu, J.E. Saal, G.S. Frankel, Controlling the corrosion resistance of multi-principal element alloys, Scripta Materialia, 188 (2020) 96-101.
[46] ASTM, D1141-98 Standard Practice for Preparation of Substitute Ocean Water, in, 2021.
[47] C. Varvenne, W.A. Curtin, Predicting yield strengths of noble metal high entropy alloys, Scripta Materialia, 142 (2018) 92-95.
[48] C. Varvenne, A. Luque, W.A. Curtin, Theory of strengthening in fcc high entropy alloys, Acta Materialia, 118 (2016) 164-176.
[49] Y. Wang, B. Goh, P. Nelaturu, T. Duong, N. Hassan, R. David, M. Moorehead, S. Chaudhuri, A. Creuziger, J. Hattrick-Simpers, D.J. Thoma, K. Sridharan, A. Couet, Integrated High-Throughput and Machine Learning Methods to Accelerate Discovery of Molten Salt Corrosion-Resistant Alloys, Advanced Science, 9 (2022) 2200370.
[50] D. Sur, E.F. Holcombe, W.H. Blades, E.A. Anber, D.L. Foley, B.L. DeCost, J. Liu, J. Hattrick-Simpers, K. Sieradzki, H. Joress, J.R. Scully, M.L. Taheri, An Experimental High-Throughput to High-Fidelity Study Towards Discovering Al–Cr Containing Corrosion-Resistant Compositionally Complex Alloys, High Entropy Alloys & Materials, 1 (2023) 336-353.
[51] X. Liu, J. Zhang, Z. Pei, Machine learning for high-entropy alloys: Progress, challenges and opportunities, Progress in Materials Science, 131 (2023) 101018.
[52] J.M. Rickman, G. Balasubramanian, C.J. Marvel, H.M. Chan, M.T. Burton, Machine learning strategies for high-entropy alloys, Journal of Applied Physics, 128 (2020) 221101.
[53] L. Qiao, Y. Liu, J. Zhu, A focused review on machine learning aided high-throughput methods in high entropy alloy, Journal of Alloys and Compounds, 877 (2021) 160295.
[54] W. Huang, P. Martin, H.L. Zhuang, Machine-learning phase prediction of high-entropy alloys, Acta Materialia, 169 (2019) 225-236.
[55] R. Feng, C. Zhang, M.C. Gao, Z. Pei, F. Zhang, Y. Chen, D. Ma, K. An, J.D. Poplawsky, L. Ouyang, Y. Ren, J.A. Hawk, M. Widom, P.K. Liaw, High-throughput design of high-performance lightweight high-entropy alloys, Nature Communications, 12 (2021) 4329.
[56] R. Li, L. Xie, W.Y. Wang, P.K. Liaw, Y. Zhang, High-Throughput Calculations for High-Entropy Alloys: A Brief Review, Frontiers in Materials, 7 (2020).
[57] M. Pourbaix, Atlas of electrochemical equilibria in aqueous solutions, in, National Association of Corrosion Engineers, Houston, Tex., 1974.

Chapter 2: Effect of Al on the corrosion resistance of CCAs: Evaluation of corrosion resistance, passive film properties, and microstructure

Abstract

A series of $Al_xCr_{0.5}Fe_2Mn_{0.25}Mo_{0.15}Ni_{1.5}Ti_{0.3}$ complex concentrated alloys with Al concentrations between 0 and 14.3 at. % were synthesized, homogenized, and characterized for microstructure and corrosion behavior. Low-Al alloys had an FCC microstructure whereas at high Al concentrations, $L2_1$ second phase regions enriched in Al, Ni, Ti are present at Al concentrations beyond 6 at. % with a third BCC-like phase enriched in Cr and Mo enriched at Al concentrations beyond 9.6 at. %. Corrosion resistance was characterized with combinations of potentiodynamic polarization, passive film growth during potentiostatic exposure, and electrochemical impedance spectroscopy in dilute NaCl at a natural pH. The highest pitting potential was found at 6 at. % with decreasing resistance to localized corrosion at higher Al concentrations primarily attributed to the presence and composition of second or third phase and their resultant interfaces which function as pit initiation sites. However, trends between Al concentration and polarization resistance or other metrics traditionally used to evaluate passivity and protectiveness were often insignificant. Protectiveness was compared to the attributes of the passive film. Al(III) was observed within the passive film at levels enriched relative to the bulk composition alongside Cr(III) and Ti(IV) species. The interplay between Al concentration, bulk microstructure phase stability, passivity, and corrosion behavior are discussed.

1.0 Introduction

Complex concentrated alloys (CCAs), a subset of the high entropy alloy (HEA) class, consist of four or more elements at concentrations ranging between 5 and 35 at. %. The characteristic multi-principal element nature of the alloys often allows for the benefits of each element to contribute to global alloy properties. Furthermore, combinations of elements often not seen in conventional alloys allows for "cocktail effect" type properties arising from elemental combinations or synergies not observed in the case of either pure element [1]. Specific design criteria to may therefore addressed by the addition of individual elements, however, it is necessary to address both adverse effects of an element and its combinations during the design process. The low density of Al and excellent air oxidation resistance of Al has made it a frequent addition to CCAs targeting low density as both a constituent of refractory-metal dominated CCAs [2, 3] and as an addition to transition-metal dominated CCAs [4-6]. Al has been shown to be effective in reducing densities in transition-metal based CCAs through both Vegard's law based predictive modeling and experimental verification [4]. Additionally, the comparatively low cost, both in terms of direct and indirect (e.g. volatility, geopolitical concentration) cost, of Al compared to other frequent alloying additions can lead to cost reduction with increasing Al composition [7].

Increasing additions of Al to CCAs often promotes the formation of new phases, particularly in the case of transition-metal based FCC CCAs [1, 4, 5, 8-10]. Phase partitioning is aided by the limited solubility of Al with Ni [11] and γ-Fe [12], two elements commonly found at high concentrations in such alloys. Furthermore, the high atomic radius and low melting temperature of Al, along with favorable enthalpies of formation for intermetallic compounds containing Al, all decrease thermodynamic indicator terms that can be used to predict single-phase stability for CCAs [1, 4, 13, 14]. Thus Al, particularly when added at high concentrations, may be reasonably expected to decrease the likelihood of single-phase microstructures when added to FCC transition-metal CCAs [4].

Al-containing CCAs with an FCC matrix have been observed with second phases including BCC [4, 5, 15-21], B2 [9, 19, 21-25], $L2_1$ (Heusler) [26-28], and $L1_2$ [24, 29]. The phase volume fraction, and by extension, the mechanical properties, have been shown to be tunable through alterations of the Al concentration. Bhattacharyya et al. [30] evaluated a series of Al-Cr-Fe-Mn-Mo-Ni-Ti CCAs with an FCC matrix. With increasing Al concentration, the alloy density decreased. Additionally, a $L2_1$ second phase formed and increased in area fraction with Al concentration, with a BCC third phase formed at high Al concentrations. The increasing $L2_1$ volume fraction was shown to significantly improve yield strength at the expense of ductility. Similar results of mechanical strengthening with Al-induced second phase formation have been obtained across a variety of systems [1, 21, 24, 29]. Despite the strong benefits of second phase formation on mechanical strengthening, such formation can have adverse consequences on CCA corrosion behavior.

Al may affect CCA corrosion behavior through both passivity and microstructural effects. Therefore, it is difficult to simplify the effect of Al addition and concentration into a singular effect on corrosion behavior. Nevertheless, several studies have evaluated the effect of Al both in transition metal CCAs and in simplified systems. Peng et al. [31] polarized a series of Fe-Al binary alloys in sulfuric acid, finding that the passivity is improved at higher Al concentrations with the improvements most notable upon reaching an approximately 15 at. % Al threshold (similar to the well-established 12 at. % Cr threshold in Fe-Cr binary alloys [32]). Springer et al. [33] surveyed a range of Fe-Cr-Al alloys via salt spray testing, finding that although Al is a less effective passivator than Cr, Al concentrations of 8-10 % can reduce the necessary Cr threshold for stable passivation, suggesting coexistence of Al and Cr in the passivation process. Rebak et al. [34] also evaluated the corrosion resistance of Fe-Cr-Al nuclear cladding, finding some compositions to be equivalent to or superior to Fe-Cr based stainless steels but did not provide guidelines for compositional optimization. Despite the potential benefits of Al addition to Fe-Cr, a clear mechanism or 'third element effect' has not been shown as in the case of high-temperature oxidation [35, 36]. One proposed mechanism involves the introduction of short-range order enhancing Cr-Cr clustering. The effects of Cr-percolation on passivity kinetics have been long-established [37], but have since been extended to Al-containing CCAs [38].

Alternative possible mechanisms involve the presence of Al within the passive film, often while coexisting with other elements. Multi-cation oxides, formed by either solid solution solubility or stochiometric line compounds, may improve the corrosion resistance of CCAs by broadening the stability range for constituent metals whose passive species may otherwise be unstable [39, 40]. Al has been shown to improve the corrosion resistance present in the passive film of Fe-Mn-Al alloys [41], an effect suggested to be more prominent when Cr is present [42]. In addition to Cr, Al has been suggested to enrich in the passive film at similar depths as Ti(IV) in Fe-Cr-Al-Ti alloys [43] along with the $Al_{1.5}TiVCr$ [44] and $Al_{0.3}Cr_{0.5}Fe_2Mn_{0.25}Mo_{0.15}Ni_{1.5}Ti_{0.3}$ [45] CCAs, further suggesting possible coexistence and demonstrating viability for the implementation of Al in CCAs depending on multiple passivating species. However, further work is necessary to evaluate the structural nature of the passive film and the nearest neighbor arrangement of Al to confirm the nature of the multi-cation interactions.

Al has been suggested to dissolve at the highest rates during open circuit corrosion of the AlCrTiV CCA [46], suggesting it may play a less prominent role in the passivity of the alloy. Furthermore, Al_2O_3 formed on pure Al is only thermodynamically stable at near-neutral pH ranges [47], which could lead to significantly reduced corrosion resistance of Al-dependent CCAs in acidic or basic environments, and has also been suggested to limit protectiveness in CCAs due to its porosity [15, 16, 48].

The benefits of Al as both a low-density element and stable passivator have often been applied in corrosion resistant CCA design, however, microstructural effects often considerably complicate the optimization of composition. Thus, in CCAs where Al leads to the formation or growth in volume fraction of additional phases, it often is regarded as having adverse effects on the corrosion resistance [8-10, 16, 18, 20, 21, 25, 48-52]. Shi et al. [9, 48, 49] developed a series of studies evaluating the corrosion behavior of a series of $Al_xCoCrFeNi$ CCAs in chloride. The lowest Al concentration (7.0 at. % Al) had a single-phase FCC microstructure that corroded via random pitting and had the best overall corrosion resistance in terms of both pitting and current densities in the passive range. At higher concentrations, BCC phases were present with random pitting at the phase interface observed at 11.1 at. % Al, and preferential dissolution of the BCC phase with the worst overall corrosion resistance at 14.9 at. % Al. The studies illustrate that Al can affect second phase formation in the microstructure, leading to inferior corrosion resistance. Lee et al. [16] evaluated the microstructure and corrosion resistance of the $Al_xCrFe_{1.5}MnNi_{0.5}$ series in sulfate and chloride solutions. The Al-free alloy had an FCC matrix. Increasing BCC volume fractions formed with Al concentration that eventually formed a single-phase BCC matrix at 11.1 at. % Al. Increasing Al concentration both increased the passive current density and decreased the Cl^--induced pitting potential, a phenomenon that was attributed to either stabilization of the BCC matrix or possible inhibition of Cr passivation.

The passive films of CCAs with multi-phase microstructures has been shown to vary in composition following the local bulk microstructure composition [53, 54]. An Al-Cr-Fe-Mn-Mo-Ni-Ti CCA with an FCC (Fe, Cr, Mo enriched) matrix and $L2_1$ (Al, Ni, Ti enriched) second phase regions showed two distinct phases in the passive film that were suggested to mainly be protected by Cr in the regions over the FCC phase and by Al and Ti in the regions over the $L2_1$ phase. The corrosion resistance of the dual-phase alloy was attributed to the simultaneous ability of both phases to passivate [54]. Therefore, it becomes necessary to ensure all phases have an adequate concentration of passivating elements when evaluating proposed CCA compositions and microstructures.

While Al can be beneficial to alloy design by reducing densities, cost, and possibly passivity, adverse effects on corrosion behavior necessitates a more thorough analysis of its effects when added in low concentrations to a multi-phase CCA system. CCAs with varying Al compositions with the ratios between all other elements held constant as balance were synthesized, analyzed for microstructure, and evaluated for corrosion resistance. Additionally, the passive film composition was characterized to determine both the enrichment of Al as well as its effects on overall passive film composition. Passive film attributes were correlated with corrosion resistance evaluated using electrochemical methods. Significant enrichment both of Al and other stable passivators could promote improved corrosion resistance. The chapter provides a comprehensive evaluation of the effect of Al concentration on the corrosion behavior of an $L2_1$-strengthened FCC CCA series at low Al levels while also developing mechanistic understanding to the well-established effects of Al on lightweight CCA corrosion resistance. The findings are discussed relative to work on systems that alter bulk microstructure phase stability and that change Al concentration while preserving a single-phase microstructure to better determine whether the effects of Al on corrosion behavior is strictly microstructural or also a function of contributions to passivity.

2.0 Experimental Methods

2.1 CCA Synthesis and Microstructural Characterization

Eight CCAs with composition listed in Table I were prepared by arc-melting pure metals (Cr > 99.2 % purity, all other metals > 99.9 % purity). Compositions had varying Al concentrations with the ratio between all other elements held constant, leading to the majority of increasing Al concentrations being compensated by decreased Fe and Ni with the concentration of most other element changing by less than 1 at. %. Phase stability was first predicted with a CALPHAD isopleth diagram developed on ThermoCalc software the TCHEA3 database. Each sample was melted and flipped five times to ensure homogeneity in a Cu hearth before suction casting into a 1 cm water-cooled Cu button mold. Samples were encapsulated under Ar and homogenized for 5 hours at 1070 ˚C before water quenching, a treatment informed by the isopleth diagram shown in Figure 1 produced with Thermocalc TCHEA3 database. A wide range of phases are predicted including single-phase FCC, alongside additions of $L2_1$, BCC, and/or B2. Compositions were confirmed to within 0.5 at. % for each element by energy dispersive spectroscopy (EDS) measurements described further below.

Table I: CCA compositions in atomic percent. Pure elements were massed to compositions below within 1% error prior to arc melting.

Alloy	Al	Cr	Fe	Mn	Mo	Ni	Ti
Al-0	0.0	10.6	42.6	5.3	3.2	31.9	6.4
Al-3.1	3.1	10.3	41.2	5.2	3.1	30.9	6.2
Al-6.0	6.0	10.0	40.0	5.0	3.0	30.0	6.0
Al-8.2	8.2	9.8	39.1	4.8	2.9	29.3	5.9
Al-9.6	9.6	9.6	38.5	4.8	2.9	28.8	5.8
Al-11.4	11.4	9.4	37.7	4.7	2.8	28.3	5.7
Al-13.0	13.0	9.3	37.0	4.6	2.8	27.8	5.6
Al-14.3[1]	14.3	9.1	36.6	4.6	1.7	27.4	6.5

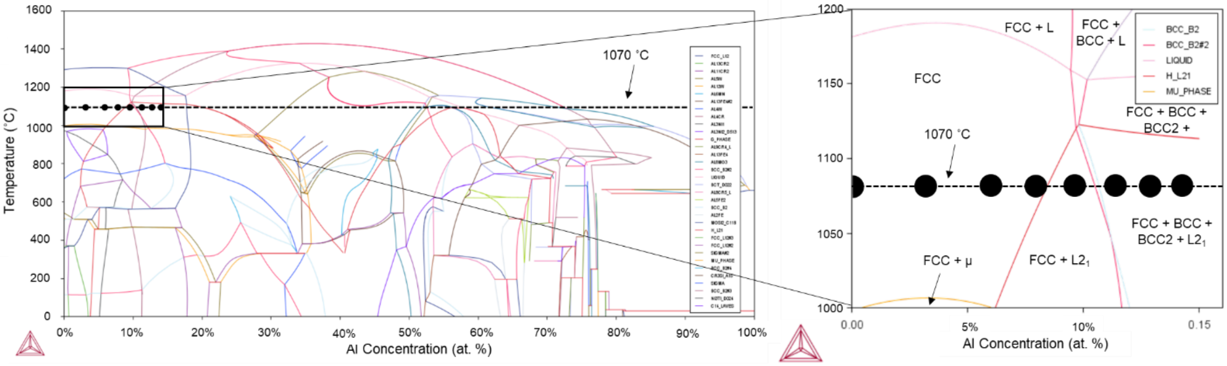

Figure 1: Isopleth diagram for the $Al_xCr_{0.5}Fe_2Mn_{0.25}Mo_{0.15}Ni_{1.5}Ti_{0.3}$ system produced with Thermocalc TCHEA3 database. Black circles indicate the synthesized compositions with the heat treatment indicated by the dashed line.

All samples were mechanically ground through 1200 grit and, in the case of microstructural and surface sensitive analysis, polished through 1-µm diamond suspension. Crystal structure of the present phases was evaluated with X-ray diffraction (XRD) with phase morphology characterized with scanning electron microscopy (SEM). A PANalytical Empyrean Diffractometer^{TM} was used for XRD with Cu Kα X-rays (1468.7 eV) and a scan rate of 0.15 °/s. The microstructure was imaged with SEM on an FEI Quanta 650^{TM} equipped with EDS in backscattered electron (BSE) and secondary electron (SE) imaging modes at an accelerating voltage of 15 keV, a spot size of 4, and a working distance of approximately 10 mm. The partitioning of elements to different phases was evaluated with EDS point scans, mapping, and a line scan with a 100 nm separation analyzed with Oxford Instruments Aztec^{TM} software. Phase area fractions were approximated with ImageJ threshold analysis.

---

[1] The Ti concentration of Al-14.3 was increased and the Mo concentration was decreased to limit undesirable fourth phase formation. The compositions are changed by less than 1 at. % from the ideal compositions for preserved elemental ratios, and thus are not expected to significantly alter trends in corrosion behavior.

2.2 Electrochemical Characterization

Corrosion behavior and passivity was evaluated with a series of electrochemical experiments. In all cases, a conventional three-electrode cell was used with the degreased CCA sample used as a working electrode, a platinum mesh counter electrode, and a saturated calomel reference electrode (SCE) relative to which all potentials (0.241 V vs. SHE) are reported. All procedures were regulated by a Gamry Instrument Reference 600+™ potentiostat and were evaluated in 0.01 M NaCl (pH ~5.75) continually bubbled with $N_{2(g)}$ throughout the duration of the test. All electrochemical tests were repeated threefold to ensure reproducibility. To evaluate the formation and corrosion resistance of the passive film, the air-formed oxide was first exposed to a cathodic reduction treatment by applying a -1.3 V_{SCE} potential for 600 s. The alloy was then potentiodynamically polarized in a cyclic manner from -1.3 to 0.8 V_{SCE} at a 0.5 mV/s scan rate. The -1.3 V_{SCE} potential for cathodic reduction was selected to expose the of any air-formed oxide to a potential below the standard reduction potential of Cr_2O_3 in a pH~5.75 environment[2]. The potential range for potentiodynamic polarization establishes considerable driving force for the formation of Al_2O_3, TiO_2, and Cr_2O_3, which are suggested to form at potentials more positive than -2.14, -1.87, and -1.30 V_{SCE}, respectively, on their respective pure metals in pH ~5.75 conditions by E-pH diagrams [47]. In-situ impedance measurements, which have been previously shown to track qualitative trends in passive film thickness [55, 56], were measured with AC monitoring at 1 Hz and an amplitude of 20 mV_{RMS} for every 0.005 V step. To evaluate the nature of pit initiation, BSE micrographs were obtained on separate runs where the polarization was terminated following the anodic current density reaching 10^{-5} $A.cm^{-2}$.

To evaluate the corrosion resistance of the air-formed passive film, a second procedure was used. The passive film was exposed to open circuit corrosion for 30 minutes directly following mechanical grinding to establish a stable open circuit potential (OCP). The dielectric behavior of the film was characterized with electrochemical impedance spectroscopy (EIS) at the stable OCP from an initial frequency of 100 kHz to a final frequency of 1 mHz at an AC amplitude of 20 mV_{RMS}. Following EIS, the film was polarized from -0.1 V relative to the OCP to 0.8 V_{SCE} before downward polarization from 0.8 to -1.3 V_{SCE} using the same in-situ impedance measurement techniques described above.

---

[2] While the standard reduction potentials of Al_2O_3 or TiO_2 on their pure constituent elements a -1.3 V_{SCE} potential has been suggested to be capable of reducing the air-formed oxide on similar alloys by in-situ impedance measurements [46]. The reduction is verified for the evaluated CCA series using similar impedance methods. Therefore, potentials below -1.3 V_{SCE} are not applied to avoid excess cathodic reaction rates.

Finally, a third sequence was used to evaluate the passive film formation trends with time. The air-formed oxide was first treated using the 600 s cathodic treatment at -1.3 V_{SCE} described above. The sample was then immediately exposed to a -0.25 V_{SCE} potential, which was indicated to be in the passive region by both initial polarization testing and previous studies, for 40 ks. Impedance was monitored in-situ every 6 s at a frequency of 1 Hz and a 20 mV_{RMS} AC amplitude.

Dissolution rates of individual elements during passive film growth with atomic emission spectroelectrochemistry (AESEC). A modified potentiostaic oxide growth procedure was repeated with the Al-6.0 CCA in a flow cell connected to a Horiba Jobin Yvon Ultima inductively coupled plasma system described elsewhere [57]. 0.1 M NaCl electrolytes with adjusted to a pH of 4 and 10 with concentrated HCl and NaOH, respectively, and were used to evaluate the effects of pH on elemental dissolution and increase dissolution rates to observable levels. A -1.3 V_{SCE} potential was first applied for 600 s to minimize the effect of the air-formed oxide. A -0.2 V_{SCE} potential, previously established to be within the Al-6.0 passive range, was then applied for 4000 s. Intensities at characteristic wavelengths (I_i) for each metal, i, were converted to dissolution rates (v_i) by normalizing to the flow rate (f) and exposure area (A). To compare elemental dissolution rates with electrochemical corrosion measurments, v_i was then converted to an equivalent current density for each element using Faraday's law, where z_i, F, and M_i refer to the charge of the most stable valence of a dissolved species for a given pH and potential [47], Faraday's constant, and the molar mass.

$$\nu_i = \frac{f I_i}{A} \tag{6}$$

$$j_i = \frac{z_i F \nu_i}{M_i} \tag{7}$$

Dissolution rates may be integrated to calculate the total mass loss rate (Q_i) with respect to time (t). Total mass loss relative to the original bulk composition (x_i) may then be calculated and compared to Fe, the metal with the highest bulk concentration, to determine the mass of remaining metal enriched at the surface ($\Theta_{i(t)}$). A further discussion of the methodology informing AESEC calculations may be found elsewhere [57].

$$Q_M(t) = \int_0^t \nu_M \tag{8}$$

$$\Theta_{\mathrm{M}}(t) = \frac{x_M Q_{Fe}(t)}{x_{Fe}} - Q_M(t) \tag{9}$$

2.3 Analysis of Passive Film Composition

For three alloys, Al-0, Al-6.0, and a third CCA with an Al concentration of 13.0 at. %, the composition and valence of the passive film was determined via X-ray photoelectron spectroscopy (XPS) following the passive film growth procedure in 0.01 M NaCl described above[3]. Directly following the film growth procedure described above, samples were transported under $N_{2(g)}$ to a PHI VersaProbe III^{TM} XPS system operating with Al Kα X-rays (1486.6 eV) over a 100 µm spot size. High resolution spectra were collected at a 26 eV pass energy with a 0.05 eV step size over the C1s, O1s, Al 2p (when present), Cr $2p_{3/2}$, Fe $2p_{1/2}$, Mn $2p_{1/2}$, Mo 3d, Ni $2p_{3/2}$, and Ti 2p core spectra, with the Fe and Mn spectra selected to avoid overlap with Ni Auger peaks. Background noise was subtracted with a Shirly background substitution before fitting data to features based off matching peak binding energy, width, and multiplet splitting to reference spectra previously obtained elsewhere [58-61]. Metallic (valance state of 0) features were fit with Doniach-Sunjic peaks to account for asymmetry while non-zero valence features were fit with Voigt peaks. Cumulative peak intensities for the non-metallic features attributable to a given element were normalized with system-specific relative sensitivity factors and then used to determine the surface cation fractions attributable to each element. The intensity of the Cr 3s peak, which overlaps the Al 2p region, was determined using the intensity of the Cr $2p_{3/2}$ spectrum normalized with system-specific relative sensitivity factors (RSF). In addition to high-resolution surface scans, low-resolution scans over each of the spectra listed above were obtained intermittent to 15 second periods of Ar sputtering over a 3 mm by 3 mm area for a total of 300 s of sputtering time. The intensities for each spectra were summed to obtain the depth profile of cation fractions for each element.

3.0 Results

3.1 CCA Phase Stability and Microstructure

XRD patterns for the CCA series following homogenization are shown in Figure 2. The FCC phase is indicated to be present for all evaluated CCAs. Additional peaks are present with increasing Al content, suggesting the formation of new phase that were indexed to $L2_1$ at Al concentrations of 6 at. % and beyond and BCC at Al concentrations of 9.6 at. % and beyond in addition to the FCC matrix. Regions of contrast in the BSE micrographs shown in Figure 3 confirm the formation of new phases. Al-0 and Al-3.1 are suggested by both XRD and BSE imaging to be a single-phase FCC matrix, whereas Al-6.0 and Al-8.2 have both an FCC matrix and $L2_1$ second phase regions generally of size scales between 1 and 10 µm. Alloys with Al contents

---

[3] A Mn-free CCA with an Al concentration of 13.6 at. % was used as a representative high-Al alloy for XPS analysis due to sample availability.

above 9 at. % all have a three-phase microstructure that was indexed by XRD to be a combination of FCC, $L2_1$, and BCC or BCC-like phases[4]. Notably, the micrographs suggest a more interspersed microstructure, as opposed to isolated phases typical of second-phase strengthened FCC matrix. The volume fraction of the $L2_1$ phase increases with Al concentration in both the two and three phase CCAs (not shown, available elsewhere [30]). The present phases are summarized and compared to CALPHAD predictions in Table II. The CALPHAD techniques correctly identified the presence of $L2_1$ and BCC-like phases at increasing Al concentrations, although the Al concentrations at which such phases form were not experimentally observed at the same values as predicted.

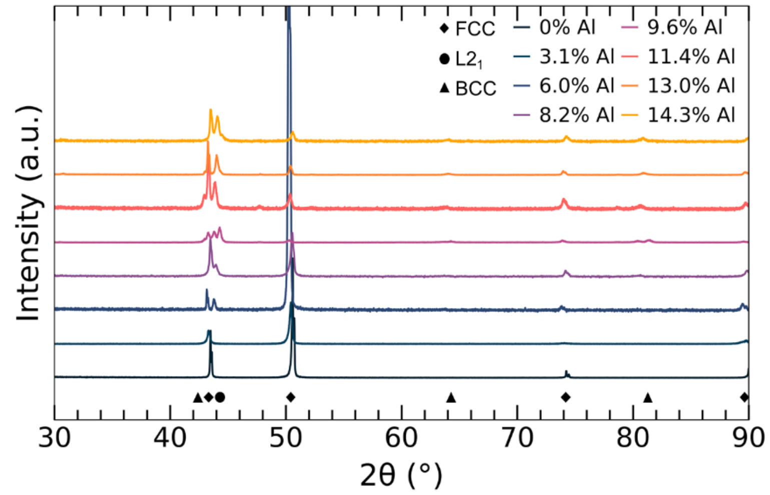

Figure 2: XRD patterns for CCA series following 6-hour homogenization at 1070 ˚C.

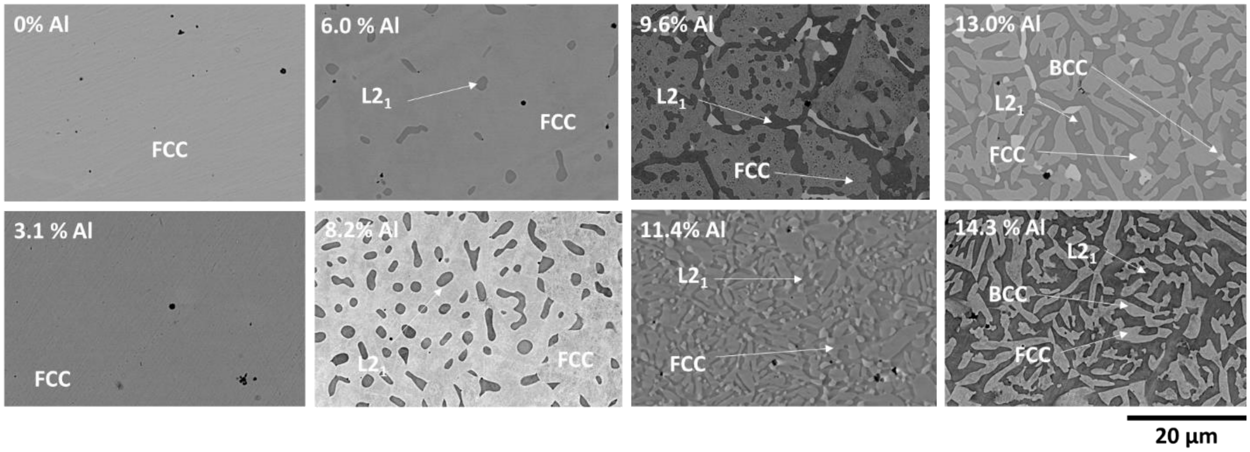

Figure 3: BSE micrographs of CCA series following 6-hour homogenization at 1070˚ C.

---

[4] The volume fraction of the BCC-like phase was too low to identify consistent superlattice peaks. The isopleth diagram in Figure 1 predicts possible stability of both the disordered BCC and ordered B2 phases. Thus, while it is indexed BCC structure, ordering characteristic of the B2 phase may also be present.

Table II: Phases present in CCAs following 6-hour homogenization at 1070 ˚C compared to computational predictions shown in Figure 1.

Alloy	**Predicted Phases from Isopleth**	**Observed Phases**
Al-0	FCC	FCC
Al-3.1	FCC	FCC
Al-6.0	FCC	FCC + $L2_1$
Al-8.2	FCC	FCC + $L2_1$
Al-9.6	FCC + $L2_1$	FCC + $L2_1$ + BCC
Al-11.4	FCC + $L2_1$	FCC + $L2_1$ + BCC
Al-13.0	FCC + $L2_1$ + BCC + BCC2	FCC + $L2_1$ + BCC
Al-14.3	FCC + $L2_1$ + BCC + BCC2	FCC + $L2_1$ + BCC

EDS maps for the six multi-phase materials are shown in Figure 4 with quantitative point scans shown in Table III. Overall compositions for each CCA confirm the accuracy of target compositions for sample synthesis. Generally, the $L2_1$ second phase is enriched Al, Ni, and Ti relative to the bulk composition. Al enrichment in the second phase likely signifies that increasing Al concentrations are compensated by increased $L2_1$ volume fraction. In the two-phase CCAs, the FCC matrix is enriched in Cr, Fe, and Mo, while Mn is observed at similar concentrations in each phase. For the three-phase alloys, the FCC phase was enriched in Fe and Cr while the BCC-like phase was enriched in Mo. The distribution of passivating elements, mainly Cr and Ti, ensures each phase has a strong passivating elements at concentrations of at least 10 at. %. Additionally, Ti nitride impurities are suggested to be present, although at significantly lower volume fractions, and thus, they may be considered negligible. Although the Al continued to partition to the $L2_1$ phase, the increasing global alloy composition of Al led to increasing Al concentrations in the FCC phase of the high-Al CCAs. Thus, it may be possible that the high Al concentrations promoted the formation of the third-phase, particularly given the unfavorable enthalpy of mixing of Al and Mo [62]. The linescan across the phase interface does not show any localized depletion near the interfaces in Al, Ni, or Ti in the matrix phase near the interface that is not observed throughout the rest of the microstructure that could possibly arise from non-equilibrium phase transitions, although it is possible that some occurs within the separation size of 100 nm.

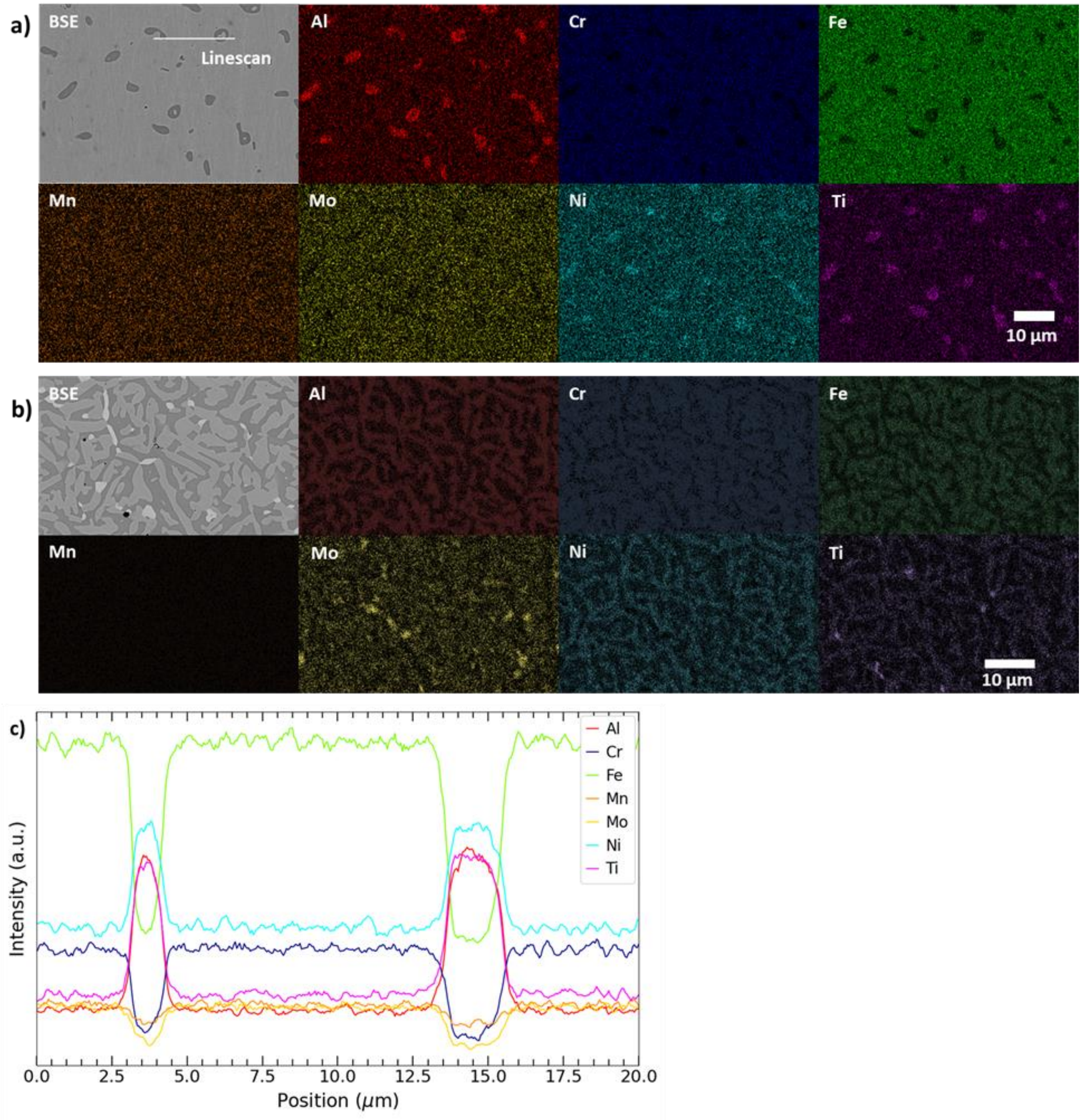

Figure 4: EDS mapping of a) Al-6.0 (FCC + L2_1) and b) Al-13.0 CCA (FCC + L2_1 + BCC) microstructures along with a c) quantitative line scan across multiple phases in the Al-6.0 microstructure. To minimize noise, a five point moving average is presented.

Table III: Quantitative EDS point scans across selected CCAs. Indicated values represent the average of at least two point scans over each phase.

Phase	Al	Cr	Fe	Mn	Mo	Ni	Ti	Area Fraction
$Al_{0.15}Cr_{0.5}Fe_2Mn_0Mo_{0.15}Ni_{1.5}Ti_{0.3}$ (Al-3.0)								
Matrix (FCC- Overall)	3.6	12.0	22.8	4.8	15.6	24.0	8.7	100 %
$Al_{0.3}Cr_{0.5}Fe_2Mn_{0.25}Mo_{0.15}Ni_{1.5}Ti_{0.3}$ (Al-6.0)								
Matrix (FCC)	3.7	11.0	42.5	5.2	3.1	28.8	5.6	95.7 %
2nd Phase ($L2_1$)	14.3	3.5	17.1	4.2	0.9	44.1	15.8	4.3 %
Overall Composition	6.4	10.2	39.7	5.2	2.6	29.7	6.1	-
$Al_{0.7}Cr_{0.5}Fe_2Mn_{0.25}Mo_{0.15}Ni_{1.5}Ti_{0.3}$ (Al-13.0)								
Matrix	6.9	13.4	50.8	0.0	3.4	22.3	3.2	53.5%
2nd Phase ($L2_1$)	24.9	4.3	22.7	0.0	1.0	38.0	9.2	38.8%
3rd Phase (BCC-like)	3.8	19.1	47.8	0.0	12.9	11.1	5.4	7.6%
Overall Composition	13.8	9.8	38.2	0.0	2.8	29.3	6.1	-

3.2 Corrosion Resistance Following Cathodic Pre-treatment

The formation and protectiveness of the passive film was evaluated with potentiodynamic polarization curves. E-log(i) plots are shown in Figure 5 with quantitative results summarized in Figure 6 and Table IV. All CCAs showed discernible passive ranges, indicating the formation of a protective oxide film. For all CCAs, the imaginary component of impedance (-Z”) increases with applied potential, indicating the formation and growth of a stable protective oxide film [63, 64], before decreasing at or near the pitting potential (E_{pit}). No critical current density is observed, possibly due to the formation of Al and/or Ti passive species below the corrosion potential (E_{corr}), which is verified by increasing -Z” magnitudes indicative to film thickening. The strong variability in the E_{corr} between alloys may be attributable to varying concentrations of dissolved oxygen in the aqueous solution, which could contribute via the oxygen reduction reaction (ORR), and should not be considered indicative of trends in the half-cell potential of the reduced metal surface[5]. Such variability also obscures any trends that may be present with Al concentration. The passive current density (i_{pass}) of CCAs containing higher Al concentrations is generally lower than that of CCAs with low Al concentrations, although a linear trend with Al concentration was not present. Decreased i_{pass} values may indicate the formation of more protective passive films, and possibly thicker passive films. However, no trends between the maximum -Z” magnitude and i_{pass} are present. The

---

[5] The selected runs shown in Figure 5 were chosen on the basis of representative pitting and repassivation potentials along with passive current density values, leading to more variability in the corrosion potential trends.

CCAs are able to form spontaneous passive films for all Al concentrations. While little trends were present with Al concentration and corrosion resistance in the passive film, the resistance of the films to localized breakdown decreases with increasing Al concentration.

-Z" generally begins to decrease at less positive potentials for alloys with higher Al concentrations, indicating film breakdown. E_{pit} decreases with Al concentration. Sharp spikes in the current density (i) and/or Z" plots suggest metastable pitting that occurred prior to E_{pit}, however no trends in the degree of metastable pitting were observed with Al content. Notably, pitting was often not observed for the Al-0 sample, with the passive film stable beyond the evaluated range (0.8 V_{SCE}). E_{pit} magnitudes are generally higher for CCAs with lower Al concentration. For instance, the lowest E_{pit} was observed for Al-9.6, the lowest Al concentration to have a three-phase microstructure, and other three-phase CCAs with higher Al concentrations had higher E_{pit}. For two selected alloys, the procedure was repeated in three electrolyte solutions with different (0.001 M, 0.1 M, and 1.0 M) NaCl concentrations to ensure findings were valid across a range of Cl^- concentrations, including those encompassing 3.56 wt. % NaCl solutions (~0.6 M) that are generally accepted as representative of marine conditions [65]. Additionally, 0.01 M NaCl solutions with the pH adjusted with either 1.0 M HCl or 1.0 M NaOH were used to evaluate the corrosion behavior at high and low pH. Pitting potentials for each electrolyte are shown in Figure 7. E_{pit} for Al-6.0 is within the range of statistical scatter of E_{pit} for 316L at all Cl^- concentrations. Al-6.0 is also suggested to have a higher E_{pit} than the 13.0% Al alloy for both evaluated Cl^- concentrations, although not always at a high level of statistical significance. E_{pit} has a slightly upward trend with pH for most alloys. While E_{pit} of Al-6.0 is within the range of statistical scatter to that of 316L in most neutral pH ranges, E_{pit} of both Al-containing CCAs is well below that of 316L in both strong acids and strong bases. E_{pit} of the Al-containing CCAs is also below that of CoCrFeMnMo in strong bases, despite the significantly higher Mn concentrations that is found detrimental corrosion resistance [66-68]. Thus, the passivity of the CCA series is validated for a wide range of Cl^- concentrations and pH, with increasing Al concentration harming the resistance to localized breakdown across a range of environments.

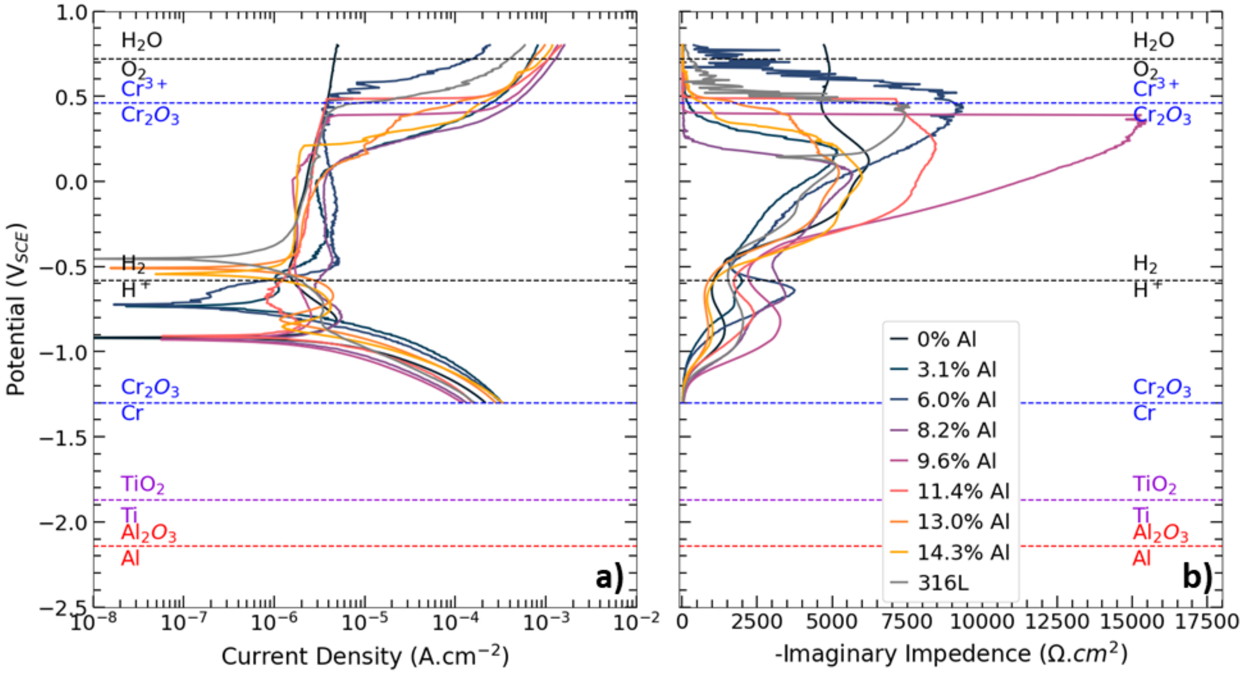

Figure 5: a) E-log(i) and **b)** Z” plots obtained during polarization of CCAs in 0.01 M NaCl (pH ~5.75) following cathodic pre-treatment (-1.3 V$_{SCE}$, 600 s). Dashed lines indicate stability ranges for the oxides of passive species formed on their pure constituent elements at a pH of 5.75 predicted by Hydra Medusa software.

Table IV: Key corrosion parameters obtained during potentiodynamic polarization of CCAs in 0.01 M NaCl (pH ~5.75) following cathodic pre-treatment (-1.3 V$_{SCE}$, 600 s). Each term indicates the mean value with a one standard deviation bound.

Alloy	**Corrosion Potential (V$_{SCE}$)**	**Pitting Potential (V$_{SCE}$)**	**Repassivation Potential (V$_{SCE}$)**	**Passive Current Density (μA.cm^{-2})**
Al-0	-0.842 +/- 0.107	0.580 +/- 0.187[6]	0.030 +/- 0.110	10.12 +/- 17.94
Al-3.1	-0.741 +/- 0.206	0.327 +/- 0.066	-0.016 +/- 0.084	2.75 +/- 1.43
Al-6.0	-0.736 +/- 0.023	0.633 +/- 0.066	0.146 +/- 0.035	3.85 +/- 0.53
Al-8.2	-0.865 +/- 0.075	0.341 +/- 0.081	-0.127 +/- 0.057	3.67 +/- 2.99
Al-9.6	-0.680 +/- 0.227	0.153 +/- 0.219	-0.189 +/- 0.118	2.92 +/- 1.22
Al-11.4	-0.893 +/- 0.011	0.371 +/- 0.068	-0.156 +/- 0.158	1.47 +/- 1.42
Al-13.0	-0.729 +/- 0.186	0.353 +/- 0.080	-0.166 +/- 0.064	3.67 +/- 2.92
Al-14.3	-0.431 +/- 0.129	0.400 +/- 0.111	-0.160 +/- 0.053	1.65 +/- 0.38
316L	-0.447 +/- 0.003	0.596 +/- 0.045	0.014 +/- 0.019	1.36 +/- 0.31

---

[6] For some Al-0 trials, pitting was not observed within the evaluated range. The pitting potential for such trials was reported as 0.8 V$_{SCE}$, but the true mean pitting potential is likely higher.

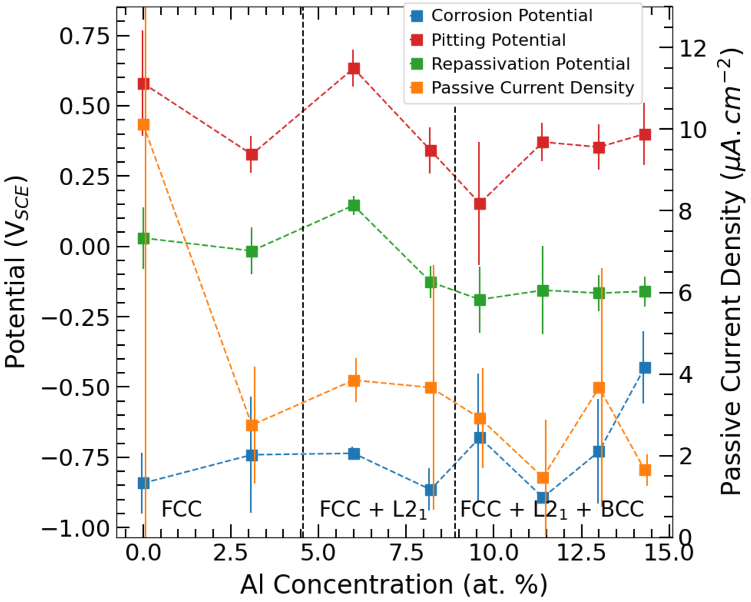

Figure 6: Summary of potentiodynamic polarization corrosion parameters shown in Table IV as a function of Al concentration and present phases. Error bars for each parameter indicate a one standard deviation range.

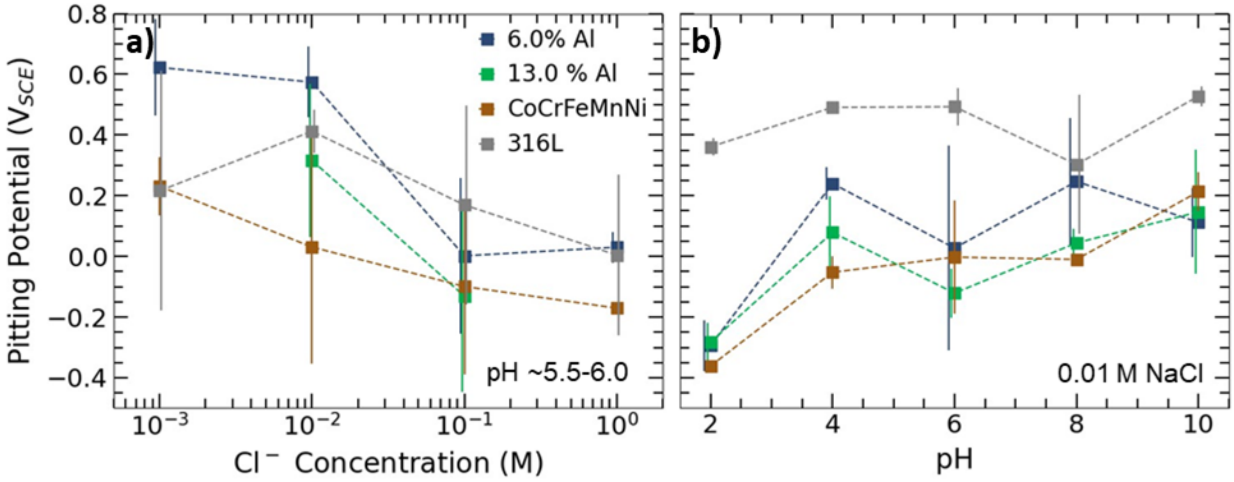

Figure 7: Pitting potentials obtained for selected CCAs in **a)** unadjusted NaCl solutions ranging from 0.001 to 1.0 M and **b)** in 0.01 M NaCl solutions adjusted to pH values ranging between 2 and 10. Error bars are indicated for one standard deviation range.

Following polarization, sample surfaces were imaged with SEM to identify the frequency and morphology of the pits. Figure 8 shows that pits selectively occurred at or near phase interfaces. No clear trends in preferential dissolution or pit propagation into any of the phases were visible. Pits generally initiate at random locations in the two single-phase CCAs and were not suggested to preferentially attack grain boundaries such as those shown in the Al-0 micrograph.

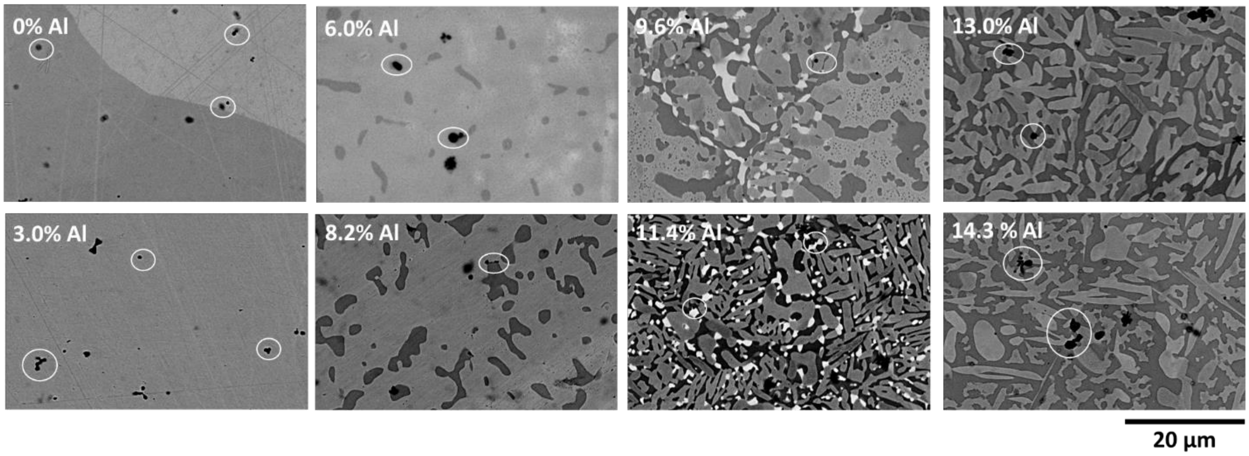

Figure 8: BSE micrographs following CCA polarization terminated upon reaching current densities of 10^{-5} A.cm^{-2} to evaluate pit initiation sites without significant degradation of the surface. Pit locations illustrating transition from random to interface pitting are circled.

3.3 Characterization and Corrosion Behavior of CCAs with Air-formed Oxide Films

The corrosion behavior of the passive films spontaneously formed during exposure to air was also characterized with EIS and potentiodynamic polarization starting slightly below the OCP to minimize any reduction of the oxide layer. E-log(i) and Z” plots obtained during potentiodynamic polarization are shown in Figure 9 with key parameters tabulated in Table V. As in the case of the passive films formed on the reduced surfaces, the highest pitting potential was observed for Al-6.0. However, no clear trends in E_{pit} were present with Al concentration. For example, despite having a similar Al content, the worst passivity was suggested for Al-8.2 and Al-9.6, where a broad passive range was not observed and active dissolution is suggested in the anodic region. In addition to increased current densities, inferior corrosion resistance of the air-formed oxides of many mid-Al CCAs is suggested by low Z” magnitudes prior to and following breakdown.

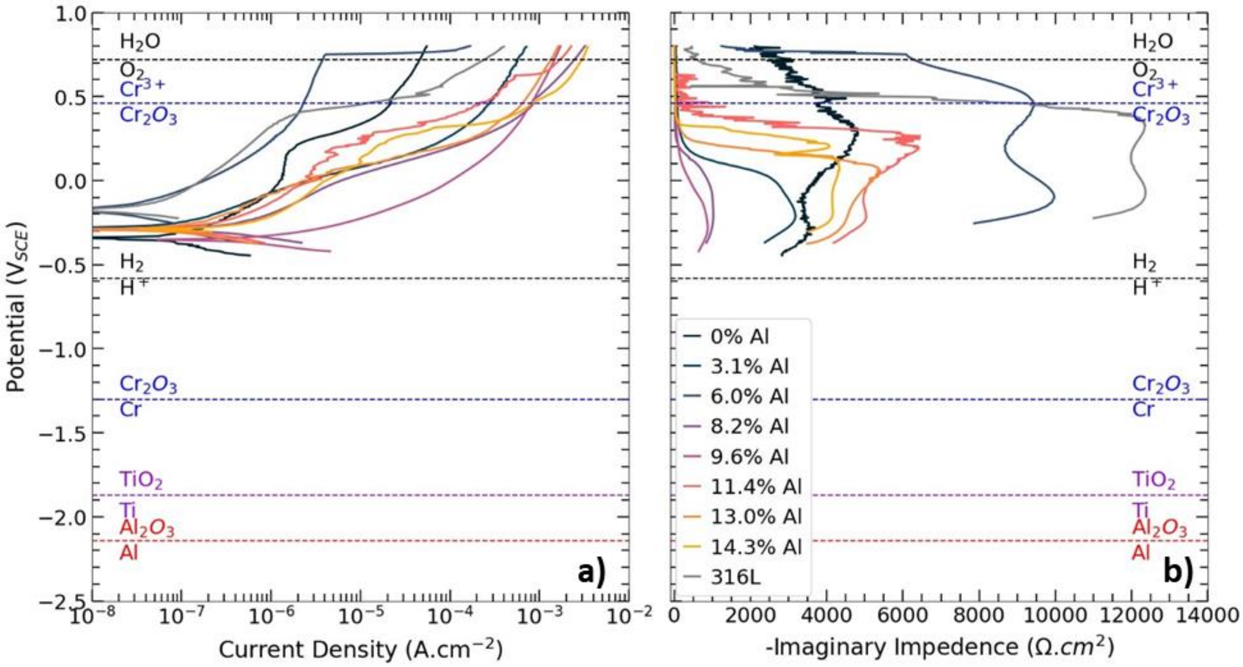

Figure 9: a) E-log(i) and **b)** Z" plots obtained during polarization of CCAs in 0.01 M NaCl (pH ~5.75) following 30 minute solution exposure of the air-formed oxide. Dashed lines indicate stability ranges for the oxides of passive species formed on their pure constituent elements at a pH of 5.75 predicted by Hydra Medusa software.

Table V: Key corrosion parameters obtained during potentiodynamic polarization of CCAs in 0.01 M NaCl (pH ~5.75) following 30 minute solution exposure of the air-formed oxide. Each term indicates the mean value with a one standard deviation bound. Repassivation potentials marked N/A indicate consistent repassivation at potentials above E_{corr} was not observed.

Alloy	Corrosion Potential (V_{SCE})	Pitting Potential (V_{SCE})	Repassivation Potential (V_{SCE})
Al-0	-0.284 +/- 0.092	0.402 +/- 0.215	-0.051 +/- 0.055
Al-3.1	-0.263 +/- 0.083	0.099 +/- 0.023	-0.027 +/- 0.012
Al-6.0	-0.173 +/- 0.008	0.631 +/- 0.243	0.185 +/- 0.152
Al-8.2	-0.311 +/- 0.024	0.074 +/- 0.028	-0.076 +/- 0.069
Al-9.6	-0.271 +/- 0.097	0.023 +/- 0.336	N/A
Al-11.4	-0.223 +/- 0.117	0.188 +/- 0.250	N/A
Al-13.0	-0.307 +/- 0.104	0.11 +/- 0.074	N/A
Al-14.3	-0.268 +/- 0.068	0.125 +/- 0.013	-0.197 +/- 0.075
316L	-0.182 +/- 0.016	0.437 +/- 0.025	0.004 +/- 0.058

The Bode plot shown in Figure 10 also shows trends in the polarization resistance with regards to Al concentration. Spectra were fit a modified Randles circuit modified to include a constant phase element (CPE) selected to shows effective comparative trends in passive film attributes in a simplified manner. The R_P term encompasses resistance attributable to both the passive film and charge transport via both oxygen anions and metal cations governing the reaction rates at the film/electrolyte interface. The simplified fit assumes the presence of a single time constant defined by the R_P term. The CPE, which contains both an admittance constant (Y_0) and CPE coefficient (α) describes the dielectric and physical attributes of the charge buildup across the oxide layer(s). The impedance (Z) at a given frequency (f) may be fit to circuit parameters using the equation below.

$$\mathrm{Z(f)} = R_s + \frac{R_p + Y_o(i2\pi f)^{\alpha}}{R_p Y_o(i2\pi f)^{\alpha}} \qquad (10)$$

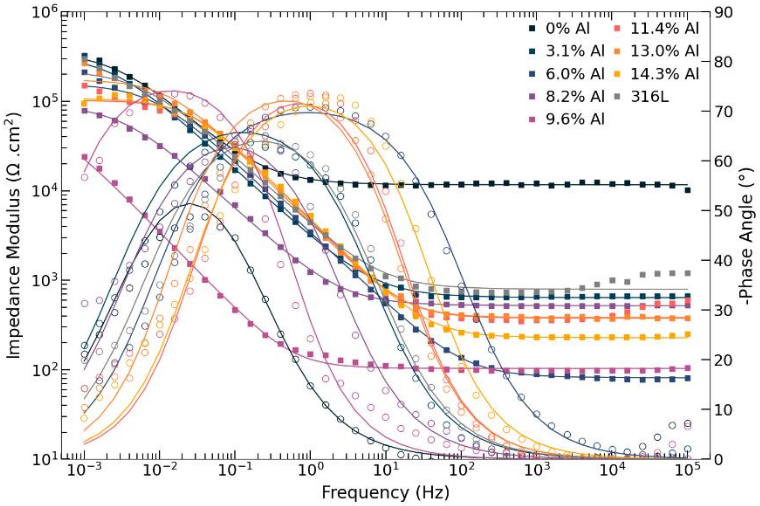

Figure 10: Bode plot obtained during EIS of CCAs with solution-exposed air-formed oxides at each CCAs OCP. Lines indicate best fits to a Randles circuit with parameters shown in Table VI.

Table VI: Randles circuit fit parameters for the EIS spectra solution-exposed air-formed oxides at each CCAs OCP.

	Al-0	**Al-3.0**	**Al-6.0**	**Al-8.2**	**Al-9.6**	**Al-11.4**	**Al-13.0**	**Al-14.3**	**316L**
R_p (kohm.cm^2)	352.2	331.5	158.5	92.3	62.8	102.3	173.9	107.6	222.7
R_s (ohm.cm^2)	11650.2	639.8	81.3	519.9	103.3	376.4	382.0	227.7	791.7
Y_0 (µS*s$^\alpha$.cm^{-2})	65.7	81.6	66.9	226.8	3225.8	43.7	47.7	43.8	122.1
α	0.770	0.783	0.802	0.785	0.874	0.870	0.859	0.846	0.781
Z(1mHz) (kohm.cm^2)	377 +/- 83	250 +/- 79	449 +/- 558	178 +/- 103	20 +/- 6	222 +/- 299	241 +/- 72	120 +/- 67	648 +/- 366

High R_P magnitudes indicate that each CCA possesses the ability to passivate. The highest R_P magnitudes occurred for Al-0 and Al-3.1, the two single-phase CCAs. Unlike the two CCAs with lowest Al concentrations, none of the multi-phase CCAs has an R_P magnitude above that of 316L. While decreasing passivity may be influenced by the formation of new phases, the still effects may be offset by combinations of Al, Cr, and Ti passive species, particularly given the enrichment of either Al, Cr, and Ti for every phase across the CCA series. Individual comparisons of the R_P magnitudes beyond 5 at. % are less prominent, often not following linear trends. Furthermore, the wide standard deviations of Z(1 mHz), a representative value for R_p, indicates that while trends in R_p are often consistent across multiple runs, comparisons between individual alloys are often not statistically significant. Additionally, all α values are above 0.8, indicating that the charge barrier created by the protective passive film more resembles the characteristic nature of an ideal capacitor (for which α=1).

3.4 Electrochemical Characterization of Passive Films Formed During Potentiostatic Exposure

To evaluate the growth of and subsequent dielectric properties of the stable passive films, the cathodically pre-treated species were exposed to a -0.25 V_{SCE} potential, a value determined to be within the passive range of the CCAs during the potentiodynamic polarization shown in Figure 11. For all CCAs, the current density (i) decreases and -Z" increases with time, indicating the formation of both a thicker and more protective passive film. For most CCAs, a sharp spike in the i vs. t plot indicates a change in sign of i from negative to positive between 10^2 and 10^4 seconds of exposure. At times past approximately 10^3 seconds, Z" often begins to level out, possibly suggesting a quasi-stable film thickness has been reached[7]. At the conclusion of the film growth, the highest Z" magnitudes are seen with the three highest Al concentrations suggesting that the oxide may be thicker. Notably, an order of magnitude increases in i was observed for Al-14.3 at times beyond 20 ks, potentially indicating instability of the passive film.

---

[7] The quasi-steady state film thickness indicated by level -Z" values may still experience limited passive film dissolution, as evidenced by the non-zero current densities, which may alter film composition. Additionally, extended aging under quasi-steady state may alter the presence long-range order or structural nature of the passive film.

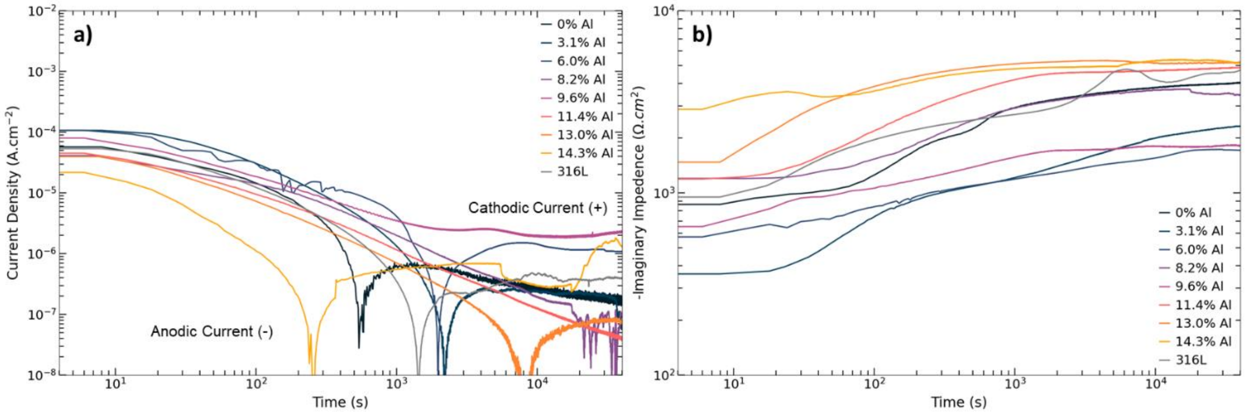

Figure 11: a) Current density and **b)**in-situ -Z” measurements during potentiostatic film growth of CCAs at -0.25 V_{SCE} in 0.01 M NaCl (pH ~5.75) following cathodic pre-treatment (-1.3 V_{SCE}, 600 s).

Figure 12 shows equivalent electron current densities representing elemental dissolution rates obtained during similar passive film growth for the Al-6.0 alloy. At low times Fe and Ni dissolve at the highest rates in the pH 4 electrolyte, whereas, in pH 10, Ni and Al dissolve at the highest rates. The dissolution current densities decrease with time, following trends in the electron current density that are attributable to the formation of a protective oxide film. The mass of each metal enriched at the surface beyond the expected amount predicted from stochiometric dissolution during and following the oxide growth calculated from dissolution rates is also shown. Cr, Mn, and Ti are suggested to have the highest levels of accumulation on the surface in the pH 4 environment, likely due to dissolution rates below the detection limits, while Ni and Al are suggested to have the highest levels of accumulation in the pH 10 environments. Al dissolves at significantly higher rates in the pH 10 electrolyte, (the Al dissolution rates in the pH 4 environment are below the detection limit), and, as a result, has comparatively lower levels of surface enrichment in the pH 10 environment.

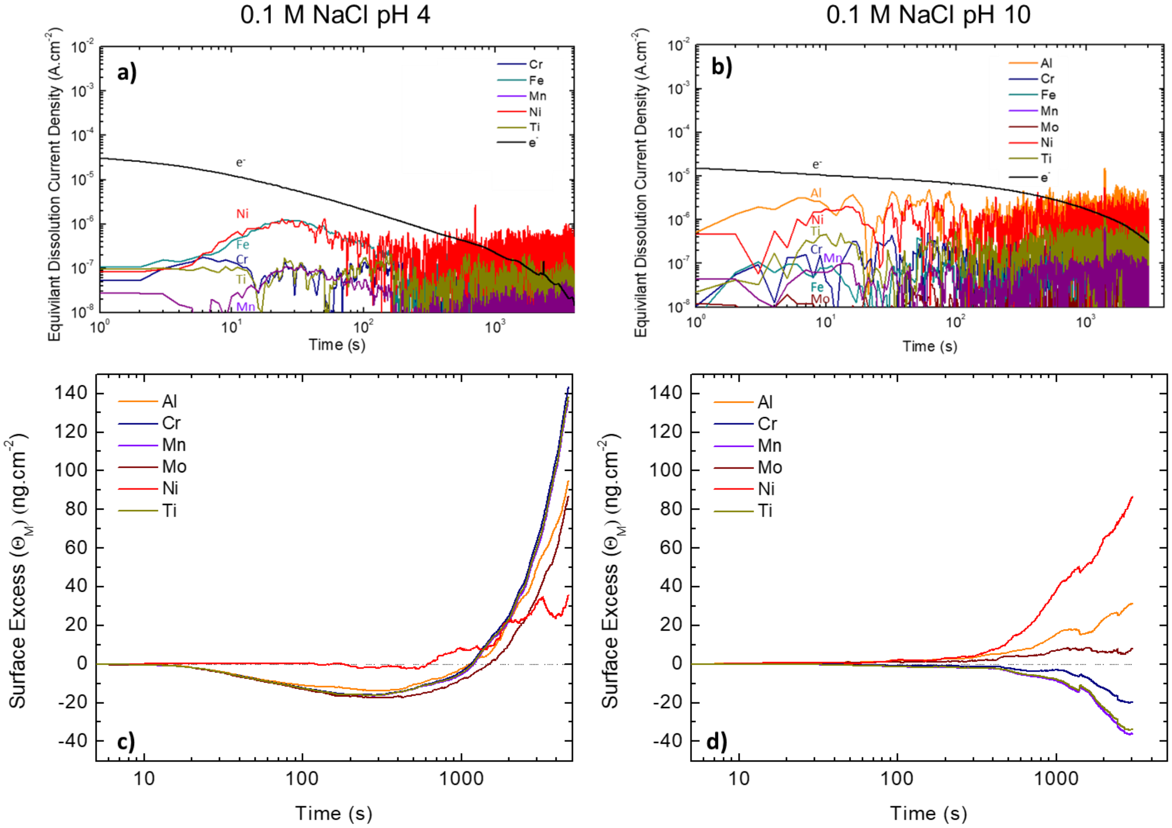

Figure 12: Equivalent current densities of in-situ elemental dissolution rates monitored via AESEC during exposure of Al-6.0 to a -0.2 V_{SCE} potential in 0.1 M NaCl adjusted to **a)** pH 4 and **b)** pH 10 at following cathodic reduction pre-treatment and enrichment calculations. Equivalent current densities are determined from the elemental intensities with equations 6 and 7 while excess accumulated mass in 0.1 M NaCl **c)** pH 4 and **d)** pH 10 was determined using equations 8 and 9. Al dissolution rates are below the detection rates in the pH 4 environment and are not shown. Excess accumulated Al was calculated assuming dissolution rates of zero.

The Bode plot obtained following the potentiostatic oxide growth at -0.25 V_{SCE} described above are shown in Figure 13 with fits tabulated in Table VII. . As in the case of the air-formed oxide, all CCAs demonstrate R_P values characteristic of spontaneous passivity. R_P values are of similar magnitudes to those of the solution-exposed air-formed passive films. No consistent linear trends are present between R_P and Al concentration, however Al-0 and Al-6.0 have the highest R_P values, consistent with trends in E_{pit} (Tables IV, V). With the exception of Al-3.1 and Al-9.6, all α values are above 0.8. Deviation from ideal capacitive behavior for the alloys may further mask trends in R_P with Al concentration.

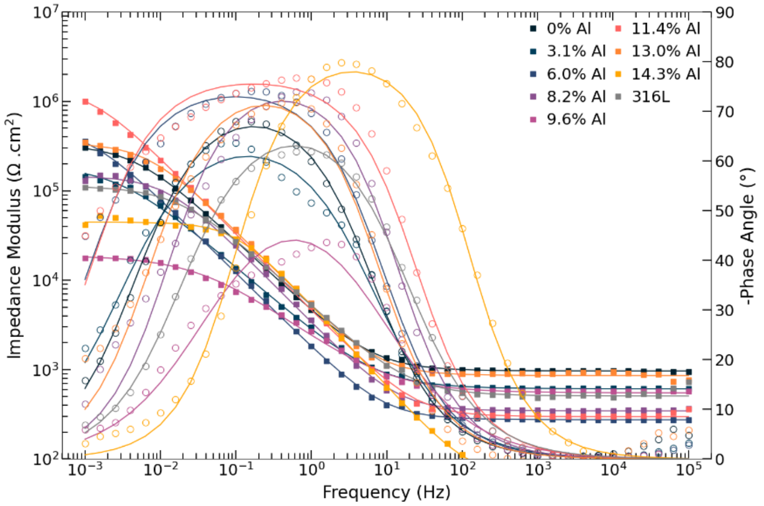

Figure 13: Bode plot obtained during EIS of CCAs with following potentiostatic oxide growth (40 ks, -0.25 V_{SCE}). Lines indicate best fits to a Randles circuit with parameters shown in Table VII.

Table VII: Randles circuit fit parameters for the EIS spectra obtained following potentiostatic oxide growth (40 ks, -0.25 V_{SCE}).

	Al-0	**Al-3.0**	**Al-6.0**	**Al-8.2**	**Al-9.6**	**Al-11.4**	**Al-13.0**	**Al-14.3**	**316L**
R_p (kohm.cm^2)	332.4	194.7	533.0	146.6	18.5	1464.5	343.8	44.7	113.3
R_s (ohm.cm^2)	965.6	610.6	275.1	345.4	550.3	297.8	859.0	64.1	506.9
Y (µS*s$^\alpha$.cm^{-2})	52.2	99.9	122.6	61.7	134.6	45.1	41.5	35.1	764.5
α	0.808	0.741	0.838	0.861	0.661	0.857	0.852	0.914	0.779
Z(1mHz) (kohm.cm^2)	491 +/- 247	180 +/- 68	452 +/- 558	162 +/- 72	13 +/- 4	394 +/- 529[8]	318 +/- 71	48 +/- 9	252 +/- 202

3.5 Composition of Passive Film Formed During Potentiostatic Exposure

The passive film chemistry was evaluated for an FCC Al-free CCA, an FCC + $L2_1$ low-Al CCA (6.0 at. %), and an FCC + L21 + BCC-like high-Al CCA (13.6 at. %)[9] following the film growth described above. Spectra fitting shown in Figure 14 provides insight into the present chemical species. All three alloys are suggested to have significant quantities of Cr(III), Ti(IV) and, when present, Al(III) in the passive film. For the Al-containing CCAs, Al was suggested to be present in the passive film as Al(III) oxide, with signal attributable to the Cr3s core spectrum also present. Cr(III) and Ti(IV) oxides were also suggested by fitting of each the respective spectra for each elements. The Cr $2p_{3/2}$ spectra also suggested the presence of

---

[8] For two runs, the impedance at a 2.51 mHz frequency was used due to premature test termination. Thus, R_p is likely higher than the indicated impedance, as reflected in the selected circuit fit.

[9] The high-Al CCA was a Mn-free CCA of composition $Al_{0.7}Cr_{0.5}Fe_2Mo_{0.15}Ni_{1.5}Ti_{0.3}$ due to sample and equipment availability. Both the structure and approximate composition of each phase are similar to those of the high-Al CCAs evaluated via EIS and polarization. Thus, the surface cation fractions may be considered representative of trends for the high-Al CCAs and is not expected to be significantly altered by the discrepancy of Mn concentration.

Cr(III) hydroxide and, in conjunction with the and Fe2p$_{1/2}$ (not shown) spectra, $FeCr_2O_4$ which indicates likely nearest-neighbor interaction and possibly the formation of a long-range ordered oxide. Ni was suggested to be present in the passive film in the form of Ni(II) hydroxide, but was not suggested to be present in the Al-free CCA. While Al concentration affects passive film cation fractions, no significant trends in the cation valance or chemical species were observed.

The total intensity of each feature assigned to passivated features by spectra fitting was normalized to obtain the cation fractions shown in Figure 15. The high-Al CCA has a higher Al surface cation fraction in the passive film, although the increase was not proportional to the increase in the bulk alloy concentration, suggesting less enrichment. The passive film of the Al-free CCA has significant Cr and Mo presence, with both element surface cation fractions enriched over four times the bulk alloy concentrations of the respective element. In addition to Al, the two multi-phase alloys both had higher concentrations of Ni and Ti in the passive film. The increasing Al, Ni and Ti cation fractions correspond with the increasing volume fraction of the L2$_1$ phase, within which they are enriched. For the high-Al CCA, where a Cr-Mo enriched third phase is present, the surface cation fractions for Cr and Mo are higher than those of the two-phase mid-Al CCA, but not higher than the Al-free single-phase FCC CCA. Thus, all phases for both the medium- and high-Al CCAs contain enriched concentrations of Al, Cr, and/or Ti, the three elements for which surface cation fractions are enriched relative to overall composition.

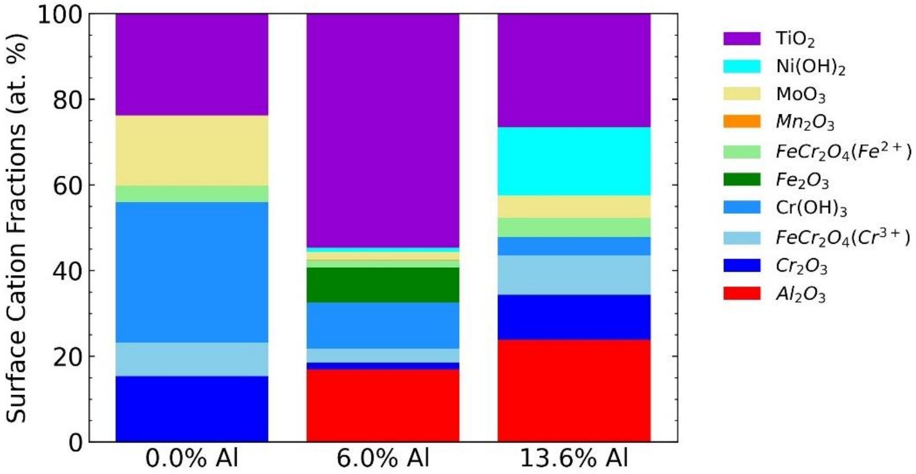

Figure 15: Surface cation fractions obtained via high-resolution XPS scans of the passive film formed following potentiostatic oxide growth (40 ks, -0.25 V_{SCE}) in 0.01 M NaCl. Surface cation fractions include intensities attributable to oxidized (non-zero valance) features normalized with relative sensitivity factors.

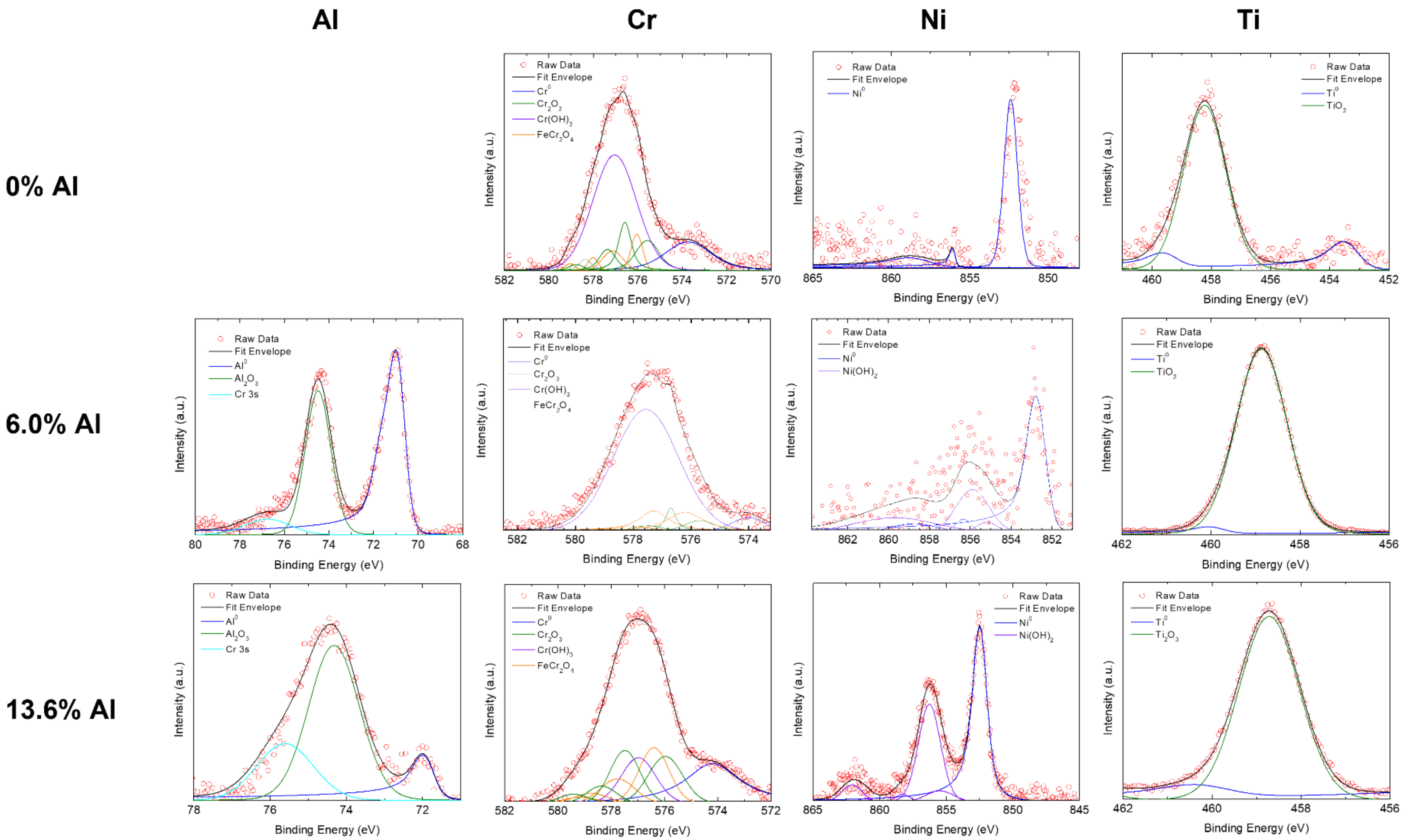

,**Figure 14:** Fit high-resolution spectra for Al-0, Al-6.0, and a third-high Al CCA ($Al_{0.3}Cr_{0.5}Fe_2Mo_{0.15}Ni_{1.5}Ti_{0.3}$) following potentiostatic oxide growth (-0.25 V_{SCE}, 40 ks) in 0.01 M NaCl (pH ~5.75). Intensities are scaled to maximum counts for each spectra as quantitative values may vary due to external factors such as surface contamination.

Variation in the passive film composition with depth is shown by sputter depth profiling in Figure 16. In the Al-0 CCA, Cr and Ti are suggested to be enriched at similar depths, with both elements having their maximum intensity between 1 and 1.5 minutes of sputtering. In the Al-6.0 CCA, the maximum intensity of Ti occurs at higher sputtering times. Therefore, the passive film may be considered more enriched in Ti closer to the metal-oxide interface. Notably, Al enrichment occurs at similar depths as Ti concentration, suggesting possible coexistence or that the Al may be protected by its proximity to the Ti-enriched layers.

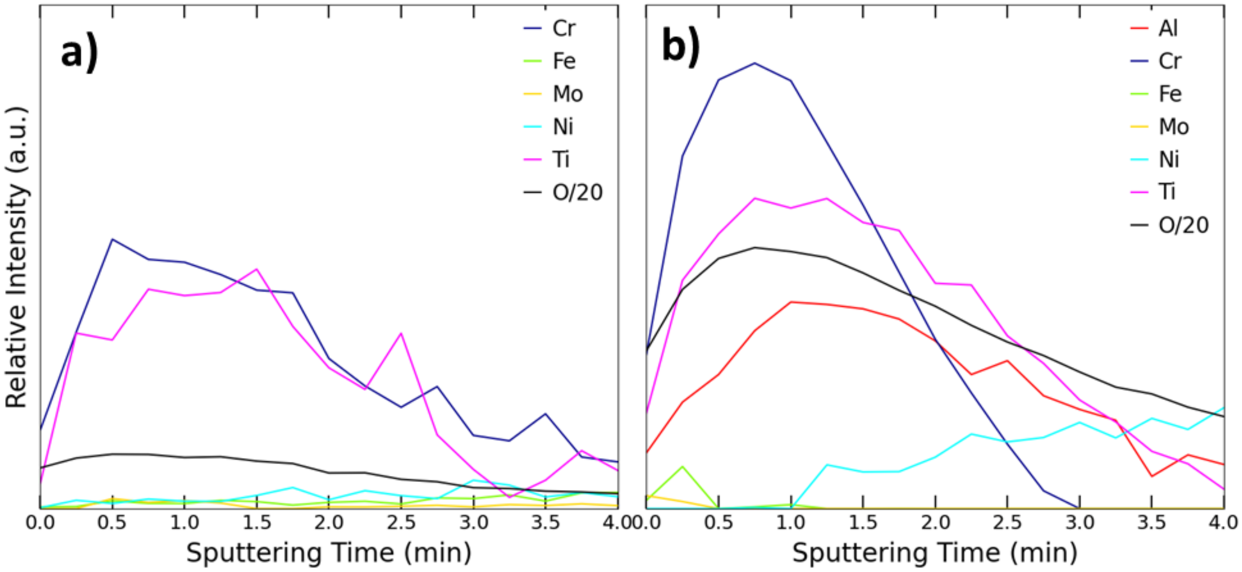

Figure 16: Sputter depth profiles scans of the oxidized species within the passive film formed following potentiostatic oxide growth (40 ks, -0.25 V_{SCE}) in 0.01 M NaCl for **a)** Al-0 and **b)** Al-6.0. Relative intensities were obtained by taking the cumulative intensity of each species attributable to oxidized features and normalizing with system-specific relative sensitivity factors.

4.0 Discussion

The microstructure, passivity, and corrosion behavior of CCAs series with increasing Al concentration was evaluated. Increasing Al concentration stabilized microstructures with more phases (Table II). The passive film chemistry was also dependent on Al concentration, with CCAs with increased Al concentrations having increased surface cation fractions of Al(III), Ni(II), and, to a less significant trend, Ti(IV) (Figure 15). Notably, no trends or critical thresholds were observed with regards to Al concentration in either the bulk alloy composition or passive film surface cation fractions, possibly due to contributions of other passivating species such as Ti(IV) and Al(III). Passivity was suggested for each CCA from i_{pass}, and R_p, and E_{pit} values; however strong trends were not present with Al concentrations (Figure 6, Tables IV, V, VII). Increase in interface area and other microstructural features may be offset by the enrichment Ti(VI), Al(III), and Cr(III) in passive film (Figure 15), although uncertainty remains with regards to the distribution of each species across multiple phases. Each factor will be discussed in further detail below.

4.1 Thermodynamic Factors Influencing Passive Film Stability

Cr, Al, and Ti are all capable of independently passivating in pure element form at the potentials indicated. The thermodynamic stability of passive species under neutral conditions that is predicted by E-pH diagrams [47] like those shown in Figure 17 is reflected in broad passive ranges for each of the elements shown in Figure 18. In each case, the metals were polarized under the same conditions with in-situ Z" also measured to track trends in passive film thickness. E-pH diagrams predict the dominant passive species to be Al_2O_3, Cr_2O_3, and TiO_2 for Al, Cr, and Ti, respectively [47].

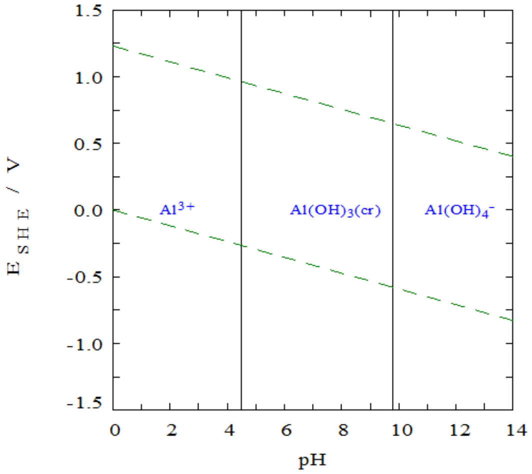

Figure 17: E-pH diagram of pure Al constructed with Hydra Medusa. Regions associated with dissolved ions indicate an equilibrium concentration of at least 10^{-6} M.

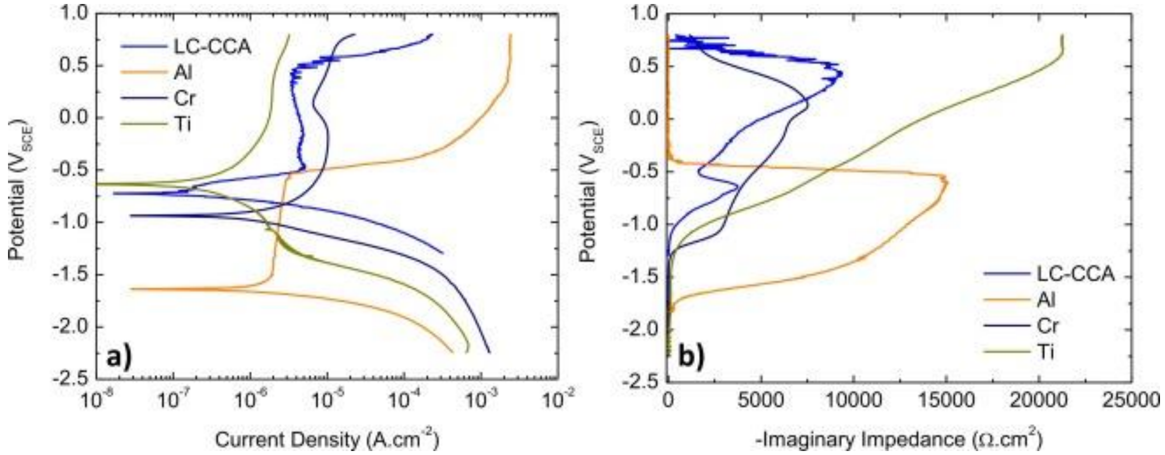

Figure 18: a) E-log(i) and b)-Z" measurements obtained during potentodynamic polarization of pure Al, Cr, and Ti compared to Al-6.0 (referred to as LC-CCA) in 0.01 M NaCl (pH ~5.75) following cathodic pre-treatment (-1.3 V_{SCE}, 600 s) reproduced from [45].

Initial estimates of passive species stability may also be predicted on the basis of free energy. Figure 19 shows the formation energies calculated via density functional theory on a per-atom basis, suggesting that Al(III) and Cr(III) oxides have the lowest formation energy, that Ti(IV) oxide is more favorable. The formation energies follow trends with the free energies of formation on a per molecule basis (-1691 kJ/mol for Al_2O_3 [69], -1050 kJ/mol for Cr_2O_3 [70], and -959 kJ/mol for TiO_2 [69]), where the species with the most favorable formation energies are those proposed to spontaneously form in passive films. The formation energies of passive species may also be utilized to compare the likelihood of each metal to enrich in the passive film. Elements with more negative formation energies (e.g., Al, Cr, Ti) are generally enriched in the passive films relative to their microstructural compositions (Figure 15), whereas those with less negative formation energies (e.g. Fe, Ni) are generally not and furthermore depleted by chemical dissolution in Cl^- containing solutions, as shown by higher dissolution rates observed via AESEC (Figure 12).

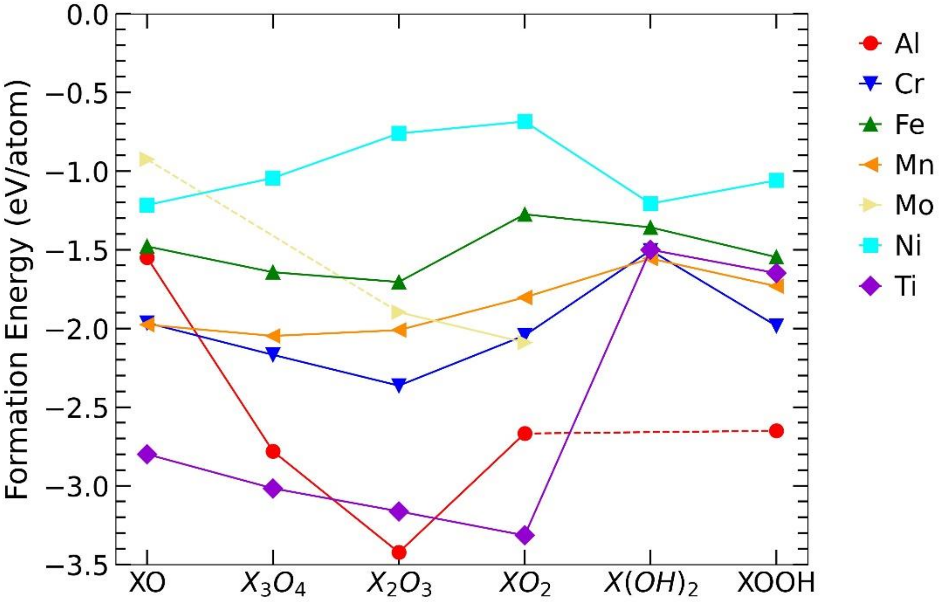

Figure 19: Formation energies at 0 K for a range of oxide, hydroxide, and oxyhydroxide species possible for each constituent element obtained from Open Quantum Materials Database [71, 72].

No clear trends in the pure element oxide breakdown behavior were observed with formation free energy. Despite Al_2O_3 being theoretically more stable than TiO_2 on a per molecule basis and Cr_2O_3 on both a per molecule and per cation basis, it is the only passive species indicated by Figure 18 to breakdown at potentials below Al-6.0 in the dilute chloride environment. Furthermore, the E-pH diagram for Al (Figure 17) shows stability of the Al oxide is not limited by high applied potentials in neutral environments, further highlighting that Al oxide stability is limited beyond thermodynamic effects. For the case of Al, Cr, and Ti, the potentials applied during both potentiodynamic polarization (Figure 5) and oxide growth during exposure to a constant potential (Figure 11) are well above the formation potentials for Al, Cr, and Ti passive species, indicating there is sufficient driving force for oxide formation. Notably, Al passive species are not stable in strongly basic solutions, unlike the case of Cr, Fe, and Ni species that form the passive film of 316L [73]. The instability of Al passive species may contribute to the decreased corrosion resistance of Al-6.0 relative to 316L despite comparable resistance in neutral solutions (Figure 9). Increased dissolution rates of Al species in basic environments are confirmed by AESEC, leading to decreased levels of enrichment at the surface (Figure 12). Decreased concentrations of Al passive species in oxide film formed in basic environments relative to those formed in acidic environments have also been confirmed in similar alloy series [74].

Figure 18 shows that the passive film of Al-6.0 breaks down at higher potentials than pure Al and has a comparable i_{pass} to Al, even though the Al concentration is well below both pure Al and the critical Al concentration suggested by Peng et al. for stable passivation in Fe-Al alloys [31] (Figure 15). Therefore, it is suggested that the effect of Al is aided by the simultaneous presence of Cr and/or Ti, evidenced by surface cation fractions obtained via XPS that show all three evaluated alloys contain enriched quantities of Cr, Ti, and (with the exception of the Al-free alloy) Al. Simultaneous presence of the three passivating species in the passive film follows trends with the Fe-Cr-Al-Ti alloy series developed to probe the interplay of the passivating elements [43]. All evaluated CCAs had similar concentrations of Cr and Ti, however, it is of note that the trends in corrosion behavior with Al content are may only be valid for CCAs that also contain sufficient quantities of Cr and/or Ti.

Cation enrichment must also be considered on the basis of individual phases. Previous work has indicated that the passive film of Ti-6.0 has two distinct phases with local enrichment determined by the bulk microstructure composition [54]. Thus, the increasing area fractions of the Al-, Ni-, and Ti-enriched $L2_1$ phase in the high Al-CCAs (Table III) likely also contribute to the higher Al and Ni cation fractions in the passive film (Figure 15). Notably, the Ti(IV) surface cation fraction is not suggested to increase, possibly due to the decreasing fraction of Ti in the bulk $L2_1$ phase of the high Al CCAs. The demonstrated ability of all the evaluated CCAs to form a stable passive film is likely made possible when enriched in Cr or Ti relative to bulk composition.

The presence of multiple passive species may also be evaluated thermodynamically by the mixing enthalpies between multiple passivating species [75]. The film breakdown resistance that is observed even for some of the high-Al CCAs (Tables IV, V) may be indicative that the high Al concentration in the passive films (Figure 15) is aided by solubility in stable Cr or Ti-based oxides. Notably, Al_2O_3 exhibits complete solid solution solubility with Cr_2O_3 [76]. While Al_2O_3 and TiO_2 do not exhibit solid solution solubility, possibility indicating a decreased thermodynamic driving force for mixture, thermodynamic stability of complex oxides such as $TiAl_2O_5$ and $Ti_7Al_2O_{15}$ indicates possible formation despite a lack of experimental validation [45].

The presence of Al in the passive film formed in chloride electrolyte of the AlCoCrFeNi CCA was suggested to increase the concentration of n-type point defects relative to the case of CoCrFeNi [77]. A decrease in corrosion resistance was observed with the addition of Al to the (Al)-Co-Cr-Fe-Ni system was attributed to the increased oxygen vacancy concentration acting as charge carriers via the point defect model [78]. The increasing Al concentration in the passive films of the high-Al CCAs (Figure 15) could contribute to the increase point defect mobility in the passive film (Figures 5, 9, Tables IV, V).

4.2 Kinetic Factors Influencing Passive Film Formation

The presence of Al as a metastable oxide must also be considered, particularly under either local or global conditions where the solution pH would not promote stable oxide presence. XPS sputter depth profiling reveals Al enrichment near the metal-oxide interface, below both protective Cr and Ti oxides, in both the evaluated CCAs (Figure 16) and Fe-Cr-Al-Ti alloys synthesized to evaluate the passive film interplay of the three elements [43]. Notably, such Al presence in the passive film is less prominent in passive films formed on Ti-free passive films formed in similar environments. Thus, Al oxide presence suggested by XPS depth profiling may be indicative of metastable Al oxide formation that is protected by the Ti oxides that form above it. Metastable Al oxide formation has been observed in similar alloys in conditions as acidic as pH 1 [79]. It is possible that similar metastable oxides form on all the Al-containing CCAs, but are only characterized by XPS when protected by stable Ti oxides. Notably, possible metastable oxides would compromise the thermodynamic conclusions regarding Al stability in the passive film. However, whether the presence of Al in the passive film in environments where Al oxides are not predicted as stable on pure of Al is metastable or thermodynamically stable based off interactions with other passive film constituent elements cannot be practically determined without further study.

Al is still suggested to be enriched at the surface at both pH values, dissolution rates did not clearly decrease with time as in the case of Fe and Ni, indicating possible continual dissolution of metastable oxides (Figure 12). However, determination of the effects of aging are difficult to confirm due to high amounts of noise at extended times. Extended aging times, such as those used in the 40 ks oxide film growth procedure prior to surface characterization, have been suggested to improve surface cation fractions attributable to more thermodynamically stable passive species, either through enriching cations with more stable passive species (e.g. Al, Cr, Ti), or by promoting the formation of suggested by XPS fitting (Figure 14) [80, 81]. Such aging may decrease the enrichment of the possibly metastable Al species in the film. Additionally, interpretation of surface enrichment calculations from AESEC remains difficult as the chemical state may not be observed. For example, despite Ni being predicted to be enriched at the surface in both environments, there is very little Ni in the passive film (Figure 15), with Ni instead often becoming enriched in an "altered zone" in the metal near the metal-oxide interface [39, 45].

The current densities observed in potentiodynamic polarization across different potentials also provide insight into the kinetics of passive film formation. The rate at which a stable passive film is able to form from a cathodically pre-treated surface may be indicated by the critical current density (i_{crit}), the maximum current density observed prior to the passive region. Decreasing i_{crit} values indicate less total charge transfer necessary prior to the formation of a stable passive film, indicating a thinner film (less monolayers) is sufficient to ensure passivity. Peng et al. showed Al generally decreases i_{crit} when added to Fe-Al alloys up to 25 at. % owing to its nature as a rapid passivator [31]. Al has also been shown to decrease i_{crit} in similar CCAs by Blades [38] et al. However, it remains unclear whether the improved passivity was attributable to the presence of Al in the passive film, or whether Al induced Cr-Cr chemical short range ordered, which improves passivity through well-established percolation models [37].

While trends in passive film formation kinetics could not be determined with i_{crit}, the protectiveness of a stable film may be evaluated via i_{pass}. Potentiodynamic polarization of the oxide films formed from cathodically pre-treated surfaces (Figure 5, Table IV) indicated generally decreasing i_{pass} values with Al content. Decreasing i_{pass} values suggest a more protective oxide layer. This indicates that despite the passive films of the Al-enriched CCAs often breaking down at or near phase boundaries that are not present in the low-Al alloys (Figure 8), such microstructural features do enhance passive current densities at potentials for which the film is stable. Furthermore, the formation of a stronger passive film suggests possible beneficial effects of Al, either through its own presence in the passive film and passivity contributions or through beneficial interactions with other passivators such as Cr or Ti.

4.3 Microstructural Effects on Corrosion Behavior

Passive film stability and formation rates are affected by both the global and local Al concentration. Thus, the distribution of Al and other passivating elements across the microstructure plays a prominent role in corrosion behavior. Therefore, the effects of Al on the presence and composition of additional phases must be considered in addition to its effects on passivity.

Al is shown to increase both the number of phases in microstructure as well as volume fraction of non-matrix phases, confirming trends computational predictions despite inaccurate quantitative predictions (Figures 1, 3, Tables II, III). As in the case of the $Al_xCoCrFeNi$ system evaluated by Shi et al [9, 49], random pitting was observed in the low-Al FCC CCAs, while the second phase interface was suggested to be a preferential site for pitting when present in the CCAs with higher Al concentration (Figure 8). The preferential dissolution of the second phase observed by Shi et al. [49] was not observed, possibly due to the enrichment of Ti in the $L2_1$ phase (Figure 4, Table III) that was not present in the Al-Ni enriched BCC phase of the Al-Co-Cr-Fe-Ni system. Therefore, the corrosion behavior of a CCA is affected by the structure and composition of second phases beyond simply whether or not a single-phase matrix is present.

The effects of Al concentration, microstructure and corrosion behavior is prominent in the observed trends with E_{pit}. Figure 20 shows a previously observed general downward trend in E_{pit} with Al concentration in the same CCA system [82]. However, increasing Al concentration does not always correspond to decreased pitting resistance for each individual CCA pair. For instance, E_{pit} increases with increases in Al concentration from Al-3.1 to Al-6.0 despite the presence of a $L2_1$ second phase that was not present for Al-3.1 (Figures 3, 4). A significant decrease in E_{pit} is observed at Al concentrations above 8.2 at. %, where the volume fraction of the $L2_1$ second phase begins to rise. Despite rising volume fractions, regions of $L2_1$ phase are typically less than 10 µm in size. At Al concentrations of 9.6 at. % and higher, a BCC-like third phase enriched in Cr and Mo was also observed (Figure 4), which also may contribute to adverse corrosion resistance [83, 84]. Thus, it is possible that a limited amount of $L2_1$ phase may be present without significantly harming corrosion resistance. Such a critical value will be dependent on the composition, and possibly environment.

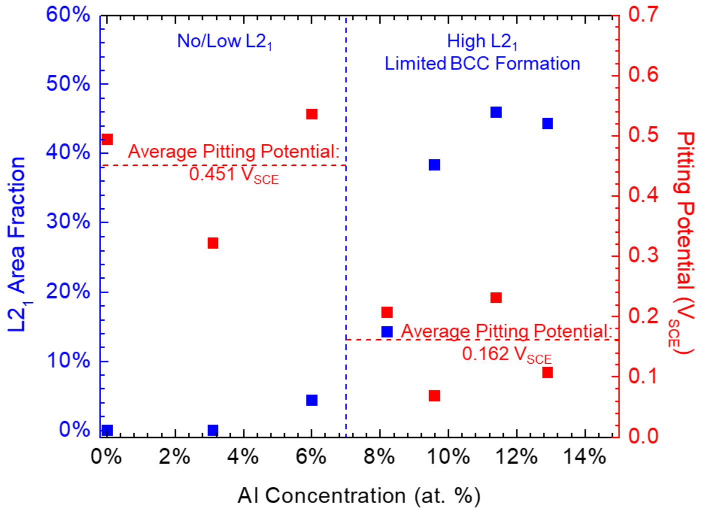

Figure 20: CCA series L2$_1$ area fractions from [30] and average pitting potential in 0.01 M NaCl (pH ~5.75) following cathodic pre-treatment (-1.3 V$_{SCE}$, 600 s) compared to Al content, reproduced from [82].

In addition to the volume fraction of the L2$_1$, the composition of the L2$_1$ phase has may also contribute to the sharp decrease in corrosion resistance beyond 8-10 at. %. While the L2$_1$ phase has a similar Al and Ti concentration in the 6.0 at. % Al CCA (where Al and Ti have the same bulk concentration), The concentration of Ti in the L2$_1$ phase of CCAs with higher Al concentration generally decreases (Table III) at levels well beyond the decrease in bulk Ti concentration (Table I) as the increasing volume fraction over which the near equivalent Ti concentration is divided. CALPHAD modeling shows the decreasing Ti concentrations are often compensated by Al sitting on the Ti sites in the L2$_1$ lattice (not shown). Given the suggested role of Ti in stabilizing Al presence in the passive film, decreasing Ti concentration in the L2$_1$ phase may limit the passivity over the L2$_1$ regions regardless of Al concentration.

Likewise, the role of the third phase must be considered. The high concentrations of Cr and Mo suggest the phase is not prone to preferential corrosion. However, the local enrichment of Cr enrichment in the BCC phase may further decrease Cr concentration in both the FCC and L2$_1$ phases, although this was not visible in the EDS point scans (Table III), possibly due to combinations of the increasing L2$_1$ volume fractions likely contributing to Cr and Mo enrichment in the FCC phase. Decreasing Cr concentrations in the L2$_1$ phase may limit the beneficial Al-Cr-Ti coexistence in the passive film, which has been suggested to improve passivity in the evaluated alloy class [45]. However, the low Cr concentration in the L2$_1$ phase and semi-quantitative nature of EDS point scans limits confirmation of such effects at a statistically significant level. The local composition of the passive film is discussed further in Chapter 6.

5.0 Conclusions

A series of homogenized $Al_xCr_{0.5}Fe_2Mn_{0.25}Mo_{0.15}Ni_{0.5}$ CCAs were synthesized and characterized to evaluate the effect of Al concentration on the interplay between microstructure, passivity and corrosion behavior. The following conclusions were observed:

- Increasing Al concentration transitioned single phase FCC microstructures to those containing Al, Ni, and Ti enriched $L2_1$ second phases with increasing volume fractions. At the highest Al concentrations, additional phases including a Mo-enriched BCC-like third phase were present. Interfaces between phases often acted as corrosion initiation sites.
- Simultaneous enrichment of Al with stable passivators Cr and Ti in the passive films. Enrichment at similar depths of Ti as well as higher Ti concentrations in the passive films of Al-containing CCAs may suggest coexistence within the passive film and possible Ti-aided stability of Al oxides.
- Metrics traditionally used to define passivity (e.g., i_{pass}, R_P, critical current density) often showed inconsistent or inconclusive trends with Al concentration. However, CCAs with lower Al concentrations with zero or low $L2_1$ volume fractions were suggested to have higher E_{pit} values, indicating superior resistance to breakdown.

Acknowledgments

This work was supported by the Office of Naval Research grants #N00014-23-1-2441 and #N00014-19-1-2420 under the directorship of Dave Shifler. Sample synthesis was performed by Jie Qi and Diego Ibarra Hoyos. Mark Wischhusen contributed to the SEM imaging, analyzed the $L2_1$ area fractions for the alloy series, and produced the isopleth diagram. S. Joseph Poon and Sean Agnew contributed to funding acquisition and supervision. Junsoo Han completed the AESEC characterization and analysis with support from Agence Nationale de Recherche, award # ANR-20-CE08-0031 (TAPAS 2020) and the facilities assistance of Kevin Ogle. The UVA Nanomaterials Characterization Facility provided the SEM, XPS, and XRD facilities, with the PHI VersaProbe III procured under NSF award # 162601.

References

[1] D.B. Miracle, O.N. Senkov, A critical review of high entropy alloys and related concepts, Acta Materialia, 122 (2017) 448-511.

[2] O.N. Senkov, C. Woodward, D.B. Miracle, Microstructure and Properties of Aluminum-Containing Refractory High-Entropy Alloys, JOM, 66 (2014) 2030-2042.

[3] O.N. Senkov, D.B. Miracle, K.J. Chaput, J.-P. Couzinie, Development and exploration of refractory high entropy alloys—A review, Journal of Materials Research, 33 (2018) 3092-3128.

[4] R. Feng, C. Lee, M. Mathes, T.T. Zuo, S. Chen, J. Hawk, Y. Zhang, P. Liaw, Design of Light-Weight High-Entropy Alloys, Entropy, 18 (2016) 333.

[5] C.-J. Tong, Y.-L. Chen, J.-W. Yeh, S.-J. Lin, S.-K. Chen, T.-T. Shun, C.-H. Tsau, S.-Y. Chang, Microstructure characterization of Alx CoCrCuFeNi high-entropy alloy system with multiprincipal elements, Metallurgical and Materials Transactions A, 36 (2005) 881-893.

[6] J.W. Yeh, S.K. Chen, S.J. Lin, J.Y. Gan, T.S. Chin, T.T. Shun, C.H. Tsau, S.Y. Chang, Nanostructured High-Entropy Alloys with Multiple Principal Elements: Novel Alloy Design Concepts and Outcomes, Advanced Engineering Materials, 6 (2004) 299-303.

[7] X. Fu, C.A. Schuh, E.A. Olivetti, Materials selection considerations for high entropy alloys, Scripta Materialia, 138 (2017) 145-150.

[8] Y. Qiu, S. Thomas, M.A. Gibson, H.L. Fraser, N. Birbilis, Corrosion of high entropy alloys, npj Materials Degradation, 1 (2017) 15.

[9] Y. Shi, L. Collins, R. Feng, C. Zhang, N. Balke, P.K. Liaw, B. Yang, Homogenization of AlxCoCrFeNi high-entropy alloys with improved corrosion resistance, Corrosion Science, 133 (2018) 120-131.

[10] Y. Shi, B. Yang, P.K. Liaw, Corrosion-Resistant High-Entropy Alloys: A Review, in: Metals, 2017.

[11] H. Okamoto, Al-Ni (aluminum-nickel), Journal of Phase Equilibria, 14 (1993) 257-259.

[12] J. Murray, Fe–Al binary phase diagram, Alloy Phase Diagrams. ASM International. OH-USA. Materials Park, 54 (1992).

[13] D.J.M. King, S.C. Middleburgh, A.G. McGregor, M.B. Cortie, Predicting the formation and stability of single phase high-entropy alloys, Acta Materialia, 104 (2016) 172-179.

[14] X. Yang, Y. Zhang, Prediction of high-entropy stabilized solid-solution in multi-component alloys, Materials Chemistry and Physics, 132 (2012) 233-238.

[15] Z. Tang, L. Huang, W. He, P.K. Liaw, Alloying and Processing Effects on the Aqueous Corrosion Behavior of High-Entropy Alloys, in: Entropy, 2014, pp. 895-911.

[16] C.P. Lee, C.C. Chang, Y.Y. Chen, J.W. Yeh, H.C. Shih, Effect of the aluminium content of AlxCrFe1.5MnNi0.5 high-entropy alloys on the corrosion behaviour in aqueous environments, Corrosion Science, 50 (2008) 2053-2060.

[17] B.-y. Li, K. Peng, A.-p. Hu, L.-p. Zhou, J.-j. Zhu, D.-y. Li, Structure and properties of FeCoNiCrCu0.5Alx high-entropy alloy, Transactions of Nonferrous Metals Society of China, 23 (2013) 735-741.

[18] D.H. Xiao, P.F. Zhou, W.Q. Wu, H.Y. Diao, M.C. Gao, M. Song, P.K. Liaw, Microstructure, mechanical and corrosion behaviors of AlCoCuFeNi-(Cr,Ti) high entropy alloys, Materials & Design, 116 (2017) 438-447.

[19] D. Yang, Y. Liu, H. Jiang, M. Liao, N. Qu, T. Han, Z. Lai, J. Zhu, A novel FeCrNiAlTi-based high entropy alloy strengthened by refined grains, Journal of Alloys and Compounds, 823 (2020) 153729.

[20] R. Hu, J. Du, Y. Zhang, Q. Ji, R. Zhang, J. Chen, Microstructure and corrosion properties of AlxCuFeNiCoCr(x = 0.5, 1.0, 1.5, 2.0) high entropy alloys with Al content, Journal of Alloys and Compounds, 921 (2022) 165455.

[21] F. Liu, Q. Song, R. Chen, W. Li, X. Song, J. Sun, C. Wang, Effects of Al and Co contents on the microstructure and properties of AlxCoCryFeNi high-entropy alloys, Materials Characterization, 203 (2023) 113108.

[22] Y. Qiu, S. Thomas, D. Fabijanic, A.J. Barlow, H.L. Fraser, N. Birbilis, Microstructural evolution, electrochemical and corrosion properties of AlxCoCrFeNiTiy high entropy alloys, Materials & Design, 170 (2019) 107698.
[23] M.M. Garlapati, M. Vaidya, A. Karati, S. Mishra, R. Bhattacharya, B.S. Murty, Influence of Al content on thermal stability of nanocrystalline AlxCoCrFeNi high entropy alloys at low and intermediate temperatures, Advanced Powder Technology, 31 (2020) 1985-1993.
[24] J. Joseph, M. Annasamy, S.R. Kada, P.D. Hodgson, M.R. Barnett, D.M. Fabijanic, Optimising the Al and Ti compositional window for the design of γ′ (L12)-strengthened Al–Co–Cr–Fe–Ni–Ti high entropy alloys, Materials Science and Engineering: A, 835 (2022) 142620.
[25] Q. Zhao, Z. Pan, X. Wang, H. Luo, Y. Liu, X. Li, Corrosion and passive behavior of AlxCrFeNi3−x (x = 0.6, 0.8, 1.0) eutectic high entropy alloys in chloride environment, Corrosion Science, 208 (2022) 110666.
[26] D. Choudhuri, T. Alam, T. Borkar, B. Gwalani, A.S. Mantri, S.G. Srinivasan, M.A. Gibson, R. Banerjee, Formation of a Huesler-like L21 phase in a CoCrCuFeNiAlTi high-entropy alloy, Scripta Materialia, 100 (2015) 36-39.
[27] Y.L. Zhao, T. Yang, J.H. Zhu, D. Chen, Y. Yang, A. Hu, C.T. Liu, J.J. Kai, Development of high-strength Co-free high-entropy alloys hardened by nanosized precipitates, Scripta Materialia, 148 (2018) 51-55.
[28] X.D. Xu, P. Liu, S. Guo, A. Hirata, T. Fujita, T.G. Nieh, C.T. Liu, M.W. Chen, Nanoscale phase separation in a fcc-based CoCrCuFeNiAl0.5 high-entropy alloy, Acta Materialia, 84 (2015) 145-152.
[29] W. Qi, W. Wang, X. Yang, G. Zhang, W. Ye, Y. Su, Y. Li, S. Chen, Effects of Al and Ti co-doping on the strength-ductility- corrosion resistance of CoCrFeNi-AlTi high-entropy alloys, Journal of Alloys and Compounds, 925 (2022) 166751.
[30] J.J. Bhattacharyya, S.B. Inman, M.A. Wischhusen, J. Qi, J. Poon, J.R. Scully, S.R. Agnew, Light Weight, Low Cost, and Compositionally Complex Multiphase Alloys with Optimized Strength, Ductility and Corrosion Resistance: Discovery, Design and Mechanistic Understandings, Materials & Design, 228 (2023).
[31] J. Peng, F. Moszner, J. Rechmann, D. Vogel, M. Palm, M. Rohwerder, Influence of Al content and pre-oxidation on the aqueous corrosion resistance of binary Fe-Al alloys in sulphuric acid, Corrosion Science, 149 (2019) 123-132.
[32] H.H. Uhlig, G.E. Woodside, Anodic Polarization of Passive and Non-passive Chromium–Iron Alloys, The Journal of Physical Chemistry, 57 (1953) 280-283.
[33] H. Springer, C. Baron, L. Tanure, M. Rohwerder, A combinatorial study of the effect of Al and Cr additions on the mechanical, physical and corrosion properties of Fe, Materials Today Communications, 29 (2021) 102947.
[34] R.B. Rebak, L. Yin, T.B. Jurewicz, A.K. Hoffman, Acid Dissolution Behavior of Ferritic FeCrAl Tubes Candidates for Nuclear Fuel Cladding, Corrosion, 77 (2021) 1321-1331.
[35] F.H. Stott, G.C. Wood, J. Stringer, The influence of alloying elements on the development and maintenance of protective scales, Oxidation of Metals, 44 (1995) 113-145.
[36] E. Airiskallio, E. Nurmi, M.H. Heinonen, I.J. Väyrynen, K. Kokko, M. Ropo, M.P.J. Punkkinen, H. Pitkänen, M. Alatalo, J. Kollár, B. Johansson, L. Vitos, Third element effect in the surface zone of Fe-Cr-Al alloys, Physical Review B, 81 (2010) 033105.
[37] K. Sieradzki, R.C. Newman, A Percolation Model for Passivation in Stainless Steels, Journal of The Electrochemical Society, 133 (1986) 1979.
[38] W.H. Blades, B.W.Y. Redemann, N. Smith, D. Sur, M.S. Barbieri, Y. Xie, S. Lech, E. Anber, M.L. Teheri, C. Wolverton, T.M. McQueen, J.R. Scully, K. Seradzki, Tuning Chemical Short-range Order for Stainless Behavior at Reduced Chromium Concentrations in Multi-principal Element Alloys, (2023).
[39] S.B. Inman, J.R. Scully, Design and Discovery of Compositionally Complex Alloys (CCA) that Include High Corrosion Resistance, Corrosion, 80 (2024) 250-258.

[40] J.R. Scully, S.B. Inman, A.Y. Gerard, C.D. Taylor, W. Windl, D.K. Schreiber, P. Lu, J.E. Saal, G.S. Frankel, Controlling the corrosion resistance of multi-principal element alloys, Scripta Materialia, 188 (2020) 96-101.
[41] Y.S. Zhang, X.M. Zhu, Electrochemical polarization and passive film analysis of austenitic Fe–Mn–Al steels in aqueous solutions, Corrosion Science, 41 (1999) 1817-1833.
[42] J. Bosch, U. Martin, W. Aperador, J.M. Bastidas, J. Ress, D.M. Bastidas, Corrosion Behavior of High-Mn Austenitic Fe–Mn–Al–Cr–C Steels in NaCl and NaOH Solutions, Materials, 14 (2021) 425.
[43] D. Sur, S.B. Inman, K.L. Anderson, J. Qi, M. Barbiari, J.R. Scully, Passivation behavior of Fe-Cr-Al-Ti alloys in sulfate containing aqueous environments, In Progress.
[44] Y. Qiu, R. Liu, T. Gengenbach, O. Gharbi, S. Choudhary, S. Thomas, H.L. Fraser, N. Birbilis, Real-time dissolution of a compositionally complex alloy using inline ICP and correlation with XPS, npj Materials Degradation, 4 (2020) 7.
[45] S.B. Inman, D. Sur, J. Han, K. Ogle, J.R. Scully, Corrosion Behavior of a Compositionally Complex Alloy Utilizing Simultaneous Al, Cr, and Ti Passivation, Corroison Science, 217 (2023) 111138.
[46] S. Choudhary, S. Thomas, D.D. Macdonald, N. Birbilis, Growth Kinetics of Multi-Oxide Passive Film Formed Upon the Multi-Principal Element Alloy AlTiVCr: Effect of Transpassive Dissolution of V and Cr, Journal of The Electrochemical Society, 168 (2021) 051506.
[47] M. Pourbaix, Atlas of electrochemical equilibria in aqueous solutions, in, National Association of Corrosion Engineers, Houston, Tex., 1974.
[48] Y. Shi, B. Yang, X. Xie, J. Brechtl, K.A. Dahmen, P.K. Liaw, Corrosion of AlxCoCrFeNi high-entropy alloys: Al-content and potential scan-rate dependent pitting behavior, Corrosion Science, 119 (2017) 33-45.
[49] Y. Shi, L. Collins, N. Balke, P.K. Liaw, B. Yang, In-situ electrochemical-AFM study of localized corrosion of AlxCoCrFeNi high-entropy alloys in chloride solution, Applied Surface Science, 439 (2018) 533-544.
[50] Y.-F. Kao, T.-J. Chen, S.-K. Chen, J.-W. Yeh, Microstructure and mechanical property of as-cast, -homogenized, and -deformed AlxCoCrFeNi (0≤x≤2) high-entropy alloys, Journal of Alloys and Compounds, 488 (2009) 57-64.
[51] C.-C. Yen, H.-N. Lu, M.-H. Tsai, B.-W. Wu, Y.-C. Lo, C.-C. Wang, S.-Y. Chang, S.-K. Yen, Corrosion mechanism of annealed equiatomic AlCoCrFeNi tri-phase high-entropy alloy in 0.5 M H2SO4 aerated aqueous solution, Corrosion Science, 157 (2019) 462-471.
[52] C.P. Lee, Y.Y. Chen, C.Y. Hsu, J.W. Yeh, H.C. Shih, Enhancing pitting corrosion resistance of AlxCrFe1.5MnNi0.5 high-entropy alloys by anodic treatment in sulfuric acid, Thin Solid Films, 517 (2008) 1301-1305.
[53] Z. Wang, Z.-X. Liu, J. Jin, D.-Z. Tang, L. Zhang, Selective corrosion mechanism of CoCrFeMoNi high-entropy alloy in the transpassive region based on the passive film characterization by ToF-SIMS, Corrosion Science, 218 (2023) 111206.
[54] S.B. Inman, M.A. Wischhusen, J. Qi, J. Poon, S.R. Agnew, J.R. Scully, Variation of the Passive Film on Compositionally Concentrated Dual-phase Al0.3Cr0.5Fe2Mn0.25Mo0.15Ni1.5Ti0.3 and Implications for Corrosion, Submitted to Metallurgical and Materials Transactions A, (2024).
[55] K.F. Quiambao, S.J. McDonnell, D.K. Schreiber, A.Y. Gerard, K.M. Freedy, P. Lu, J.E. Saal, G.S. Frankel, J.R. Scully, Passivation of a corrosion resistant high entropy alloy in non-oxidizing sulfate solutions, Acta Materialia, 164 (2019) 362-376.
[56] K. Lutton, K. Gusieva, N. Ott, N. Birbilis, J.R. Scully, Understanding multi-element alloy passivation in acidic solutions using operando methods, Electrochemistry Communications, 80 (2017) 44-47.
[57] K. Ogle, Atomic Emission Spectroelectrochemistry: Real-Time Rate Measurements of Dissolution, Corrosion, and Passivation, Corrosion, 75 (2019) 1398-1419.

[58] J. Baltrusaitis, B. Mendoza-Sanchez, V. Fernandez, R. Veenstra, N. Dukstiene, A. Roberts, N. Fairley, Generalized molybdenum oxide surface chemical state XPS determination via informed amorphous sample model, Applied Surface Science, 326 (2015) 151-161.

[59] M.C. Biesinger, L.W.M. Lau, A.R. Gerson, R.S.C. Smart, Resolving surface chemical states in XPS analysis of first row transition metals, oxides and hydroxides: Sc, Ti, V, Cu and Zn, Applied Surface Science, 257 (2010) 887-898.

[60] M.C. Biesinger, B.P. Payne, A.P. Grosvenor, L.W.M. Lau, A.R. Gerson, R.S.C. Smart, Resolving surface chemical states in XPS analysis of first row transition metals, oxides and hydroxides: Cr, Mn, Fe, Co and Ni, Applied Surface Science, 257 (2011) 2717-2730.

[61] A. Obrosov, R. Gulyaev, A. Zak, M. Ratzke, M. Naveed, W. Dudzinski, S. Weiß, Chemical and Morphological Characterization of Magnetron Sputtered at Different Bias Voltages Cr-Al-C Coatings, in: Materials, 2017.

[62] A. Takeuchi, A. Inoue, Classification of Bulk Metallic Glasses by Atomic Size Difference, Heat of Mixing and Period of Constituent Elements and Its Application to Characterization of the Main Alloying Element, MATERIALS TRANSACTIONS, 46 (2005) 2817-2829.

[63] Y.-M. Chen, N.G. Rudawski, E. Lambers, M.E. Orazem, Application of impedance spectroscopy and surface analysis to obtain oxide film thickness, Journal of The Electrochemical Society, 164 (2017) C563.

[64] B. Hirschorn, M.E. Orazem, B. Tribollet, V. Vivier, I. Frateur, M. Musiani, Determination of effective capacitance and film thickness from constant-phase-element parameters, Electrochimica Acta, 55 (2010) 6218-6227.

[65] ASTM, G61-86 Standard Test Method for Conducting Cyclic Potentiodynamic Polarization Measurements for Localized Corrosion Susceptibility of Iron-, Nickel-, or Cobalt-Based Alloys, in, 2018.

[66] H. Torbati-Sarraf, M. Shabani, P.D. Jablonski, G.J. Pataky, A. Poursaee, The influence of incorporation of Mn on the pitting corrosion performance of CrFeCoNi High Entropy Alloy at different temperatures, Materials & Design, 184 (2019) 108170.

[67] J. Yang, J. Wu, C.Y. Zhang, S.D. Zhang, B.J. Yang, W. Emori, J.Q. Wang, Effects of Mn on the electrochemical corrosion and passivation behavior of CoFeNiMnCr high-entropy alloy system in H2SO4 solution, Journal of Alloys and Compounds, 819 (2020) 152943.

[68] S.B. Inman, J. Han, A.Y. Gerard, J. Qi, M.A. Wischhusen, S.R. Agnew, S.J. Poon, K. Ogle, J.R. Scully, Effect of Mn Content on the Passivation and Corrosion of Al0.3Cr0.5Fe2MnxMo0.15Ni1.5Ti0.3 Compositionally Complex Face-Centered Cubic Alloys, Corrosion, 78 (2021) 32-48.

[69] J.D. Cox, D.D. Wagman, V.A. Medvedev, CODATA Key Values for Thermodynamics, in, New York, 1989.

[70] S.E. Ziemniak, L.M. Anovitz, R.A. Castelli, W.D. Porter, Thermodynamics of Cr2O3, FeCr2O4, ZnCr2O4, and CoCr2O4, The Journal of Chemical Thermodynamics, 39 (2007) 1474-1492.

[71] S. Kirklin, J.E. Saal, B. Meredig, A. Thompson, J.W. Doak, M. Aykol, S. Rühl, C. Wolverton, The Open Quantum Materials Database (OQMD): assessing the accuracy of DFT formation energies, npj Computational Materials, 1 (2015) 15010.

[72] J.E. Saal, S. Kirklin, M. Aykol, B. Meredig, C. Wolverton, Materials Design and Discovery with High-Throughput Density Functional Theory: The Open Quantum Materials Database (OQMD), JOM, 65 (2013) 1501-1509.

[73] Z. Wang, E.-M. Paschalidou, A. Seyeux, S. Zanna, V. Maurice, P. Marcus, Mechanisms of Cr and Mo Enrichments in the Passive Oxide Film on 316L Austenitic Stainless Steel, Frontiers in Materials, 6 (2019) 232.

[74] S.B. Inman, J. Han, M.A. Wischhusen, J. Qi, S.R. Agnew, K. Ogle, J.R. Scully, Passivation and Localized Corrosion Resistance of Al0.3Cr0.5Fe2MoxNi1.5Ti0.3 Compositionally Complex Alloys: Effect of Mo Content, Corroison Science, 227 (2024) 111692.

[75] K. Wang, J. Han, A.Y. Gerard, J.R. Scully, B.-C. Zhou, Potential-pH diagrams considering complex oxide solution phases for understanding aqueous corrosion of multi-principal element alloys, npj Materials Degradation, 4 (2020) 35.
[76] P. Zhao, H. Zhao, J. Yu, H. Zhang, H. Gao, Q. Chen, Crystal structure and properties of Al2O3-Cr2O3 solid solutions with different Cr2O3 contents, Ceramics International, 44 (2018) 1356-1361.
[77] C.B. Nascimento, U. Donatus, C.T. Ríos, R.A. Antunes, Electronic properties of the passive films formed on CoCrFeNi and CoCrFeNiAl high entropy alloys in sodium chloride solution, Journal of Materials Research and Technology, 9 (2020) 13879-13892.
[78] D.D. Macdonald, The Point Defect Model for the Passive State, Journal of The Electrochemical Society, 139 (1992) 3434.
[79] D. Sur, E.F. Holcombe, W.H. Blades, E.A. Anber, D.L. Foley, B.L. DeCost, J. Liu, J. Hattrick-Simpers, K. Sieradzki, H. Joress, J.R. Scully, M.L. Taheri, An Experimental High-Throughput to High-Fidelity Study Towards Discovering Al–Cr Containing Corrosion-Resistant Compositionally Complex Alloys, High Entropy Alloys & Materials, 1 (2023) 336-353.
[80] K. Lutton, J. Han, H.M. Ha, D. Sur, E. Romanovskaia, J.R. Scully, Passivation of Ni-Cr and Ni-Cr-Mo Alloys in Low and High pH Sulfate Solutions, Journal of The Electrochemical Society, 170 (2023) 021507.
[81] K. Orson, E. Romanovskaia, A. Costine, J. Han, K. Ogle, J.R. Scully, P. Reinke, Corrosion Resistance, Composition, and Stratification of Passive Films: Ni-22Cr and Ni-22Cr-6Mo Alloys Passivated and Exposure Aged in Acidic Chloride Solutions, Journal of The Electrochemical Society, 171 (2024) 011505.
[82] S.B. Inman, J.R. Scully, Design and Discovery of Compositionally Complex Alloys (CCA) that Include High Corrosion Resistance, Accepted to Corrosion, (2024).
[83] Y.L. Chou, J.W. Yeh, H.C. Shih, The effect of molybdenum on the corrosion behaviour of the high-entropy alloys Co1.5CrFeNi1.5Ti0.5Mox in aqueous environments, Corrosion Science, 52 (2010) 2571-2581.
[84] W. Wang, J. Wang, H. Yi, W. Qi, Q. Peng, Effect of Molybdenum Additives on Corrosion Behavior of (CoCrFeNi)100−xMox High-Entropy Alloys, in: Entropy, 2018.

Chapter 3: Effect of Ti on the Corrosion Resistance of an Al-Cr-Fe-Mn-Mo-Ni Dual Phase CCA Series

Abstract

Five $Al_{0.3}Cr_{0.5}Fe_2Mn_{0.25}Mo_{0.15}Ni_{1.5}Ti_x$ (x = 0, 0.15, 0.3, 0.5, 0.7) compositionally concentrated alloys were synthesized and annealed at 1070 °C forming alloys with a single-phase FCC matrix for alloys with Ti concentrations up to 3 at. %. At Ti concentrations of 6 at. % and above, an $L2_1$ phase enriched in Al, Ti and Ni was present within the FCC matrix. At Ti concentrations of 9.6 at. % Ti and above, a three-phase microstructure containing FCC + $L2_1$ + Laves phases was formed, with the Laves third phases enriched in Cr and Mo. Global corrosion resistance was evaluated in dilute chloride solutions at neutral pH. Increasing Ti concentrations were suggested to improve alloy passivity, evidenced by generally lower current densities and higher impedance magnitudes for both single and multi-phase microstructures. Pitting and repassivation potentials as a function of Ti content were the greatest at Ti concentrations of 6.0 at. %. Resistance to localized corrosion was suggested to improve with Ti concentration before reaching an optimal concentration and beginning to decrease, potentially due to the formation of new phases such as Laves whose interfaces are prone to localized corrosion. Passive film composition was characterized indicating Ti(IV) is a prominent constituent in the passive films of this Ti-containing alloy despite only being enriched relative to bulk composition in the $L2_1$ phase. Moreover, surface Ti(IV) cation fractions for a three-phase CCA with 9.6 at. % Ti were not higher than that of a two-phase CCA with 6.0 at. % Ti. Ti may affect overall corrosion behavior through its presence in the passive film as well as by triggering microstructural changes that may compromise the ability of an alloy to protect multiple phases simultaneously. These factors are discussed with regard to compositionally concentrated alloy design.

1.0 Introduction

Ti is a frequent addition to both refractory [1-6] and transition-metal [3, 5, 7-9] based complex concentrated alloys (CCAs) providing a wide range of properties including mechanical strength [6, 7, 10, 11], low densities [3, 4, 8, 12-15], high-temperature oxidation resistance [9, 16, 17], and aqueous corrosion resistance [1, 4, 6, 18].

Strong aqueous corrosion resistance has long-been observed for both pure Ti and Ti-based alloys [19-21]. Alloys such as Ti-6Al-4V have shown viability for corrosion resistance in both biological [22-24] and marine [25, 26] environments. The beneficial attributes of Ti to corrosion resistance are attributable to the thermodynamic stability of TiO_2 across a broad range of environments [27, 28]. The oxide is commonly suggested to be amorphous [29, 30], but rutile structures are frequently observed following rapid anodic growth [31, 32] or exposure to increased temperature [28, 33]. Limited presence of hydrogen or hydroxide ions have also been suggested within TiO_2 films, potentially promoting layering behavior [28], but there is little experimental characterization of passive films with multiple sub-oxide species.

Similar to the case of Ti-dominated alloys, TiO_2 presence may improve the passivity of alloys for which Ti is a constituent element. For example, the addition of Ti to Fe-Ti binary alloys at concentrations as low as 38 at. % has been shown to allow for the formation of a stable TiO_2 passive film in hydrochloric acid, enabling passivity and improving corrosion resistance [34]. Thus, co-constituent alloying elements must be considered for their ability to allow for Ti passivity, particularly for alloys designed with low Ti concentrations.

Additionally, Ti may act as a co-constituent passivator with other passivating elements such as Cr [35]. Like Cr, Ti has been suggested to improve the stability and increase the passive window width of Fe and Al-containing passive films [36, 37], possibly due to the ranges of stable pH for TiO_2 stability being considerably larger than those of the oxides for Fe, Al, or even Cr [27]. However, unlike the case of the Cr_2O_3-Al_2O_3 system, complete solid solution miscibility is not present between TiO_2 and Cr_2O_3 or Al_2O_3 [38, 39], possibly due to insolubility driven by differences in crystal structure. In addition to solid solution oxides, stochiometric line compounds such as $TiAl_2O_5$ [39], $TiCr_2O_5$, and several other Ti-Cr-O compounds [38] may form on the basis of formation energy [40]; however, there is little evidence for experimental observation of Ti-containing complex oxides. The presence of stochiometric line compounds has been theorized as potentially improving passive film stability by improving the potentials and/or pH ranges at which an otherwise unstable constituent species may be stable [40, 41]. However, there is little definitive evidence as to whether stochiometric line compounds improve corrosion resistance relative to solid solution oxides. Significant overlap in the depth profiles of Al-Cr-Ti-V [42], Fe-Cr-Al-Ti [43] and Al-Cr-Fe-Mn-Mo-Ni-Ti [35] passive films suggests that Ti may coexist with Al and Cr; however, further work is necessary to evaluate the precise structural nature of the passive film, notably the structure and nearest neighbor arrangement of elements. Surface and depth profiling with X-ray photoelectron spectroscopy further suggests potential Ti coexistence with Al and/or Cr in additional systems, although enriched levels may vary with depth [4, 8, 44].

The presence of Ti in CCAs, and therefore their passive films, is often suggested to affect corrosion resistance across both single-phase and multi-phase systems [10, 18, 45, 46]. Doping of Ti oxide films has been shown to play a strong effect on oxygen evolution kinetics and corrosion resistance [47], potentially by altering local Ti valence states [48], highlighting the importance of cation miscibility even at small concentrations. Furthermore, the concentration of oxygen vacancies has been tied to the presence, concentration, and/or valence of Ti in the passive film [49-52]. Given oxygen vacancies' frequent role as charge carriers through the passive film, increasing vacancy concentration can affect passivation and dissolution kinetics [53]. Ti can also improve corrosion resistance as a major constituent in the passive film. For example, when added at a concentration of 30 at. % to equimolar CoCrFeNi, the corrosion resistance was suggested to improve, most notably in terms of a broader passive range leading to improved pitting resistance in chloride solutions despite the initiation of a Ti-enriched second phase [54].

In some cases, the formation of a new phase outweighs the benefits of Ti additions on corrosion resistance relative to a Ti-free single-phase solid solution CCA. Notably, the addition of Ti promotes phase segregation and decreases overall corrosion resistance when added to the AlCoCuFeNi [55] (BCC/B2 prior to the formation of FCC and Laves phases with the addition of 16.7 at. % Ti) and $Al_{0.3}CrFe_{1.5}MnNi_{0.5}$ [56] (BCC prior to the formation of FCC, Cr_9Al_{17}, and CrNiFe phases with the addition of 18.5 at. % Ti) systems. Ti has been further suggested to promote the formation of new phases across the $Al_2CrFeNiCoCuTi_x$ [57], $AlCoCrFeNiTi_x$ [58] systems. Furthermore, the passivating elements in the aforementioned systems are often locally depleted in one or more phases as a result of increasing Ti concentrations, although an overview of the effects on corrosion resistance was not provided.

While multi-phase alloys frequently have decreased corrosion resistance relative to their single-phase counterparts, the structure and composition of the second phase can influence the magnitude of such effects. Dual-phase CCAs with an FCC matrix containing Ti, Al, and Ni can form an ordered phase such as Huesler ($L2_1$) [59, 60], whereas Ti-free dual-phase CCAs with Al often have comparatively less ordered

Al-Ni enriched B2 or BCC phases [61-66]. Joseph et al. observed increasing volume fractions of the ordered $L1_2$ phase in an FCC matrix with increasing Ti/Al ratios in the $Ni_{51}Co_{18}Fe_5Cr_{10}Al_{16-X}Ti_X$ system [67]. Despite frequent adverse corrosion resistance of dual-phase microstructure CCAs [18], corrosion resistance comparable to 316L stainless steel has been observed in FCC CCAs with a Ti-enriched $L2_1$ second phase [35]. Local characterization of passive film chemistry has shown that the passive film contains multiple phases with the composition and size scale informed by the bulk microstructure. The corrosion behavior multi-phase CCAs is informed by the passivity and corrosion behavior of each individual constituent phase (Chapter 6). Thus, it is necessary to ensure both phases contain adequate concentrations of at least at least one stable passivating element (i.e., Cr remains enriched in the FCC matrix and Ti is enriched in the $L2_1$ second phase). In summary, the likelihood of second-phases limitations adds further complexity to the effects of Ti on corrosion behavior.

Xiao et al. [55] compared AlCoCuFeNi and AlCrCoCuFeNi CCAs with and without equimolar Ti additions. For both alloy systems, the only second phase present in the Ti-free CCAs was disordered BCC. Ti additions to both alloys introduced a Laves phase as well as stabilized an ordered B2 phase. The Ti-containing alloys were suggested to have inferior corrosion resistance in chloride solution on the basis of corrosion potential, corrosion current density, and polarization resistance relative to the Ti-free alloys of otherwise equal composition. However, the effect of Ti on passivity and film breakdown were not explored, and thus possible passivity benefits of Ti were not addressed. Qi et al. [7] observed improved passive and corrosion current densities with the addition of Al and Ti to CoCrFeNi, but the pitting potential decreased due to the stabilization of the B2 phase and $L1_2$ nanoprecipitates within the FCC matrix. Significant Al, Cr, and Ti presence was shown in the passive film, suggesting Ti plays an active role in improving passivity and is likely enriched relative to bulk composition. However, precise surface cation fractions were not provided. Although the microstructural refinement affected corrosion behavior, it is unclear to what degree Ti is responsible due to the mutual addition with Al.

Ti clearly has a key role in the passivity and corrosion resistance of CCAs. However, the prominent effects on microstructure, most frequently through the stabilization of often undesirable phases, may also have undesirable effects on overall corrosion resistance. Despite the ability of Ti to form a stable passive film, it could possibly decrease corrosion resistance relative to a single-phase solid solution with lower concentrations of or no Ti, particularly if a phase depleted in passivating elements is formed. While such effects of Ti are well-studied, studies evaluating the behavior of alloys with a range of Ti concentrations are comparatively less frequent, and often evaluated on coatings as opposed to bulk samples [57, 60].

This highlights a need to further evaluate the effect of minor Ti additions in across a wide range of compositions, providing a basis to optimize Ti concentration for a given CCA system. Compositions allowing for significant Ti enrichment in the passive film could allow for the formation of a continuous TiO_2-containing passive film which could improve corrosion resistance while maintaining bulk compositions low enough to avoid the formation of detrimental phases depleted in passivating elements. Optimization may be further affected by the tendency of Ti to decrease density and increase the cost of transition metal based CCAs while also often improving the mechanical strength and/or decreasing ductility when stabilizing second phases [11, 55, 58], similar to the effects of Al as described in Chapter 2.

This study explores the effects of Ti concentration on a series of $Al_{0.3}Cr_{0.5}Fe_2Mn_{0.25}Mo_{0.15}Ni_{1.5}Ti_x$ CCAs with Ti concentrations between 0.0 and 13.0 at. % Ti. The phases present, second phase morphology, and composition of each phase are characterized with combinations of X-ray diffraction (XRD), scanning electron microscopy (SEM), and energy dispersive spectroscopy (EDS). Significant microstructural focus is allocated to ensuring whether any phases are depleted in passivating elements. The corrosion behavior is then evaluated with combinations of potentiodynamic polarization and electrochemical impedance spectroscopy (EIS), while trends in the presence of Ti in the passive film are evaluated with X-ray photoelectron spectroscopy (XPS). The findings are used to uncover the degree of enrichment of Ti(IV) in the passive films, the nature of multi-cation oxide formation, and to inform compositional optimization in the $Al_{0.3}Cr_{0.5}Fe_2Mn_{0.25}Mo_{0.15}Ni_{1.5}Ti_x$ system and used to establish governing factors that may be extended across the Ti-containing CCA design space.

2.0 Experimental Methods

2.1 Alloy Synthesis and Microstructural Characterization

Five CCAs in the $Al_{0.3}Cr_{0.5}Fe_2Mn_{0.25}Mo_{0.15}Ni_{1.5}Ti_x$ ($x = 0, 0.15, 0.3, 0.5, 0.7$) system with compositions listed in Table I were synthesized from high-purity elements (Cr > 99.2%, all other metals > 99.9%) and arc melted into button samples 1 cm in diameter. Samples were flipped and remelted five times to ensure homogeneity before encapsulation in quartz tubing under Ar, a 6-hour homogenization heat treatment at 1070 ˚C, and quenching in water. Proposed compositions were first modeled with an isopleth diagram developed with CALPHAD techniques using ThermoCalc software operating with the TCHEA3 database. Compositions and heat treatments were selected with the goal of reducing cost and density, ensuring an adequate concentration of passivating elements, and targeting a second-phase reinforced FCC microstructure using methods described elsewhere [68]. The compositions of Mn [69] and Mo [70] were informed by previous work in alloying systems varying the concentrations of each respective elements.

Accuracy of targeted compositions within 0.5 at. % for each element were verified by EDS point scans of selected alloys following homogenization described further below.

Table I: CCA compositions in atomic percent. Pure elements were massed to compositions below within 1% error prior to arc melting.

Alloy	**Al**	**Cr**	**Fe**	**Mn**	**Mo**	**Ni**	**Ti**
Ti-0	6.4	10.6	42.6	5.3	3.2	31.9	0.0
Ti-3.1	6.2	10.3	41.2	5.2	3.1	30.9	3.1
Ti-6.0	6.0	10.0	40.0	5.0	3.0	30.0	6.0
Ti-9.6	5.8	9.6	38.5	4.8	2.9	28.8	9.6
Ti-13.0	5.6	9.3	37.0	4.6	2.8	27.8	13.0

Following homogenization, samples were mechanically ground through 1200 grit paper, and further polished through 1 μm diamond suspension in the case of microstructural and surface analysis. Present phases were identified via XRD with an PANalytical Empyrean Diffractometer^{TM} operating with Cu Kα X-rays (1468.7 eV) and a scan rate of 0.15 ˚/s. Additionally, microstructures were imaged with a FEI Quanta 650^{TM} scanning electron microscope operating in back scattered electron (BSE) mode at an accelerating voltage of 15 keV, a spot size of 4, and a working distance of approximately 10 mm. Partitioning of elements across phases was characterized with EDS point scans and mapping and analyzed with Oxford Instruments Aztec^{TM} software.

2.2 Electrochemical Characterization

A conventional three-electrode cell regulated by a Gamry Instrument Reference 600+™ potentiostat was used for electrochemical characterization of the corrosion behavior. The CCA samples with an exposure area[10] of 0.784 cm^2 defined by a rubber O-ring acted as the working electrode with a platinum mesh counter electrode and a saturated calomel reference electrode (SCE, 0.241 V vs. SHE) relative to which all potentials are reported. 0.01 M NaCl with a natural pH of approximately 5.75 was used as the electrolyte for all experiments to examine the passive region. Select experiments were performed in 0.001, 0.1, and 1 M NaCl with a natural pH ranging between 5.5 and 6. $N_{2(g)}$ was continually bubbled during the experiments to minimize the effects of dissolved oxygen. All electrochemical experiments were repeated threefold for each synthesized CCA as well as commercially produced (North American Steel) 316L to ensure reproducibility.

---

[10] For tests requiring ex-situ characterization that prohibited the use of epoxy mounting (polarization with subsequent pit imaging, potentiostatic oxide growth with subsequent XPS characterization), a smaller exposure area of 0.1 cm^2 was used. The change is accounted for with area-normalized current and impedance parameters.

First, potentiodynamic polarization was used to characterize the formation and breakdown behavior of the passive film. To minimize the effects of the air-formed oxide, a cathodic potential of -1.3 V_{SCE} was first applied for 600 s. The potential was then swept from -1.3 to 0.8 V_{SCE} at a rate of 0.5 mV/s before a reverse scan from 0.8 to -1.3 V_{SCE}. Additionally, the impedance of the film was monitored in-situ during the polarization by applying three AC cycles at every 5 mV applied at a frequency of 1 Hz and an amplitude of 20 mV_{RMS} to provide qualitative trends in passive film thickness using previously described relationships [71-73]. The potential range was selected to ensure a sufficient driving force for the reduction of Cr-dominated air-formed oxide[11] (predicted to reduce at potentials more negative than -1.30 V_{SCE} in pH ~5.75 by E-pH diagrams [27]) as well as to ensure sufficient driving force for the subsequent formation of Al_2O_3, TiO_2, and Cr_2O_3 (which are suggested by E-pH diagrams to form at potentials more positive than -2.14, -1.87, and -1.30 V_{SCE}, respectively, on their respective pure metals in pH ~5.75 conditions [27]). An additional trial was repeated and terminated upon the anodic current density exceeding 10^{-5} A/cm^2 and then imaged via SEM to identify pit initiation sites and morphology.

For potentiodynamic polarization of the Ti-6.0 alloy, elemental dissolution rates were tracked in-situ via Inductively Coupled Plasma Atomic Emission Spectroelectrochemistry (AESEC). A Horiba Jobin Yvon Ultima system described elsewhere [74] was utilized with a 0.5 m polychromator. Mo signal was obtained with a monochromator with a focal length of 1.0 m to improve resolution. To increase dissolution rates above the elemental detection limits, a more aggressive 0.1 M NaCl solution adjusted to a pH of 4 with concentrated HCl was used. Additionally, the $N_{2(g)}$ bubbling and cathodic pre-treatments were bypassed. Elemental intensities at characteristic wavelengths (I_M) were converted dissolution rates (ν_M) with f and A referring to the flow rate and area, respectively. Equivalent dissolution rates were then converted to equivalent current densities (j_M) via Faraday's law with z_M, F, and M_M referring to the elemental charge, Faraday's constant, and the molar mass, respectively. A more thorough discussion of the calculation methodology is provided elsewhere [74].

$$\nu_M = \frac{f I_M}{A} \tag{1}$$

$$j_M = \frac{z_M F \nu_M}{M_M} \tag{2}$$

---

[11] While more negative potentials are necessary to reduce Al_2O_3 or TiO_2 on pure Al or Ti, respectively, previous work in the alloy system has shown a -1.3 V_{SCE} potential to be sufficient to reduce the air-formed oxide [35]. More negative potentials are not used to avoid excessive cathodic reaction rates beyond those necessary to reduce the air-formed oxide. The lack of an air-formed oxide is verified for the evaluated alloy series via in-situ impedance measurements described above.

The corrosion behavior of the CCAs with air-formed oxides was also evaluated. First, open circuit potential (OCP) of the air-formed oxide was monitored for 1800 s. The impedance was then characterized with EIS at a frequency range from 100 kHz to 1 mHz with 5 points measured per decade and an AC sinusoidal amplitude of 20 mV_{RMS}. Following EIS, the alloy was polarized from -0.1 V relative to the established OCP to 0.8 V_{SCE} at a 0.5 mV/s scan rate in the upward direction and then polarized from 0.8 to -1.3 V_{SCE} with the reverse scan described above.

Finally, to characterize the composition and corrosion behavior of a stable passive film formed electrochemically, a third procedure was utilized. The CCA was first exposed to the -1.3 V_{SCE} cathodic treatment described above for 600 s to reduce the effects of the air-formed oxide. A -0.25 V_{SCE} potential, determined to be within the passive range of all evaluated CCAs evaluated during initial polarization testing, was then applied for 40 ks, during which the current density and in-situ impedance (1 Hz, 20 mV_{RMS}) were monitored. The oxide was then characterized with EIS at -0.25 V_{SCE}, otherwise with the same parameters described above (100 kHz to 1 mHz, 20 mV_{RMS}, 5 points/decade). Finally, OCP of the alloy was monitored for 30 minutes.[12]

2.3 Chemical Analysis of Passive Film

Three CCAs with Ti concentrations of 0, 6.0, and 9.6 at. % were selected to evaluate the effect of Ti content on passive film composition and chemistry. A passive film was grown for 40 ks and characterized with EIS at -0.25 V_{SCE} using the procedure described above before transfer under $N_{2(g)}$ to a PHI VersaProbe III™ XPS system. High-resolution spectra were collected over the C1s, O1s, Al 2p, Cr $2p_{3/2}$, Fe $2p_{1/2}$[13], Mn $2p_{1/2}$, Mo 3d, Ni $2p_{3/2}$, and Ti $2p_{3/2}$ (when present) core spectra with Al Kα X-rays (1486.6 eV), a 100 µm spot size, a 26 eV pass energy and a 0.05 eV step size. A Shirly background substitution was first used to remove background noise before fitting of features to asymmetric Doniach-Sunjic peaks for metallic or zero-valance solute trapped feature or symmetric Voight peaks for oxidized cations. Peaks were fit to reference spectra obtained elsewhere from combinations of binding energy, width, amplitude, and multiplet splitting [75-78]. Following fitting of the high-resolution spectra, the intensities (I) of all features attributable to oxidized features (non-zero valance) were summed. The intensities were then normalized to the relative sensitivity factors (RSF) obtained from PHI Mulitipak™ software for each spectrum and

---

[12] For XPS surface characterization, the final OCP step was bypassed to minimize exposure prior to surface characterization.

[13] Due to overlap with Ni auger peaks, traditionally utilized Fe $2p_{3/2}$ and Mn $2p_{3/2}$ core series were eschewed in favor of the $2p_{1/2}$ series.

divided over the cumulative intensity for each element to obtain the surface cation fraction (X^S) as shown below.

$$X_A^S = \frac{\frac{I_A}{RSF_A}}{\Sigma \frac{\mathrm{I_X}}{RSF_X}} \qquad (3)$$

3.0 Results

3.1 CCA Microstructure

XRD patterns shown in Figure 1 indicate the presence of single phase over low Ti concentrations with second and third phase formation at higher Ti concentrations. All CCAs are suggested to contain the FCC phase. Beyond 6.0 at. % Ti, a second BCC-like phase that has been identified elsewhere as $L2_1$ is indexable [68]. Finally, at concentrations at 9.6 at. % Ti and above, a third phase is present. Although the exact structure cannot be indexed due to low intensity, the many peaks present suggest likely ordering and/or the presence of a non-cubic lattice. The isopleth diagram for the $Al_{0.3}Cr_{0.5}Fe_2Mn_{0.25}Mo_{0.15}Ni_{1.5}Ti_x$ system shown in Figure 2 indicates the stability of C14 Laves beyond 8 at. % Ti, suggesting a likely Laves structure for the third phase found in Ti-9.6 and Ti-13.0. The diagram further suggests increasing volume fractions of the $L2_1$ and Laves phases with increasing Ti concentrations.

The experimentally observed present phases for the synthesized alloy series are compared to those predicted by ThemoCalc for each composition in Table II. Notably, $L2_1$ presence is not predicted by the isopleth diagram at Ti concentrations below 12 at. % Ti, indicating possible metastable presence in Ti-6.0 and Ti-9.6.

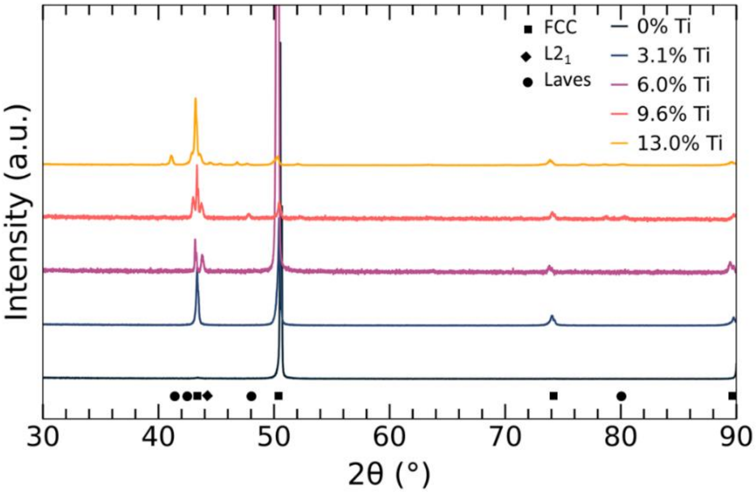

Figure 1: XRD patterns of synthesized CCAs following 6-hour homogenization at 1070˚C with indexed peaks for the FCC, L21, and suggested Laves phases.

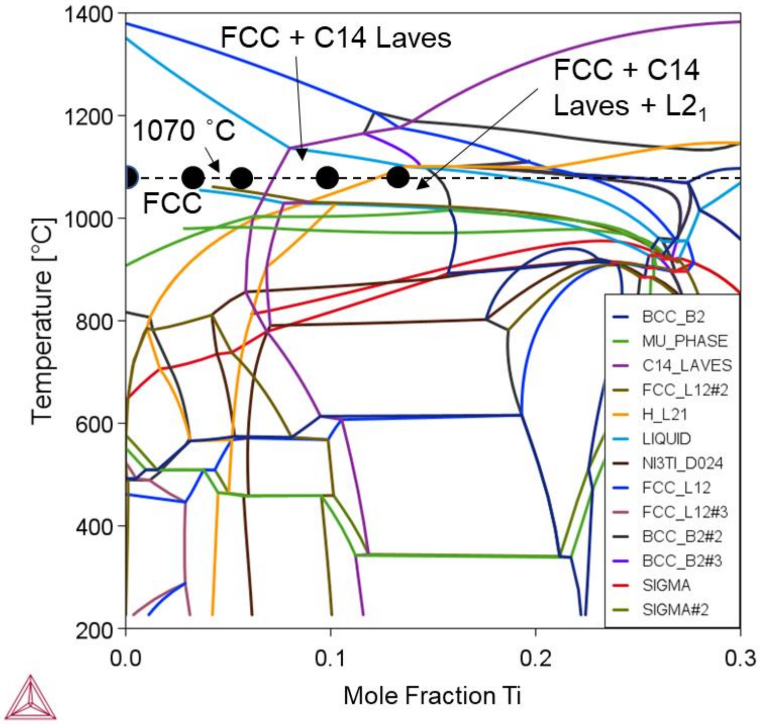

Figure 2: Isopleth diagram of $Al_{0.3}Cr_{0.5}Fe_2Mn_{0.25}Mo_{0.15}Ni_{1.5}Ti_x$ system produced in ThermoCalc with TCHEA3 database. Regions consisting of the CCA series following homogenization are labeled with predicted microstructure. The temperature for heat treatment is identified by the dashed line with synthesized compositions indicated by black circles.

Table II: Phases present in CCAs following 6-hour homogenization at 1070 ˚C compared to computational predictions shown in Figure 2.

Alloy	**Predicted Phases from Isopleth**	**Observed Phases**
Ti-0	FCC	FCC
Ti-3.1	FCC	FCC
Ti-6.0	FCC	FCC + L2$_1$
Ti-9.6	FCC + Laves	FCC + L2$_1$ + Laves
Ti-13.0	FCC + L2$_1$ + Laves	FCC + L2$_1$ + Laves

The presence of additional phases with increasing Ti concentration is confirmed by the BSE micrographs shown in Figure 3. For the 6.0 at. % Ti CCA, the alloy L2$_1$ second phase regions on the order of that are less than 10 µm. In the two high-Ti CCAs, larger regions of approximately 10 µm that alternate between L2$_1$ and Laves phase regions are present.

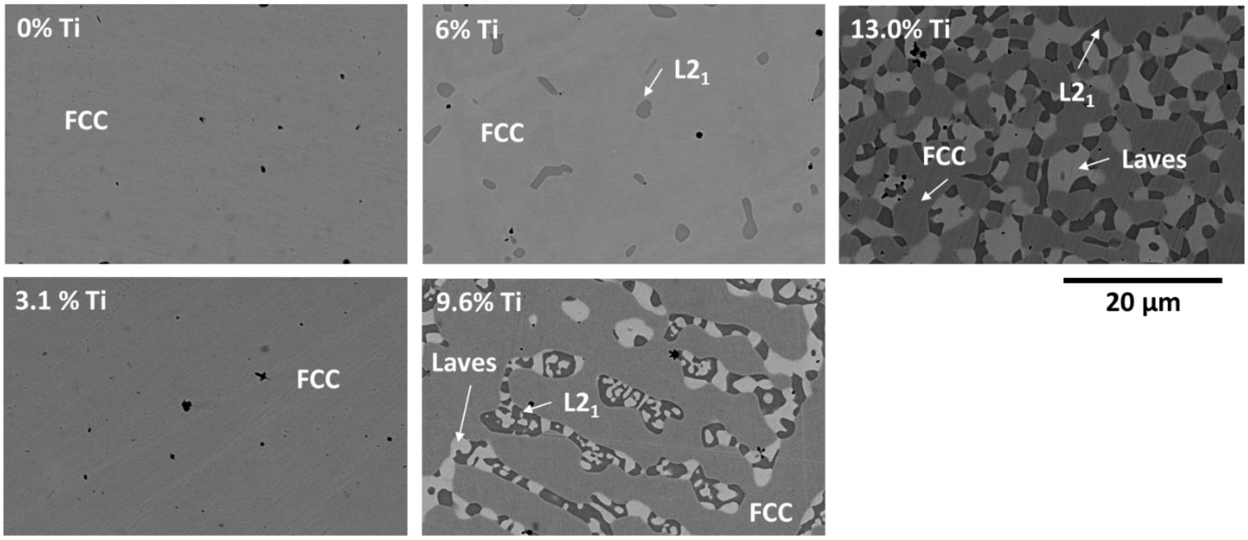

Figure 3: BSE micrographs of CCAs following 6-hour homogenization at 1070˚C.

EDS mapping and point scans of selected CCAs shown in Figure 4 and Table III, respectively, reveal which elements are enriched in each phase. In Ti-6.0, the FCC matrix is enriched in Fe, Mn, Mo, and Cr relative to the bulk composition shown in Table I. The L2$_1$ phase is enriched in Al, Ni, and Ti. Furthermore, the area fractions obtained via ImageJ threshold analysis indicate the phase fraction of the FCC matrix is significantly higher than that of the L2$_1$ phase.

Ti-13.0 has a three-phase microstructure with an additional Laves phase that is enriched in Cr, Fe, and Mo relative to the bulk composition. The FCC matrix is enriched in Fe, Cr, and Mn relative to bulk alloy composition, but unlike Ti-6.0, is not enriched in Mo. The L2$_1$ phase remains enriched in Al, Ni, and Ti. Both the L2$_1$ second phase and Laves third phase have similar phase fractions, and are both present at higher fractions than the L2$_1$ phase of the lower Ti-concentration CCAs such as Ti-6.0. For both Ti-6.0 and Ti-13.0, every phase is enriched in at least one stable passivating element, either Cr or Ti, relative to the bulk alloy composition (Table I). Linescans across the FCC-L2$_1$ interface for Ti-6.0 presented in Chapter 2 do not suggest local depletion of Al, Ni, or Ti in the matrix phase near the interface relative to the composition far from the interface, however, the absence of localized depletion cannot be confirmed due to low resolution. Point scans of Ti-0 and global alloy compositions obtained from the mapping of Ti-6.0 and Ti-9.6 suggest the true composition is within 0.5 at. % of the initial targeted compositions, suggesting that there was no significant material loss during arc-melting.

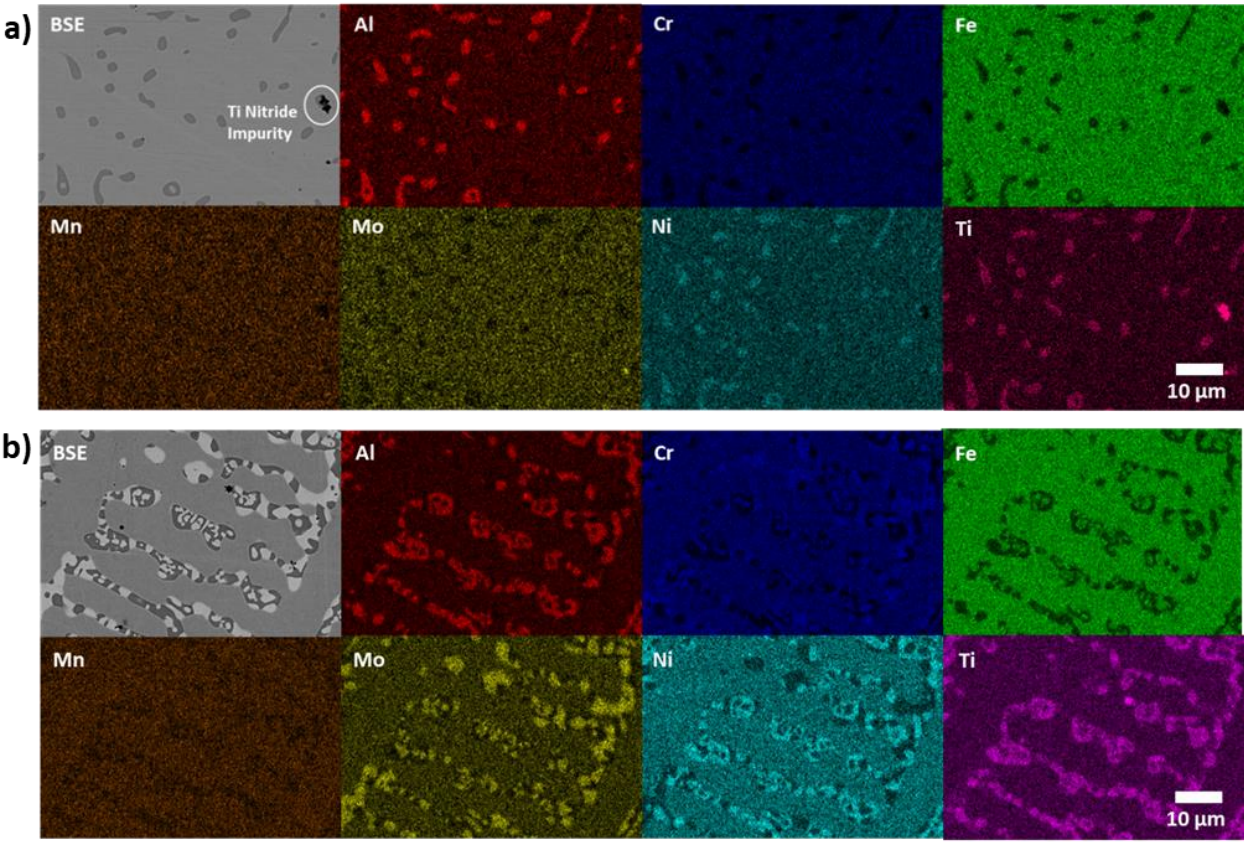

Figure 4: EDS mapping of **a)** Ti-6.0 (FCC + $L2_1$) and **b)** Ti-9.6 (FCC + $L2_1$ + Laves) microstructures.

Table III: Phase compositions for selected alloys identified with EDS point scans. Each term represents the mean value of at least three scans, while global compositions were obtained from quantitative analysis of the mapping area. Area fractions for each phase are identified by ImageJ threshold analysis.

Phase	Al	Cr	Fe	Mn	Mo	Ni	Ti	Area Fraction
$Al_{0.3}Cr_{0.5}Fe_2Mn_0Mo_{0.15}Ni_{1.5}$ (Ti-0)								
Matrix (FCC- Overall)	6.2	10.9	42.5	5.2	3.5	31.6	0.0	100 %
$Al_{0.3}Cr_{0.5}Fe_2Mn_{0.25}Mo_{0.15}Ni_{1.5}Ti_{0.3}$ (Ti-6.0)								
Matrix (FCC)	3.70	11.0	42.5	5.2	3.1	28.8	5.6	95.67 %
2nd Phase ($L2_1$)	14.3	3.5	17.1	4.2	0.9	44.1	15.8	4.33 %
Overall Composition	6.4	10.2	39.7	5.2	2.6	29.7	6.1	-
$Al_{0.3}Cr_{0.5}Fe_2Mn_{0.25}Mo_{0.15}Ni_{1.5}Ti_{0.7}$ (Ti-13.0)								
Matrix	3.8	10.2	42.7	5.0	2.2	28.6	7.6	67.14 %
2nd Phase ($L2_1$)	18.1	1.9	12.4	2.9	0.3	44.3	20.2	14.34%
3rd Phase (Laves)	2.0	15.3	44.7	4.3	7.8	15.6	10.3	18.52%
Overall Composition	5.7	9.8	38.3	4.6	2.8	29.0	9.8	-

3.2 Polarization of CCAs Following Cathodic Pre-treatment

Potentiodynamic polarization was used to characterize the electrochemical behavior and corrosion resistance of the CCAs. An E-log(i) plot obtained during polarization of the series of CCAs that were first cathodically pre-treated to evaluate film formation on a reduced or minimized oxide metal surface is shown in Figure 5. Additionally, in-situ impedance (Z”) measurements are also shown along with key parameters tabulated in Table IV and shown in Figure 6. Spontaneous passivity is shown for all evaluated CCAs in the dilute chloride solution, which is expected given the ability of both Al and Ti to form spontaneous passive films below the potential for hydrogen evolution under neutral conditions as indicated by the horizontal lines at each elements reduction potential [27]. For all alloys, Z” immediately begins to rise with potential, suggesting the passive film grows in thickness directly proportionality to Z”. No clear critical current densities are discernible. which, along with the continually increasing Z” magnitudes, suggest that no active to passive transitions were observed.

No clear trends between E_{corr} and Ti concentration were suggested. Ti-13.0 shows a significantly higher E_{corr}, but the deviations are not suggested to be statistically significant and could arise from oxygen reduction caused by incomplete dissolved oxygen purging during $N_{2(g)}$ bubbling. High E_{corr} values could additionally be influenced by incomplete reduction of air-formed oxide, particularly given the standard reduction potential of Ti being below the -1.3 V_{SCE} potential used for cathodic reduction. However, the low -Z” values for all alloys at -1.3 V_{SCE} suggest complete or near-complete reduction, as opposed to the comparatively much higher values of the air-formed oxides characterized in section 3.3. Alternatively, it is possible that limited oxide growth occurred between the beginning of the polarization process and E_{corr} given the stability of Al, Ti, and Cr passive species over the potential range. Between 0 and 9.6 at. % Ti, i_{pass} decreases with Ti concentration, signifying the formation of a thicker and/or more protective passive film. Between 9.6 and 13 at. % Ti, i_{pass} rises, although not at a significant level. Pitting was the dominant breakdown mechanism for all CCAs with some crevice corrosion also observed. Intermittent increases in current density along with corresponding decreases in Z” suggest metastable pitting that repassivated prior to complete film breakdown. E_{pit} was highest for Ti-6.0 while Ti-0 has the lowest E_{pit}. The lack of a well-defined vertical passive range for Ti-0 suggests a weak or non-protective passive film, leading to both low E_{pit} and high i_{pass} values. Notably, E_{pit} for Ti-6.0 exceeds the potential for which Cr_2O_3 is stable on pure Cr, indicating a partially protective oxide remains, likely due the stability of Al- and Ti-containing passive species [79]. While no trends were present between Ti concentration and Z” at -0.25 V_{SCE}, the potential at which i_{pass} was defined, Ti-6.0 reached the highest -Z” magnitude of all tested CCAs, suggesting the formation of a thicker passive film during polarization. The increase is attributable to the higher E_{pit} allowing for increased time and/or driving force for film formation at increased potentials where the films of other CCAs had already broken down. Finally, E_{rep} follows similar trends as E_{pit}, with the Ti-0 having the minimum value and Ti-6.0 having the maximum value[14].

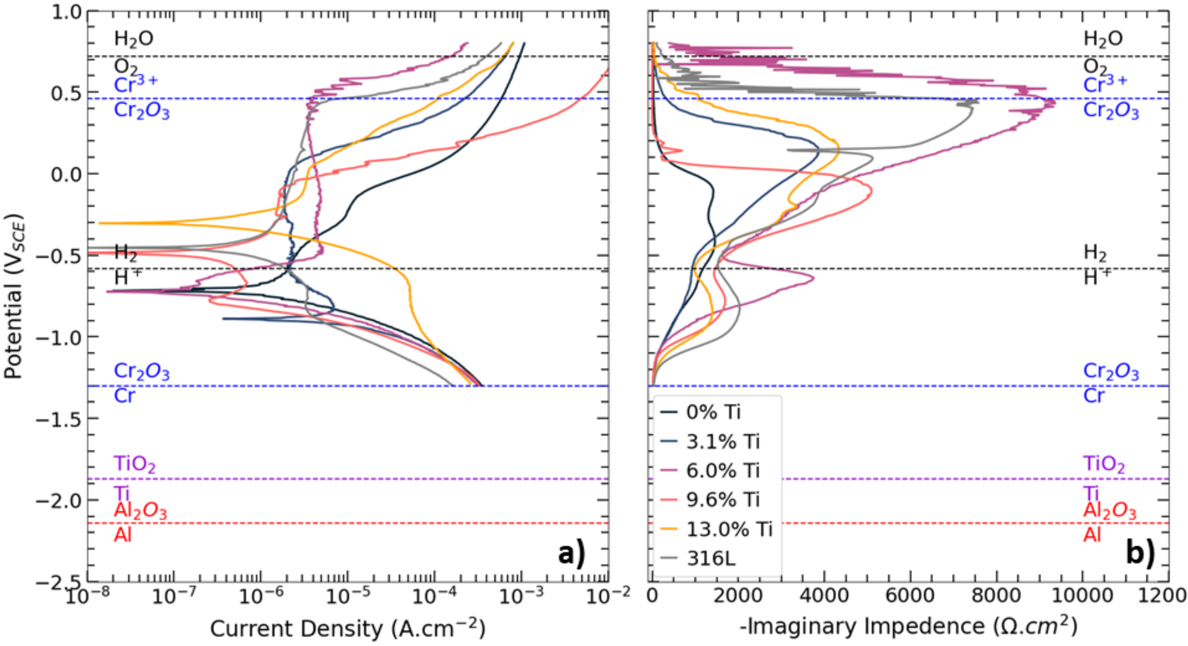

Figure 5: a) E-log(i) and **b)** -Z" plots obtained during polarization of CCAs in 0.01 M NaCl (pH ~5.75) following cathodic pre-treatment (-1.3 V_{SCE}, 600 s). Dashed lines indicate stability ranges for the oxides of passive species formed on their pure constituent elements and water constituents at a pH of 5.75 predicted by Hydra Medusa software.

Table IV: Key corrosion parameters obtained during potentiodynamic polarization of CCAs in 0.01 M NaCl (pH ~5.75) following cathodic pre-treatment (-1.3 V_{SCE}, 600 s). Each term indicates the mean value with a one standard deviation bound.

Alloy	**Corrosion Potential (V_{SCE})**	**Pitting Potential (V_{SCE})**	**Repassivation Potential (V_{SCE})**	**Passive Current Density ($\mu A/cm^2$)**
Ti-0	-0.741 +/- 0.034	0.048 +/- 0.050	-0.220 +/- 0.014	9.1 +/- 2.1
Ti-3.1	-0.873 +/- 0.017	0.338 +/- 0.048	-0.100 +/- 0.035	5.6 +/- 6.1
Ti-6.0	-0.736 +/- 0.023	0.633 +/- 0.066	0.146 +/- 0.035	3.9 +/- 0.5
Ti-9.6	-0.787 +/- 0.262	0.332 +/- 0.173	-0.109 +/- 0.132	1.5 +/- 1.2
Ti-13.0	-0.469 +/- 0.244	0.397 +/- 0.045	-0.111 +/- 0.097	4.8 +/- 6.3
316L	-0.447 +/- 0.003	0.596 +/- 0.045	0.014 +/- 0.019	1.4 +/- 0.3

---

[14] Downward scans are not shown in Figure 5 to ensure data visibility. The tabulated E_{rep} values are obtained at the crossover point, or the potential at which the downward scan current density is less than that of the upward anodic scan at the same potential.

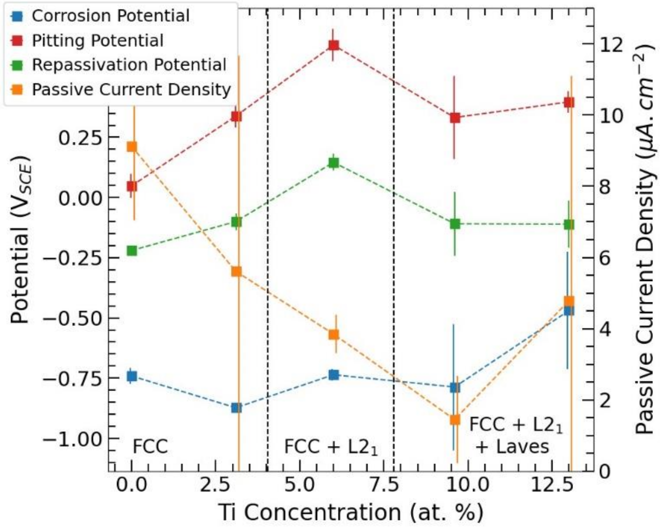

Figure 6: Summary of potentiodynamic polarization corrosion parameters shown in Table IV as a function of Ti concentration and microstructure. Error bars for each parameter indicate a one standard deviation range.

Potentiodynamic polarization was also evaluated for both the best-performing and worst performing CCAs (Ti-6.0 and Ti-0) across a range of NaCl concentrations. Representative E-log(i) curves alongside trends in E_{pit} as a function of Cl^- concentration are shown in Figure 7. Increasing E_{pit} values from Ti-0 to Ti-6.0, indicating Ti addition improves the corrosion resistance across all evaluated NaCl concentrations. The pitting potentials decreases with increased NaCl concentration at similar rates for both CCAs. Current densities for Ti-0 generally increase with NaCl concentration, while such trends were less prominent for Ti-6.0.

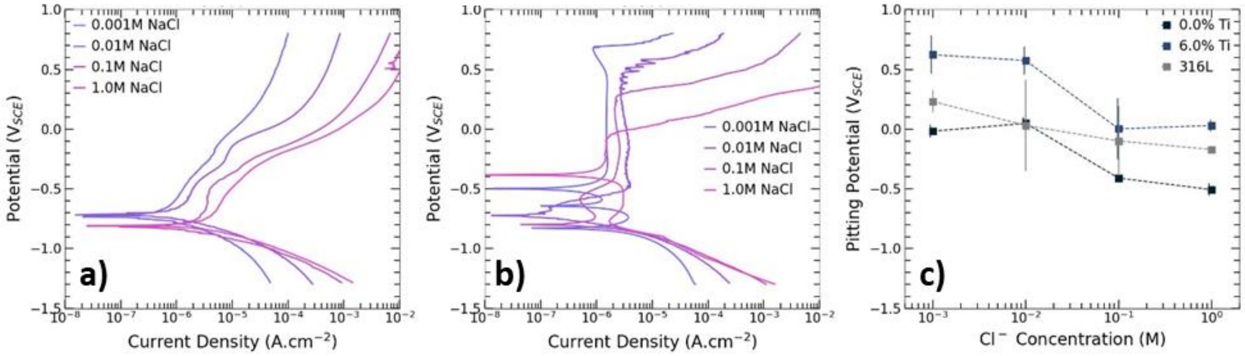

Figure 7: E-log(i) plots obtained during polarization of **a)** Ti-0 and **b)** Ti-6.0 in NaCl ranging in concentrations from 0.001 to 1.0 M (pH ~5.5-6.0) following cathodic pre-treatment (-1.3 V_{SCE}, 600 s) along with **c)** comparisons of pitting potential for each CCA and 316L as a function of electrolyte concentration. Error bars for each parameter indicate a one standard deviation range.

Elemental dissolution equivalent current densities obtained during potentiodynamic polarization of Ti-6.0 in 0.1 M NaCl adjusted to pH 4 are shown in Figure 8. At high potentials, Fe dissolves at the highest rates followed by Ni and Cr, in part due to their high concentrations in the bulk alloy. Equivalent current densities in the anodic region are not suggested to be proportional to the composition of either phase. Thus, preferential congruent dissolution of either phase, which would lead to increased dissolution of the enriched elements in the phase, is not suggested to be present. Ti dissolves at low rates both within the passive range and the anodic range, although quantitative comparisons between elements are difficult due to high levels of noise within the passive range as well as dissolution rates approaching the detection limit.

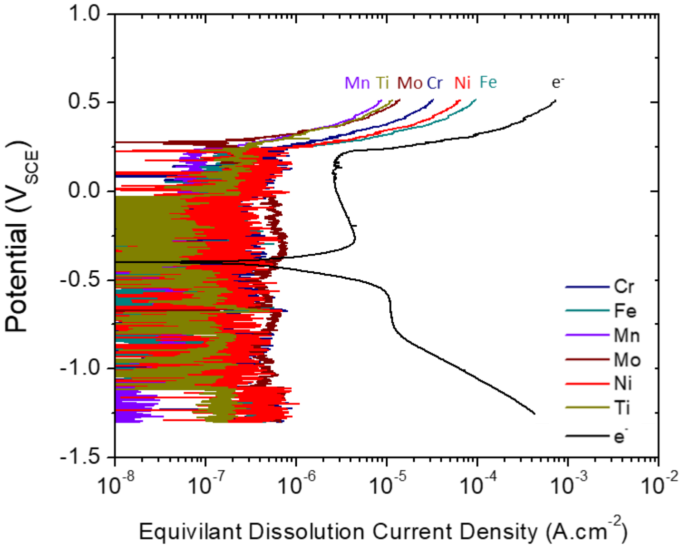

Figure 8: Equivalent current densities obtained from AESEC during potentiodynamic polarization of Ti-6.0 in 0.1 M NaCl adjusted to pH 4 reproduced from [35]. Al equivalent dissolution current densities are generally below the detection limit and are not shown due to high levels of noise.

Micrographs of the CCA surfaces following polarization are shown in Figure 9. For the single-phase CCAs (Ti-0 and Ti-3.1), pitting appears to initiate at random locations, whereas for the multi-phase CCAs (Ti-6.0, Ti-9.6, and Ti-13.0), pitting preferentially occurs at or near phase interfaces. None of the phases is suggested to be preferentially dissolved, however, the polarization was terminated prior to significant pit propagation.

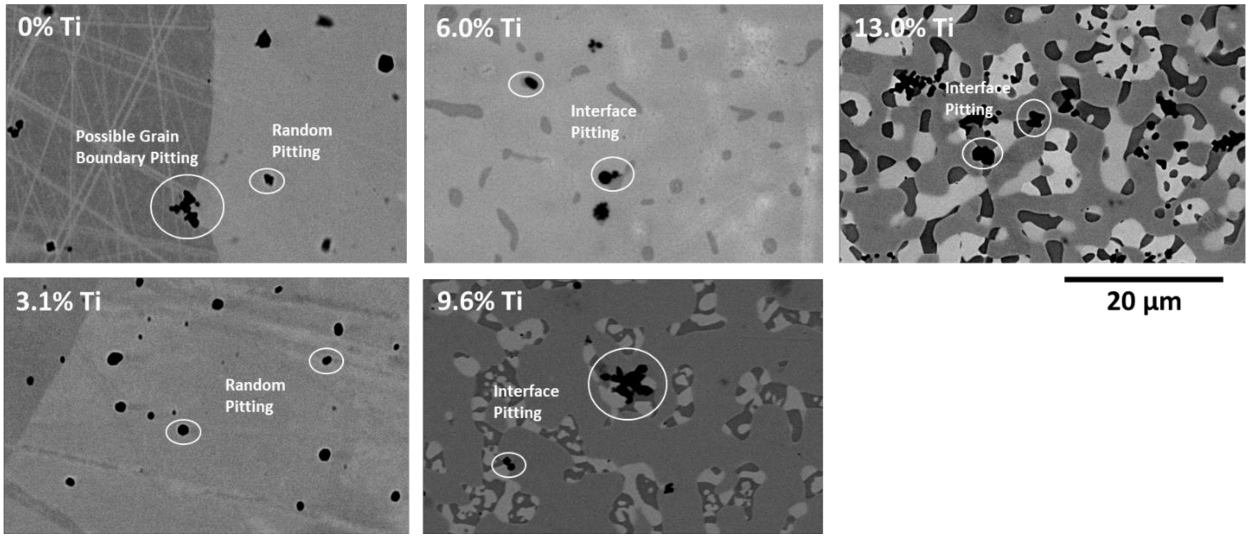

Figure 9: BSE of micrographs showing pit locations and morphology relative to CCA microstructural features. Potentiodynamic polarization in 0.01 M NaCl described above was terminated upon reaching a current density of 10^{-5} A/cm^2 prior to imaging. Pit locations illustrating transition from random to interface pitting are circled.

3.3 Characterization of CCAs with Air-Formed Oxides

Polarization and in-situ Z” measurements were also evaluated for a CCA series initiating slightly below the OCP to characterize the corrosion behavior of the CCAs without reduction of the air-formed oxide films. These are shown in Figure 10 and summarized in Table V. Similar to the case of the oxide formed on the reduced metal surface, polarization of the air-formed solution-exposed oxides shows the lowest values of both E_{pit} and E_{rep} for Ti-0, suggesting inferior corrosion resistance. Additionally, Ti-6.0 has the highest E_{corr} value while Ti-0 has the lowest, although other CCAs have E_{corr} values within the statistical scatter of Ti-0. All three parameters are suggested to increase with Ti concentration between 0 and 6 at. % Ti. However, such trends do not extend to Ti-9.6, the first CCA to have three phases. Despite increasing values from Ti-9.6 to Ti-13.0 for all three values, Ti-6.0 remains the only tested CCAs to exceed 316L in any of the evaluated parameters, suggesting all the other CCAs have inferior corrosion resistance to 316L.

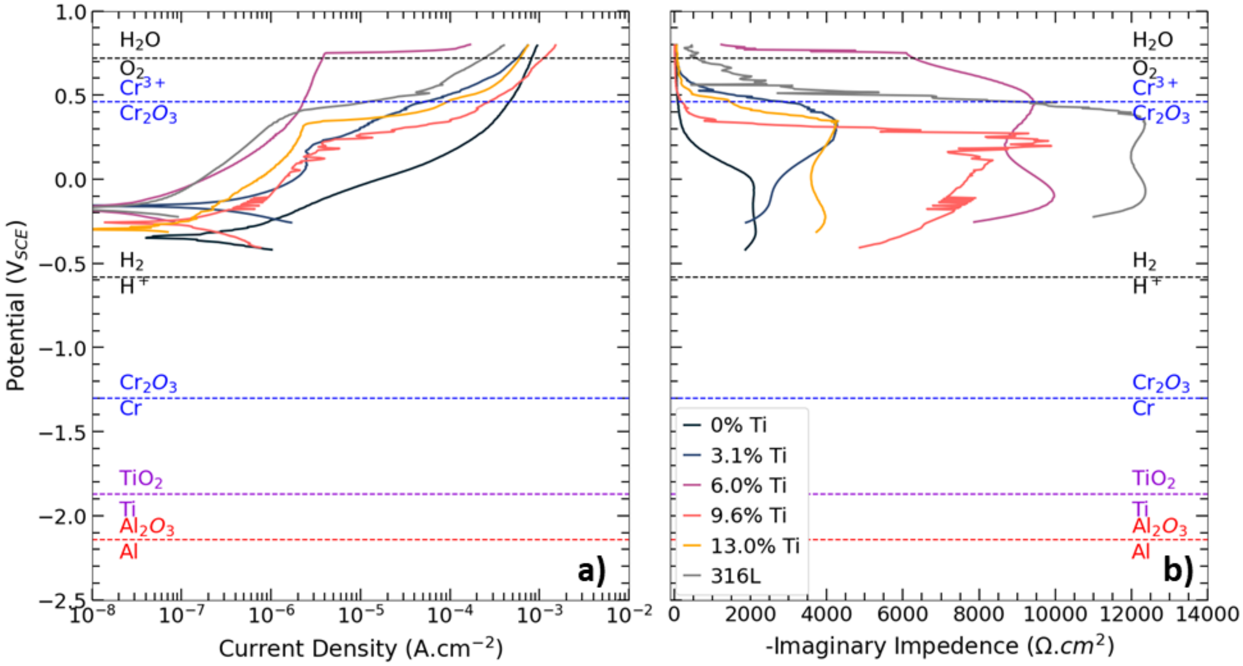

Figure 10: a) E-log(i) and **b)** -Z" plots obtained during polarization of CCAs with air-formed oxide in 0.01 M NaCl (pH ~5.75). Dashed lines indicate stability ranges for the oxides of passive species formed on their pure constituent elements and water constituents at a pH of 5.75 predicted by Hydra Medusa software.

Table V: Key corrosion parameters obtained during potentiodynamic polarization of CCAs in 0.01 M NaCl (pH ~5.75) following 30 minute solution exposure of the air-formed oxide. Each term indicates the mean value with a one standard deviation bound.

Alloy	**Corrosion Potential (V_{SCE})**	**Pitting Potential (V_{SCE})**	**Repassivation Potential (V_{SCE})**
Ti-0	-0.381 +/- 0.287	-0.092 +/- 0.319	-0.306 +/- -0.244
Ti-3.1	-0.219 +/- 0.062	0.251 +/- 0.103	-0.149 +/- 0.095
Ti-6.0	-0.173 +/- 0.008	0.631 +/- 0.243	0.185 +/- 0.152
Ti-9.6	-0.339 +/- 0.118	0.235 +/- 0.021	-0.253 +/- 0.004
Ti-13.0	-0.252 +/- 0.058	0.405 +/- 0.083	-0.090 +/- 0.064
316L	-0.182 +/- 0.016	0.437 +/- 0.025	0.004 +/- 0.058

CCAs with air-formed oxides were also characterized with EIS to characterize the passive film prior to polarization. A representative Bode plot along with tabulated fit parameters for a Randles circuit modified to include a constant phase element (CPE) are shown in Figure 11 and Table VI, respectively. Impedance (Z) at a given frequency (f) may be calculated from equivalent circuit parameters including the polarization resistance (R_p), solution resistance (R_s), CPE coefficient (α), and admittance constant (Y_0) as shown below. The R_P term describes transport O^{2-} anion and metal cations as the charged species and compensating defects to preserve electroneutrality (e.g., electrons, holes) affect interfacial electrochemical reaction rates. The CPE contains information on the dielectric and physical attributes of oxide in stratified layers [80]. The simplified circuit fits the behavior to a single time constant dominated for which resistance is dominated by the R_p term, allowing for an overall sense of oxide protectiveness.

$$Z(f) = R_s + \frac{R_p + Y_o(i2\pi f)^{\alpha}}{R_p Y_o(i2\pi f)^{\alpha}} \qquad (9)$$

High α values for all CCAs indicate that the fits are representative of near-capacitive behavior usually associated with protective oxides [72]. Generally, it is found that R_p increases with Ti concentration for air formed oxides exposed to solution, with trends in the fit spectra validated by similar trends in the low-frequency impedance modulus of supplemental runs. Increasing R_p magnitudes suggest the formation of a more protective passive films with increasing Ti concentration. It is notable that the presence of a multi-phase microstructures does not lower R_P. None of the phase angle plots suggests the presence of multiple CPEs, however, the change in shape of the Nyquist plots (not shown) at low-frequencies indicate possible mass transfer-controlled kinetics, particularly in the case of Ti-3.1. Such mass transport kinetics are usually attributable to transport by migration and diffusion through the through the passive film [80]. Given the variance in low-frequency impedance magnitude values between runs, uncertainty remains in quantitative R_p comparisons such as the observed for decrease for Ti-3.1 relative to Ti-0.

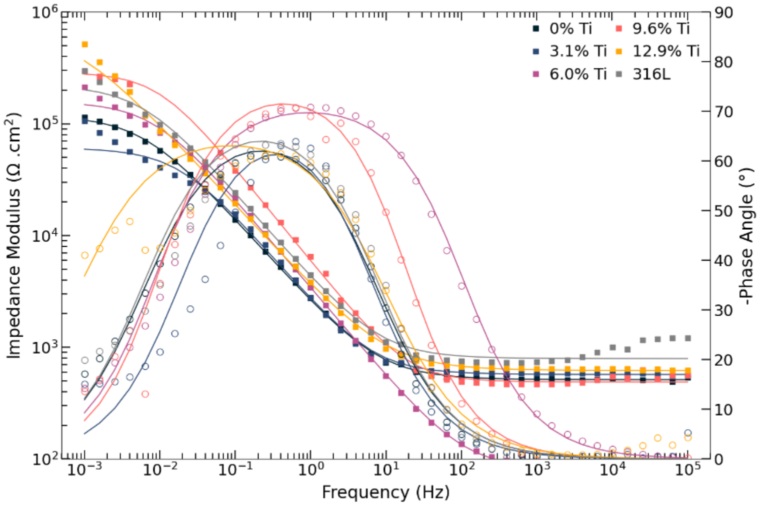

Figure 11: Bode plot obtained during EIS of CCAs with solution-exposed air-formed oxides at each CCAs OCP. Lines indicate best fits to a Randles circuit with parameters shown in Table VI.

Table VI: Randles circuit fit parameters for the EIS spectra of the air formed oxides exposed to solution at OCP.

Alloy	**Ti-0**	**Ti-3.1**	**Ti-6.0**	**Ti-9.6**	**Ti-13.0**	**316L**
R_p (kohm.cm^2)	119.6	60.6	158.5	290.2	682.3	222.7
R_s (ohm.cm^2)	512.7	571.0	81.3	488.4	620.3	791.7
Y_0 (µS*s$^\alpha$.cm^{-2})	100.4	91.0	66.9	36.2	74.8	58.7
α	0.765	0.795	0.802	0.845	0.736	0.781
Z(1mHz) (kohm.cm^2)	83 +/- 27	161 +/- 78	449 +/- 558	663 +/- 585	428 +/- 159	648 +/- 366

3.4 Growth and Electrochemical Properties of Passive Film Formed in Electrolyte Solution

The formation of the passive film from a reduced metal surface was also evaluated. Figure 12 shows current density and Z" measurements obtained during exposure of cathodically pre-treated surfaces to an applied potential of -0.25 V_{SCE}. In addition to being above the oxide formation potentials of Al, Cr, Ti, and Mo in pH ~5.75 conditions [27], the potential is also shown to be within the passive range of all evaluated CCAs previously determined with potentiodynamic polarization. For all CCAs, the current density initially becomes less negative, suggesting the formation of a stable passive film. Between 10^3 and 10^4 seconds, the sign of the current density changes to cathodic for all CCAs. Z" generally increases for at least 10^4 seconds, indicating the formation of a thicker passive film, before leveling out. No clear trends are present regarding the film growth kinetics with Ti concentration, with deviations between CCAs potentially obscured within statistical scatter.

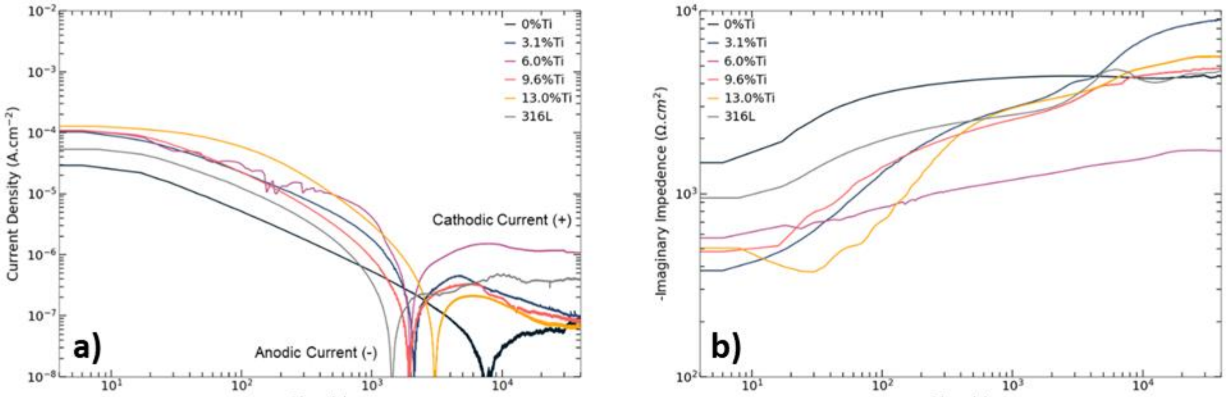

Figure 12: a) Current density and **b)** in-situ -Z" measurements during potentiostatic film growth of CCAs at -0.25 V_{SCE} in 0.01 M NaCl (pH ~5.75) with a 6 s period following cathodic pre-treatment (-1.3 V_{SCE}, 600 s).

Following film growth, the CCAs were characterized by EIS. Selected spectra fit to the Randles circuit described above are shown in Figure 13. Tabulated fit parameters are shown in Table VII. All fits indicate an α value above 0.75, suggesting capacitive behavior indicative of passive film formation. All of the CCAs have R_p values higher than that of 316L. No abrupt drops for multi-phase CCAs were observed relative to the single-phase CCAs and differences between the individual CCAs are not statistically significant. Thus, unlike the case of the air-formed oxides, R_p is not suggested to increase with Ti concentrations, Ti-6.0 has a lower impedance modulus at 1 Hz, the frequency at which the in-situ impedance data was collected during film growth than all other CCAs. However, the decreased magnitude might be a result of differing time constant behavior evidence in the frequency shift indicated by the Ti-6.0 phase angle plot, and the R_p values show that the decreased Z” values during film growth are not indicative of inferior corrosion resistance.

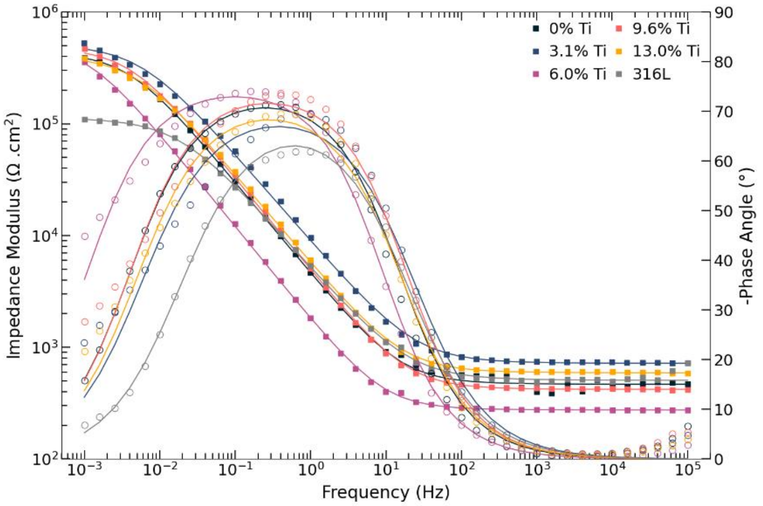

Figure 13: Bode plot obtained during EIS of CCAs with following potentiostatic oxide growth (40 ks, -0.25 V_{SCE}). Lines indicate best fits to a Randles circuit with parameters shown in Table VI.

Table VII: Randles circuit fit parameters for the EIS spectra shown in Figure 13.

Alloy	**Ti-0**	**Ti-3.1**	**Ti-6.0**	**Ti-9.6**	**Ti-13.0**	**316L**
R_p (kohm.cm^2)	437.5	517.3	533.0	482.9	407.5	113.3
R_s (ohm.cm^2)	467.6	719.6	275.1	420.5	591.4	506.9
Y_0 (µS*s$^\alpha$.cm^{-2})	48.5	26.7	122.6	44.5	40.6	46.9
α	0.825	0.788	0.838	0.832	0.805	0.779
Z(1 mHz) (kohm.cm^2)	48 +/- 9	404 +/- 308	452 +/- 558	491 +/- 168	342 +/- 58	252 +/- 202

3.5 Composition and Chemical Properties of Passive Film Formed in Electrolyte Solution

The composition of the passive film was analyzed with XPS for a low- (Ti-0), medium- (Ti-6.0), and high-Ti (Ti-9.6) CCA with FCC, FCC+$L2_1$, and FCC+$L2_1$+Laves microstructures, respectively. Fit spectra for passivating elements Al, Cr, and Ti are shown in Figure 14. The presence of passive species for Al and Ti, elements enriched in the $L2_1$ phase, alongside Cr, which is enriched in the FCC and Laves phases, suggest passivity is present over both phases. Ti spectra contain features attributable to Ti(IV) oxide for both Ti-

9.6 but not for Ti-6.0, with Ti^0 (unoxidized metallic signal) is observed for Ti-9.6[15]. Signal attributable to Al^0, Al(III), and the Cr3s core series is observed for all three CCAs. All Cr spectra showed features attributable to high concentrations of Cr(III) hydroxide with Cr(III) oxide and unoxidized Cr^0 also present. Additionally possible $FeCr_2O_4$ spinel presence is indicated for the Ti-0 and Ti-6.0 passive films by the Cr and Fe (not shown) spectra, but not for that of Ti-9.6. While the decrease in Ti concentration may affect the local ordering of Fe(II)/Fe(III) and Cr(III) within the passive film, given that the Cr spectra are dominated by $Cr(OH)_3$ and the generally low signal for Fe(II)/Fe(III) passive species, confirming the nature of Fe-Cr interaction as well as the degree of long-range order remains difficult.

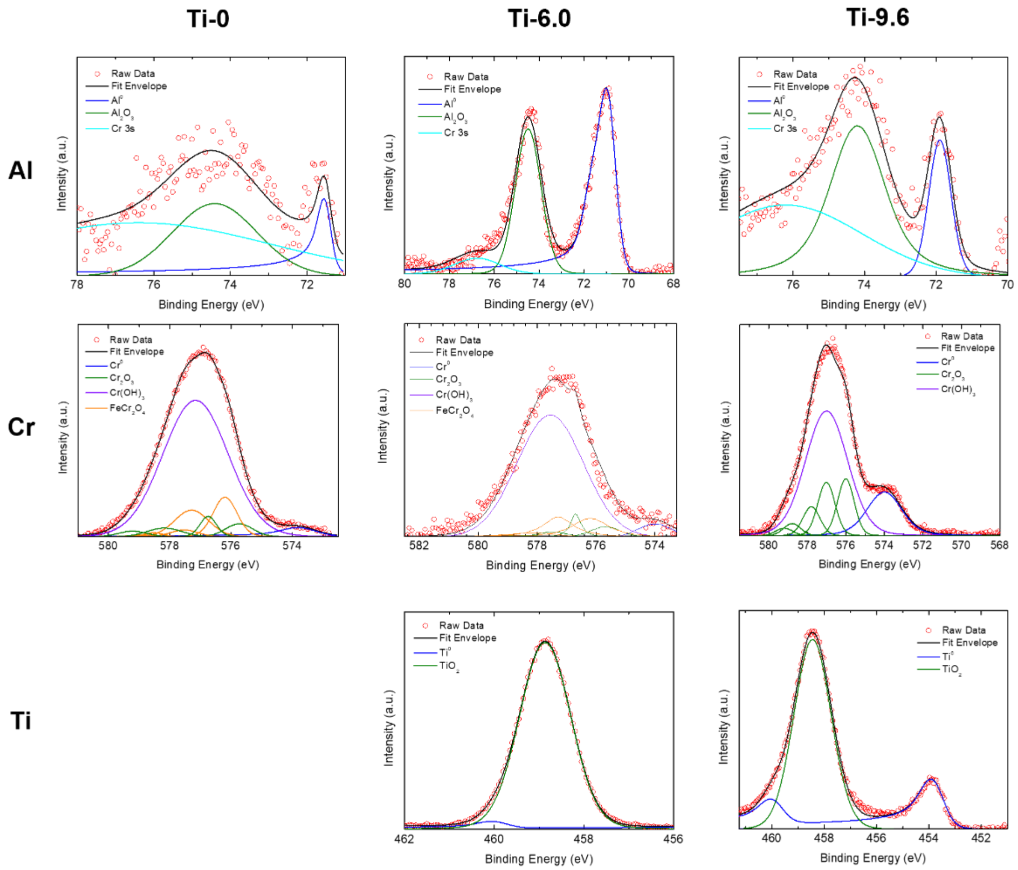

Figure 14: Fit high-resolution spectra for selected CCAs following potentiostatic oxide growth (-0.25 V_{SCE}, 40 ks) in 0.01 M NaCl (pH ~5.75). Intensities are scaled to maximum counts for each spectra as quantitative values may vary due to external factors such as surface contamination.

---

[15] The evaluated binding energy range for the high-resolution $Ti2p_{3/2}$ scan of Ti-6.0, which does not characteristic binding energies of Ti^0, was defined by initial high-intensity survey scans (not shown). The initial survey scans shown no signal in the characteristic Ti^0 binding energy range.

Surface cation fractions are shown in Figure 15 and tabulated in Table VIII. Cr(III) is enriched, mainly in the form of Cr(III) hydroxide, relative to its bulk composition in all three alloys, and is the largest constituent cation at the surface in two of the three CCAs. For the two Ti-containing CCAS, Ti(IV) oxide is also enriched relative to its bulk composition. Despite the increase in overall Ti composition from Ti-6.0 to Ti-9.6, the Ti(IV) concentration at the surface is suggested to decrease. Al(III) present in all three films, at concentrations that are enriched relative to the bulk concentration of each CCA. The distribution of Al in the passive film may be affected by its preferential partitioning to the L2$_1$ phase and away from both the FCC and Laves phases where it is depleted. Significant Mo(VI) presence is also suggested as well as low concentrations of Fe(II)/Fe(III), Mn(II), and Ni(II). However, no clear trends are present with Ti concentration.

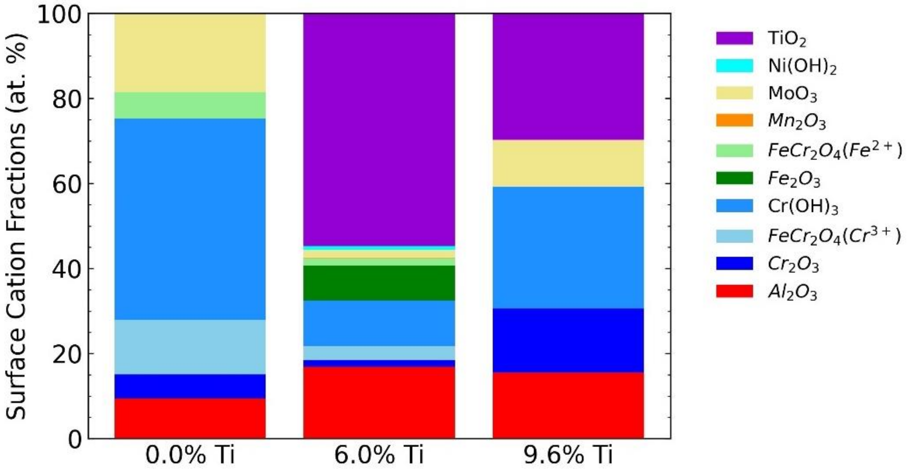

Figure 15: Surface cation fractions for selected CCAs from Table VII

Table VIII: Surface cation fractions in atomic percent obtained via high-resolution XPS scans of the passive film formed following potentiostatic oxide growth (40 ks, -0.25 V_{SCE}) in 0.01 M NaCl. Surface cation fractions include intensities attributable to oxidized (non-zero valance) features normalized with relative sensitivity factors. Bolded terms are enriched relative to bulk composition.

Cation	**0% Ti**	**6% Ti**	**9.6 % Ti**
Al(III)	**9.4%**	**16.9%**	**15.5%**
Cr(III)	**65.8%**	**15.5%**	**43.7%**
Fe(II)/(III)	6.3%	9.8%	0.0%
Mn(II)	0.0%	0.1%	0.0%
Mo(VI)	**18.6%**	1.9%	**11.0%**
Ni(II)	0.0%	1.0%	0.0%
Ti(IV)	0.0%	**54.9%**	**29.7%**

4.0 Discussion

4.1 Thermodynamics of Passive Film Formation

All evaluated CCAs are suggested to form thermodynamically stable and protective passive films as evidenced by combinations of broad passive ranges and increasing -Z” values observed during potentiodynamic polarization (Figures 5, 10), high R_P magnitudes determined by EIS (Figures 11, 13, Tables V, VI), and increasing -Z” values accompanied by decreasing current densities during potentiostatic oxide growth (Figure 12). Such behavior is observed for both single-phase CCAs as well as those containing additional $L2_1$ and/or Laves phases. The maintenance of passivity, despite second phase formation, distinguishes the evaluated CCA class from many multi-phase CCAs. It is enabled by ensuring both phases have at least one passivating element enriched in each phase (e.g., Cr in the FCC matrix and Laves, Ti in the $L2_1$) and the expectation that each phase forms a passive film with a unique composition (Chapter 6). Protective oxide species are predicted to be thermodynamically stable when considering exposure of pure Al, Cr, Fe, and Ti to -0.25 V_{SCE} in pH ~5.75 chloride solution, the environment used for potentiostatic oxide growth [27]. The presence of localized breakdown as well as non-zero -Z” values indicate the presence of a stable passive film beyond the range of Cr_2O_3 stability. This suggests that oxide stability is substantial due to Al and Ti alloying and due to subsequent Al(III) and/or Ti(IV) participation in passivation despite their low concentrations in the bulk alloy. Low dissolution current densities for all elements during potentiodynamic polarization (Figure 8), despite the predicted dissolution for Al, Fe, Mn, Mo, and Ni in pH 4 environments [27], provides further evidence that Ti(IV) containing passive films prevail despite thermodynamically predicted dissolution of other elements. Thus, the passive films of the CCAs are defined by the contributions of multiple cations within the passive film.

While convex hull and E-pH diagrams are effective in predicting whether the formation of an oxide film will be thermodynamically favorable, they are insufficient in predicting which oxides will be comparatively more prevalent. The free energy of formation (ΔG°) may also be used to compare the driving force for passivation among multiple species. For example, ΔG° of Al_2O_3, Cr_2O_3, and TiO_2, (-1690 kJ/mol [81], -1050 kJ/mol [82], and -970 kJ/mol [81] , respectively) are all more negative on a per molecule basis than that of Fe_2O_3 (-742 kJ/mol [81]). Furthermore, ΔG° of TiO_2 is more negative than Cr_2O_3 and comparable to Al_2O_3 when considered on a per atom basis. More negative ΔG° values indicate a higher driving force for passivation, leading to Al(III), Ti(IV) and Cr(III) enrichment that is often observed relative to bulk concentration while Fe(II)/Fe(III) is depleted for all CCAs (Figure 15). Possible $FeCr_2O_4$ formation suggested by XPS fitting (Figure 14) may be driven by the more negative ΔG° (-1340 kJ/mol [82]) as well as the extended 40 ks exposure, which has been suggested to lead to the enrichment of comparatively more thermodynamically stable species in Ni-Cr-Mo alloys [83]. Figure 16 surveys a range of passive species collected using density functional theory calculations with methodologies developed elsewhere [84, 85].

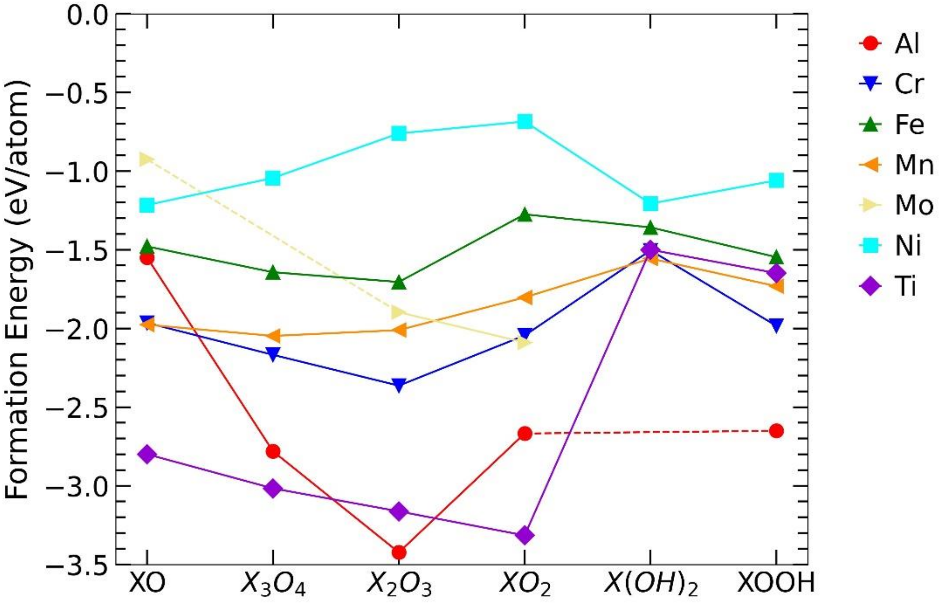

Figure 16: Formation energies at 0 K for a range of oxide, hydroxide, and oxyhydroxide species possible for each constituent element obtained from Open Quantum Materials Database [84, 85].

Additionally, ΔG˚ indicates the most thermodynamically stable oxide species for a given element. For Ti, the most energetically stable oxide is suggested to be TiO_2 whereas the Cr species with the lowest formation energy on a per atom basis is Cr_2O_3. Notably, such calculations do not account for the local availability of oxide and/or hydroxide anions, which may lead to discrepancies between the most thermodynamically stable chemical species and those suggested to be present by XPS fitting (Figure 14).

In addition to favorable stoichiometric single element oxides and the possibility of long-range ordered oxide formation, the possibility of oxide mixing may further contribute to stability in the passive film. For example, Wang et al. suggested the free energy of mixing (ΔG_{mix}) for Fe_2O_3 and Cr_2O_3 may further promote mixed oxide stability during aqueous passivation of CCAs [86]. However, such effects may be less prominent for Ti(IV) given the different structures and valence states suggested for the oxides (Figure 14) as well as the large two-phase regions present in the Cr_2O_3-TiO_2 [87] and Al_2O_3-TiO_2 [88] phase diagrams. While many stable complex oxides are present in the phase diagrams at room temperature, including

Al_2TiO_5, $Ti_4Cr_2O_{11}$, $Ti_5Cr_2O_{11}$, $Ti_6Cr_2O_{11}$, $Ti_7Cr_2O_{11}$, and more, although none has been experimentally confirmed to form in aqueous environments.

4.2 Kinetics of Passive Film Formation

Work in the Fe-Cr-Al-Ti system has shown that quaternary alloys with higher Ti concentrations may have multiple oxide layers form whereas alloys with less Ti may have the majority of Ti(IV) dissolved in an unlayered solid solution oxide [43]. Such layering may be influenced by the limited solubility of Ti(IV) species in Fe(II)/Fe(III) or Cr(III) dominated passive films. In both the Fe-Cr-Al-Ti [43] and Al-Cr-Fe-Mn-Mo-Ni-Ti [35] systems, Ti is suggested to be more enriched in inner layers closer to the metal-oxide interface than other passivators such as Cr(III). Notably, Ti is often enriched at similar depths as Al, possibly allowing the stabilization Al(III) either through thermodynamic mixing effects and/or stable Ti(IV) enriched layers protecting metastable Al(III) that may otherwise dissolve in the absence of Ti. While inner-oxide enriched Ti(IV) may not be observed to the same degree by XPS it could still contribute to overall passivity, leading to the high impedance moduli and low i_{pass} magnitudes (Figures 5, 6, 12, Tables IV, VII) of Ti-rich CCAs such as Ti-13.0.

In addition to the global composition, the ability to passivate may be considered on a basis of the composition of constituent phases. Previous work on Ti-6.0 has shown that the passive film formed over the FCC phase has considerably higher Cr surface cation fractions in the passive film, while the film formed over the $L2_1$ phase has higher concentrations of Al, Ni, and Ti (Chapter 6). The local compositions within the passive follow trends with enriched elements in individual microstructural phases relative to global alloy composition (Table II). Therefore, although not characterized, the Laves phase formed in Ti-9.6 and Ti-13.0 likely also has Cr and Mo enriched over it. In addition to bulk microstructure compositions affecting the local availability of each metal, surface enrichment may be affected by other constituent elements. For example, in the FCC phase, Cr is generally surrounded by Fe and Ni, two metals with relatively unstable oxides. Thus, there may be a comparatively stronger driving force for Cr oxidation. Alternatively, the $L2_1$ phase has high concentrations of Al and Ti, whose thermodynamic stable passive films may form quicker, allowing less time for Cr to oxidize and obtain the same surface cation fraction as seen over the FCC phase. The nature of the passive film highlights the utility of ensuring passivating elements are divided between phases. While it is possible that passivation over individual phases may occur over different timescales, distinct regimes were not clearly identifiable during characterization of potentiostatic oxide growth (Figure 12) nor was either phase suggested to preferentially dissolve at stochiometric ratios by AESEC (Figure 8).

Additionally, Ti(IV) presence in the passive film may improve passivity through its effects on other constituent elements, in particular, Al. In the Fe-Cr-Al-Ti system, the surface cation fraction of Al(III) is suggested to increase in the passive films formed in pH 4 Na_2SO_4 solutions with Ti concentration, despite being unstable in pH 4 environments and having to compete with thermodynamically stable Ti(IV) species [27]. Additionally, previous depth profiling [35] has shown Al(III) is often enriched in the inner oxide at similar locations to Ti(IV), suggesting Ti(IV) may improve Al(III) stability. Similar Al(III) and Ti(IV) enrichment at inner oxide layers has been previously observed for Ti-6.0 [35]. Therefore, it is possible that some benefits of Ti(IV) on Al(III) stability may extend into the evaluated CCA series, possibly explaining the significant increase in Al(III) surface cation fractions from Ti-0 to Ti-6.0 (Figure 15, Table VIII). Possible mechanisms include both thermodynamically influenced mixing benefits, complex oxide formation, as well as the formation of a protective Ti(IV) layer that enables metastable Al(III) species that dissolve in the absence of protective Ti-enriched oxides, to be protected [43]. Enrichment of Al(III) and Ti(IV) may be predicted from low elemental dissolution rates observed via AESEC during similar film growth treatments [35]. However, the high detection limit for Al signal makes it difficult to establish the stability of Al species at early times prior to the formation of a stable, Ti-enriched passive film, making mechanistic identification difficult. Al(III) has the lowest surface cation fraction for Ti-9.6. While Al(III) surface cation fractions could be artificially lowered due to decreased mean free paths from inner-oxide layering, such effects are unlikely to be prominent given that significant signal for unoxidized Al^0 metal was observed at levels well beyond that which is attributable to unoxidized Al(III) (Figure 14). Furthermore, an increased degree of layering may contribute to the decreasing Ti surface cation fractions in Ti-9.6 relative to Ti-6.0 (Figure 15), as inner-layer enrichment would contribute to decreased levels of signal observed via XPS.

4.3 Microstructural Effects on Corrosion Behavior

CCAs with higher Ti concentrations generally demonstrate superior passivity. suggesting that the $L2_1$ and/or Laves phases formed at high Ti-concentrations do not directly harm ability of the high-Ti CCAs to passivate. One possible explanation relies on the composition of the phases. The strong corrosion resistance of Ti-6.0 has been previously tied to ensuring both phases are enriched in at least one passivating elements (e.g., Cr in the FCC matrix, Ti in the $L2_1$ second phase) [35, 40]. The Ti concentration in the $L2_1$ phase increases with overall Ti concentration in the alloy. This ensures adequate Ti concentrations within each phase, unlike the case varying Al concentration (Chapter 2), where increasing Al concentrations are suggested to decrease the Ti concentration in the $L2_1$ phase (Chapter 2), leading to inferior resistance to localized corrosion. Given the prominence of Ti(IV) in the passive films (Figure 15,

Table VIII) and that pure Ti is shown to be more resistant to localized breakdown than Al under the conditions used in this work [35], it may be reasonably inferred that the incremental contributions of increased Ti concentration on the $L2_1$ phase are less detrimental than those of increasing Al concentrations, leading to the improved corrosion resistance of high-Ti CCAs relative to high-Al CCAs. Similarly, the Laves phase introduced in Ti-9.6 and Ti-13.0 is enriched in Cr and Mo, two element capable of forming stable passive film. The formation of a Laves phase led to decreasing Cr concentration in other phases. For instance, the Cr concentration in the FCC matrix is lower in Ti-13.0 (10.2 at. %) than both the single-phase Ti-0 (10.9 at. %) and two-phase Ti-6.0 (11.1 at. %) (Table III). Regardless, passivity may be achieved by CCAs with Cr concentrations as low as 10 at. % in the presence of other passivators such as the ~7 at. % Ti present in the FCC phase of Ti-13.0 (Table II) [35], however; in addition to the ability to passivate, the effect of Ti on the breakdown behavior in Cl^- containing solutions must be considered.

Ti-0 is suggested by both potentiodynamic polarization (Figures 5, 7, 10, Tables IV, V) and EIS of the air-formed oxide (Figure 11, Table VI) to have inferior corrosion resistance to the Ti-containing CCAs. following trends established for the Fe-Ti system in concentrated HCl by Kim et al. [34]. Such improvements indicate Ti addition is beneficial in a single phase microstructure for its contributions to passivity, and can even improve corrosion resistance despite the introduction of a new phase [54]. However, the introduction of a multi-phase microstructure can promote localized corrosion, as identified by the preferential pitting at phase interfaces observed in micrographs obtained following polarization (Figure 9). While Ti addition improved the pitting resistance of Ti-0 accords a range of Cl concentrations (Figure 7) despite the formation of an FCC-$L2_1$ interface, such trends were not present at high Ti concentrations. E_{pit} of Ti-9.6 and Ti-13.0 is lower than that of Ti-6.0 for the CCAs with passive films both during air exposure (Figure 10, Table V) and potentiodynamic polarization of a reduced surface (Figures 5, 6, Table IV). Similar trends were also observed with regards to repassivation (Figure 6, Tables IV, V). Given that pitting was disproportionately observed at or near phase interfaces for the multi-phase CCAs, the effect of microstructure and phase interfaces must be considered as in the case of the effect of Al (Chapter 2).

Thus, trade-offs may be present between global beneficial effects of Ti concentration on passivity and adverse consequences of microstructurally influenced localized corrosion. E_{pit} was not suggested to decrease until Ti concentrations of 9.6 at. % (Figure 5, 6, 10, Table IV, V), the first CCA that had a three-phase microstructure (Figures 1, 3, Table II), possibly indicating such adverse microstructural effects are more prominent at the point of initiation of the Laves phase. However, the Laves interfaces do not show more frequent pitting than other interfaces (Figure 9). Thus, the effects of Laves presence on overall alloy must be considered. For instance, while the FCC phase of Ti-13.0 maintains sufficient Cr concentrations to form a stable passive film, it could possibly be more susceptible to localized corrosion.

Compositions maximizing Ti concentration while preserving a two-phase microstructure could be targeted for corrosion resistance; however, it would be necessary to ensure each phase maintains an adequate concentration of passivating elements. Furthermore, targeting such a two-phase microstructure might be restricted to specific phase structures such as FCC+L2_1. The Fe-Cr-Al-Ti system is a notable example, where increasing Ti concentration led to the formation of a Laves phase which, as in the case of the evaluated CCA system, was suggested to harm the corrosion resistance [43]. Increasing Ti concentrations may also increase the likelihood of formation of Ti nitride impurities such as those observed in Figure 4. In addition to drawbacks of the undesirable presence or composition of additional phases in the bulk microstructure, decreases in corrosion resistance at high Ti concentrations could be attributable to the lower Ti(IV) surface cation fractions and/or decreased concentrations at the oxide-metal interface (Figure 15, Table VIII). Regardless of mechanism, it is of note that the optimal composition would be significantly dependent on the alloy system as well as on other processing parameters that may affect alloy microstructure.

5.0 Conclusions

Five CCAs in the Al-Cr-Fe-Mn-Mo-Ni-Ti system with variable Ti concentrations ranging from 0 to 13.0 at. % were synthesized, homogenized, and evaluated for corrosion resistance. The effects of Ti concentration on microstructure, passivity, localized corrosion, and passive film chemistry were evaluated. The following conclusions were observed:

- The microstructure transitioned from single-phase FCC, to an FCC matrix enriched in Fe, Cr, and Mo relative to bulk alloy compositions with L2_1 second phase regions enriched in Al, Cr, and Ti. At Ti concentrations above 9.6 at. %, a third phase of likely C14 Laves structure enriched in Fe, Cr, and Mo was present.
- Electrochemical parameters traditionally associated with passivity (e.g., i_{pass}, R_p) often showed improved results with increasing Ti concentrations whereas those associated with localized breakdown (e.g., E_{pit}, E_{rep}) were maximized at 6 at. % Ti before decreasing at higher Ti concentrations. High-Ti concentration may harm the resistance to localized corrosion by

initiating second and third-phase formation, with interfaces acting as a preferential pitting site.

- The passive film is suggested to be dominated by Cr(III) and Ti(IV). Ti(IV) surface cation fractions observed via XPS did not increase between the two CCAs evaluated, potentially due to differing passive film layering and/or changes in thicknesses.

Acknowledgments

This work was supported by the United States Office of Naval Research grants #N00014-23-1-2441 and #N00014-19-1-2420 under the directorship of David Shifler. Sample synthesis was provided by Diego Ibarra Hoyos and Jie Qi under the guidance of S. Joseph Poon. AESEC analysis was completed by Junsoo Han with support from Kevin Ogle and Agence Nationale de Recherche, award # ANR-20-CE08-0031 (TAPAS 2020). The contributions of Mark Wischhusen and Sean Agnew are acknowledged. SEM, XPS, and XRD facilities and training was provided by the University of Virginia Nanomaterials Characterization Facility. The PHI VersaProbe III was supported NSF award # 162601 with technical assistance provided by Catherine Dukes and Angela Gerard.

References

[1] J. Jayaraj, C. Thinaharan, S. Ningshen, C. Mallika, U. Kamachi Mudali, Corrosion behavior and surface film characterization of TaNbHfZrTi high entropy alloy in aggressive nitric acid medium, Intermetallics, 89 (2017) 123-132.

[2] A. Chavan, S. Mandal, M. Roy, Cobalt free refractory high entropy alloys for total joint arthroplasty: In-vitro wear, corrosion and cytocompatibility evaluation, Journal of Alloys and Compounds, 938 (2023) 168499.

[3] W. Xiong, L. Cheng, S. Zhan, A.X.Y. Guo, P.K. Liaw, S.C. Cao, Recent Advances on Lightweight High-Entropy Alloys: Process, Design, and Applications, High Entropy Alloys & Materials, (2023).

[4] M. Li, Q. Chen, X. Cui, X. Peng, G. Huang, Evaluation of corrosion resistance of the single-phase light refractory high entropy alloy TiCrVNb0.5Al0.5 in chloride environment, Journal of Alloys and Compounds, 857 (2021) 158278.

[5] D.B. Miracle, O.N. Senkov, A critical review of high entropy alloys and related concepts, Acta Materialia, 122 (2017) 448-511.

[6] B. Chen, X. Li, W. Chen, L. Shang, L. Jia, Microstructural evolution, mechanical and wear properties, and corrosion resistance of as-cast CrFeNbTiMox Refractory high entropy alloys, Intermetallics, 155 (2023) 107829.

[7] W. Qi, W. Wang, X. Yang, G. Zhang, W. Ye, Y. Su, Y. Li, S. Chen, Effects of Al and Ti co-doping on the strength-ductility- corrosion resistance of CoCrFeNi-AlTi high-entropy alloys, Journal of Alloys and Compounds, 925 (2022) 166751.

[8] U. Martin, J. Ress, P. Pérez, P. Adeva, D.M. Bastidas, Corrosion Behavior of Al10Cr30Fe25Mn30Ti5 High-Entropy Alloy: Microstructural, Electrochemical, and Surface Analysis, in: Metals, 2022.

[9] G.-S. Ham, Y.-K. Kim, Y.S. Na, K.-A. Lee, Effect of Ti Addition on the Microstructure and High-Temperature Oxidation Property of AlCoCrFeNi High-Entropy Alloy, Metals and Materials International, 27 (2021) 156-165.

[10] M. Wu, R.C. Setiawan, D.Y. Li, Benefits of passive element Ti to the resistance of AlCrFeCoNi high-entropy alloy to corrosion and corrosive wear, Wear, 492-493 (2022) 204231.

[11] X.X. Liu, S.G. Ma, W.D. Song, D. Zhao, Z.H. Wang, Microstructure evolution and mechanical response of Co-free Ni2CrFeAl0.3Tix high-entropy alloys, Journal of Alloys and Compounds, 931 (2023) 167523.

[12] R. Feng, C. Lee, M. Mathes, T.T. Zuo, S. Chen, J. Hawk, Y. Zhang, P. Liaw, Design of Light-Weight High-Entropy Alloys, Entropy, 18 (2016) 333.

[13] R. Feng, C. Zhang, M.C. Gao, Z. Pei, F. Zhang, Y. Chen, D. Ma, K. An, J.D. Poplawsky, L. Ouyang, Y. Ren, J.A. Hawk, M. Widom, P.K. Liaw, High-throughput design of high-performance lightweight high-entropy alloys, Nature Communications, 12 (2021) 4329.

[14] X. Huang, J. Miao, A.A. Luo, Lightweight AlCrTiV high-entropy alloys with dual-phase microstructure via microalloying, Journal of Materials Science, 54 (2019) 2271-2277.

[15] P. Chauhan, S. Yebaji, V.N. Nadakuduru, T. Shanmugasundaram, Development of a novel light weight Al35Cr14Mg6Ti35V10 high entropy alloy using mechanical alloying and spark plasma sintering, Journal of Alloys and Compounds, 820 (2020) 153367.

[16] Z.-S. Nong, Y.-N. Lei, J.-C. Zhu, Wear and oxidation resistances of AlCrFeNiTi-based high entropy alloys, Intermetallics, 101 (2018) 144-151.

[17] E. Osei-Agyemang, G. Balasubramanian, Surface oxidation mechanism of a refractory high-entropy alloy, npj Materials Degradation, 3 (2019) 20.

[18] Y. Qiu, S. Thomas, M.A. Gibson, H.L. Fraser, N. Birbilis, Corrosion of high entropy alloys, npj Materials Degradation, 1 (2017) 15.

[19] N.P. Sazhin, U.S.N. Aeronautics, S. Administration, Titanium Alloys for Modern Technology, National Aeronautics and Space Administration, for sale by the Clearinghouse for Federal Scientific and Technical Information, Springfield, Va., 1959.
[20] J.D. Jackson, W.K. Boyd, Corrosion of Titanium, Defense Metals Information Center, Battelle Memorial Institute, 1966.
[21] J.J. Noël, N. Ebrahimi, D.W. Shoesmith, Corrosion of Titanium and Titanium Alloys, in, 2018.
[22] M.A. Khan, R.L. Williams, D.F. Williams, The corrosion behaviour of Ti–6Al–4V, Ti–6Al–7Nb and Ti–13Nb–13Zr in protein solutions, Biomaterials, 20 (1999) 631-637.
[23] S. Tamilselvi, V. Raman, N. Rajendran, Corrosion behaviour of Ti–6Al–7Nb and Ti–6Al–4V ELI alloys in the simulated body fluid solution by electrochemical impedance spectroscopy, Electrochimica Acta, 52 (2006) 839-846.
[24] V.A. Alves, R.Q. Reis, I.C.B. Santos, D.G. Souza, T. de F. Gonçalves, M.A. Pereira-da-Silva, A. Rossi, L.A. da Silva, In situ impedance spectroscopy study of the electrochemical corrosion of Ti and Ti–6Al–4V in simulated body fluid at 25°C and 37°C, Corrosion Science, 51 (2009) 2473-2482.
[25] M. Atapour, A. Pilchak, G.S. Frankel, J.C. Williams, M.H. Fathi, M. Shamanian, Corrosion Behavior of Ti-6Al-4V with Different Thermomechanical Treatments and Microstructures, Corrosion, 66 (2010) 065004-065004-065009.
[26] J. Yang, H. Yang, H. Yu, Z. Wang, X. Zeng, Corrosion Behavior of Additive Manufactured Ti-6Al-4V Alloy in NaCl Solution, Metallurgical and Materials Transactions A, 48 (2017) 3583-3593.
[27] M. Pourbaix, Atlas of electrochemical equilibria in aqueous solutions, in, National Association of Corrosion Engineers, Houston, Tex., 1974.
[28] J.J. Noel, The electrochemistry of titanium corrosion, (1999).
[29] C.K. Dyer, J.S.L. Leach, Breakdown and Efficiency of Anodic Oxide Growth on Titanium, Journal of The Electrochemical Society, 125 (1978) 1032.
[30] J.S.L. Leach, B.R. Pearson, Crystallization in anodic oxide films, Corrosion Science, 28 (1988) 43-56.
[31] M.R. Kozlowski, P.S. Tyler, W.H. Smyrl, R.T. Atanasoski, Anodic TiO2 Thin Films: Photoelectrochemical, Electrochemical, and Structural Study of Heat-Treated and Modified Films, Journal of The Electrochemical Society, 136 (1989) 442.
[32] P.S. Tyler, M.R. Kozlowski, W.H. Smyrl, R.T. Atanasoski, Photoelectrochemical microscopy as a probe of localized properties of thin TiO2 films, Journal of Electroanalytical Chemistry, 237 (1987) 295-302.
[33] O. Durante, C. Di Giorgio, V. Granata, J. Neilson, R. Fittipaldi, A. Vecchione, G. Carapella, F. Chiadini, R. DeSalvo, F. Dinelli, V. Fiumara, V. Pierro, I.M. Pinto, M. Principe, F. Bobba, Emergence and Evolution of Crystallization in TiO2 Thin Films: A Structural and Morphological Study, in: Nanomaterials, 2021.
[34] H. Kim, N. Akao, N. Hara, K. Sugimoto, Comparison of Corrosion Resistances Between Fe2 O 3 - TiO2 Artificial Passivation Film and Passivation Film on Fe-Ti Alloy, Journal of The Electrochemical Society, 145 (1998) 2818.
[35] S.B. Inman, D. Sur, J. Han, K. Ogle, J.R. Scully, Corrosion Behavior of a Compositionally Complex Alloy Utilizing Simultaneous Al, Cr, and Ti Passivation, Corroison Science, 217 (2023) 111138.
[36] W.-C. Luu, W.-C. Chiang, J.-K. Wu, Effect of Cr and Ti additions on the corrosion behavior of Fe3Al alloys in chloride-containing sulfuric acid solutions, Materials Letters, 59 (2005) 3295-3298.
[37] R.A. Rodríguez-Díaz, J. Uruchurtu-Chavarín, A. Molina-Ocampo, J. Porcayo-Calderón, M. González-Pérez, J.M. López-Oglesby, J.G. Gonzalez-Rodríguez, J.A. Juárez-Islas, Corrosion Behavior of Fe-Al Alloy Modified with Cr and Ti in Simulated Physiological Human Media, International Journal of Electrochemical Science, 8 (2013) 958-972.
[38] A.S. Berezhnoi, N.V. Gul´ko, Phase Diagrams of the Systems Cr2O3-TiO2 and Cr2O3-ZrO2 (in Ukrainian), Dopovidi An Ukrainskoi RSR, serija B, Geologija, Geofisika, Khimija i Biologija, 1968 (1968) 250-253.

[39] L. Kaufman, Calculation of multicomponent ceramic phase diagrams, Physica B+C, 150 (1988) 99-114.
[40] S.B. Inman, J.R. Scully, Design and Discovery of Compositionally Complex Alloys (CCA) that Include High Corrosion Resistance, Corrosion, (2024) 4451.
[41] J.R. Scully, S.B. Inman, A.Y. Gerard, C.D. Taylor, W. Windl, D.K. Schreiber, P. Lu, J.E. Saal, G.S. Frankel, Controlling the corrosion resistance of multi-principal element alloys, Scripta Materialia, 188 (2020) 96-101.
[42] Y. Qiu, R. Liu, T. Gengenbach, O. Gharbi, S. Choudhary, S. Thomas, H.L. Fraser, N. Birbilis, Real-time dissolution of a compositionally complex alloy using inline ICP and correlation with XPS, npj Materials Degradation, 4 (2020) 7.
[43] D. Sur, S.B. Inman, K.L. Anderson, J. Qi, M. Barbiari, J.R. Scully, Passivation behavior of Fe-Cr-Al-Ti alloys in sulfate containing aqueous environments, In Progress.
[44] S. Choudhary, Y. Qiu, S. Thomas, N. Birbilis, Element-resolved electrochemical analysis of transpassive dissolution and repassivation behavior of the multi-principal element alloy AlTiVCr, Electrochimica Acta, 362 (2020) 137104.
[45] M. Ibrahim, S. El-Hadad, W. Khalifa, M. Shoeib, Effect of Ti Addition and Heat Treatment on Electrochemical Properties of Cast Fe35Mn31Ni18Al13Tix HEAs, International Journal of Metalcasting, 17 (2023) 888-899.
[46] X. Liang, Y. Su, T. Yang, Z. Dai, Y. Wang, Effect of Ti Addition on the Microstructure and Corrosion Resistance of AlCrCuFeNiNb0.2 High-Entropy Alloy, JOM, 75 (2023) 428-436.
[47] M.C. Groenenboom, R.M. Anderson, D.J. Horton, Y. Basdogan, D.F. Roeper, S.A. Policastro, J.A. Keith, Doped Amorphous Ti Oxides To Deoptimize Oxygen Reduction Reaction Catalysis, The Journal of Physical Chemistry C, 121 (2017) 16825-16830.
[48] S. Li, J. Fu, Improvement in corrosion protection properties of TiO2 coatings by chromium doping, Corrosion Science, 68 (2013) 101-110.
[49] Y. Qiu, S. Thomas, R.K. Gupta, T. Gengenbach, R. Jones, N. Birbilis, A Surface Study of the Native Oxide upon a Compositionally Complex Alloy, Corrosion, 74 (2018) 1312-1317.
[50] S. Ishihara, E. Tochigi, R. Ishikawa, N. Shibata, Y. Ikuhara, Atomic structures of Ti-doped α-Al2O3 Σ13 grain boundary with a small amount of Si impurity, Journal of the American Ceramic Society, 103 (2020) 6659-6665.
[51] C. Ma, K. Chen, C. Liang, C.-W. Nan, R. Ishikawa, K. More, M. Chi, Atomic-scale origin of the large grain-boundary resistance in perovskite Li-ion-conducting solid electrolytes, Energy & Environmental Science, 7 (2014) 1638-1642.
[52] A. Chen, W.-F. Chen, T. Majidi, B. Pudadera, A. Atanacio, M. Manohar, L.R. Sheppard, R. Liu, C.C. Sorrell, P. Koshy, Mo-doped, Cr-Doped, and Mo–Cr codoped TiO2 thin-film photocatalysts by comparative sol-gel spin coating and ion implantation, International Journal of Hydrogen Energy, 46 (2021) 12961-12980.
[53] D.D. Macdonald, The Point Defect Model for the Passive State, Journal of The Electrochemical Society, 139 (1992) 3434.
[54] Y. Qiu, M.A. Gibson, H.L. Fraser, N. Birbilis, Corrosion characteristics of high entropy alloys, Materials Science and Technology, 31 (2015) 1235-1243.
[55] D.H. Xiao, P.F. Zhou, W.Q. Wu, H.Y. Diao, M.C. Gao, M. Song, P.K. Liaw, Microstructure, mechanical and corrosion behaviors of AlCoCuFeNi-(Cr,Ti) high entropy alloys, Materials & Design, 116 (2017) 438-447.
[56] B. Ren, R. Zhao, Z.-X. Liu, S.-k. Guan, H.-S. Zhang, Microstructure and properties of Al0.3CrFe1.5MnNi0.5Ti x and Al0.3CrFe1.5MnNi0.5Si x high-entropy alloys, Rare Metals, 33 (2014) 149-154.

[57] X.W. Qiu, Y.P. Zhang, C.G. Liu, Effect of Ti content on structure and properties of Al2CrFeNiCoCuTix high-entropy alloy coatings, Journal of Alloys and Compounds, 585 (2014) 282-286.
[58] Y.J. Zhou, Y. Zhang, Y.L. Wang, G.L. Chen, Solid solution alloys of AlCoCrFeNiTix with excellent room-temperature mechanical properties, Applied Physics Letters, 90 (2007) 181904.
[59] K. Ishikawa, I. Ohnuma, R. Kainuma, K. Aoki, K. Ishida, Phase equilibria and stability of Heusler-type aluminides in the NiAl–Ni2AlTi–Ni2AlY (Y: V, Cr or Mn) systems, Journal of Alloys and Compounds, 367 (2004) 2-9.
[60] Y. Xu, G. Wang, Q. Song, X. Lu, Z. Li, Q. Zhao, Y. Chen, Microstructure, mechanical properties, and corrosion resistance of SiC reinforced AlxCoCrFeNiTi1-x high-entropy alloy coatings prepared by laser cladding, Surface and Coatings Technology, 437 (2022) 128349.
[61] C.-C. Yen, H.-N. Lu, M.-H. Tsai, B.-W. Wu, Y.-C. Lo, C.-C. Wang, S.-Y. Chang, S.-K. Yen, Corrosion mechanism of annealed equiatomic AlCoCrFeNi tri-phase high-entropy alloy in 0.5 M H2SO4 aerated aqueous solution, Corrosion Science, 157 (2019) 462-471.
[62] F. Liu, Q. Song, R. Chen, W. Li, X. Song, J. Sun, C. Wang, Effects of Al and Co contents on the microstructure and properties of AlxCoCryFeNi high-entropy alloys, Materials Characterization, 203 (2023) 113108.
[63] D. Yang, Y. Liu, H. Jiang, M. Liao, N. Qu, T. Han, Z. Lai, J. Zhu, A novel FeCrNiAlTi-based high entropy alloy strengthened by refined grains, Journal of Alloys and Compounds, 823 (2020) 153729.
[64] M.M. Garlapati, M. Vaidya, A. Karati, S. Mishra, R. Bhattacharya, B.S. Murty, Influence of Al content on thermal stability of nanocrystalline AlxCoCrFeNi high entropy alloys at low and intermediate temperatures, Advanced Powder Technology, 31 (2020) 1985-1993.
[65] Q. Zhao, Z. Pan, X. Wang, H. Luo, Y. Liu, X. Li, Corrosion and passive behavior of AlxCrFeNi3−x (x = 0.6, 0.8, 1.0) eutectic high entropy alloys in chloride environment, Corrosion Science, 208 (2022) 110666.
[66] Y. Shi, L. Collins, R. Feng, C. Zhang, N. Balke, P.K. Liaw, B. Yang, Homogenization of AlxCoCrFeNi high-entropy alloys with improved corrosion resistance, Corrosion Science, 133 (2018) 120-131.
[67] J. Joseph, M. Annasamy, S.R. Kada, P.D. Hodgson, M.R. Barnett, D.M. Fabijanic, Optimising the Al and Ti compositional window for the design of γ′ (L12)-strengthened Al–Co–Cr–Fe–Ni–Ti high entropy alloys, Materials Science and Engineering: A, 835 (2022) 142620.
[68] J.J. Bhattacharyya, S.B. Inman, M.A. Wischhusen, J. Qi, J. Poon, J.R. Scully, S.R. Agnew, Light Weight, Low Cost, and Compositionally Complex Multiphase Alloys with Optimized Strength, Ductility and Corrosion Resistance: Discovery, Design and Mechanistic Understandings, Materials & Design, 228 (2023).
[69] S.B. Inman, J. Han, A.Y. Gerard, J. Qi, M.A. Wischhusen, S.R. Agnew, S.J. Poon, K. Ogle, J.R. Scully, Effect of Mn Content on the Passivation and Corrosion of Al0.3Cr0.5Fe2MnxMo0.15Ni1.5Ti0.3 Compositionally Complex Face-Centered Cubic Alloys, Corrosion, 78 (2021) 32-48.
[70] S.B. Inman, J. Han, M.A. Wischhusen, J. Qi, S.R. Agnew, K. Ogle, J.R. Scully, Passivation and Localized Corrosion Resistance of Al0.3Cr0.5Fe2MoxNi1.5Ti0.3 Compositionally Complex Alloys: Effect of Mo Content, Corroison Science, 227 (2024) 111692.
[71] Y.-M. Chen, N.G. Rudawski, E. Lambers, M.E. Orazem, Application of impedance spectroscopy and surface analysis to obtain oxide film thickness, Journal of The Electrochemical Society, 164 (2017) C563.
[72] B. Hirschorn, M.E. Orazem, B. Tribollet, V. Vivier, I. Frateur, M. Musiani, Determination of effective capacitance and film thickness from constant-phase-element parameters, Electrochimica Acta, 55 (2010) 6218-6227.
[73] K. Lutton, K. Gusieva, N. Ott, N. Birbilis, J.R. Scully, Understanding multi-element alloy passivation in acidic solutions using operando methods, Electrochemistry Communications, 80 (2017) 44-47.
[74] K. Ogle, Atomic Emission Spectroelectrochemistry: Real-Time Rate Measurements of Dissolution, Corrosion, and Passivation, Corrosion, 75 (2019) 1398-1419.

[75] M.C. Biesinger, L.W.M. Lau, A.R. Gerson, R.S.C. Smart, Resolving surface chemical states in XPS analysis of first row transition metals, oxides and hydroxides: Sc, Ti, V, Cu and Zn, Applied Surface Science, 257 (2010) 887-898.
[76] M.C. Biesinger, B.P. Payne, A.P. Grosvenor, L.W.M. Lau, A.R. Gerson, R.S.C. Smart, Resolving surface chemical states in XPS analysis of first row transition metals, oxides and hydroxides: Cr, Mn, Fe, Co and Ni, Applied Surface Science, 257 (2011) 2717-2730.
[77] J. Baltrusaitis, B. Mendoza-Sanchez, V. Fernandez, R. Veenstra, N. Dukstiene, A. Roberts, N. Fairley, Generalized molybdenum oxide surface chemical state XPS determination via informed amorphous sample model, Applied Surface Science, 326 (2015) 151-161.
[78] A. Obrosov, R. Gulyaev, A. Zak, M. Ratzke, M. Naveed, W. Dudzinski, S. Weiß, Chemical and Morphological Characterization of Magnetron Sputtered at Different Bias Voltages Cr-Al-C Coatings, in: Materials, 2017.
[79] S.B. Inman, D. Sur, J. Han, K. Ogle, J.R. Scully, Corrosion behavior of a compositionally complex alloy utilizing simultaneous Al, Cr, and Ti passivation, Corrosion Science, 217 (2023) 111138.
[80] J.R. Scully, D.C. Silverman, M.W. Kendig, Electrochemical Impedance: Analysis and Interpretation, in, 1993.
[81] J.D. Cox, D.D. Wagman, V.A. Medvedev, CODATA Key Values for Thermodynamics, in, New York, 1989.
[82] S.E. Ziemniak, L.M. Anovitz, R.A. Castelli, W.D. Porter, Thermodynamics of Cr2O3, FeCr2O4, ZnCr2O4, and CoCr2O4, The Journal of Chemical Thermodynamics, 39 (2007) 1474-1492.
[83] K. Orson, E. Romanovskaia, A. Costine, J. Han, K. Ogle, J.R. Scully, P. Reinke, Corrosion Resistance, Composition, and Stratification of Passive Films: Ni-22Cr and Ni-22Cr-6Mo Alloys Passivated and Exposure Aged in Acidic Chloride Solutions, Journal of The Electrochemical Society, 171 (2024) 011505.
[84] J.E. Saal, S. Kirklin, M. Aykol, B. Meredig, C. Wolverton, Materials Design and Discovery with High-Throughput Density Functional Theory: The Open Quantum Materials Database (OQMD), JOM, 65 (2013) 1501-1509.
[85] S. Kirklin, J.E. Saal, B. Meredig, A. Thompson, J.W. Doak, M. Aykol, S. Rühl, C. Wolverton, The Open Quantum Materials Database (OQMD): assessing the accuracy of DFT formation energies, npj Computational Materials, 1 (2015) 15010.
[86] K. Wang, J. Han, A.Y. Gerard, J.R. Scully, B.-C. Zhou, Potential-pH diagrams considering complex oxide solution phases for understanding aqueous corrosion of multi-principal element alloys, npj Materials Degradation, 4 (2020) 35.
[87] H.D. Werner, N. Jahrbuch Miner. Monatshefte, (1974) 218-234.
[88] S.M. Lang, C.L. Fillmore, L.H. Maxwell, The System Beryllia-Alumina-Titania: Phase Relations and General Physical Properties of ThreeComponent Porcelains, Journal of Research of the National Bureau of Standards 48 (1952) 298-312.

Chapter 4: Effect of Mn Content on the Passivation and Corrosion of $Al_{0.3}Cr_{0.5}Fe_2Mn_xMo_{0.15}Ni_{1.5}Ti_{0.3}$ Complex Concentrated FCC Alloys

This chapter was published in CORROSION with coauthors J. Han, A.Y. Gerard, J. Qi, M.A. Wischhusen, S. R. Agnew, S. J. Poon, K. Ogle, and J.R. Scully. The citation for the article is provided below.

S.B. Inman, J. Han, A.Y. Gerard, J. Qi, M.A. Wischhusen, S.R. Agnew, S.J. Poon, K. Ogle, J.R. Scully, Effect of Mn Content on the Passivation and Corrosion of Al0.3Cr0.5Fe2MnxMo0.15Ni1.5Ti0.3 Compositionally Complex Face-Centered Cubic Alloys, Corrosion, 78 (2021) 32-48.

Abstract

$Al_{0.3}Cr_{0.5}Fe_2Mn_xMo_{0.15}Ni_{1.5}Ti_{0.3}$ (x = 0, 0.25, 0.5, 1) complex concentrated alloys are synthesized and annealed at 1070 °C to form two-phase alloys with an FCC matrix and a second phases enriched in Al, Ti and Ni with slightly reduced density, raw element costs, and passivating elements distributed across both phases. The global corrosion resistance is evaluated in 0.01 and 0.1 M NaCl at both natural pH and pH 4. Overall corrosion resistance is suggested to be optimized at Mn concentrations of 5.0 at. %, indicated by pitting potentials comparable to or exceeding those of 316L stainless steel. Improvements in corrosion resistance and optimization of Mn concentration are further assessed by polarization, impedance, and gravimetric analysis after extended aqueous exposure. The fate of individual elements during the dissolution and passivation processes is evaluated with in-situ atomic emission spectroelectrochemistry and ex-situ x-ray photoelectron spectroscopy. Passivity was derived from combinations of Ti^{4+}, Cr^{3+}, and Al^{3+} oxides in an undetermined solid solution or complex oxide. Enhanced corrosion resistance is attributed to the improved chemical homogeneity of passivating elements within the two-phase microstructure while the decreased corrosion resistance of alloys with higher Mn concentrations is attributed to high Mn dissolution rates and/or destabilization of the passive films. The underlying effects of Mn in the design of corrosion resistant lightweight complex concentrated alloys are discussed.

1.0 Introduction

Complex concentrated alloys (CCAs), a broad alloy class which include high entropy alloys (HEAs) and multi-principal element alloys (MPEAs), involve combinations of four or more elements with compositions above 5 at. %. Compositions may deviate from the equimolar constraints that typically define HEAs, greatly increasing the alloy compositional space [1, 2]. These alloys show promise in producing superior corrosion resistance as well as other desirable properties but the ideal selection of alloying elements for a specific property has not been mastered. Moreover, low cost materials with reduced density are possible in light weight high entropy alloys particularly with less expensive alloying elements such as Al and Fe. The high configurational entropy from multiple elements at significant concentrations increases the likelihood of overcoming enthalpy driven segregation and preserving single-phase stability [1, 3]. Composition based thermodynamic parameters indicated below may be used to predict phase stability. Single-phase stability is increasingly likely with a configurational entropy (ΔS_{mix}) above 1.5R (where R is the ideal gas constant and c_i corresponds to the concentration of element i), an enthalpy of mixing (ΔH_{mix}) calculated by the Miedema model [4, 5] less negative than -16.25 kJ/mol (where ΔH_{ij} corresponds to the enthalpy of mixing of elements i and j), and/or an atomic radius (r) mean squared deviation (δ) of less than 4.7%. [1]

$$\Delta S_{mix} = -R\sum_{i=1}^{n}(c_i \ln(c_i)) \qquad (1)$$

$$\Delta H_{mix} = \sum_{i=1, i\neq j}^{n} 4\Delta H_{i,j}^{mix} c_i c_j \qquad (2)$$

$$\delta = \sqrt{\sum_{i=1}^{n} c_i \left(1 - \frac{r_i}{\bar{r}}\right)^2} \qquad (3)$$

Moreover, Yang and Zhang [6] and King et al. [4] calculated dimensionless empirical indexes (Ω and Φ respectively) from thermodynamic indicators to predict CCA single-phase stability. Accuracy in the prediction of single-phase stability is improved relative to single parameter criteria by combining multiple thermodynamic values including ΔS_{mix}, ΔH_{mix}, the weighted average melting temperature (T_m), and the enthalpy of the most stable intermetallic binary phase (ΔH_{IM}) into a single term. Single-phase stability is considered likely at values of Ω above 1.1 and Φ above 1.0 where:

$$\Omega = \frac{T_m \Delta S_{mix}}{|\Delta H_{mix}|} \qquad (4)$$

$$\Phi = \left|\frac{\Delta H_{mix} - T_m \Delta S_{mix}}{\Delta H_{IM}}\right| \qquad (5)$$

Further prediction of single-phase stability can be obtained via CALPHAD approaches as well as by combining binary phase diagram analysis with machine learning methods [2, 7].

It has been suggested that CCAs with good mechanical strength [3, 8, 9] and corrosion resistance benefit from homogenous solid-solution distribution of elements, including key of passivating elements Cr, Al, and Ti [10-12]. Unique combinations and distributions of passivating elements in CCAs, often through elemental synergies not observed in conventional alloys, assist in the formation of stable passive films that prevent further environmental degradation [11-17].

The use of Al and Ti has been under increased investigation to reduce the density and increase mechanical strength of CCAs. [18, 19] Although both elements spontaneously passivate and Ti has been shown to increase corrosion resistance in CCAs [11, 20], FCC alloys reliant on Al and Ti to passivate may have their corrosion resistance decreased by the elements' propensity to form second phases including BCC [1, 16, 18, 19, 21-23], B2 [18, 23, 24], and Heusler ($L2_1$) [1, 25, 26] phases. Second phase formation driven by Al or Ti, often interacting with Ni [18, 19, 23, 27], creates both phase interfaces and areas depleted in passivating elements, both of which are potential initiation sites for localized corrosion [28]. Increased second phase volume fractions in the $Al_xCoCrFeNi$ system driven by higher Al concentrations lead to decreased pitting potentials and increased passive currents or localized attack in the Al-rich BCC phase [29].

To improve elemental homogeneity in an FCC matrix, elements conventionally established as austenitic stabilizers may be utilized. Many CCAs, including the first transition metal HEAs developed by Cantor et al. [30], utilize Co, Mn, and Ni to stabilize the FCC structure. While Co and Ni often increase alloy cost and density, Mn could potentially function as a cost-effective FCC stabilizer [31, 32]. The equimolar introduction of Mn to the AlCrFeNiTi HEA eliminated the formation of a Laves phase and decreased the magnitude of Cr segregation [27]. Higher Mn concentrations in the $(FeNi)_{77-x}Cr_{15}Mn_xAl_4Ti_4$ system were computationally modeled to increase the volume fraction of the FCC matrix while changing the stable second phase from the ordered FCC-like $L1_2$ to Laves and BCC phases [33]. Equimolar Mn addition to a mechanically alloyed TiCrFeNi HEA, however, does not remove the Sigma phase that can be eliminated upon Co alloying, suggesting Mn may not be as effective as other austenitic stabilizers [34]. Additionally, it has been proposed that Mn could provide improved mechanical ductility by promoting twinning or transformation induced plasticity to increase CCA ductility [35, 36].

While Mn has been long established as an austenitic stabilizer in stainless steels [37, 38], it is often dismissed in alloy design due to its contributions to poor corrosion resistance. Extensive work in the Fe-Mn-Al system has associated high Mn concentrations with poor corrosion resistance, most prominently attributed to the formation of MnS inclusions [39]. Mn is also detrimental to corrosion resistance due to high elemental dissolution rates [40-43]. Higher Mn concentrations lead to increased levels of pitting and decreased corrosion resistance in the single-phase Fe-Cr-Mn tertiary system, potentially attributable to Mn decreasing the activity of Cr during the passivation process [44]. Similar trends have been observed in single-phase CCAs. Most noticeably, corrosion resistance is improved by removing Mn from equimolar CoCrFeMnNi in sulfate [45] and chloride [46] solutions. The high diffusivity of Mn in CoCrFeMnNi [47], fast transport rates in Mn oxides, and the instability of Mn-rich passive films [14, 15, 27, 45] may all contribute to the poor corrosion resistance of Mn containing alloys.

Alternatively, Kukshal et al. [48] evaluated Mn additions in the dual phase $AlCr_{1.5}CuFeNi_2Mn_x$ system up to 13.3 at. %, finding increased corrosion resistance with Mn additions that was attributed to improved Cr and Ni distribution in solid solution. Wong et al. [49] found that Mn concentrations up to 6.3 at. % have an insignificant effect on the corrosion resistance of FCC $Al_{0.3}CoCrFeNiMn_x$, with higher Mn concentrations slightly lowering the corrosion potential. Kim and Kim [50] observed an increase in the open circuit potential during immersion of a Mn-containing steel that was not observed in the otherwise identical Mn-free composition. Rodriguez et al. [51] developed a series of Co-Cr-Fe-Mn-Ni type CCAs with varying Mn concentrations. Corrosion resistance was weakened in alloys with greater than 15 at. % Mn, particularly when coupled with decreasing Cr concentrations.

Elements enriched in the passive films are expected to have a negative free energy of formation and kinetically lower electrochemical or chemical dissolution rates during incongruent dissolution of the passivating material, a phenomenon experimentally verified in the BCC $Al_{1.5}TiVCr$ CCA by Qiu et al. [52]. Han et al. [53] tracked elemental dissolution rates for $Ni_{38}Fe_{20}Cr_{22}Mn_{10}Co_{10}$ in a 0.1 M NaCl, pH 4 solution. Potential dependent Mn dissolution was observed; Mn dissolved incongruently at rates significantly below those of Ni and Fe at 0.1 V_{SCE} whereas it dissolved congruently at 0.0 V_{SCE}. Surface enrichment of Mn in the passivating oxides at 0.1 V_{SCE} was verified by X-ray photoelectron spectroscopy (XPS) using 3p core level analysis. At 0.0 V_{SCE}, a more corrosion resistant passive film formation was indicated by the higher oxide resistance obtained by electrochemical impedance spectroscopy (EIS) than that obtained at 0.1 V_{SCE}. Better protection was attributed to a lower extent of Mn incorporation in the passive film at this potential. Mn incorporation in oxides could occur by the formation of stable stoichiometric tertiary spinel oxides. $FeMn_2O_4$ [54], $MnCr_2O_4$ [55], and $NiMn_2O_4$ [56] stability has been thermodynamically simulated but such ordered spinels have not been experimentally verified to form during aqueous passivation in CoCrFeMnNi [57] or any other Mn-containing CCAs to the authors' best knowledge. The aforementioned findings suggest that corrosion resistance of CCAs is considerably more complex than an inverse proportionality to Mn content. A well-established connection between the alloy nanostructure, microstructure, composition, passive film chemistry, and film protectiveness is currently lacking.

While potential drawbacks of Mn for corrosion resistance are well established, two key gaps in the current understanding introduce potential caveats. First, much of the work on the effect of Mn on corrosion resistance focuses on CCAs with Mn compositions of at least 15 at. %, where rapid, preferential dissolution and unprotective Mn oxides can easily harm corrosion resistance in ways that may not occur at lower concentrations. Second, there has been little work on the effect of Mn in Al and/or Ti containing multiphase CCAs. The transition metal HEAs CoCrFeMnNi and CoCrFeNi both possess a single-phase FCC microstructure [58] making it difficult to evaluate the trade-offs between benefits of improved homogeneity from Mn on corrosion distinct from the potential detrimental effect of Mn on oxide protectiveness.

The objective of this work was to examine the effect of Mn in a lightweight alloy with three passivating elements Al, Ti, Cr, one potential oxide dopant element Mo, and a number of Austenitic stabilizing elements. The alloys were designed to minimize density and cost while maximizing corrosion resistance and are stipulated to have an FCC matrix. Four CCAs with Mn concentrations ranging from 0 to 17.4 at. % were synthesized and characterized to find the optimal Mn concentration to improve corrosion resistance. The role of Mn in the design of lightweight CCAs is investigated by elementally resolved in situ and ex situ techniques.

2.0 Experimental Methods

2.1 CCA Synthesis and Microstructural Characterization

Four CCAs with compositions listed in Table I were synthesized by arc-melting from high purity (Cr greater 99.2 %, all other metals greater than 99.9%) elements and suction cast in a water-cooled copper hearth under argon atmosphere. Alloys were flipped five times to ensure chemical homogeneity before encapsulation into quartz tubes under argon and a five-hour annealing treatment at 1070 °C followed by a water quench. The compositions and heat treatment were chosen to promote the formation of an FCC matrix while balancing cost, density, and passivating element concentration with machine learning methods discussed elsewhere [2, 59]. The $Al_{0.3}Cr_{0.5}Fe_2Mn_xMo_{0.15}Ni_{1.5}Ti_{0.3}$ system was also modeled with CALPHAD utilizing ThermoCalc 2019b software and the TCHEA3 database for Mn concentrations between 0 and 25 at % to predict the thermodynamically stable phases for each synthesized alloy. [60] Relevant thermodynamic parameters are calculated in Table II utilizing previously established atomic radius [61] and enthalpy of mixing [62] values. It was found that the "high" enthalpy criterion, ΔS/R, Ω, and Φ where almost met or met while the δ criterion was, expectedly, not achieved. Prediction of an FCC matrix along with a second phases was achieved by machine learning [2]. Samples were cold-mounted in non-conductive epoxy, ground with SiC paper through 1200 grit, and degreased with isopropyl alcohol before electrochemical testing. Diamond polishing suspensions through 0.25 microns were used, followed by 0.05-micrometer colloidal silica suspension, to prepare samples for microstructure and surface chemical analysis. The phases in each alloy were identified via x-ray diffraction (XRD) using Cu Kα X-rays (1468.7 eV) on a PANalytical Empyrean Diffractometer™ at a scan rate of 0.15 °/s. The samples were characterized through scanning electron microscopy (SEM) using backscattered electron (BSE) imaging on an FEI Quanta 650™ operating at an accelerating voltage of 15 keV, a spot size of 4, and working distance of approximately 10 mm. The chemical compositions of the samples were evaluated via point scans and mapping with energy dispersive spectroscopy (EDS) analyzed using Oxford Instruments AZtec™ software. Area fractions of second phase regions were calculated with ImageJ using a brightness threshold to isolate at least 300 precipitates across multiple micrographs per alloy. The calculated area fraction of second phase was taken to be equivalent to the volume fraction of second phase in the material.

Table I: Compositions of synthesized CCAs in atomic percent. Compositions given for 316L indicate an average of the accepted composition range.

Alloy	Al	Co	Cr	Fe	Mn	Mo	Ni	Ti
$Al_{0.3}Cr_{0.5}Fe_2Mn_0Mo_{0.15}Ni_{1.5}Ti_{0.3}$	6.3%	-	10.5%	42.1%	**-**	3.2%	31.6%	6.3%
$Al_{0.3}Cr_{0.5}Fe_2Mn_{0.25}Mo_{0.15}Ni_{1.5}Ti_{0.3}$	6.0%	-	10.0%	40.0%	**5.0%**	3.0%	30.0%	6.0%
$Al_{0.3}Cr_{0.5}Fe_2Mn_{0.5}Mo_{0.15}Ni_{1.5}Ti_{0.3}$	5.7%	-	9.5%	38.1%	**9.5%**	2.9%	28.6%	5.7%
$Al_{0.3}Cr_{0.5}Fe_2Mn_1Mo_{0.15}Ni_{1.5}Ti_{0.3}$	5.2%	-	8.7%	34.8%	**17.4%**	2.6%	26.1%	5.2%
CoCrFeMnNi	-	20%	20%	20%	20%	-	20%	-
316L	-	-	18.3%	66.7%	2.1%	1.5%	11.4%	-

Table II: Phase stability indicators calculated from the alloy's compositions. Bolded terms indicate values associated with single-phase stability in CCAs.

Alloy	**ΔH (kJ/mol)**	**ΔS/R**	**δ (%)**	**Ω**	**Φ**
$Al_{0.3}Cr_{0.5}Fe_2Mn_0Mo_{0.15}Ni_{1.5}Ti_{0.3}$	-11.07	1.42	8.61	**1.94**	0.929
$Al_{0.3}Cr_{0.5}Fe_2Mn_{0.25}Mo_{0.15}Ni_{1.5}Ti_{0.3}$	-10.74	**1.55**	8.42	**2.16**	0.968
$Al_{0.3}Cr_{0.5}Fe_2Mn_{0.5}Mo_{0.15}Ni_{1.5}Ti_{0.3}$	-10.39	**1.60**	8.25	**2.29**	0.976
$Al_{0.3}Cr_{0.5}Fe_2Mn_1Mo_{0.15}Ni_{1.5}Ti_{0.3}$	-9.77	**1.64**	7.90	**2.45**	0.963
CoCrFeMnNi	-4.16	**1.61**	**3.90**	**5.79**	**3.533**
316L	-1.85	0.97	**3.96**	**8.22**	**2.130**

2.2 Electrochemical Characterization of CCAs

Samples, along with equimolar CoCrFeMnNi and commercially procured (North American Steel) 316L stainless steel controls, were potentiodynamically polarized with a Gamry Instrument Reference 600+™ potentiostat and a conventional three electrode cell including the CCA sample with an exposed area of 0.785 cm^2 as the working electrode, a platinum mesh counter electrode, and a saturated calomel reference electrode (SCE) relative to which all potentials hereafters are reported. The electrolyte solution was either 0.01 M NaCl, 0.1 M NaCl with the pH unadjusted (approximately 5.75), or 0.1 M NaCl titrated to pH 4 with 1 M HCl. Solutions were dissolved in deionized water and continually bubbled with nitrogen gas throughout testing. Dilute solutions were preferred to observe passivation behavior before interference from localized corrosion. In initial tests, a -1.3 V_{SCE} potential was applied for 600 s to minimize the effect of the air-formed oxide. Cathodic reduction was followed by an upward anodic potential scan from -1.3 to +0.8 V_{SCE} with a voltage step of 5 mV, continually monitoring the imaginary component of the impedance (Z_{img}) throughout polarization at a frequency of 1 Hz with an AC voltage of 20 mV_{rms}, as previously utilized for to evaluate trends in oxide thickness [14, 63]. By modeling the oxide film as a constant phase element (CPE) fit to a phase shift (α), resistivity at the interface between the electrolyte and passive film (ρ_δ), applied frequency (f), dielectric constant (κ), vacuum permittivity (ε_o), and exposed area of the working electrode (A), Z_{img} may be modeled as directly proportional to the oxide thickness (l_{ox}) [64, 65].[16]

---

[16] Although oxide thicknesses could be quantified with a dielectric constant and resistivity estimated from XPS based surface analysis, such assumptions were not made to characterize the film during polarization due to the changing oxide film composition. Therefore, trends in the Z_{img} measured during polarization and/or potentiostatic holds should be regarded as qualitative descriptions of the oxide thickness.

$$|Z_{img}| = \frac{l_{ox}\rho_{\delta}^{1-\alpha}\sin(\frac{\alpha\pi}{2})(1+2.88(1-\alpha)^{2.375})}{2\pi f\kappa\epsilon_o A} \quad (6)$$

Finally, the sample was polarized in the reverse direction (+0.8 to -1.3 V_{SCE}) with otherwise identical methods. Pitting potentials are defined at the potential where the current density first reaches 10^{-5} A/cm^2 and zero current potentials are defined where the net applied current density is equal to zero.

To characterize the oxide films spontaneously formed in air and modified by OCP exposure, a second procedure was utilized. Directly after grinding a new surface (approximately ten minutes at room temperature, 62% relative humidity), open circuit potential (OCP) was monitored for 1800 s in 0.01 M NaCl. Potentiostatic EIS was conducted at the potential of the final OCP measurement at a frequency range from 100 kHz to 1 mHz with 5 points/decade and an AC voltage of 20 mV_{rms}. The sample was polarized with a potential scan from 0.1 V below OCP to +0.8 V_{SCE} with the same continual impedance monitoring methodology utilized during previous polarization experiments followed by a reversed downward scan (+0.8 to -1.3 V_{SCE}).

To characterize the passive oxide growth, a potential of -1.3 V_{SCE} was applied to each CCA for 600 s before applying a constant potential of -0.25 V_{SCE} for 40 ks, verified to be within the passive range of all tested alloys via potentiodynamic polarization. The Z_{img} was continually characterized every 6 seconds at a frequency of 1 Hz and an AC voltage of 20 mV_{rms} to monitor oxide growth during the potentiostatic hold. The potentiostatic EIS described above was carried out at -0.25 V_{SCE} to characterize the surface after the potentiostatic hold. EIS spectra were fit to a simplified Randles' circuit model containing a CPE with Gamry Echem Analyst software to obtain the polarization resistance of the oxide film.

To examine the effects of a longer time of corrosion, 1 cm diameter buttons with a thickness of approximately 0.25 cm were measured for mass to 0.01 mg precision and fully immersed for 25 days in 0.1 M NaCl. Corrosion products were rinsed with nitric acid under ASTM Standard G1 C.7.4 [66] and the sample was remeasured for mass. The change in mass was normalized to exposed surface area to calculate the mass loss rate and to a weighted elemental average density to obtain the penetration rate. An 1800 s OCP measurement followed by the EIS spectrum described above at each alloy's respective OCP was collected in a separate flat cell both directly prior to and following immersion of $Al_{0.3}Cr_{0.5}Fe_2Mn_0Mo_{0.15}Ni_{1.5}Ti_{0.3}$ and $Al_{0.3}Cr_{0.5}Fe_2Mn_{0.25}Mo_{0.15}Ni_{1.5}Ti_{0.3}$.

Atomic emission spectroelectrochemistry (AESEC) was used to monitor individual elemental dissolution rates alongside electron current density. Dissolved elements were transferred through a flow cell to a Horiba Jobin Yvon Ultima 2C^{TM} inductively coupled plasma atomic emission spectrometer (ICP-AES). The dissolution rates of each alloying element in $Al_{0.3}Cr_{0.5}Fe_2Mn_0Mo_{0.15}Ni_{1.5}Ti_{0.3}$, $Al_{0.3}Cr_{0.5}Fe_2Mn_{0.25}Mo_{0.15}Ni_{1.5}Ti_{0.3}$, and $Al_{0.3}Cr_{0.5}Fe_2Mn_1Mo_{0.15}Ni_{1.5}Ti_{0.3}$ alloys were monitored by emission intensity at a characteristic wavelength of each element with a polychromator at a 0.5 m focal length. A monochromator was used to have an improved signal resolution of Mo or Cr. Elemental dissolution rates (v_M) were converted to an equivalent elemental current density (j_M) with Faraday's law, providing a comparable basis to electron current density (j_e). A theoretical basis for AESEC and comprehensive methodology may be found elsewhere [67]. AESEC experiments were performed in a 0.1 M NaCl pH 4 solution to increase the dissolution rate to an observable level. Dissolution rates were monitored during potentiodynamic polarization following a 600 s exposure to open circuit corrosion and an application of a -1.3 V_{SCE} potential for 600 s. Potentials were swept from -1.3 V_{SCE} to +0.8 V_{SCE} with a scan rate of 0.5 mV/s. Dissolution rates were monitored during a 600 s exposure to open circuit corrosion and during a directly following 4 ks potentiostatic hold at -0.2 V_{SCE} (bypassing any cathodic reduction). The test time was decreased relative to electrochemical tests to ensure plasma stability.

2.3 Characterization of Passive Film Composition

Chemical compositions of passive films grown on $Al_{0.3}Cr_{0.5}Fe_2Mn_{0.25}Mo_{0.15}Ni_{1.5}Ti_{0.3}$ and $Al_{0.3}Cr_{0.5}Fe_2Mn_1Mo_{0.15}Ni_{1.5}Ti_{0.3}$ during the 40 ks potentiostatic hold were characterized with XPS spectra acquired with Al Kα X-rays (1486.6 eV) at a 26 eV pass energy, 45° take off angle, and with a 100 µm spot size in a PHI VersaProbe III^{TM} system. High resolution spectra over the Al 2p, Cr $2p_{3/2}$, Fe $2p_{1/2}$, Mn $2p_{1/2}$, Mo 3d, Ni $2p_{3/2}$, and Ti $2p_{3/2}$ core spectra were shifted utilizing C 1s = 284.8 eV and deconvoluted with Shirley background subtractions, Doniach-Sunjic peaks for metallic features, and Voigt functions for oxidized features with KOLXPD™ analysis software. Metal and oxidized peaks were identified by considering position, shape, and multiplet splitting identified from reference spectra of Al [68], Ti [69], Mo [70], the first-row transition metals [71], and their oxidized compounds. In the case of Fe and Mn, where Ni Auger peaks overlap the $2p_{3/2}$ spectrum, [72] a constant binding energy shift for each compound relative to the reference $2p_{3/2}$ spectra was assumed. Cation fractions were normalized with relative sensitivity factors obtained from Phi Multipak^{TM} software. The overlap between the Al 2p spectrum and Cr 3s spectrum was accounted for by fixing the magnitude of Cr 3s signal based on the intensity obtained in the Cr $2p_{3/2}$ region normalized by relative sensitivity factors. Cation fractions were evaluated as the proportion of each elements normalized intensities for all oxidized states summed relative to that of all elements' oxidized state intensities. The cation enrichment (or depletion) factors f_A for each individual element "A" were calculated from the surface composition (X^S), in this case, the oxide cation fraction obtained by XPS, relative to the sum of the bulk compositional fraction all other constituent elements (X_j) normalized to their bulk alloy compositions (X^b) [73]:

$$f_A = \frac{\dfrac{X_A^S}{X_A^S + \Sigma_j X_J^S}}{\dfrac{X_A^b}{X_A^b + \Sigma_j X_J^b}} \qquad (7)$$

3.0 Results

3.1 Microstructural Characterization of CCAs

XRD suggests an FCC matrix indexable to a lattice parameter of 3.63 Å for alloys with all Mn concentrations, as shown in Figure 1. Second phase regions of either BCC or ordered BCC-type (B2/$L2_1$) are visible in the XRD data for $Al_{0.3}Cr_{0.5}Fe_2Mn_0Mo_{0.15}Ni_{1.5}Ti_{0.3}$ and $Al_{0.3}Cr_{0.5}Fe_2Mn_{0.25}Mo_{0.15}Ni_{1.5}Ti_{0.3}$, the two alloys with the lowest Mn concentration, however, noise in XRD data prevents accurate phase identification from additional peaks. The CALPHAD modeling seen in Figure 2 does not accurately identify the phase structure, suggesting the synthesized alloys would form a single FCC phase, however, it does indicate a broad FCC-$L1_2$ phase region above 1290 °C which broadens slightly with Mn content from 0-25 at. %. Below this temperature many phases are formed including $L2_1$, Mu, Laves, and Sigma depending on the exact Mn content. Second phase regions on the order of single microns with similar spacing distributions are visible in the BSE micrographs for all four CCAs (Figure 3). There is a non-monotonic trend of second phase area fraction and Mn concentration.

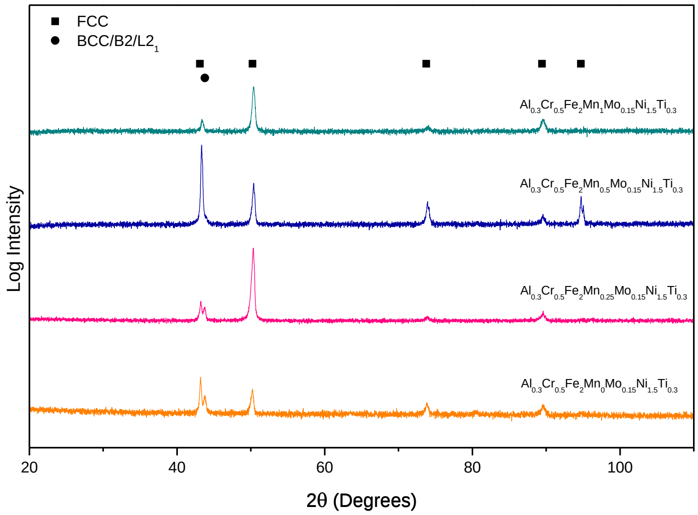

Figure 1: XRD patterns for synthesized CCAs indexed to FCC and BCC/B2/L2$_1$ phases

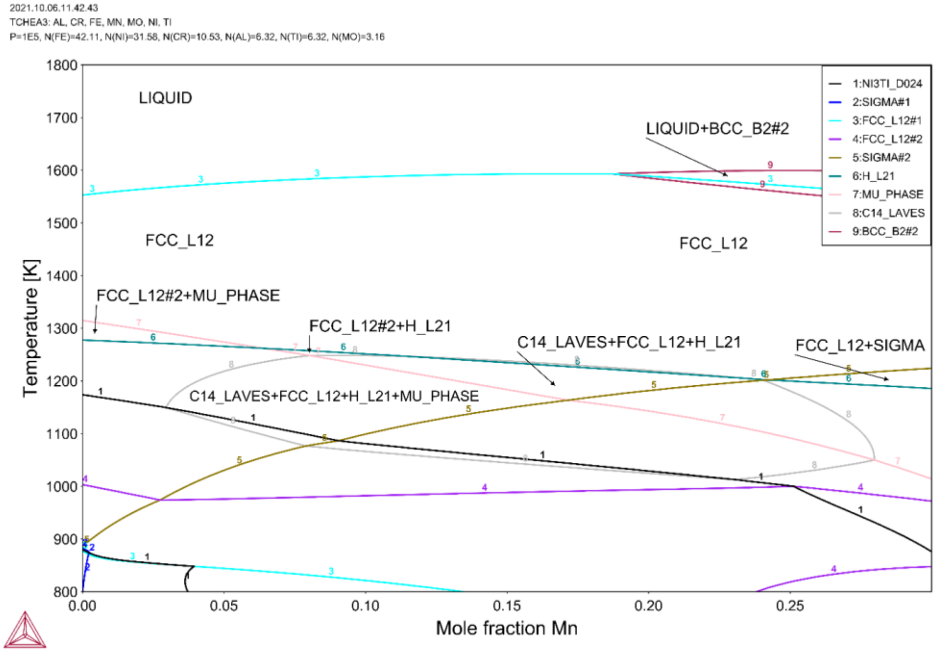

Figure 2: $Al_{0.3}Cr_{0.5}Fe_2Mn_xMo_{0.15}Ni_{1.5}Ti_{0.3}$ system modeled with CALPHAD from Thermocalc TCHEA3 database

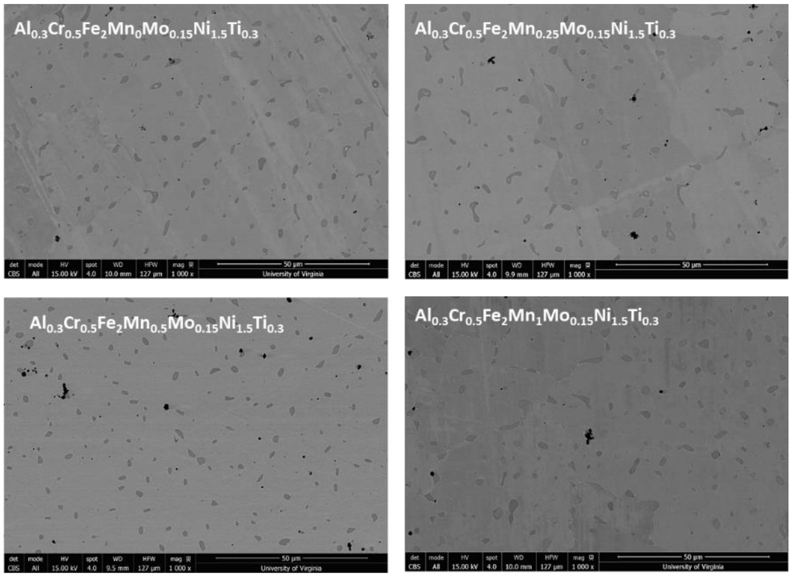

Figure 3: BSE images of CCA microstructures

EDS mapping (Figure 4) and point scans (Table III) suggest Fe, Cr, and Mo enrichment in the matrix and Al, Ti, and Ni enrichment in the second phase regions relative to the bulk metal concentrations. Fe and Ni have the highest concentrations in the matrix and second phase, respectively. Mn has a similar concentration in both regions in all CCAs. The differences in matrix and second phase particle compositions for each element generally have the highest magnitude for $Al_{0.3}Cr_{0.5}Fe_2Mn_0Mo_{0.15}Ni_{1.5}Ti_{0.3}$. The other CCAs have similar composition ratios between the phases for most elements regardless of Mn concentration. Ti and N rich or Al, Ti, and O rich impurities from contamination during synthesis are also present in low quantities throughout the microstructures. No consistent trends in $L2_1$ area fraction are observed with Mn concentration.

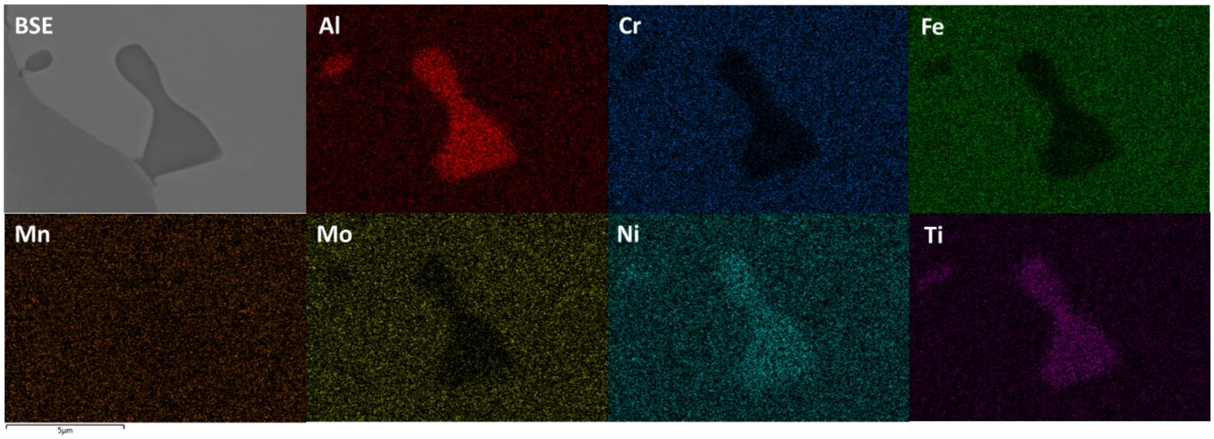

Figure 4: A representative second phase containing region identified with BSE imaging and EDS mapping demonstrating elemental segregation in $Al_{0.3}Cr_{0.5}Fe_2Mn_{0.25}Mo_{0.15}Ni_{1.5}Ti_{0.3}$

Table III: Elemental fractions obtained with EDS point scans in the matrix and second phase of the synthesized CCAs. Area fraction referrers to the cross sectional second phase area fraction calculated through microstructural analysis with ImageJ.

Phase	Al	Cr	Fe	Mn	Mo	Ni	Ti	Area Fraction
$Al_{0.3}Cr_{0.5}Fe_2Mn_0Mo_{0.15}Ni_{1.5}Ti_{0.3}$								
Matrix	3.73	11.58	44.67	-	3.24	30.65	6.13	96.04 %
2nd Phase	15.28	2.50	13.95	-	0.51	47.26	20.49	3.96 %
$Al_{0.3}Cr_{0.5}Fe_2Mn_{0.25}Mo_{0.15}Ni_{1.5}Ti_{0.3}$								
Matrix	3.70	11.02	42.49	5.24	3.12	28.78	5.63	95.67 %
2nd Phase	14.31	3.54	17.13	4.24	0.87	44.08	15.83	4.33 %
$Al_{0.3}Cr_{0.5}Fe_2Mn_{0.5}Mo_{0.15}Ni_{1.5}Ti_{0.3}$								
Matrix	5.22	9.95	39.85	9.37	2.66	27.78	5.17	96.70%
2nd Phase	17.10	3.21	18.20	8.44	0.69	40.97	11.40	3.30%
$Al_{0.3}Cr_{0.5}Fe_2Mn_1Mo_{0.15}Ni_{1.5}Ti_{0.3}$								
Matrix	4.39	9.31	35.78	18.71	1.97	25.16	4.69	94.37 %
2nd Phase	15.27	2.88	14.96	15.73	0.58	39.39	11.19	5.63 %

3.2 AC and DC Electrochemical Corrosion Results on CCAs

Figure 5a reports anodic and cathodic polarization curves in 0.01 M NaCl in E-log(i) format after applying a -1.3 V_{SCE} potential for 600 s to minimize the effect of the native oxide for $Al_{0.3}Cr_{0.5}Fe_2Mn_0Mo_{0.15}Ni_{1.5}Ti_{0.3}$, $Al_{0.3}Cr_{0.5}Fe_2Mn_{0.25}Mo_{0.15}Ni_{1.5}Ti_{0.3}$, $Al_{0.3}Cr_{0.5}Fe_2Mn_{0.5}Mo_{0.15}Ni_{1.5}Ti_{0.3}$, and $Al_{0.3}Cr_{0.5}Fe_2Mn_1Mo_{0.15}Ni_{1.5}Ti_{0.3}$. The dilute solution is utilized to observe the passive range prior to breakdown. The E-log(i) plot for the experimental CCAs is compared to CoCrFeMnNi and 316L stainless steel. The E-log(i) data shows the improved corrosion resistance of $Al_{0.3}Cr_{0.5}Fe_2Mn_{0.25}Mo_{0.15}Ni_{1.5}Ti_{0.3}$ relative to CCAs with both higher and lower Mn contents, evidenced by the lower current density of $Al_{0.3}Cr_{0.5}Fe_2Mn_{0.25}Mo_{0.15}Ni_{1.5}Ti_{0.3}$ in the passive potential domain. The pitting potential of $Al_{0.3}Cr_{0.5}Fe_2Mn_{0.25}Mo_{0.15}Ni_{1.5}Ti_{0.3}$ is comparable to that of 316L and is higher than all other tested CCAs. Current spikes before a sharp increase suggest metastable pitting and passive film breakdown. Overall, the CCAs show generally higher passive current densities than 316L. Both increased current densities in the passive potential domain and more negative zero current potentials of the CCAs relative to 316L suggest that the passive films are less protective on the CCAs thus the alloys are less polarizable. CoCrFeMnNi, which has a significantly higher Mn concentration to 316L, has inferior corrosion resistance despite greater Cr concentration.

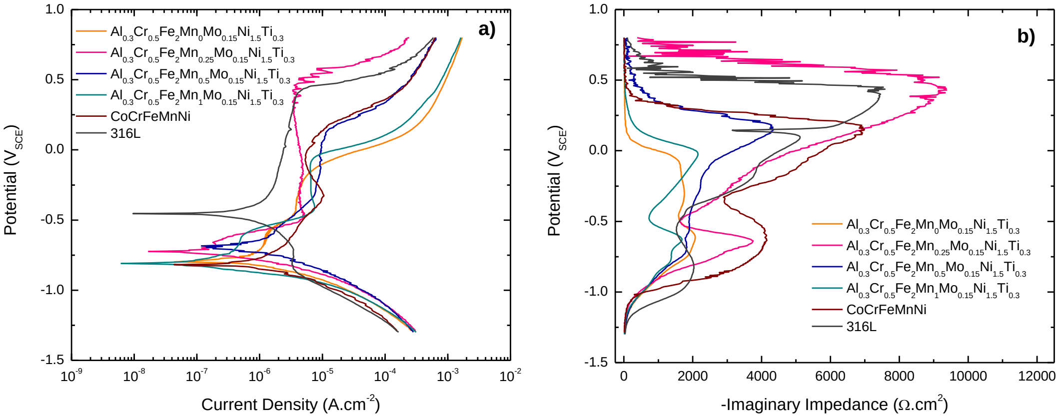

Figure 5: a) E-log(i) curves and **b)** in-situ imaginary impedance measurements obtained during upward polarization of CCAs in 0.01 M NaCl after a 600s application of a -1.3 V_{SCE} potential compared to CoCrFeMnNi and 316L

In-situ Z_{img} measurements (Figure 5b) indicate multiple peaks and generally increase in magnitude throughout the upward potential sweep. The parameter increases at potential below -1.0 V_{SCE} indicative of less noble oxides forming early in the scan. From -0.5 to +0.5 V_{SCE} the change in Z_{img} is linear suggesting oxide thickness is directly proportional to applied potential. This parameter decreases near the pitting potentials with varying degrees of abruptness. Sharp decreases in Z_{img} may indicate the passive film breakdown coinciding with sharp current spikes in current in the E-log(i) plots. It should be noted that the Z_{img} of $Al_{0.3}Cr_{0.5}Fe_2Mn_{0.25}Mo_{0.15}Ni_{1.5}Ti_{0.3}$ is greater than all other CCAs, CoCrFeMnNi, and 316L at most potentials, which may indicate the formation of a relatively thicker and/or more corrosion resistant passive film with different composition and dielectric constant.

The corrosion products formed during electrochemical measurement are generally translucent and either grey or colorless. Pitting is the most prevalent form of corrosion damage visible and is suggested to be the primary cause of passive film breakdown. Significant crevice corrosion was not visible at the sample-epoxy interface. Pitting occurs over the entire surface of the sample; however, a cluster of large pits is frequently seen in the center of the sample.

The cyclic polarization scans (Figure 6) show a similar repassivation potential to 316L, defined where current densities return to levels lower than the passive current, during the downward scan of $Al_{0.3}Cr_{0.5}Fe_2Mn_{0.25}Mo_{0.15}Ni_{1.5}Ti_{0.3}$ relative to 316L. The lower current densities in the downward scan and higher repassivation potential suggest improved repassivation in $Al_{0.3}Cr_{0.5}Fe_2Mn_{0.25}Mo_{0.15}Ni_{1.5}Ti_{0.3}$ relative to 316L. $Al_{0.3}Cr_{0.5}Fe_2Mn_{0.25}Mo_{0.15}Ni_{1.5}Ti_{0.3}$ has a higher repassivation potential than all other CCAs, further justifying it as the most corrosion resistant CCA evaluated. Similar to $Al_{0.3}Cr_{0.5}Fe_2Mn_{0.25}Mo_{0.15}Ni_{1.5}Ti_{0.3}$ and

316 L, a positive hysteresis is present in the downward polarization scans of all other tested alloys (not shown). The pitting, repassivation, and zero current potentials determined from polarization in 0.01 M NaCl are given in Figure 7 and Table IV, which enable comparison of the corrosion resistance between CCAs as a function of Mn content. The pitting potentials decrease with increased Mn content beyond 5 at. %, which suggest poor corrosion resistance for the high Mn CCAs. Trends in the zero current potential are not as prominent, partially attributable to the inconsistency of $Al_{0.3}Cr_{0.5}Fe_2Mn_{0.5}Mo_{0.15}Ni_{1.5}Ti_{0.3}$ results. Interestingly, both the highest and lowest Mn concentrations show the lowest pitting, zero current, and repassivation potentials in 0.01 M NaCl, suggesting the presence of an optimal Mn concentration between the extremes.

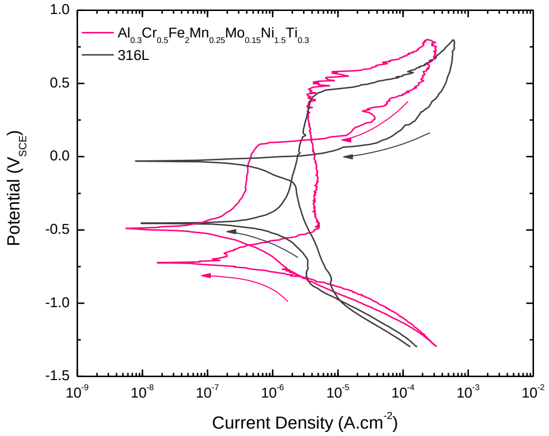

Figure 6: E-log(i) curves of cyclic polarization of $Al_{0.3}Cr_{0.5}Fe_2Mn_{0.25}Mo_{0.15}Ni_{1.5}Ti_{0.3}$ and 316L in 0.01 M NaCl. Scan direction is indicated by arrows.

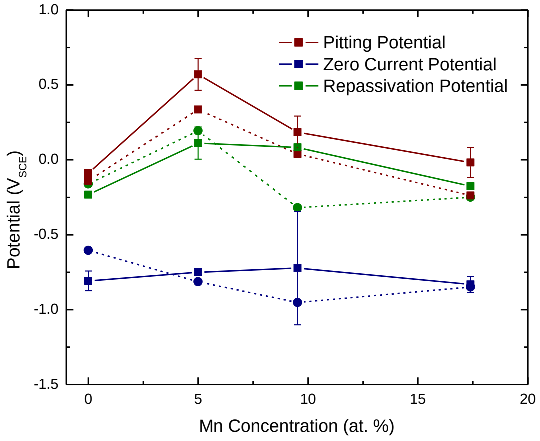

Figure 7: Pitting, zero current, and repassivation potentials measured during polarization of the CCAs in 0.01 M NaCl. Error bars correspond to one standard deviation from the indicated potentials. The pitting, zero current, and repassivation potentials in 0.1 M NaCl indicated by dashed lines are provided for comparative purposes.

Table IV: Pitting (E_{pit}), repassivation (E_{rep}), and zero current ($E_{i=0}$) potentials of the CCAs polarized in 0.01 M NaCl both directly after a 600s cathodic reduction at -1.3 V_{SCE} and bypassing the treatment to characterize the air-formed oxide. The indicated current densities, i(E = -0.25 V_{SCE}), were obtained within the passive range during polarization.

	Post-reduction Solution Formed Oxide				**Air-formed Oxide**		
Alloy	**E_{pit} (V_{SCE})**	**E_{rep} (V_{SCE})**	**$E_{i=0}$ (V_{SCE})**	**i(E = -0.25 V_{SCE}) (μA.cm^{-2})**	**E_{pit} (V_{SCE})**	**E_{rep} (V_{SCE})**	**$E_{i=0}$ (V_{SCE})**
$Al_{0.3}Cr_{0.5}Fe_2Mn_0Mo_{0.15}Ni_{1.5}Ti_{0.3}$	-0.188	-0.227	-0.797	4.69	N/A	-0.149	-0.253
$Al_{0.3}Cr_{0.5}Fe_2Mn_{0.25}Mo_{0.15}Ni_{1.5}Ti_{0.3}$	0.464	0.117	-0.720	4.51	0.749	0.300	-0.166
$Al_{0.3}Cr_{0.5}Fe_2Mn_{0.5}Mo_{0.15}Ni_{1.5}Ti_{0.3}$	0.276	0.076	-0.354	2.90	0.453	0.151	-0.196
$Al_{0.3}Cr_{0.5}Fe_2Mn_1Mo_{0.15}Ni_{1.5}Ti_{0.3}$	-0.049	-0.172	-0.802	6.68	N/A	-0.290	-0.181
CoCrFeMnNi	0.069	-0.125	-0.819	8.45	0.263	-0.292	-0.299
316L	0.403	0.004	-0.455	1.71	0.396	0.060	-0.134

Electrochemical response in a more concentrated Cl^- environments was evaluated by potentiodynamic polarization in 0.1 M NaCl (Figure 8). Similar E-log(i) trends and effects of Mn are observed as those obtained from polarization in 0.01 M NaCl (Figure 7). The increase in Cl^- concentration decreases pitting potential from those obtained in 0.01 M NaCl. A grey or gold corrosion product slightly more opaque than when formed 0.01 M NaCl is visible after polarization. $Al_{0.3}Cr_{0.5}Fe_2Mn_{0.25}Mo_{0.15}Ni_{1.5}Ti_{0.3}$ has the highest pitting potential of all alloys, similar to the results observed in 0.01 M NaCl. At low potentials, however, $Al_{0.3}Cr_{0.5}Fe_2Mn_0Mo_{0.15}Ni_{1.5}Ti_{0.3}$ and CoCrFeMnNi both have lower current densities and higher Z_{img} values than $Al_{0.3}Cr_{0.5}Fe_2Mn_{0.25}Mo_{0.15}Ni_{1.5}Ti_{0.3}$. The correlation between passive current density and Mn content is more prominent in 0.1 M NaCl than in 0.01 M NaCl. In 0.1 M NaCl pH 4 solution, similar qualitative trends were observed (Figure 9). Passive film breakdown occurred in the form of pitting with limited crevice corrosion. The three CCAs with Mn concentrations below 10 at. % showed similar breakdown potentials, while a decrease with higher Mn concentration, confirming trends established in neutral solutions. The Z_{img} component during polarization was significantly lower across most potentials for the oxide film grown in pH 4 than those grown in neutral solutions or formed during exposure to air. It should be noted that the highest Mn containing alloys all had a low Z_{img} at 0 V_{SCE}.

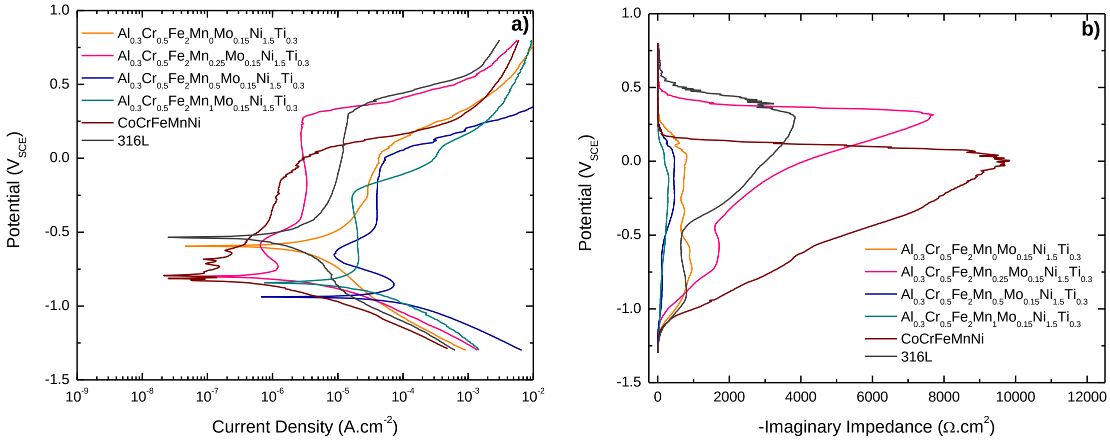

Figure 8: a) E-log(i) curves and **b)** in-situ imaginary impedance measurements obtained during upward polarization of CCAs in 0.1 M NaCl after a 600s application of a -1.3 V_{SCE} potential

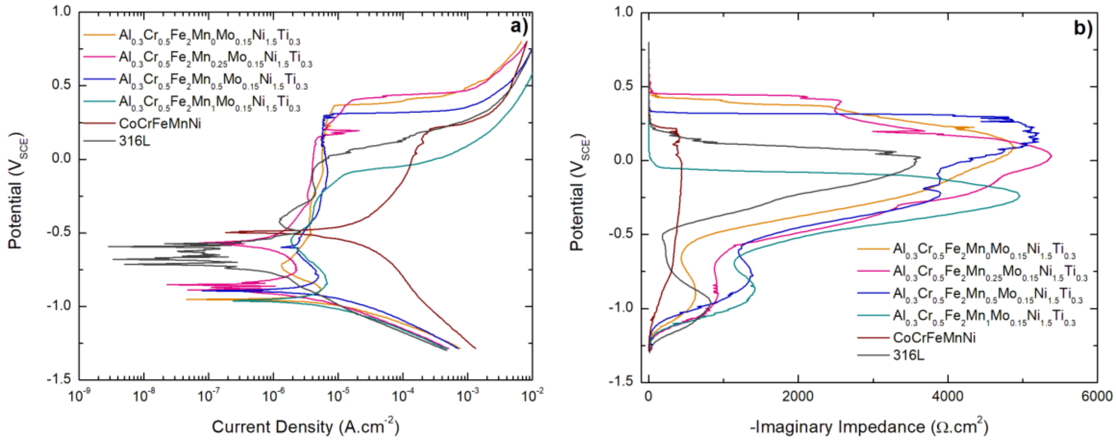

Figure 9: a) E-log(i) curves and **b)** in-situ imaginary impedance measurements obtained during upward polarization of CCAs in 0.1 M NaCl pH 4 after a 600s application of a -1.3 V_{SCE} potential

Figure 10 shows polarization curves in 0.01 M NaCl intended to characterize the corrosion resistance of natural oxide films formed by air exposure directly after grinding. Polarization curves of the air-formed oxides obtained after exposure to open circuit corrosion for 1800 s show similar trends as those after reduction at -1.3 V_{SCE}. $Al_{0.3}Cr_{0.5}Fe_2Mn_{0.25}Mo_{0.15}Ni_{1.5}Ti_{0.3}$ shows a higher pitting potential that is over 0.35 V above that of 316L and is higher than all other CCAs. The Z_{img} of $Al_{0.3}Cr_{0.5}Fe_2Mn_0Mo_{0.15}Ni_{1.5}Ti_{0.3}$, $Al_{0.3}Cr_{0.5}Fe_2Mn_1Mo_{0.15}Ni_{1.5}Ti_{0.3}$, and CoCrFeMnNi continuously decreases with increasing potential, suggesting oxide instability in the solution, whereas it sharply decreases at the breakdown potentials in $Al_{0.3}Cr_{0.5}Fe_2Mn_{0.25}Mo_{0.15}Ni_{1.5}Ti_{0.3}$ and 316L. Weakening and/or partial breakdown of the air-formed oxide may occur on some alloys during initial exposure to the solution with no applied potential, as OCP decreases during the 1800 s measurement prior to polarization for $Al_{0.3}Cr_{0.5}Fe_2Mn_0Mo_{0.15}Ni_{1.5}Ti_{0.3}$,

$Al_{0.3}Cr_{0.5}Fe_2Mn_1Mo_{0.15}Ni_{1.5}Ti_{0.3}$, and CoCrFeMnNi. In contrast, OCP increases for $Al_{0.3}Cr_{0.5}Fe_2Mn_{0.25}Mo_{0.15}Ni_{1.5}Ti_{0.3}$, $Al_{0.3}Cr_{0.5}Fe_2Mn_{0.5}Mo_{0.15}Ni_{1.5}Ti_{0.3}$, and 316L (not shown).

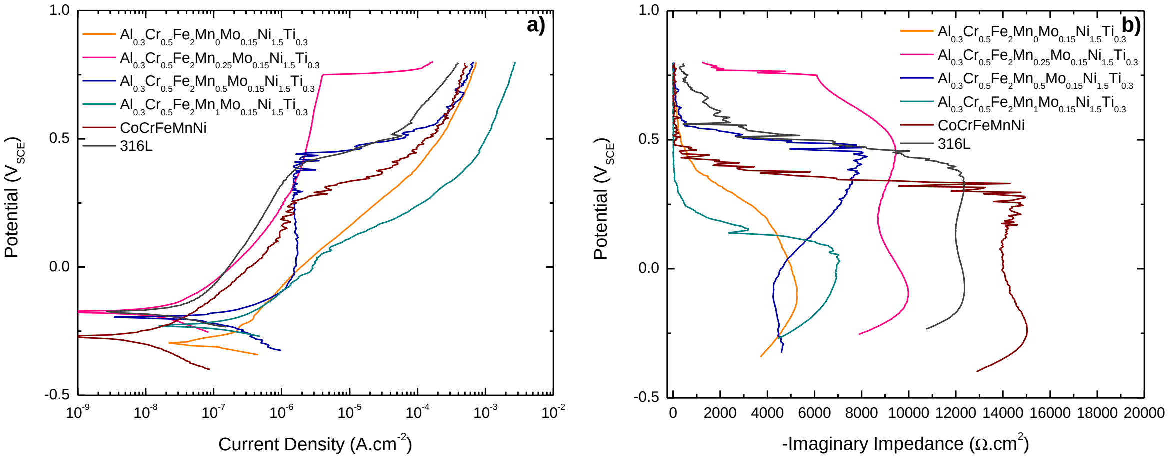

Figure 10: a) E-log(i) polarization curves and **b)** in-situ impedance measurements obtained during polarization in 0.01 M NaCl directly after open circuit monitoring of the air-formed oxide

The effect of Mn on pitting potential is more obvious in air-formed oxides than those formed after a reduction treatment in the same solution. Additionally, both the zero current and repassivation potentials of $Al_{0.3}Cr_{0.5}Fe_2Mn_{0.25}Mo_{0.15}Ni_{1.5}Ti_{0.3}$ are greater than the other CCAs, with both potentials decreasing in CCAs with increased Mn content beyond 5 at. % (Figure 11). Figure 12 shows the maximum Z_{img} measured in-situ during polarization. In both the oxide formed after a cathodic treatment and the air formed oxide, $Al_{0.3}Cr_{0.5}Fe_2Mn_{0.25}Mo_{0.15}Ni_{1.5}Ti_{0.3}$ has the highest maximum Z_{img} with the magnitude decreasing with increased Mn concentration.

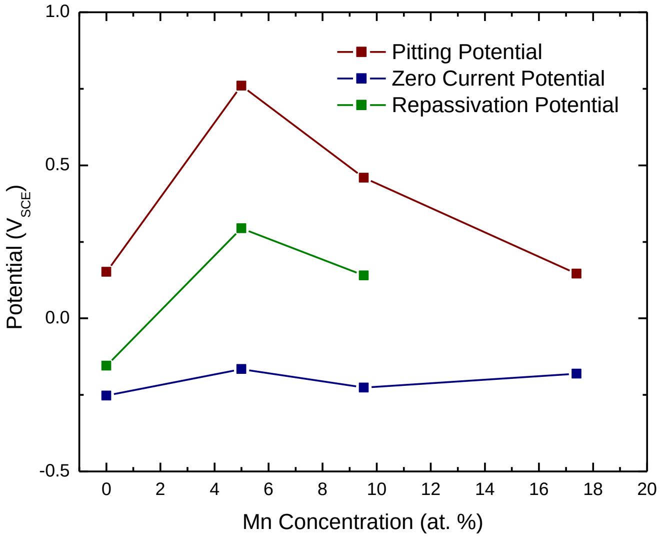

Figure 11: Pitting, zero current, and repassivation potentials measured during polarization in 0.01 M NaCl directly after open circuit monitoring of the air-formed oxide. A repassivation potential could not be defined for $Al_{0.3}Cr_{0.5}Fe_2Mn_1Mo_{0.15}Ni_{1.5}Ti_{0.3}$ as the downward scan current density never reestablished as lower than the upward scan current density for any given potential.

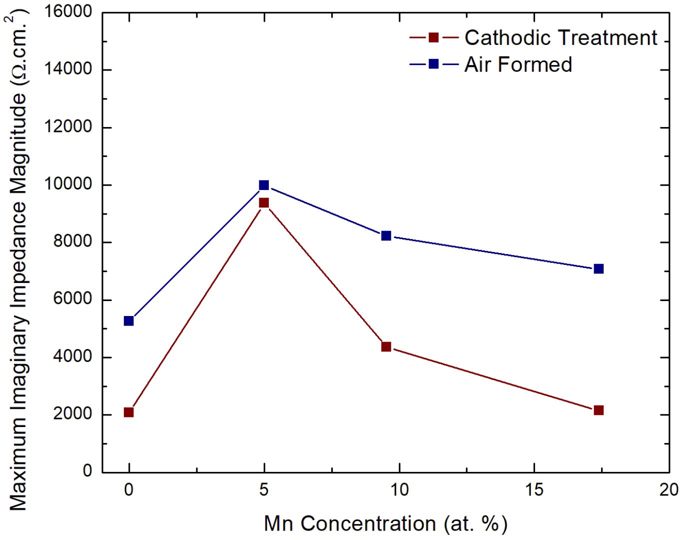

Figure 12: Maximum imaginary components measured in-situ at 1 Hz during polarization of post-cathodic treatment and air-formed oxides in 0.01 M NaCl.

Figure 13 reports the current density (i) (Figure 13a) and Z_{img} (Figure 13b) during oxide growth with an applied potential of -0.25 V_{SCE} for 40 ks in 0.01 M NaCl. As the potential is applied directly after a -1.3 V_{SCE} treatment, the oxide is assumed to be passivated on a reduced metal surface. During the potentiostatic measurement, decreases in current density between 10 and 1000 s are indicative of a growing passive film. Discerning oxide growth before 10 s is difficult as the time range approaches the impedance recording period of 6 s per measurement. In $Al_{0.3}Cr_{0.5}Fe_2Mn_{0.25}Mo_{0.15}Ni_{1.5}Ti_{0.3}$ and $Al_{0.3}Cr_{0.5}Fe_2Mn_1Mo_{0.15}Ni_{1.5}Ti_{0.3}$, the reaction undergoes a transition from cathodic to anodic, indicated by the sharp drop on the log i vs. log t plot as i approaches zero. At the transition, the current direction changes from positive to negative. Z_{img} increases over the same time and then levels off suggesting a limiting film thickness.

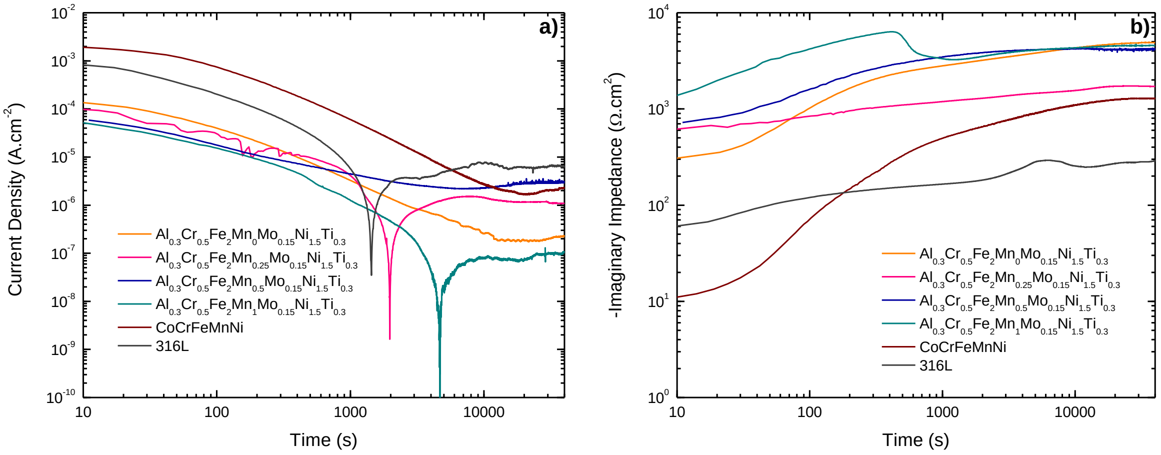

Figure 13: a) Current density and **b)** the imaginary impedance component measured in-situ at 1 Hz during the application of a -0.25 V_{SCE} potential for 40 ks in 0.01 M NaCl

Potentiostatic EIS was carried out for each alloy at the conclusion of the 40 ks growth period and fit to a Randles' circuit model (Figure 14). Table V shows the polarization resistances and phase shift proposed by circuit fitting. 1 Hz is within the linear capacitive region of the Bode plot for all alloys, validating the selection of the frequency for single frequency EIS characterization. $Al_{0.3}Cr_{0.5}Fe_2Mn_{0.25}Mo_{0.15}Ni_{1.5}Ti_{0.3}$ has the highest polarization resistance, suggesting that this alloy would show the highest corrosion resistance. However, the other CCAs show higher impedance moduli than $Al_{0.3}Cr_{0.5}Fe_2Mn_{0.25}Mo_{0.15}Ni_{1.5}Ti_{0.3}$ in the high frequency domain, including 1 Hz which is consistent with the higher impedance moduli seen approaching 40 ks during single frequency EIS (Figure 13a). $Al_{0.3}Cr_{0.5}Fe_2Mn_0Mo_{0.15}Ni_{1.5}Ti_{0.3}$, $Al_{0.3}Cr_{0.5}Fe_2Mn_{0.5}Mo_{0.15}Ni_{1.5}Ti_{0.3}$, and $Al_{0.3}Cr_{0.5}Fe_2Mn_1Mo_{0.15}Ni_{1.5}Ti_{0.3}$ all have lower polarization resistances and generally lower phase angles compared to $Al_{0.3}Cr_{0.5}Fe_2Mn_{0.25}Mo_{0.15}Ni_{1.5}Ti_{0.3}$. Although high α terms indicate the passive films approach capacitor behavior, deviation from pure capacitive behavior is present. There is no strong correlation between α and Mn content.

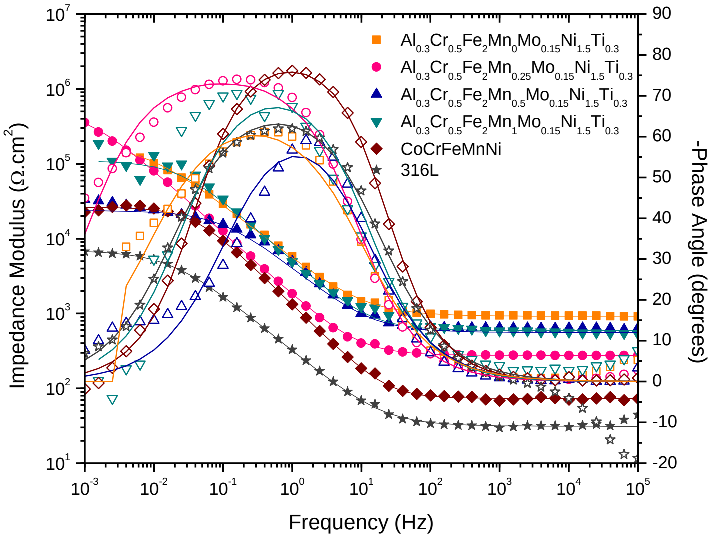

Figure 14: Bode plot obtained in 0.01 M NaCl at -0.25 V_{SCE} for the oxide films grown during the preceding 40 ks potentiostatic hold fit with simplified Randles' circuits

Table V: Polarization resistances and phase shifts (α) determined by circuit model fitting of EIS obtained after a 40 ks exposure to -0.25V_{SCE} in 0.01 M NaCl

Alloy	**Polarization Resistance (Ω.cm^2)**	**α**
$Al_{0.3}Cr_{0.5}Fe_2Mn_0Mo_{0.15}Ni_{1.5}Ti_{0.3}$	188000	0.749
$Al_{0.3}Cr_{0.5}Fe_2Mn_{0.25}Mo_{0.15}Ni_{1.5}Ti_{0.3}$	533000	0.838
$Al_{0.3}Cr_{0.5}Fe_2Mn_{0.5}Mo_{0.15}Ni_{1.5}Ti_{0.3}$	23300	0.787
$Al_{0.3}Cr_{0.5}Fe_2Mn_1Mo_{0.15}Ni_{1.5}Ti_{0.3}$	109000	0.834
CoCrFeMnNi	26200	0.908
316L	116000	0.779

Corrosion performance in short term tests was verified over long exposure periods. During 25-day full immersion in 0.1 M NaCl, the OCP of $Al_{0.3}Cr_{0.5}Fe_2Mn_{0.25}Mo_{0.15}Ni_{1.5}Ti_{0.3}$ rose from -0.358 to -0.283 V_{SCE} while the $Al_{0.3}Cr_{0.5}Fe_2Mn_0Mo_{0.15}Ni_{1.5}Ti_{0.3}$ OCP decreased from -0.022 to -0.253 V_{SCE}. EIS measured at OCP for $Al_{0.3}Cr_{0.5}Fe_2Mn_0Mo_{0.15}Ni_{1.5}Ti_{0.3}$ (Figure 15a) shows impedance modulus (Z_{mod}) generally decreases after a 25-day immersion. A distinct change in the phase angle plot after immersion may suggest the loss of a CPE and a resultant change in oxide film composition or thickness. Contrastingly, $Al_{0.3}Cr_{0.5}Fe_2Mn_{0.25}Mo_{0.15}Ni_{1.5}Ti_{0.3}$ shows similar Z_{mod} and phase angle trends both before and after immersion (Figure 15b), which may suggest increasing stability of the passive film relative to $Al_{0.3}Cr_{0.5}Fe_2Mn_0Mo_{0.15}Ni_{1.5}Ti_{0.3}$. As the presence of Mn is the main compositional difference between the CCAs with other elemental concentrations remaining nearly constant, the increase in Z_{mod} in the low frequency region of $Al_{0.3}Cr_{0.5}Fe_2Mn_{0.25}Mo_{0.15}Ni_{1.5}Ti_{0.3}$ between measurements before and after immersion that was not observed in $Al_{0.3}Cr_{0.5}Fe_2Mn_0Mo_{0.15}Ni_{1.5}Ti_{0.3}$ could be attributed to small additions of Mn. Table

VI shows the mass loss rates obtained during the immersion period. As the recorded mass loss rate for $Al_{0.3}Cr_{0.5}Fe_2Mn_{0.25}Mo_{0.15}Ni_{1.5}Ti_{0.3}$ approaches the precision of the scale, it was reported as trace, however it may be safely considered lower than the rates of all other tested CCAs and comparable to 316L stainless steel. Beyond $Al_{0.3}Cr_{0.5}Fe_2Mn_{0.25}Mo_{0.15}Ni_{1.5}Ti_{0.3}$, the mass loss rate increases with higher Mn concentrations. The lower mass loss rate of $Al_{0.3}Cr_{0.5}Fe_2Mn_{0.25}Mo_{0.15}Ni_{1.5}Ti_{0.3}$ than $Al_{0.3}Cr_{0.5}Fe_2Mn_0Mo_{0.15}Ni_{1.5}Ti_{0.3}$ is consistent with the higher Z_{mod} values for $Al_{0.3}Cr_{0.5}Fe_2Mn_{0.25}Mo_{0.15}Ni_{1.5}Ti_{0.3}$ after 25 days of immersion. Limited pitting was visible on all alloys with some corrosion product present before rinsing. SEM images obtained after immersion (Figure 16) suggest that while pits are present in the matrix, they are more prevalently found near the matrix-second phase interface. Pit growth across the interface into both phases roughly equally makes determination of an initiation site relative to the interface difficult, however, the symmetry of the pit across the interface suggests that initiation may occur at the interface rather than beside it.

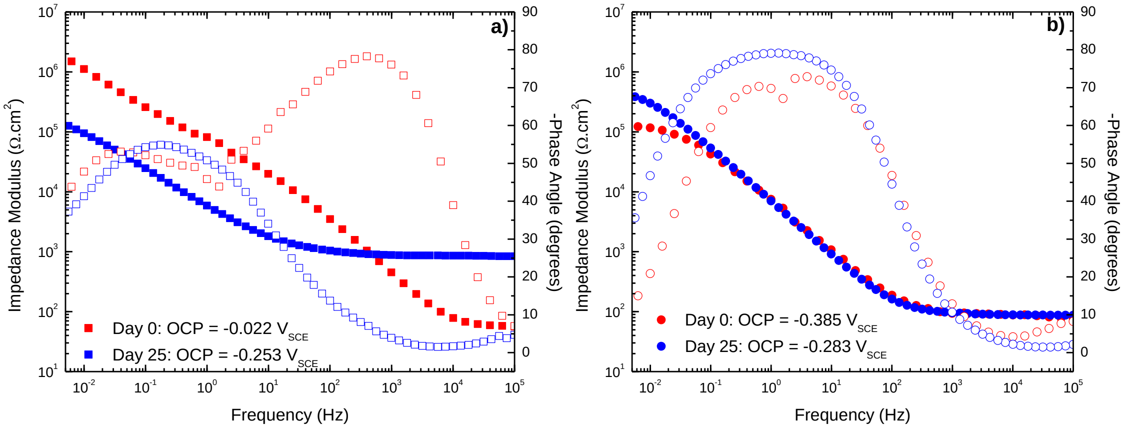

Figure 15: Bode plot of **a)** $Al_{0.3}Cr_{0.5}Fe_2Mn_0Mo_{0.15}Ni_{1.5}Ti_{0.3}$ and **b)** $Al_{0.3}Cr_{0.5}Fe_2Mn_{0.25}Mo_{0.15}Ni_{1.5}Ti_{0.3}$ obtained prior to and directly following 25-day immersion in 0.1 M NaCl. Spectra were measured at the open circuit potentials indicated in the figure legends.

Table VI: Mass loss rates obtained during immersion in 0.1 M NaCl. Mass changes in $Al_{0.3}Cr_{0.5}Fe_2Mn_{0.25}Mo_{0.15}Ni_{1.5}Ti_{0.3}$ and 316L approached the tolerance of the scale and were reported as trace.

Alloy	Mass Loss Rate ($mg.cm^{-2}.year^{-1}$)	Penetration Rate ($\mu m.year^{-1}$)
$Al_{0.3}Cr_{0.5}Fe_2Mn_0Mo_{0.15}Ni_{1.5}Ti_{0.3}$	10.1	13.0
$Al_{0.3}Cr_{0.5}Fe_2Mn_{0.25}Mo_{0.15}Ni_{1.5}Ti_{0.3}$	Trace	Trace
$Al_{0.3}Cr_{0.5}Fe_2Mn_{0.5}Mo_{0.15}Ni_{1.5}Ti_{0.3}$	2.2	2.9
$Al_{0.3}Cr_{0.5}Fe_2Mn_1Mo_{0.15}Ni_{1.5}Ti_{0.3}$	7.8	10.0
CoCrFeMnNi	9.5	11.9
316L	Trace	Trace

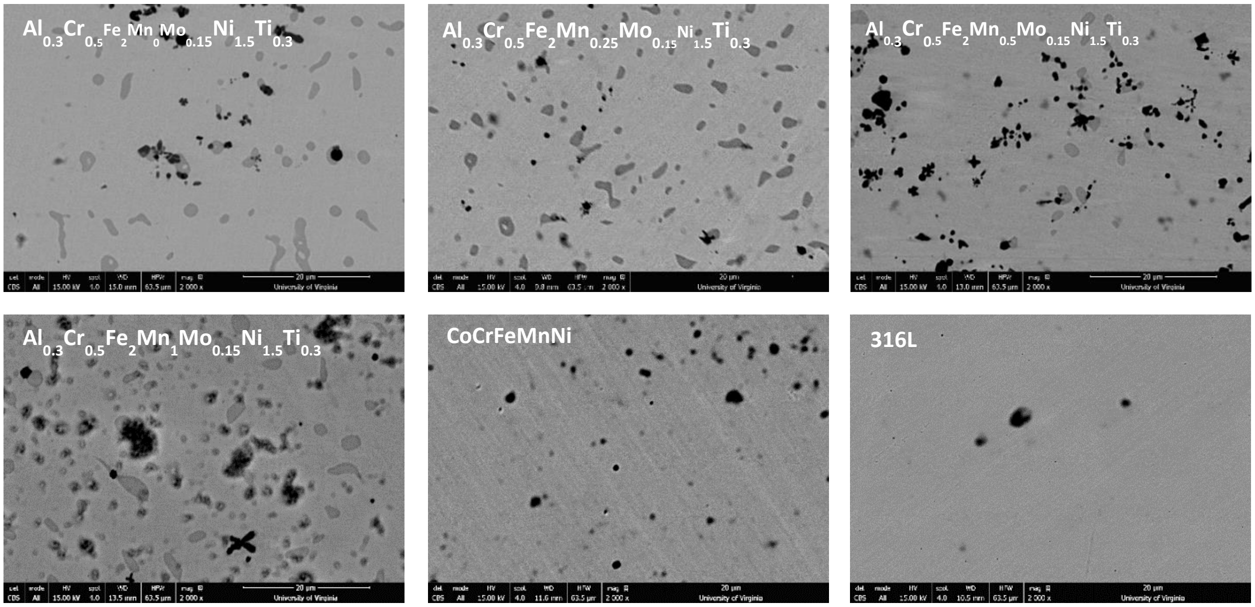

Figure 16: BSE images of CCA pit morphology after immersion in 0.1 M NaCl

3.3 Elemental Dissolution Rates by Atomic Emission Spectroelectrochemistry

Figure 17 reports elemental dissolution currents (j_M) measured by AESEC during open circuit exposure in 0.1 M NaCl pH 4. The breakdown morphologies and potential trends are consistent with those observed in Figure 9 despite changes in the zero current potential from the lack of $N_{2(g)}$ bubbling. Fe and Ni show the highest dissolution rates for all CCAs investigated. Cr initially shows a dissolution rate peak, then decays below the limit for reliable detection, suggesting passivation incorporating Cr^{3+}. Mo, Ti, and Al dissolution rates are below the detection limit. The sum of the elemental dissolution rates detected by AESEC ($\sum j_M$) for $Al_{0.3}Cr_{0.5}Fe_2Mn_{0.25}Mo_{0.15}Ni_{1.5}Ti_{0.3}$ at a near steady state dissolution ($1.8 \pm 1.1\ \mu A/cm^2$) is lower than those of $Al_{0.3}Cr_{0.5}Fe_2Mn_0Mo_{0.15}Ni_{1.5}Ti_{0.3}$ ($2.3 \pm 0.9\ \mu A/cm^2$) and $Al_{0.3}Cr_{0.5}Fe_2Mn_1Mo_{0.15}Ni_{1.5}Ti_{0.3}$

(9.1 ± 2.9 µA/cm^2), which may indicate better corrosion resistance of $Al_{0.3}Cr_{0.5}Fe_2Mn_{0.25}Mo_{0.15}Ni_{1.5}Ti_{0.3}$ during open circuit dissolution despite all three alloys being suggested to possess a Cr-containing protective film. For $Al_{0.3}Cr_{0.5}Fe_2Mn_1Mo_{0.15}Ni_{1.5}Ti_{0.3}$, j_{Mn} is 0.87 ± 0.04 µA/cm^2 at 600 s, close to j_{Fe} and j_{Ni} despite the lower concentration in the alloy. For the $Al_{0.3}Cr_{0.5}Fe_2Mn_{0.25}Mo_{0.15}Ni_{1.5}Ti_{0.3}$, the j_{Mn} at 600 s is only 0.04 ± 0.02 µA/cm^2, approximately 22 times lower than that of the $Al_{0.3}Cr_{0.5}Fe_2Mn_1Mo_{0.15}Ni_{1.5}Ti_{0.3}$.

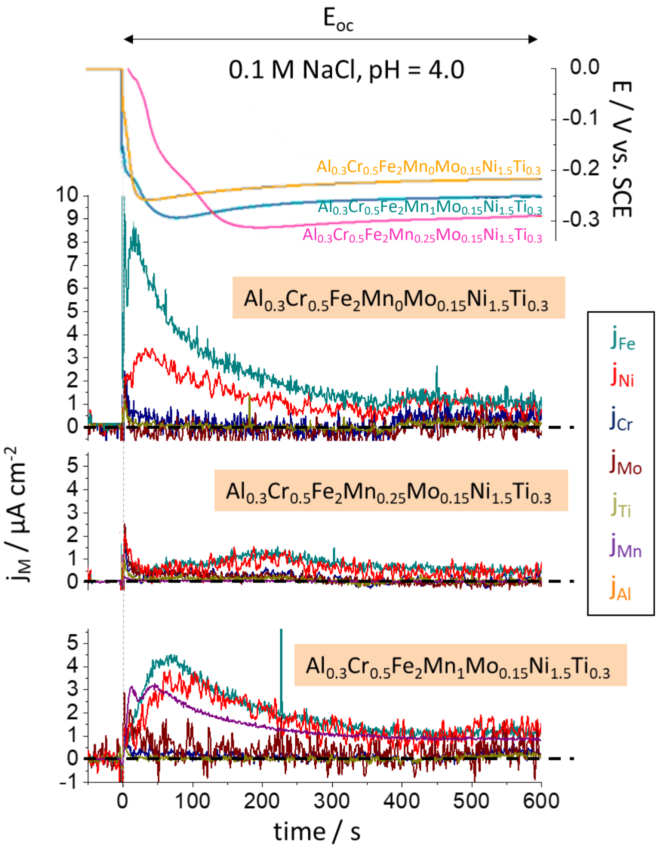

Figure 17: Elemental dissolution rates monitored by AESEC during exposure to open circuit potential of $Al_{0.3}Cr_{0.5}Fe_2Mn_0Mo_{0.15}Ni_{1.5}Ti_{0.3}$, $Al_{0.3}Cr_{0.5}Fe_2Mn_{0.25}Mo_{0.15}Ni_{1.5}Ti_{0.3}$, and $Al_{0.3}Cr_{0.5}Fe_2Mn_{0.25}Mo_{0.15}Ni_{1.5}Ti_{0.3}$ in 0.1 M NaCl pH 4

The Mn dissolution rates measured in-situ during upward polarization performed after a 600 s potential hold at -1.3 V_{SCE} in $Al_{0.3}Cr_{0.5}Fe_2Mn_{0.25}Mo_{0.15}Ni_{1.5}Ti_{0.3}$ and $Al_{0.3}Cr_{0.5}Fe_2Mn_1Mo_{0.15}Ni_{1.5}Ti_{0.3}$ are compared alongside the electron current densities (j_e) in Figure 18. It should be noted that Mn dissolves below the breakdown potential, near 0.0 V_{SCE}, in $Al_{0.3}Cr_{0.5}Fe_2Mn_1Mo_{0.15}Ni_{1.5}Ti_{0.3}$ while Mn dissolution starts from the onset potential of transpassive dissolution for $Al_{0.3}Cr_{0.5}Fe_2Mn_{0.25}Mo_{0.15}Ni_{1.5}Ti_{0.3}$. j_{Mn} for

$Al_{0.3}Cr_{0.5}Fe_2Mn_1Mo_{0.15}Ni_{1.5}Ti_{0.3}$ in both the passive and transpassive domain is approximately 2 orders of magnitude higher than for $Al_{0.3}Cr_{0.5}Fe_2Mn_{0.25}Mo_{0.15}Ni_{1.5}Ti_{0.3}$.

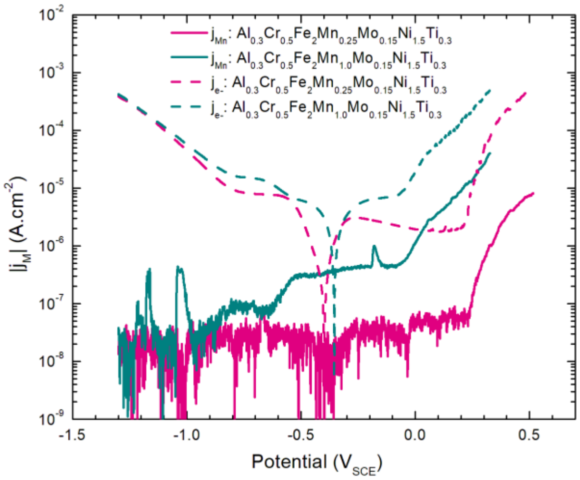

Figure 18: Mn (j_{Mn}) and electron current density (j_e) of $Al_{0.3}Cr_{0.5}Fe_2Mn_{0.25}Mo_{0.15}Ni_{1.5}Ti_{0.3}$ and $Al_{0.3}Cr_{0.5}Fe_2Mn_{1.0}Mo_{0.15}Ni_{1.5}Ti_{0.3}$ alloys monitored by AESEC during potentiodynamic polarization following a 600 s applied potential at -1.3 V_{SCE} in 0.1 M NaCl pH 4

Dissolution currents of $Al_{0.3}Cr_{0.5}Fe_2Mn_{0.25}Mo_{0.15}Ni_{1.5}Ti_{0.3}$ constituent elements monitored at an applied potential of -0.2 V_{SCE} in 0.1 M NaCl pH 4 (Figure 19) are highest for Fe and Ni, where dissolution peaks are visible in the initial several hundreds of seconds. Traditional passivators such as Ti, Cr, Al, and Mo are below the detection limit. Notably, the Mn dissolution rate is significantly below Fe and Ni and is comparable to the passivating elements. The elemental dissolution is reasonably consistent with the thermodynamic prediction at pH 4, -0.2 V_{SCE} shown in Table VII.

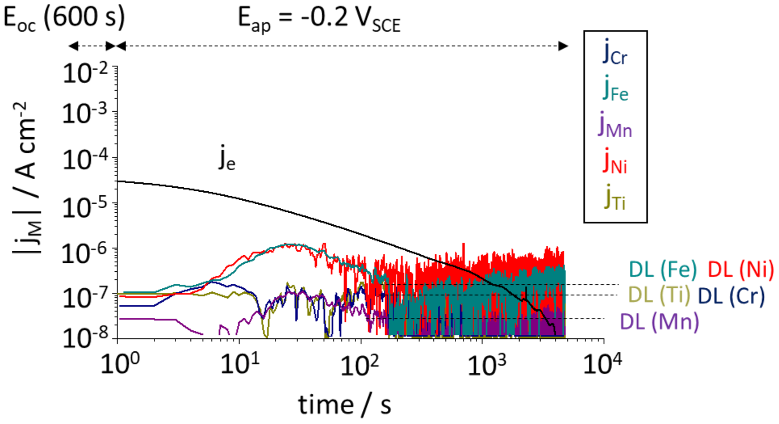

Figure 19: Elemental dissolution rates of $Al_{0.3}Cr_{0.5}Fe_2Mn_{0.25}Mo_{0.15}Ni_{1.5}Ti_{0.3}$ during a 4 ks potentiostatic hold at -0.2 V_{SCE} following a 600 s exposure to open circuit potential in 0.1 M NaCl pH 4. j_e indicates the electron current density. Horizontal dashed lines indicate the detection limit (DL) for each element. j_{Al} and j_{Mo} were below the detection limits and are not plotted.

Table VII: Elemental summary of open circuit dissolution in 0.1 M NaCl at pH 4 monitored by AESEC. Thermodynamically stable species in 0.1 M NaCl pH 4 at 25°C predicted by Hydra Medusa^{TM} software using its default database are provided for comparative purposes.

Alloy		OCP (-0.3 V_{SCE} ~ -0.2 V_{SCE})
$Al_{0.3}Cr_{0.5}Fe_2Mn_0Mo_{0.15}Ni_{1.5}Ti_{0.3}$		Initial Fe, Ni dissolution
$Al_{0.3}Cr_{0.5}Fe_2Mn_{0.25}Mo_{0.15}Ni_{1.5}Ti_{0.3}$		Initial Fe, Ni dissolution
$Al_{0.3}Cr_{0.5}Fe_2Mn_1Mo_{0.15}Ni_{1.5}Ti_{0.3}$		Initial Fe, Ni, Mn dissolution
Thermodynamics (Hydra Medusa)	Soluble	$Cr(OH)^{2+}$, Mn^{2+}, Ni^{2+}, Fe^{2+}, Al^{3+}
	Non soluble	MoO_2(cr), TiO_2(cr)

3.4 Analysis of Passive Film Compositions by XPS

High-resolution XPS spectra obtained after the 40 ks potentiostatic hold experiments (Figure 13) suggest formation of a passive film consisting of both oxides and hydroxides. The XPS spot size encompasses both the matrix and second phase. Selected fits for Ti, Cr, and Al, three important passivating elements, along with crude Mn fits, are shown in Figure 20. Chemically shifted (oxidized atoms) peaks are utilized in the calculation of passive film cation fractions and signal attributable to bulk metal peaks were neglected. In the case of Mo, Al, and Mn, it is possible to see a chemical shift and thus ascertain cation fractions, but it is not feasible to further deconvolute the oxidized or metal peaks where necessary due to low signal and high levels of noise. A crude fit of the Mn $2p_{1/2}$ spectrum at the maximum possible concentration not exceeding XPS signal noise was applied as previously utilized for other CCAs [14]. Any analysis of Mn cation fractions or surface enhancement is intended as an upper bound to a range of possible Mn concentrations.

Cation fractions from the high-resolution spectra are shown in Figure 21 and Table VIII. The passive film of $Al_{0.3}Cr_{0.5}Fe_2Mn_{0.25}Mo_{0.15}Ni_{1.5}Ti_{0.3}$, which exhibits the best corrosion resistance for the alloy system explored herein, is enriched in Ti, Al, and Cr relative to the alloy composition. Ti constitutes the majority of the passive film and may be presumed to be enriched in the passive film formed over the second phase given preferential segregation into the second phase of the microstructure. Al is enriched in the $Al_{0.3}Cr_{0.5}Fe_2Mn_{0.25}Mo_{0.15}Ni_{1.5}Ti_{0.3}$, but not in the $Al_{0.3}Cr_{0.5}Fe_2Mn_{0.25}Mo_{0.15}Ni_{1.5}Ti_{0.3}$ film, possibly due to increasing Al dissolution due to the less protective film. Although all elements are present in both phases, Al, Ni, and Ti are enriched in the second phase while Co, Fe, Mn, and Mo are predominant found in the matrix (Figure 4, Table III).

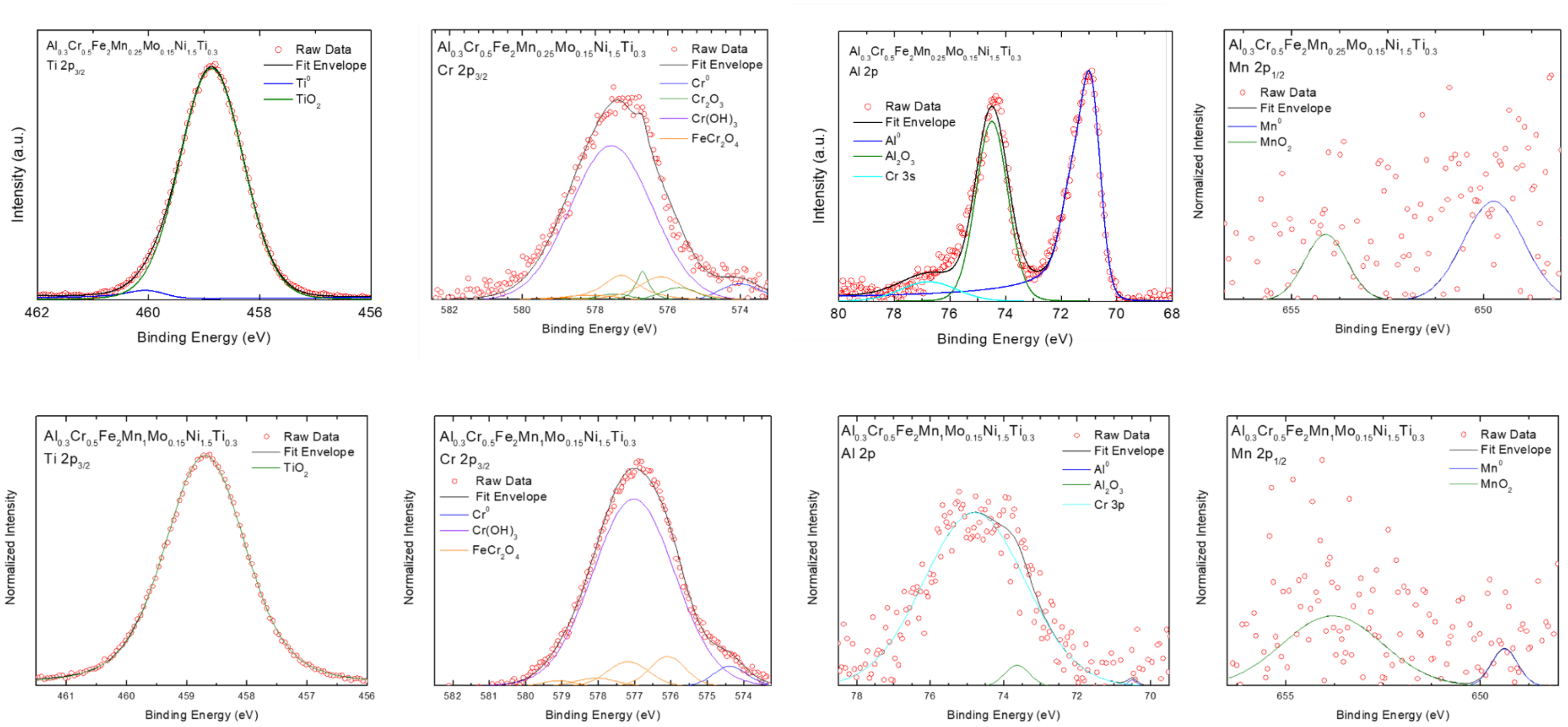

Figure 20: Deconvoluted XPS spectra and fits for key passivating elements and Mn. Intensities are scaled to maximum counts for each spectra as quantitative values may vary due to external factors such as surface contamination.

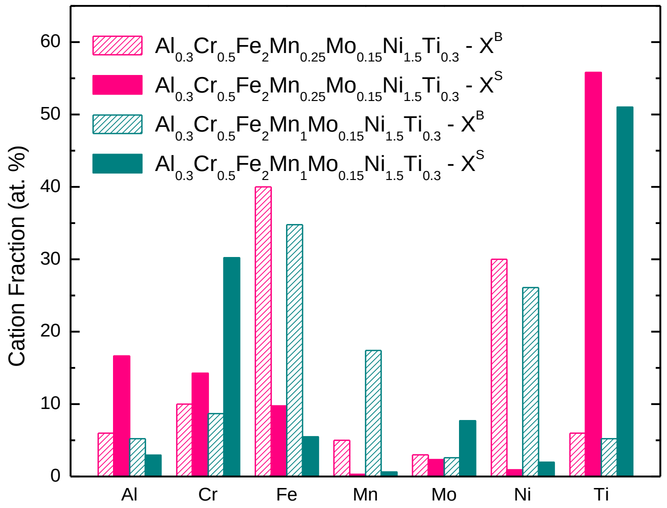

Figure 21: Passivated cation fractions calculated from deconvolution of XPS data. Passivated cation fractions obtained via XPS (X^S) for $Al_{0.3}Cr_{0.5}Fe_2Mn_{0.25}Mo_{0.15}Ni_{1.5}Ti_{0.3}$ and $Al_{0.3}Cr_{0.5}Fe_2Mn_{0.25}Mo_{0.15}Ni_{1.5}Ti_{0.3}$ are compared to their alloy compositions (X^B) to highlight elemental enrichment or depletion in the passive films.

Table VIII: Cation fractions determined by XPS and surface enrichment calculations for each element

Alloy	$Al_{0.3}Cr_{0.5}Fe_2Mn_{0.25}Mo_{0.15}Ni_{1.5}Ti_{0.3}$		$Al_{0.3}Cr_{0.5}Fe_2Mn_1Mo_{0.15}Ni_{1.5}Ti_{0.3}$	
Metal	**X^S (at. %)**	**f**	**X^S (at. %)**	**f**
Al	16.9	2.82	3.0	0.58
Cr	15.5	1.55	30.2	3.47
Fe	9.8	0.25	5.5	0.16
Mn	0.1	0.02	0.6	0.04
Mo	1.9	0.63	7.7	2.95
Ni	1.0	0.03	2.0	0.08
Ti	54.9	9.15	51.0	9.78

In the case of Fe and Cr, a proportion of the spectra is indexed to $FeCr_2O_4$, manually preserving the stoichiometric ratio between normalized intensities. The oxidized species of both Ni and Al are accompanied by significant intensities at binding energies corresponding to elemental zero valence state metal peaks. The high dissolution rates of Fe and Ni observed with AESEC during a potentiostatic hold under similar conditions (Figure 19) may be corelated to the depletion of those elements measured by XPS. Cr and Ti dissolution rates were under the detection limit which supports the notion of the enrichment of Cr and Ti indicated by XPS (Figure 21, Table VIII).

The passive film of $Al_{0.3}Cr_{0.5}Fe_2Mn_1Mo_{0.15}Ni_{1.5}Ti_{0.3}$ is enriched in Ti, Cr, and, at a small ratio, Mo. Unlike in the case of $Al_{0.3}Cr_{0.5}Fe_2Mn_{0.25}Mo_{0.15}Ni_{1.5}Ti_{0.3}$, Al is depleted in the passive film. It should be noted that Mn is suggested to be depleted based on the low XPS signal in both CCAs despite the high bulk content in $Al_{0.3}Cr_{0.5}Fe_2Mn_1Mo_{0.15}Ni_{1.5}Ti_{0.3}$. Elemental fractions for Mn in each CCA's passive film are no greater than 0.1 at. % and 0.6 at. % for $Al_{0.3}Cr_{0.5}Fe_2Mn_{0.25}Mo_{0.15}Ni_{1.5}Ti_{0.3}$ and $Al_{0.3}Cr_{0.5}Fe_2Mn_1Mo_{0.15}Ni_{1.5}Ti_{0.3}$ respectively, suggesting roughly similar depletion factors. Fe is suggested to be present in lower proportions in the passive film of $Al_{0.3}Cr_{0.5}Fe_2Mn_1Mo_{0.15}Ni_{1.5}Ti_{0.3}$ than in the film of $Al_{0.3}Cr_{0.5}Fe_2Mn_{0.25}Mo_{0.15}Ni_{1.5}Ti_{0.3}$. Al and Ti are observed at lower proportions with increased Mn content in the alloy. Contrastingly, the proportions of Cr and Mo cations increase in the $Al_{0.3}Cr_{0.5}Fe_2Mn_1Mo_{0.15}Ni_{1.5}Ti_{0.3}$ spectra. These hint at the importance of Ti, Al, Cr and Mo and show the elusiveness of Mn. Never the less, evidence is strong for the optimization of Mn over several environments and evaluated by 5 different methods.

4.0 Discussion

4.1 Microstructural Aspects Related to Mn

Small additions of Mn are suggested to increase the homogeneity of the microstructure. Although none of the microstructures explored herein is suggested to be single-phase, the increased likelihood of single-phase stability may be quantified with increases in configurational entropy and decreases in the average radius mismatch. Both the Ω indicator proposed by Zhang [6] and the Φ indicator proposed by King [4] increase with Mn content (Table II). Single-phase stability is predicted for all CCAs by Ω and ΔS_{mix} terms but the high enthalpy of mixing between Ti and Ni keeps the Φ term below King's proposed threshold. [4] A high lattice mismatch term likely prevents complete solubility, as δ is still above the 4.7% threshold proposed by Feng [1] for all CCAs, which likely causes phase segregation as single-phase CCAs typically satisfy both thermodynamic indicator and δ thresholds [1]. Phase contrast was observed with Mn concentrations approaching 20 at. %, validating calculations suggesting a Mn concentration of over 75 at. %, well outside the feasible range for corrosion resistant design, would be necessary to obtain a δ value below 4.7%. Although the single-phase stability predicted by CALPHAD modeling in Figure 2 was not observed experimentally, the widening temperature range of the single-phase FCC region may suggest increased stability of the FCC phase with increasing Mn concentration below 20 at.%.

Although multiple phases are present, EDS suggests the CCAs with higher Mn concentration have improved compositional homogeneity (Figure 4, Table III). Most noticeably, the ratio of Ti concentration in the second phase relative to the matrix is generally lower in alloys containing Mn. A decreased concentration gradient between the matrix and the second phase may minimize local chemical heterogeneity, particularly near the interface where pits often form (Figure 15). Given that Ti is suggested by XPS to play a key role in passivation, the effect may contribute to vulnerability to localized corrosion with the chemical heterogeneity and structural disorder contributing to a susceptible site.

Even though Mn promotes homogeneous distribution of passivating elements, it has its own detrimental effects as an oxide film former. Mn_2O_3 in Fe-Mn alloys and elsewhere is forms an unprotective oxide marked by fast ionic transport rates and internal voiding during oxidation. Poor corrosion resistance is seen in many binary alloys [74]. Instability of Mn in the passive films may be driven in part by the low solubility of Mn oxides with other oxides including Al_2O_3 and Cr_2O_3 [15]. This accounts for the poor polarization resistance in high Mn alloys assuming Mn oxides form, which is addressed below.

4.2 Thermodynamic Aspects of Oxides Formed on Al-Cr-Fe-Mn-Mo-Ni-Ti Alloys

The high number of constituent elements greatly increases the range of oxide species that may be thermodynamically stable. Three types of oxides are possible: kinetically limited solute captured, thermodynamically stable solid solutions and specific stoichiometric oxides such as spinels. Ni, Mo, and Mn were not found in oxides in high enough cation fraction to accommodate spinels given to preserve stoichiometric ratios. Other specific oxides that can not be ruled out based on thermodynamic stability include but are not limited to $FeCr_2O_4$, $Cr_2Ti_2O_7$, $TiAl_2O_5$, and $TiFeO_3$ [75]. Each metal may passivate in multiple potential valence states, leading to a wide range in potential species. Furthermore, interaction with water also introduces the possibility of forming hydroxide or oxyhydroxide species. In addition to differences in free energy of formation, the stable oxide for a given metal may be altered by the local activity of oxygen.

The predicted oxide stoichiometry, as suggested by the lowest free energy of formation for each metal in the system is Al_2O_3, Cr_2O_3, Fe_2O_3, Mn_3O_4, MoO_2, NiO, and TiO_2 [76]. Such insoluble oxide species are present in the potential-pH diagrams for all pure elements found in the tested alloys, though applied potential and solution environment may alter the most thermodynamically stable species and often are not proposed to be the stable species under the tested conditions [77].

Although the formation energy of Mn_3O_4 (-197.7 kJ/mol) is more negative than that of Mn_2O_3 (-194.2 kJ/mol), MnO_2 (-174.2 kJ/mol), and MnO (-190.4 kJ/mol), the similar magnitudes suggest the prevailing oxide species may vary by environment [76]. The potential-pH diagram suggests applied potential ranges for the stability of Mn_3O_4, Mn_2O_3, and MnO_2 depend on the potential along with $Mn(OH)_2$ [78]. Mn may also be a constituent in multi-element oxides. Although there are multiple possible ordered tertiary oxides that could be thermodynamically stable, the low concentrations of Mn in both the bulk alloy and in the passive film make the formation of such compounds unlikely. Therefore, limited Mn solubility in other oxide structures or trapping near the interface may be more likely than a defined Mn oxide or possibly beneficial Mn-containing tertiary oxide such as Mn_3O_4, $MnFe_2O_4$ or $MnAl_2O_4$.

4.3 Experimental Validation and Kinetic Limitations

While thermodynamic predictions may determine the most energetically favorable oxide structure, such predictions are often not reliable in experimental settings, particularly given the complications of a seven-element alloy space. Through combinations of XPS characterization of the passive film and AESEC characterization of the dissolution rates, the fate of individual elements during the passivation process may be determined. Each alloy and phase subcomponent may contain similar concentrations of passivating elements Cr, Ti, and Al (Tables I, III) yet corrosion performance is distinctly dependent on Mn. Changes in the enrichment of individual element between the CCAs help elucidate the effect of Mn concentration on the elements and their role in corrosion resistance. A complexity here is the accounting for the oxide formed over two phases, where Mn concentration affects the degree of partitioning between an Al, Ti, Ni phase and the matrix enriched in Cr, Mo, and Fe. The Ti enrichment factor in the $Al_{0.3}Cr_{0.5}Fe_2Mn_1Mo_{0.15}Ni_{1.5}Ti_{0.3}$ passive film is slightly lower than in $Al_{0.3}Cr_{0.5}Fe_2Mn_{0.25}Mo_{0.15}Ni_{1.5}Ti_{0.3}$ and is compensated by increasing Cr passivation (Figure 21, Table VIII). Corrosion resistance may be enhanced by having a key passivating element, either Cr or Ti, enriched in both the matrix and second phase regions of the microstructure.

Within the $Al_{0.3}Cr_{0.5}Fe_2Mn_xMo_{0.15}Ni_{1.5}Ti_{0.3}$ system, the optimal Mn concentration for corrosion resistance is suggested to be near 5 at. %. Compositions above 5 at. % Mn may decrease corrosion resistance, but do not leave the alloys as vulnerable to corrosion as compositions near 20 at. %. Therefore, the Mn concentrations can be slightly increased to further decrease alloy cost and density or to target mechanical ductility, however the composition ranges near 25 at. % that have been suggested to be necessary to demonstrate significant twinning induced plasticity in Fe-Mn-Al steels [79] would significantly harm the corrosion resistance of the alloy. Utilizing Mn as a partial replacement for Ni would reduce the alloy density and cost while preserving some of the austenitic stability. However, Mn may not be as effective of an austenitic stabilizer as Ni under many conditions [37] and the corrosion resistance of a CCA series with increasing Mn content and decreasing Ni content remains unexplored.

5.0 Conclusions

Four Al and Ti containing CCAs with varying Mn contents were synthesized and evaluated for corrosion resistance. All CCAs possessed a two-phase microstructure with Al, Ni, and Ti enriched in the second phase. Mn had similar concentrations across both phases and was the only element not significantly enriched or depleted in the second phase. Furthermore, the CCAs with Mn tended to have lower magnitudes of compositional difference between phases than the CCA without, potentially affecting the formation of pitting sites. In dilute chloride solutions, adding 5 at. % Mn increased pitting and repassivation potentials and improved overall corrosion resistance of the oxide films formed on reduced metal surfaces, challenging traditional intuition that suggests completely avoiding Mn. Similar trends were verified with increased chloride concentrations and by evaluating the air-formed passive layer. In a CCA with a high Mn concentration, the dissolution rates of both Mn and other constituent elements increased, and overall corrosion resistance decreased. Thus, while small amounts of Mn may improve corrosion resistance from their effects on the composition of each phase, high concentrations are shown to harm overall corrosion resistance. Both Ti and Cr appear to play key roles in passivation based upon their surface enrichment, although the structure of the complex oxide remains undetermined. Mn was significantly depleted from the passive films. Similar intuition may be utilized for the optimization of Mn in other CCA systems containing Al and Ti as the alloy space grows in prominence with the increasing demand for low cost, lightweight CCAs.

Acknowledgments

This work was supported by the U.S. Office of Naval Research through award #N00014-19-1-2420 under the directorship of Dr. Airan Perez. Author K. Ogle and the AESEC experiments were supported by the Agence Nationale de Recherche, grant # ANR-20-CE08-0031 (Tapas 2020). Utilization of the PHI VersaProbe III$^{\text{TM}}$, Quanta 650 SEM$^{\text{TM}}$, and Empyrean X-ray Diffractometer$^{\text{TM}}$ within the UVA Nanoscale Materials Characterization Facility (NMCF) was fundamental to the completion of this work. The PHI VersaProbe III$^{\text{TM}}$ system was supported by NSF Award #162601.

References

[1] R. Feng, C. Lee, M. Mathes, T.T. Zuo, S. Chen, J. Hawk, Y. Zhang, P. Liaw, Design of Light-Weight High-Entropy Alloys, Entropy, 18 (2016) 333.
[2] J. Qi, A.M. Cheung, S.J. Poon, High Entropy Alloys Mined From Binary Phase Diagrams, Scientific Reports, 9 (2019) 15501.
[3] D.B. Miracle, O.N. Senkov, A critical review of high entropy alloys and related concepts, Acta Materialia, 122 (2017) 448-511.
[4] D.J.M. King, S.C. Middleburgh, A.G. McGregor, M.B. Cortie, Predicting the formation and stability of single phase high-entropy alloys, Acta Materialia, 104 (2016) 172-179.
[5] A. Miedema, Simple model for alloys, Philips Tech. Rev, 33 (1973) 149-160.
[6] X. Yang, Y. Zhang, Prediction of high-entropy stabilized solid-solution in multi-component alloys, Materials Chemistry and Physics, 132 (2012) 233-238.
[7] J. Qi, A.M. Cheung, S.J. Poon, Navigating the Complex Compositional Landscape of High-Entropy Alloys, 2021.
[8] E. Menou, F. Tancret, I. Toda-Caraballo, G. Ramstein, P. Castany, E. Bertrand, N. Gautier, P.E.J. Rivera Díaz-Del-Castillo, Computational design of light and strong high entropy alloys (HEA): Obtainment of an extremely high specific solid solution hardening, Scripta Materialia, 156 (2018) 120-123.
[9] C. Varvenne, A. Luque, W.A. Curtin, Theory of strengthening in fcc high entropy alloys, Acta Materialia, 118 (2016) 164-176.
[10] P. Lu, J.E. Saal, G.B. Olson, T. Li, O.J. Swanson, G.S. Frankel, A.Y. Gerard, K.F. Quiambao, J.R. Scully, Computational materials design of a corrosion resistant high entropy alloy for harsh environments, Scripta Materialia, 153 (2018) 19-22.
[11] Y. Qiu, M.A. Gibson, H.L. Fraser, N. Birbilis, Corrosion characteristics of high entropy alloys, Materials Science and Technology, 31 (2015) 1235-1243.
[12] Y. Qiu, S. Thomas, M.A. Gibson, H.L. Fraser, N. Birbilis, Corrosion of high entropy alloys, npj Materials Degradation, 1 (2017) 15.
[13] K.F. Quiambao, S.J. McDonnell, D.K. Schreiber, A.Y. Gerard, K.M. Freedy, P. Lu, J.E. Saal, G.S. Frankel, J.R. Scully, Passivation of a corrosion resistant high entropy alloy in non-oxidizing sulfate solutions, Acta Materialia, 164 (2019) 362-376.
[14] A.Y. Gerard, J. Han, S.J. McDonnell, K. Ogle, E.J. Kautz, D.K. Schreiber, P. Lu, J.E. Saal, G.S. Frankel, J.R. Scully, Aqueous passivation of multi-principal element alloy Ni38Fe20Cr22Mn10Co10: Unexpected high Cr enrichment within the passive film, Acta Materialia, 198 (2020) 121-133.
[15] K. Wang, J. Han, A.Y. Gerard, J.R. Scully, B.-C. Zhou, Potential-pH diagrams considering complex oxide solution phases for understanding aqueous corrosion of multi-principal element alloys, npj Materials Degradation, 4 (2020) 35.
[16] Z. Tang, L. Huang, W. He, P.K. Liaw, Alloying and Processing Effects on the Aqueous Corrosion Behavior of High-Entropy Alloys, Entropy, 16 (2014) 895-911.
[17] J.R. Scully, S.B. Inman, A.Y. Gerard, C.D. Taylor, W. Windl, D.K. Schreiber, P. Lu, J.E. Saal, G.S. Frankel, Controlling the corrosion resistance of multi-principal element alloys, Scripta Materialia, 188 (2020) 96-101.
[18] D. Yang, Y. Liu, H. Jiang, M. Liao, N. Qu, T. Han, Z. Lai, J. Zhu, A novel FeCrNiAlTi-based high entropy alloy strengthened by refined grains, Journal of Alloys and Compounds, 823 (2020) 153729.
[19] D.H. Xiao, P.F. Zhou, W.Q. Wu, H.Y. Diao, M.C. Gao, M. Song, P.K. Liaw, Microstructure, mechanical and corrosion behaviors of AlCoCuFeNi-(Cr,Ti) high entropy alloys, Materials & Design, 116 (2017) 438-447.
[20] E. Osei-Agyemang, G. Balasubramanian, Surface oxidation mechanism of a refractory high-entropy alloy, npj Materials Degradation, 3 (2019) 20.

[21] C.P. Lee, C.C. Chang, Y.Y. Chen, J.W. Yeh, H.C. Shih, Effect of the aluminium content of AlxCrFe1.5MnNi0.5 high-entropy alloys on the corrosion behaviour in aqueous environments, Corrosion Science, 50 (2008) 2053-2060.
[22] B.-y. Li, K. Peng, A.-p. Hu, L.-p. Zhou, J.-j. Zhu, D.-y. Li, Structure and properties of FeCoNiCrCu0.5Alx high-entropy alloy, Transactions of Nonferrous Metals Society of China, 23 (2013) 735-741.
[23] Y. Qiu, S. Thomas, D. Fabijanic, A.J. Barlow, H.L. Fraser, N. Birbilis, Microstructural evolution, electrochemical and corrosion properties of AlxCoCrFeNiTiy high entropy alloys, Materials & Design, 170 (2019) 107698.
[24] Y. Shi, L. Collins, R. Feng, C. Zhang, N. Balke, P. Liaw, B. Yang, Homogenization of Al CoCrFeNi high-entropy alloys with improved corrosion resistance, Corrosion Science, 133 (2018) 121-130.
[25] K. Ishikawa, I. Ohnuma, R. Kainuma, K. Aoki, K. Ishida, Phase equilibria and stability of Heusler-type aluminides in the NiAl–Ni2AlTi–Ni2AlY (Y: V, Cr or Mn) systems, Journal of Alloys and Compounds, 367 (2004) 2-9.
[26] D. Choudhuri, T. Alam, T. Borkar, B. Gwalani, A.S. Mantri, S.G. Srinivasan, M.A. Gibson, R. Banerjee, Formation of a Huesler-like L21 phase in a CoCrCuFeNiAlTi high-entropy alloy, Scripta Materialia, 100 (2015) 36-39.
[27] Z.-S. Nong, Y.-N. Lei, J.-C. Zhu, Wear and oxidation resistances of AlCrFeNiTi-based high entropy alloys, Intermetallics, 101 (2018) 144-151.
[28] Y. Shi, L. Collins, N. Balke, P.K. Liaw, B. Yang, In-situ electrochemical-AFM study of localized corrosion of AlxCoCrFeNi high-entropy alloys in chloride solution, Applied Surface Science, 439 (2018) 533-544.
[29] Y. Shi, L. Collins, R. Feng, C. Zhang, N. Balke, P.K. Liaw, B. Yang, Homogenization of AlxCoCrFeNi high-entropy alloys with improved corrosion resistance, Corrosion Science, 133 (2018) 120-131.
[30] B. Cantor, I.T.H. Chang, P. Knight, A.J.B. Vincent, Microstructural development in equiatomic multicomponent alloys, Materials Science and Engineering: A, 375-377 (2004) 213-218.
[31] J.A. Ober, Mineral commodity summaries 2018, in: Mineral Commodity Summaries, Reston, VA, 2018, pp. 204.
[32] S. Singerling, C. Tuck, 2015 Minerals Yearbook, volume I, Metals and Minerals, in: Minerals Yearbook, Reston, VA, 2018, pp. 25.21-25.14.
[33] Y.L. Zhao, T. Yang, J.H. Zhu, D. Chen, Y. Yang, A. Hu, C.T. Liu, J.J. Kai, Development of high-strength Co-free high-entropy alloys hardened by nanosized precipitates, Scripta Materialia, 148 (2018) 51-55.
[34] R.K. Mishra, R.R. Shahi, Phase evolution and magnetic characteristics of TiFeNiCr and TiFeNiCrM (M=Mn, Co) high entropy alloys, Journal of Magnetism and Magnetic Materials, 442 (2017) 218-223.
[35] Y. Deng, C.C. Tasan, K.G. Pradeep, H. Springer, A. Kostka, D. Raabe, Design of a twinning-induced plasticity high entropy alloy, Acta Materialia, 94 (2015) 124-133.
[36] D. Raabe, D. Ponge, O. Dmitrieva, B. Sander, Designing Ultrahigh Strength Steels with Good Ductility by Combining Transformation Induced Plasticity and Martensite Aging, Advanced Engineering Materials, 11 (2009) 547-555.
[37] R.L. Klueh, P.J. Maziasz, E.H. Lee, Manganese as an austenite stabilizer in Fe-Cr-Mn-C steels, Materials Science and Engineering: A, 102 (1988) 115-124.
[38] M.H. Brown, W.B. Delong, Stainless Steels and Other Ferrous Alloys, Industrual and Engineering Chemistry, 39 (1947) 1248-1254.
[39] M.A. Baker, J.E. Castle, The initiation of pitting corrosion at MnS inclusions, Corrosion Science, 34 (1993) 667-682.
[40] Y.S. Zhang, X.M. Zhu, Electrochemical polarization and passive film analysis of austenitic Fe–Mn–Al steels in aqueous solutions, Corrosion Science, 41 (1999) 1817-1833.

[41] S. Fajardo, I. Llorente, J.A. Jiménez, J.M. Bastidas, D.M. Bastidas, Effect of Mn additions on the corrosion behaviour of TWIP Fe-Mn-Al-Si austenitic steel in chloride solution, Corrosion Science, 154 (2019) 246-253.
[42] X.M. Zhu, Y.S. Zhang, Investigation of the Electrochemical Corrosion Behavior and Passive Film for Fe-Mn, Fe-Mn-Al, and Fe-Mn-Al-Cr Alloys in Aqueous Solutions, Corrosion, 54 (1998) 98010003.
[43] J. Bosch, U. Martin, W. Aperador, J.M. Bastidas, J. Ress, D.M. Bastidas, Corrosion Behavior of High-Mn Austenitic Fe–Mn–Al–Cr–C Steels in NaCl and NaOH Solutions, Materials, 14 (2021) 425.
[44] K. Park, H. Kwon, Effects of Mn on the localized corrosion behavior of Fe–18Cr alloys, Electrochimica Acta, 55 (2010) 3421-3427.
[45] J. Yang, J. Wu, C.Y. Zhang, S.D. Zhang, B.J. Yang, W. Emori, J.Q. Wang, Effects of Mn on the electrochemical corrosion and passivation behavior of CoFeNiMnCr high-entropy alloy system in H2SO4 solution, Journal of Alloys and Compounds, 819 (2020) 152943.
[46] H. Torbati-Sarraf, M. Shabani, P.D. Jablonski, G.J. Pataky, A. Poursaee, The influence of incorporation of Mn on the pitting corrosion performance of CrFeCoNi High Entropy Alloy at different temperatures, Materials & Design, 184 (2019) 108170.
[47] K.Y. Tsai, M.H. Tsai, J.W. Yeh, Sluggish diffusion in Co–Cr–Fe–Mn–Ni high-entropy alloys, Acta Materialia, 61 (2013) 4887-4897.
[48] V. Kukshal, A. Patnaik, I.K. Bhat, Effect of Mn on corrosion and thermal behaviour of AlCr1.5CuFeNi2Mnx high-entropy alloys, IOP Conference Series: Materials Science and Engineering, 377 (2018) 012023.
[49] S.-K. Wong, T.-T. Shun, C.-H. Chang, C.-F. Lee, Microstructures and properties of Al0.3CoCrFeNiMnx high-entropy alloys, Materials Chemistry and Physics, 210 (2018) 146-151.
[50] M.J. Kim, J. Kim, Effect of Manganese on the Corrosion Behavior of Low Carbon Steel in 10 wt.% Sulfuric Acid, International journal of electrochemical science, 10 (2015) 6872-6885.
[51] A. Rodriguez, J.H. Tylczak, M. Ziomek-Moroz, Corrosion Behavior of CoCrFeMnNi High-Entropy Alloys (HEAs) Under Aqueous Acidic Conditions, ECS Transactions, 77 (2017) 741-752.
[52] Y. Qiu, R. Liu, T. Gengenbach, O. Gharbi, S. Choudhary, S. Thomas, H.L. Fraser, N. Birbilis, Real-time dissolution of a compositionally complex alloy using inline ICP and correlation with XPS, npj Materials Degradation, 4 (2020) 7.
[53] J. Han, X. Li, A.Y. Gerard, P. Lu, J.E. Saal, G.S. Frankel, K. Ogle, J.R. Scully, Potential Dependent Mn Oxidation and Its Role in Passivation of Ni38Fe20Cr22Mn10Co10 Multi-Principal Element Alloy Using Multi-Element Resolved Atomic Emission Spectroelectrochemistry, Journal of The Electrochemical Society, 168 (2021) 051508.
[54] L. Kjellqvist, M. Selleby, Thermodynamic Assessment of the Fe-Mn-O System, Journal of Phase Equilibria and Diffusion, 31 (2010) 113-134.
[55] L. Kjellqvist, M. Selleby, Thermodynamic assessment of the Cr–Mn–O system, Journal of Alloys and Compounds, 507 (2010) 84-92.
[56] L. Kjellqvist, M. Selleby, Thermodynamic assessment of the Mn–Ni–O system, International Journal of Materials Research, 101 (2010) 1222-1231.
[57] H. Luo, Z. Li, A.M. Mingers, D. Raabe, Corrosion behavior of an equiatomic CoCrFeMnNi high-entropy alloy compared with 304 stainless steel in sulfuric acid solution, Corrosion Science, 134 (2018) 131-139.
[58] H. Xiao, Y. Liu, K. Wang, Z. Wang, T. Hu, T. Fan, L. Ma, P. Tang, Effects of Mn Content on Mechanical Properties of FeCoCrNiMnx ($0 \leq x \leq 0.3$) High-Entropy Alloys: A First-Principles Study, Acta Metallurgica Sinica (English Letters), 34 (2020) 455–464.
[59] J. Qi, A.M. Cheung, S.J. Poon, Navigating the Complex Compositional Landscape of High-Entropy Alloys.
[60] Thermocalc Software Version 2019b TCHEA High-Entropy Alloys v9.1 (accessed 3 August 2020), in.

[61] E. Clementi, D.L. Raimondi, W.P. Reinhardt, Atomic Screening Constants from SCF Functions. II. Atoms with 37 to 86 Electrons, The Journal of Chemical Physics, 47 (1967) 1300-1307.
[62] A. Takeuchi, A. Inoue, Classification of Bulk Metallic Glasses by Atomic Size Difference, Heat of Mixing and Period of Constituent Elements and Its Application to Characterization of the Main Alloying Element, MATERIALS TRANSACTIONS, 46 (2005) 2817-2829.
[63] K. Lutton, K. Gusieva, N. Ott, N. Birbilis, J.R. Scully, Understanding multi-element alloy passivation in acidic solutions using operando methods, Electrochemistry Communications, 80 (2017) 44-47.
[64] B. Hirschorn, M.E. Orazem, B. Tribollet, V. Vivier, I. Frateur, M. Musiani, Constant-Phase-Element Behavior Caused by Resistivity Distributions in Films, Journal of The Electrochemical Society, 157 (2010) C452.
[65] B. Hirschorn, M.E. Orazem, B. Tribollet, V. Vivier, I. Frateur, M. Musiani, Constant-Phase-Element Behavior Caused by Resistivity Distributions in Films, Journal of The Electrochemical Society, 157 (2010) C458.
[66] ASTM G1-03(2017)e1, in: Standard Practice for Preparing, Cleaning, and Evaluating Corrosion Test Specimens, West Conshohocken, PA, 2017.
[67] K. Ogle, Atomic Emission Spectroelectrochemistry: Real-Time Rate Measurements of Dissolution, Corrosion, and Passivation, Corrosion, 75 (2019) 1398-1419.
[68] U.-E. Charles-Granville, C. Liu, J.R. Scully, R.G. Kelly, An RDE Approach to Investigate the Influence of Chromate on the Cathodic Kinetics on 7XXX Series Al Alloys under Simulated Thin Film Electrolytes, Journal of The Electrochemical Society, 167 (2020) 111507.
[69] M.C. Biesinger, L.W.M. Lau, A.R. Gerson, R.S.C. Smart, Resolving surface chemical states in XPS analysis of first row transition metals, oxides and hydroxides: Sc, Ti, V, Cu and Zn, Applied Surface Science, 257 (2010) 887-898.
[70] J. Baltrusaitis, B. Mendoza-Sanchez, V. Fernandez, R. Veenstra, N. Dukstiene, A. Roberts, N. Fairley, Generalized molybdenum oxide surface chemical state XPS determination via informed amorphous sample model, Applied Surface Science, 326 (2015) 151-161.
[71] M.C. Biesinger, B.P. Payne, A.P. Grosvenor, L.W.M. Lau, A.R. Gerson, R.S.C. Smart, Resolving surface chemical states in XPS analysis of first row transition metals, oxides and hydroxides: Cr, Mn, Fe, Co and Ni, Applied Surface Science, 257 (2011) 2717-2730.
[72] L. Wang, D. Mercier, S. Zanna, A. Seyeux, M. Laurent-Brocq, L. Perrière, I. Guillot, P. Marcus, Study of the surface oxides and corrosion behaviour of an equiatomic CoCrFeMnNi high entropy alloy by XPS and ToF-SIMS, Corrosion Science, 167 (2020) 108507.
[73] J.E. Castle, K. Asami, A more general method for ranking the enrichment of alloying elements in passivation films, Surface and Interface Analysis, 36 (2004) 220-224.
[74] S. Sahu, O. Swanson, T. Li, A. Gerard, J. Scully, G. Frankel, Localized Corrosion Behavior of Non-Equiatomic NiFeCrMnCo Multi-Principal Element Alloys, Electrochimica Acta, 354 (2020) 136749.
[75] Thermocalc Software Version 2019b TCFE Steels/Fe-Alloys v9.1 (accessed 3 August 2020), in.
[76] A. Jain, S.P. Ong, G. Hautier, W. Chen, W.D. Richards, S. Dacek, S. Cholia, D. Gunter, D. Skinner, G. Ceder, K.A. Persson, The Materials Project: A materials genome approach to accelerating materials innovation, APL Materials, 1 011002.
[77] T.C. Kaspar, D.K. Schreiber, S.R. Spurgeon, M.E. McBriarty, G.M. Carroll, D.R. Gamelin, S.A. Chambers, Built-In Potential in Fe2O3-Cr2O3 Superlattices for Improved Photoexcited Carrier Separation, Advanced Materials, 28 (2016) 1616-1622.
[78] M. Pourbaix, Atlas of Electrochemical Equilibria in Aqueous Solutions, National Association of Corrosion Engineers, 1974.
[79] O. Grässel, L. Krüger, G. Frommeyer, L.W. Meyer, High strength Fe–Mn–(Al, Si) TRIP/TWIP steels development — properties — application, International Journal of Plasticity, 16 (2000) 1391-1409.

Chapter 5: Passivation and Localized Corrosion Resistance of $Al_{0.3}Cr_{0.5}Fe_2Mo_xNi_{1.5}Ti_{0.3}$ Complex Concentrated Alloys: Effect of Mo Content

This chapter was published in Corrosion Science with coauthors J. Han, J. Qi, M.A. Wischhusen, S. R. Agnew, K. Ogle, and J.R. Scully. The citation for the article is provided below.

S.B. Inman, J. Han, M.A. Wischhusen, J. Qi, S.R. Agnew, K. Ogle, J.R. Scully, Passivation and Localized Corrosion Resistance of Al0.3Cr0.5Fe2MoxNi1.5Ti0.3 Compositionally Complex Alloys: Effect of Mo Content, Corroison Science, 227 (2024) 111692.

Abstract

$Al_{0.3}Cr_{0.5}Fe_2Mo_xNi_{1.5}Ti_{0.3}$ (x = 0, 0.05, 0.15) FCC+$L2_1$ complex concentrated alloys are investigated using electrochemical and surface science methods in 0.1 M Na_2SO_4 and 0.1 M NaCl at pH 4 and 10. Mo is mainly found in the FCC phase and amplifies Al and Ti partitioning. The passive film is enriched in Cr(III), Ti(IV), Mo(IV)/Mo(VI), and (at pH 4) Al(III) with elemental fates tracked during film formation and dissolution. Mo presence does not enhance Cr or Ni passivation, instead promoting Ti(IV). Pitting and repassivation potentials increase at higher Mo concentrations, suggesting improved resistance to localized corrosion often initiated at FCC-$L2_1$ interfaces.

1.0 Introduction

Complex concentrated alloys (CCAs), alloys which contain four or more elements at concentrations above 5 at. %, can have a range of beneficial properties including mechanical strength and corrosion resistance [1-5]. Improved homogeneity of passivating elements is often suggested to limit localized solute depletion that may function as preferential sites for localized corrosion [1, 2].

Light-weight elements, particularly Al and Ti, can impart both corrosion resistance and reduced density when added to CCAs [3, 6]. In particular, passivity may be enhanced by simultaneous presence with Cr in the passive film [7, 8]. However, increased Al and/or Ti concentrations in face centered cubic (FCC) CCAs have been shown to lead to the formation of BCC [6, 9-15], B2 [11, 14, 16], and/or Heusler [6, 17-19] phases, where the second phase regions are enriched in Al, Ti, and often Ni [13, 14, 18, 20]. Interfaces created by such secondary phase formation have been suggested to function as initiation sites for localized corrosion, decreasing overall corrosion resistance despite the thermodynamic stability of Ti and Al oxides[17] [15, 18, 21]. Thus, phase stability issues limit Al and/or Ti concentration, necessitating further alloying additions to limit the effects of microstructural segregation-driven localized corrosion.

Mo has been long established as improving corrosion resistance, most commonly in stainless steels [22, 23]. Although there is no universal agreement for the mechanism behind the contribution of Mo to the corrosion resistance of stainless steels, it is generally accepted as effective in preventing localized corrosion mechanisms such as pitting. Newman suggested Mo, in its non-oxidized state, acts as a corrosion inhibitor in stainless steels [24] while Hashimoto et al. proposed inhibition occurs via a Mo oxyhydroxide layer [25]. Alternatively, Mo has been suggested to be present in the passive films across multiple valences and species [23, 26, 27]. Mo has also been shown to improve repassivation ability and rates in stainless steels and Ni-Cr-Mo alloys [28, 29], potentially due to redeposition after dissolution [30]. Tranchida et al. suggested Mo slows transpassive dissolution rates by doping the Cr oxide film formed on stainless steels and altering the band gap to limit the formation of unstable Cr species [31].

Lutton et al. evaluated alloying Ni-Cr binary alloys with Mo, finding Mo to improve the corrosion resistance and increase the enrichment of Cr in the passive film in acidic and basic NaCl solutions [32]. The phenomena were attributed to a favorable Cr-Mo synergy promoting O adsorption and low concentrations of oxidized Mo acting as a doping agent in the passive film. Lloyd et al. suggested Mo

---

[17] High temperature annealing treatments may limit localized solute depletion, however, two-phase equilibrium microstructures allow individual phases to be depleted of individual passivating elements, increasing the risk of localized corrosion.

addition to Ni-Cr alloys to be most significant at high potentials where Cr(VI) is stable, attributing the beneficial effects of Mo to limitations of Cr-induced transpassivity [33]. Additionally, Mo addition allows for stable oxide formation over grain facets at orientations for which it does not occur on Ni-Cr binaries of the same Cr content [34]. Such Ni-Cr-Mo alloys have been utilized to form a baseline survey of potential mechanisms for the beneficial contributions of Mo to the corrosion resistance of FCC steels and similar alloys [27, 35]. While Mo addition has been suggested to be beneficial for both Fe-Cr and Ni-Cr based alloys, similar effects are not suggested in Cr-free counterparts [23, 36, 37]. For this reason, Mo is considered to have synergetic behavior with Cr.

Alloying benefits of Mo have been shown to extend into CCA microstructures. For example, when alloyed to the Co-Cr-Fe-Ni system, Mo may enhance mechanical strength by acting as a solid solution strengthener [38]. Dai et al. evaluated varying annealing procedures to optimize the mechanical and corrosion resistance of $FeCoCrNiMo_{0.1}$ CCAs [39]. At high Mo concentrations, second phase strengthening is possible though second phase formation in FCC CCAs, in part due to the well-established ferritic stabilization of Mo in conventional Fe alloys. In the $AlCoCrFeNiMo_x$ system, higher Mo concentrations increase strength by forming an eutectic structure with a second phase enriched in Cr, Fe, and Mo [40]. Mo frequently combines with Cr by forming σ or μ intermetallic phases [20, 40-46].

Mo, and its influence on second phase formation, has also been shown to affect the corrosion resistance of CCAs such as those in the Co-Cr-Fe-Mn-Ni system [7, 20, 37, 39, 41, 42, 46-48] pioneered by Cantor et al. [49]. Niu et al. showed increasing Mo content improved corrosion resistance in the $CoCrFeNiMo_x$ system in addition to improving mechanical strength due to the formation of σ and μ intermetallic phases ranging from nm to µm size scale. A Mo concentration of 11.1 at. % had the highest corrosion potential of all tested compositions and formed few stable pits [46]. Similarly, Wang et al. observed more positive pitting potentials in chloride environments with increased Mo concentration added to the $(CoCrFeNi)_{1-x}Mo_x$ system. However, more frequent pitting, higher current densities, and a more negative corrosion potential were observed with 3 wt. % Mo added due to the formation of a σ phase. Such decreases were not observed during polarization in sulfuric acid [20]. Unlike most cases, where σ phases are likely at higher Mo concentrations, Linder et al. observed σ phase only at low Mo concentrations in magnetron sputtered $CoCrFeMo_xNi$ thin films. Little effect was observed on room temperature corrosion behavior in acidic sulfate solutions, however, corrosion resistance improved with Mo concentration at 80 ˚C. Additionally, increased surface cation fractions of both Cr and Mo were observed in the passive film of the CCAs with increasing Mo concentration [48].

Chou et al. evaluated the corrosion resistance of the $Co_{1.5}CrFeNi_{1.5}Ti_{0.5}Mo_x$ CCA system [41]. Increasing Mo concentrations marked a transition from single phase FCC to an FCC with σ phase dendritic microstructure. The corrosion resistance decreased with increased Mo concentration in both acidic (H_2SO_4) and basic (NaOH) solutions. In neutral NaCl solutions, the Mo-free CCA had a distinct pitting potential well below the potentials of similar current increases for all evaluated Mo containing CCAs, which dissolved in a transpassive manner following formation of a stable passive film. The breakdown behavior of the Mo-containing CCAs was identified by a negative hysteresis and verified by scanning electron microscopy (SEM) imaging to indicate a lack of pitting. Improved resistance to general corrosion at lower Mo concentrations and to pitting corrosion at higher concentration suggests that the optimal Mo concentration for passivity and localized corrosion resistance may differ.

Similarly, Rodriguez et al. observed an increased breakdown potential and improved repassivation behavior with the addition of 7.64 at. % Mo to the $CoCrFeNi_2$ CCA [42]. Improved overall corrosion resistance was speculated to occur due to the formation of an improved protective layer at grain boundaries and other preferential sites for localized corrosion. Shang et al. evaluated the microstructure and corrosion resistance of a series of $CoCrFeMnNiMo_x$ CCAs [43]. Increased Mo concentration was suggested to improve the corrosion resistance. However, concentrations which were high enough to promote the formation of a σ phase were suggested to harm corrosion resistance. Mo was observed in the oxide film with X-ray photoelectron spectroscopy (XPS) surface analysis, suggesting it may play a role in the passivation process. The existing body of work highlights how balancing the beneficial pitting and passivity contributions with phase partitioning, intermetallic formation, cost, and density consequences adds considerable complexity to optimization of Mo concentration in CCAs.

Although Mo has well established benefits to corrosion resistance within traditional binary alloys as well as the CCA field, the addition to Al and Ti-containing CCAs is notably less explored. Mo has been shown to improve corrosion resistance in the Al-Ti-Mo system, although it also promoted chemical segregation leading to microgalvanic corrosion [50]. Limited work has suggested increased Mo concentrations in Al and Ti containing CCAs with modest Cr concentrations also promote the formation of separate phases [40, 41]. Furthermore, the increase in alloy density from Mo additions runs contrary to the light-weight applications for which Al and Ti CCAs are often targeted [6]. Despite potential adverse effects on microstructural stability, Mo may be beneficial to Cr-lean, Al and Ti containing CCA design space, particularly as such alloys have often been shown to have multi-phase microstructures vulnerable to localized corrosion at phase interfaces [15, 18, 21, 51]. Thus, it is necessary to evaluate the effect of Mo on the corrosion and passivity of such CCAs to optimize compositions.

This work investigates three $Al_{0.3}Cr_{0.5}Fe_2Mo_xNi_{1.5}Ti_{0.3}$ (x = 0, 0.05, 0.15) containing CCAs of FCC + $L2_1$ microstructure from a CCA alloy system designed and optimized for mechanical strength, ductility, and toughness [52]. The concentration of Mo is adjusted to evaluate the optimal concentrations for passivation and corrosion resistance in an alloy system that is dependent on three elements (Al, Cr, and Ti) for passivity [7], as opposed to traditional alloys such as stainless steels with high Cr content and Cr-dominated passive films [53]. The effects on phase content, passive film chemical composition, and elemental dissolution are observed with X-ray diffraction (XRD) and SEM, XPS and atomic emission spectroelectrochemistry (AESEC) respectively. While minimizing Mo concentration may decrease alloy cost and density, as well as improve compositional homogeneity, concentrations below a critical threshold may leave the alloys vulnerable to localized corrosion. The determining factors for compositional optimization and the role of Mo in the passivation and corrosion process will be discussed.

2.0 Experimental Methods

2.1 Alloy Synthesis and Microstructural Characterization

Three CCAs with the compositions $Al_{0.3}Cr_{0.5}Fe_2Mo_xNi_{1.5}Ti_{0.3}$ (x = 0, 0.05, 0.15) listed in Table I, henceforth referred to as Mo-0, Mo-1.1, and Mo-3.2 with regards to Mo concentrations in at. %, were synthesized via arc melting into a water-cooled copper hearth under Ar cover gas from high purity (greater than 99.9%, Cr greater than 99.2 %) elements. Compositions were selected based on pervious work in similar systems targeting light-weight, low-cost, corrosion resistance CCAs [7, 18, 52] and were predicted to have an FCC matrix with Heusler ($L2_1$) second phases with computational methods discussed elsewhere [52, 54]. Samples were remelted and flipped five times to ensure chemical homogeneity before being suction cast in a copper mold to produce disk-shape samples with 5 mm thickness and 10 mm diameter. Cast samples were encapsulated under Ar into quartz tubes and annealed for five hours at 1070 °C before quenching in water. Samples were mechanically ground with SiC paper up to 1200 grit and, in the case of microstructural and surface chemistry analysis, polished with polycrystalline suspension through 0.25 microns before cleaning with acetone and isopropyl alcohol.

Table I: Nominal CCA and 316L compositions in atomic percent. Pure elements were massed within 1% error of the tabulated compositions prior to arc melting. The 316L compositions are defined as the median of the acceptable range and also include minor amounts of C, N, P, S, and/or Si.

Alloy	**Al**	**Cr**	**Fe**	**Mo**	**Ni**	**Ti**
Mo-0	6.5%	10.9%	43.5%	**0.0%**	32.6%	6.5%
Mo-1.1	6.5%	10.8%	43.2%	**1.1%**	32.3%	6.5%
Mo-3.2	6.3%	10.5%	42.1%	**3.2%**	31.6%	6.3%
316L	0.0%	17.0%	68.5%	**2.5%**	12.0%	0.0%

Phases present in the microstructure were identified with XRD using Cu Kα X-rays (1468.7 eV) at a scan rate of 0.15 °/s on a PANalytical Empyrean Diffractometer™ using Bragg-Brentano focusing geometry. The optics used were a 4 mm mask, 0.25° divergence slit, 1.52 mm anti-scatter slit, and 1.15° Soller slit on the incident beam side with a 16.8 mm anti-scatter slit and 2.3° Soller slit on the diffracted beam side. The microstructure was imaged with SEM on an FEI Quanta 650™ in backscattered electron (BSE) imaging mode at an accelerating voltage of 15 keV, a probe size of approximately 4 nm, and a working distance of approximately 10 mm. Energy dispersive spectroscopy (EDS) was utilized in both point scan and mapping mode to evaluate phase composition and was analyzed with Oxford Instruments Aztec™ software. Phase fractions were approximated from brightness threshold analysis of the BSE micrographs via ImageJ.

2.2 Electrochemical Characterization

A conventional three-electrode cell connected to a Gamry Instrument Reference 600+™ potentiostat was utilized for electrochemical testing with the sample as the working electrode, a platinum mesh counter electrode, and a saturated calomel reference electrode (SCE) relative to which all potentials hereafter are reported. An area of 0.1 cm^2 was exposed via a rubber O-ring to electrolyte solutions of 0.1 M NaCl adjusted to both pH 4 and 10 with concentrated HCl and NaOH respectively to evaluate corrosion behavior over a range of environments with differing stability levels of Mo. The electrolyte was continually bubbled with $N_{2(g)}$ throughout testing to reduce the activity of dissolved oxygen. All samples were compared to a commercially procured (North American Steel) 316L stainless steel (UNS S31600) control of a comparable Mo concentration (2-3 at. %). Three procedures were utilized to provide a comprehensive analysis of the passivity and corrosion resistance of the alloys.

The solution-exposed air-formed oxide film was electrochemically characterized by measuring the open circuit potential (OCP) for 1800 s directly after grinding. OCP measurement was followed by electrochemical impedance spectroscopy (EIS) at the final OCP measured between frequencies of 1 MHz and 5 mHz with 8 points/decade and an applied AC potential of 20 mV_{rms}. EIS spectra were fit to a Randles circuit modified to include a constant phase element (CPE) with Gamry Echem Analyst software^{TM}. The procedure was repeated after 20-day immersion in 0.1 M NaCl pH 4 alongside mass loss measurements. Surfaces for each alloy were then imaged with SEM in BSE mode.

Second, to observe the passivation behavior, the air-formed oxide was first exposed to a cathodic reduction treatment by applying a -1.3 V_{SCE} potential for 600 s, which has been shown in previous work to adequately minimize the air-formed oxide in similar CCAs via in-situ impedance measurements [7, 18, 55]. The sample was then potentiodynamically polarized in the forward direction from -1.3 to +0.8 V_{SCE} at a scan rate of 0.5 mV/s followed by a reverse scan (+0.8 to -1.3 V_{SCE}, 0.5 mV/s). To analyze the polarization behavior in the absence of localized corrosion, the procedure was repeated in 0.1 M Na_2SO_4 with the pH adjusted to 4 and 10 with concentrated H_2SO_4 and NaOH respectively. Finally, an oxide film was grown in the passive range by first exposing the sample to the -1.3 V_{SCE} cathodic treatment and then applying a potential step to -0.2 V_{SCE} for 10 ks. The potential was determined to be in the passive range by initial potentiodynamic polarization testing. Following the potentiostatic hold, a potentiostatic EIS experiment was carried out at an applied potential of -0.2 V_{SCE} (1 MHz to 5 mHz, 8 points/decade, 20 mV_{rms}, modified Randles circuit fitting) before OCP was recorded for 1800 s. All electrochemical experiments were repeated threefold to ensure reproducibility. The pitting potential (E_{pit}) in NaCl was defined at the potential for which anodic current densities exceeded 10^{-4} $A.cm^{-2}$ with abrupt change in slope. Statistically distributed properties obtained during potentiodynamic polarization testing in chloride solutions such as pitting and repassivation potentials necessitated additional replication. Cumulative probability plots were developed in accordance with ASTM G16-95[18] [56] with methods previously adapted to characterize localized corrosion in Ni-based Mo-containing alloys [57, 58].

2.3 Identification of Dissolution Rates

To identify the fate of individual elements in passivation and dissolution, AESEC was utilized on Mo-3.2 and pure Mo samples during the polarization and potentiostatic film growth procedures described above. The electrolyte solution containing dissolved elements was transported to a Horiba Jobin Yvon Ultima 2C^{TM} inductively coupled plasma atomic emission spectrometer (ICP-AES) via a flow cell. Elemental dissolution rates were evaluated by monitoring emission intensity at a characteristic wavelength for each element. A polychromator at a focal length of 0.5 m was utilized alongside a monochromator used to

---

[18] For the passive current density probability plots, the procedure was modified to take the linear regression from the logarithm of the current densities.

obtain a better signal resolution of Mo, Cr or Al depending on the electrolyte condition. To compare to electron current density (j_e), elemental dissolution rates were converted to an equivalent current density (j_M) with Faraday's law. A more thorough scientific basis and methodology for AESEC analysis is available elsewhere [59]. Dissolution rates in Ar-deaerated 0.1 M NaCl pH 4 and 0.1 M NaCl pH 10 were monitored during potentiodynamic polarization from -1.3 to +1.0 V_{SCE} (0.5 mV/s) following a 600 s exposure to OCP and a 600 s cathodic treatment at -1.3 V_{SCE}. Additionally, dissolution rates were monitored during potentiostatic passive film formation (-0.2 V_{SCE}, 4 ks) directly after exposure to OCP, bypassing any cathodic reduction. The test time was decreased relative to previous electrochemical tests to ensure plasma stability.

2.4 Characterization of Passive Film Chemistry

XPS was utilized to characterize the passive film composition and valence. Each sample was exposed to a 600 s cathodic treatment at -1.3 V_{SCE} followed by a 10 ks potentiostatic hold at -0.2 V_{SCE}, the potential and time used for the potentiostatic oxide growth procedure described above. Samples were transported under $N_{2(g)}$ directly to a PHI VersaProbe III^{TM} XPS system, bypassing any EIS and OCP measurement. Al Kα X-rays (1486.6 eV) at a 26 eV pass energy, 45° take off angle, and with a 100 µm spot size[19] were used. High resolution spectra were collected over the Al 2p, Cr $2p_{3/2}$, Fe $2p_{1/2}$, Mo 3d, Ni $2p_{3/2}$, and Ti $2p_{3/2}$ core spectra with energy bounds defined by an initial survey scan. Spectra were calibrated with C 1s set to 284.8 eV and deconvoluted with a Shirley background correction, Doniach-Sunjic peaks for metallic features, and Voigt functions for oxidized features with KOLXPD™ analysis software. Peak deconvolutions were constrained by position, full-width half maximum, and multiple splitting utilizing spectra of known reference compounds obtained elsewhere [60-63]. As Ni Auger peaks overlap the Fe $2p_{3/2}$ core spectrum, a constant position shift between the experimentally obtained Fe $2p_{1/2}$ spectrum and reference spectra in the Fe $2p_{3/2}$ spectrum was assumed to identify chemical species. The intensity of the Cr 3s spectrum, which overlaps the Al 2p spectrum, was fixed based on the intensity of the Cr $2p_{3/2}$ spectrum adjusted with relative sensitivity factors. Cation fractions were evaluated as the proportion of the intensities of the oxidized states for each element normalized with relative sensitivity factors as discussed below. Multi-cation species (e.g. spinels) are only suggested for alloys for which good fit

---

[19] The XPS spot size is significantly larger than any second phase regions, limiting the ability to evaluate the lateral variation in passive film chemistry with regards to the bulk phase over which the film was grown. XPS measurements are obtained over a large enough area that they may be reasonably assumed to be representative of the entirety of the microstructure. High-resolution evaluation of the passive film chemistry with regards to phase interfaces in the microstructure will form the basis for a future study.

agreement is obtained when fit to both core spectra with the peak intensity constrained by fixing cation fractions for each species to stoichiometric ratios between each element.

For each metal (M), the total surface cation fraction intensity (I_M) was obtained as the sum of all intensities (I_i^{ox}) of oxidized features (single-metal oxides, hydroxides, and complex oxides) for a given core spectra.

$$I_M = \sum_{i=0}^{n} I_i^{ox} \tag{1}$$

Summed intensities were normalized with relative sensitivity factors (R_M) for each metal core spectrum specific to the PHI VersaProbe III^{TM} system obtained via PHI Multipak^{TM} software. The surface cation fraction (S_M) was defined normalized intensity for a given metal's core spectrum relative to the sum of normalized core spectra intensities for all metals in the CCA.

$$S_M = \frac{\frac{I_M}{R_M}}{\sum_{M=0}^{n} \frac{I_M}{R_M}} \tag{2}$$

Elements for which the surface cation fraction is greater than the bulk alloy composition (B_M) shown in Table I ($S_M > B_M$) are considered enriched for a given alloy and film growth condition while surface cation fractions less than the bulk composition ($S_M < B_M$) indicate depletion.

3.0 Results

3.1 Characterization of Alloy Microstructure

The CCAs are suggested by XRD patterns shown in Figure 1 to have a predominantly FCC microstructure with a second phase also detected. The second phase has been suggested to be $L2_1$ using methods discussed elsewhere [52]. Figure 2 indicates second-phase regions are of single-micrometer size. The phase volume and morphology is similar across all three CCAs with Mo-1.1 and Mo-3.2 having slightly higher $L2_1$ volume fractions than Mo-0.

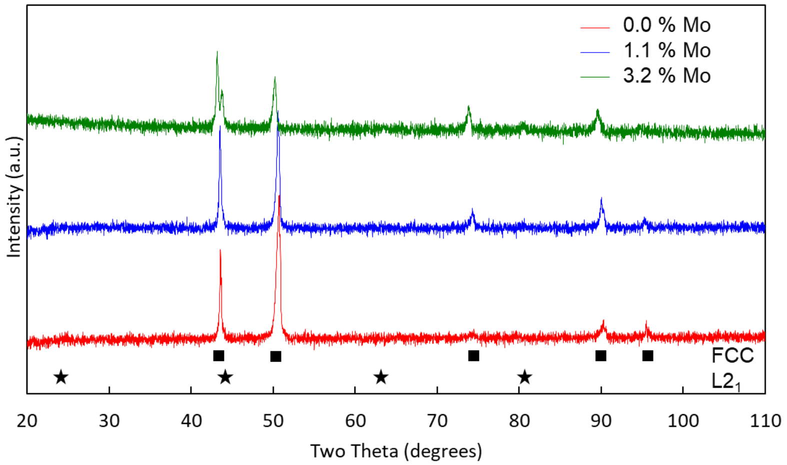

Figure 1: XRD patterns for synthesized and homogenized CCAs. Square and star indexes identify corresponding diffraction peaks for FCC and $L2_1$ phases respectively.

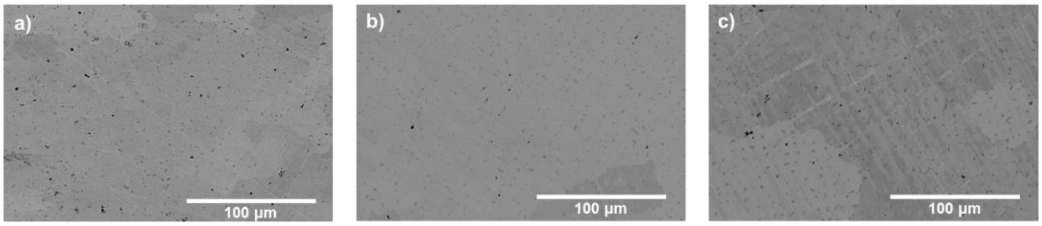

Figure 2: BSE micrographs of a) Mo-0, b) Mo-1.1, and c) Mo-3.2 microstructures

EDS point scans for each CCA (Table II) and mapping (Figure 3) both suggest the matrix to be enriched in Fe, Cr, and Mo, while the second phase is enriched in Al, Ti, and Ni with each element present in both phases. Generally, the degree of Al and Ti partitioning increases with Mo content, with Mo-0 exhibiting the most chemically homogenous microstructure with regards to the ratios between the concentrations of each element in the FCC matrix compared to $L2_1$ EDS point scans.

Table II: Elemental fractions obtained from EDS point scans over matrix and second phase regions of each CCA and area fractions obtained via ImageJ analysis of a series of BSE micrographs.

Phase	Al	Cr	Fe	Mo	Ni	Ti	Area
Mo-0							
Matrix	7.8	13.5	52.8	-	18.6	7.3	96.9%
2nd Phase	18.7	4.3	18.9	-	42.5	15.6	3.1%
Mo-1.1							
Matrix	6.1	11.5	44.1	1.3	31.1	5.9	95.6%
2nd Phase	20.5	2.3	13.4	Trace	45.1	18.7	4.4%
Mo-3.2							
Matrix	3.7	11.6	44.7	3.2	30.7	6.1	96.0%
2nd Phase	15.3	2.5	13.9	0.5	47.3	20.5	4.0%

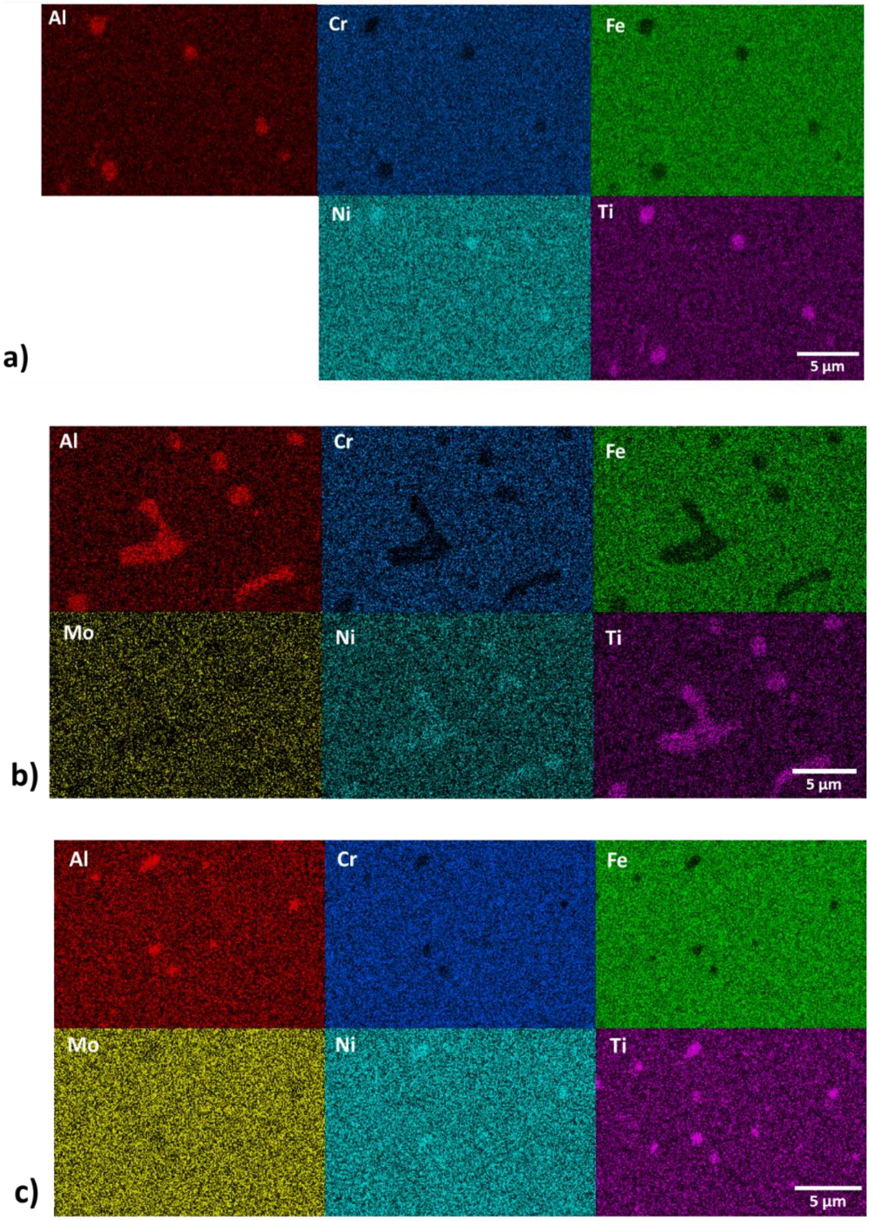

Figure 3: EDS mapping of a) Mo-0, b) Mo-1.1, and c) Mo-3.2 microstructures

3.2 Characterization of Passivity and Transpassive Breakdown by Potentiodynamic Polarization in Cl^- Free Electrolytes

E-log(i) curves obtained in acidic and basic Na_2SO_4 solutions, which allow for characterization of the passivation process without Cl^- induced breakdown, are shown in Figure 4 with key corrosion parameters listed in Table III. All materials passivate either spontaneously or after an active to passive transition, although no clear trends are present regarding the critical current density and critical potential. Critical current densities and potentials are further obscured by changes in sign of the current density prior to the formation of a stable passive film for Mo-0 in pH 4 and Mo-1.1 in pH 10. In both environments, Mo-1.1 has the highest passive current density (i_{pass}). i_{pass} of Mo-0 is comparable to that of 316L in the pH 4 solution, but 316L has a lower i_{pass} than all CCAs at pH 10. Increasing current densities representative of transpassive dissolution of the passive film are not observed within the evaluated potential range for any of the CCAs. However, such behavior is suggested for the Al and Ti-free 316L at potentials above 0.6 V_{SCE}. No trends in corrosion potential (E_{corr}) are observable.

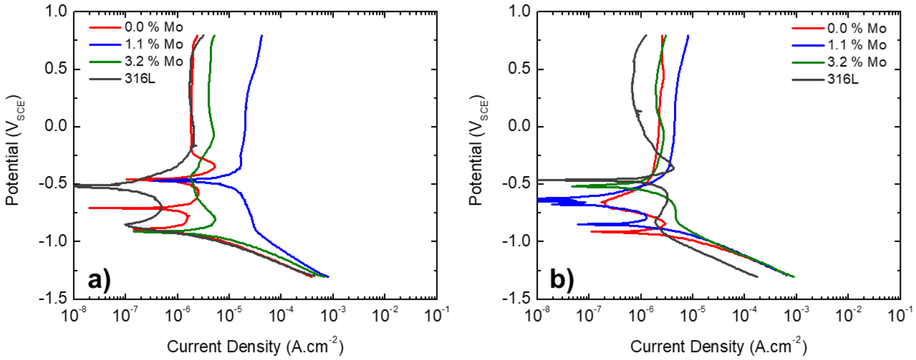

Figure 4: Potentiodynamic polarization of CCAs and 316L in $N_{2(g)}$ bubbled **a)** 0.1 M Na_2SO_4 pH 4 and **b)** 0.1 M Na_2SO_4 pH 10 following cathodic reduction pre-treatment (600 s, − 1.3 V_{SCE}).

Table III: Selected corrosion parameters from potentiodynamic polarization of CCAs in 0.1 M Na_2SO_4 pH 4 and 0.1 M Na_2SO_4 pH 10 following cathodic reduction pre-treatment (600 s, − 1.3 V_{SCE}). Each term includes the average value with a one standard deviation bound.

Alloy	**E_{corr} (V_{SCE})**	**i_{pass} (μA.cm^{-2})**	**E_{corr} (V_{SCE})**	**i_{pass} (μA.cm^{-2})**
	0.1 M Na_2SO_4 pH 4		0.1 M Na_2SO_4 pH 10	
Mo-0	-0.946 +/- 0.294	2.51 +/- 0.68	-1.12 +/- 0.26	2.27 +/- 0.27
Mo-1.1	-1.062 +/- 0.208	25.46 +/- 23.18	-1.12 +/- 0.23	6.32 +/- 3.54
Mo-3.2	-1.172 +/- 0.239	4.05 +/- 1.26	-0.88 +/- 0.06	2.54 +/- 0.85
316L	-1.011 +/- 0.253	1.40 +/- 0.45	-0.84 +/- 0.03	1.03 +/- 0.27

3.3 Characterization of Passivity and Localized Breakdown by Potentiodynamic Polarization in Cl^- Containing Electrolytes

Figure 5 shows representative E-log(i) curves in acidic and basic NaCl solutions and selected probability plots with key parameters quantified in Table IV. E_{corr} generally increases with increased Mo concentration in the pH 4 solution. Opposite trends are seen in the pH 10 solution, potentially driven by the solubility of MoO_4^{2-} in basic environments and resultant dissolution and depletion of Mo from the oxide [64]. i_{pass} is lower in pH 10 than in pH 4 for all CCAs with the lowest values observed for Mo-0 in pH 4 and similar values for each CCA in pH 10.

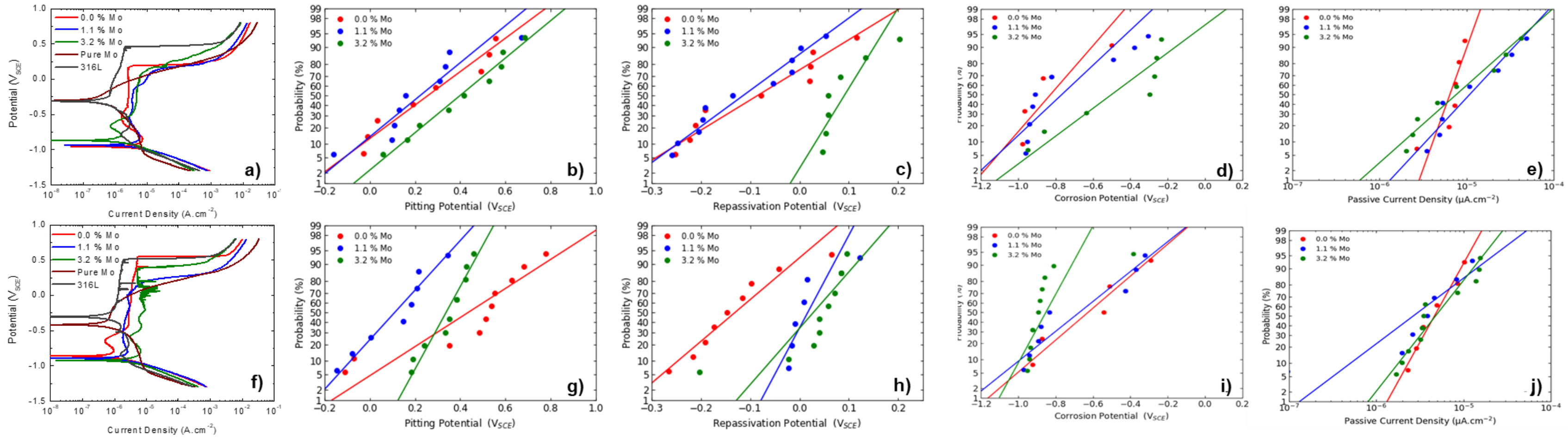

Figure 5: **a,f)** E-log(i) and cumulative probability plots for **b, g)** pitting potential, **c, h)** repassivation potential, **d, i)** corrosion potential, and **e, j)** passive current density summarizing potentiodynamic polarization of CCAs, pure Mo, and 316L in $N_{2(g)}$ bubbled **a-e)** 0.1 M NaCl pH 4 and **f-g)** 0.1 M NaCl pH 10 following cathodic reduction pre-treatment (600 s, − 1.3 V_{SCE}).

Table IV: Selected corrosion parameters for potentiodynamic polarization shown in Figure 5 obtained in 0.1 M NaCl pH 4 and 0.1 M NaCl pH 10. Each term includes the mean value bounded by a one standard deviation range.

	0.1 M NaCl pH 4				**0.1 M NaCl pH 10**			
Alloy	**E_{corr} (V_{SCE})**	**E_{pit} (V_{SCE})**	**E_{rep} (V_{SCE})**	**i_{pass} ($\mu A.cm^{-2}$)**	**E_{corr} (V_{SCE})**	**E_{pit} (V_{SCE})**	**E_{rep} (V_{SCE})**	**i_{pass} ($\mu A.cm^{-2}$)**
Mo-0	-0.827 +/- 0.194	0.256 +/- 0.231	-0.086 +/- 0.129	6.88 +/- 2.13	-0.627 +/- 0.237	0.435 +/- 0.285	-0.131 +/- 0.094	5.38 +/- 2.96
Mo-1.1	-0.767 +/- 0.238	0.222 +/- 0.218	-0.115 +/- 0.106	16.78 +/- 15.55	-0.675 +/- 0.26	0.11 +/- 0.157	0.016 +/- 0.049	4.86 +/- 3.93
Mo-3.2	-0.501 +/- 0.285	0.399 +/- 0.204	0.091 +/- 0.053	13.76 +/- 13.98	-0.852 +/- 0.153	0.338 +/- 0.094	0.028 +/- 0.084	6.59 +/- 5.31
316L	-0.372 +/- 0.062	0.465 +/- 0.008	-0.072 +/- 0.079	0.18 +/- 0.05	-0.307 +/- 0.004	0.431 +/- 0.111	-0.019 +/- 0.004	0.130 +/- 0.028

All three CCAs generally have lower localized corrosion resistance than 316L in the Cl^--containing solutions, with passive films breaking down by pitting and limited crevice corrosion. The repassivation potentials (E_{rep}) obtained from downward scans indicate the presence of positive trends with increasing Mo concentration. Although the distribution of E_{rep} increases from Mo-0 to Mo-3.2 in both environments, Mo-1.1 has a similar distribution to Mo-0 in the pH 4 environment whilst it is similar to that of Mo-3.2 in the pH 10 environment. Similar trends are shown for the E_{pit} in the pH 4 environment, with the E_{pit} increasing by nearly 0.15 V from Mo-0 to Mo 3.2. The increase suggests Mo increases the resistance of the passive film to localized breakdown or that the stabilization and propagation stages are affected. However, E_{pit} is higher for Mo-0 in the pH 10 environment, deviating from the trends established for E_{rep} and E_{pit} in the pH 4 environment. Neither E_{pit} nor E_{rep} are affected to a statistically significant level by pH, with the notable exception of the increased E_{pit} of Mo-0 in the pH 10 solution. Intermediate spikes before breakdown in the E-log(i) curves, most noticeably those of Mo-3.2 and 316L, suggest breakdown and repassivation due to metastable pitting. Neither the passivation nor breakdown behavior of any of the CCAs resembled that of pure Mo.

AESEC was utilized to track individual elemental dissolution rates during upward polarization of the Mo-3.2 alloy (Figure 6). The elemental dissolution rates are presented in equivalent current densities with the oxidation states used to calculate them indicated in the parenthesis. At both pH 4 and pH 10, elemental dissolution rates are mostly below the detection level at potentials in the passive regime (approximately -0.45 to -0.20 V_{SCE} for pH 4 and -0.8 to -0.15 V_{SCE} for pH 10). For example, at pH 4, Ni and Fe begin to dissolve at potentials near E_{pit} (-0.07 V_{SCE}) while other elements dissolve at more positive potentials (0.07 V_{SCE} for Cr, 0.17 V_{SCE} for Mo, Al, and Ti). At higher potentials (above 0.0 V_{SCE}), the elemental dissolution rates are not proportional to the composition of either phase.

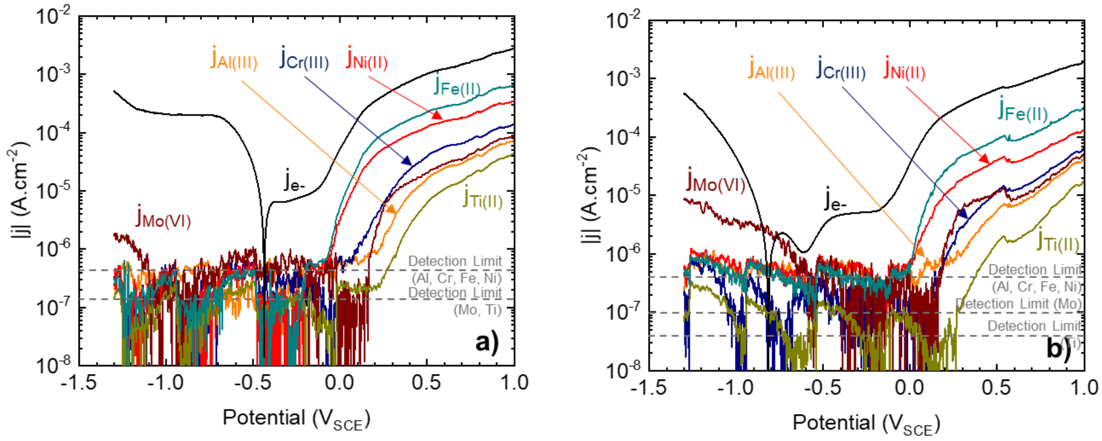

Figure 6: Equivalent current densities of in-situ elemental dissolution rates monitored via AESEC during upward polarization of Mo-3.2 in $N_{2(g)}$ bubbled **a)** 0.1 M NaCl pH 4 and **b)** 0.1 M NaCl pH 10. Dashed lines indicate element detection limits.

The Mo-3.2 elemental dissolution rates within the transpassive region calculated from the equivalent current densities are presented in Table V. Only the Ni and Fe compositions were remarkably different in that the dissolved Ni was lower than the expected alloy composition (31.6 at. % Ni), and the dissolved Fe (53.6% for pH 4 and 58.5% for pH 10) was higher than the alloy composition (42.1 at. % Fe) in both pHs. Lower Mo contents than the expected alloy composition from Table I (3.2 at. % Mo) indicate slight Mo enrichment.

Table V: Proportion of transpassive elemental dissolution attributable to each element in at. %. Values are determined from the ratios of equivalent current densities obtained via AESEC at E = 1.0 V_{SCE} during LSV in 0.1 M NaCl at pH 4 and 10 for Mo-3.2 shown in Figure 6. Bolded terms indicate dissolution rates higher than the bulk alloy composition suggesting depletion.

Electrolyte	Al	Cr	Fe	Mo	Ni	Ti
0.1 M NaCl pH 4	4.1%	7.6%	**53.6%**	2.5%	28.6%	3.6%
0.1 M NaCl pH 10	4.0%	7.7%	**58.5%**	2.8%	23.8%	3.2%

Dissolution of Mo in the cathodic region is observed for both Mo-3.2 and pure Mo (Figure 7b) for both environments with significantly higher Mo dissolution rates in pH 10. The higher Mo dissolution in the cathodic potential range at pH 10 may be attributed to the dissolution of the pre-existing Mo-based corrosion products formed after mechanical grinding. A significantly high cathodic current density at the level of $-1*10^{-4}$ A.cm^{-2} is observed for both Mo-3.2 (Figure 6a) and pure Mo (Figure 7a) at pH 4 with relatively low Mo dissolution rate compared to that at pH 10. Notably, Mo dissolution shows an increased Tafel slope relative to other elements for both pH 4 and pH 10.

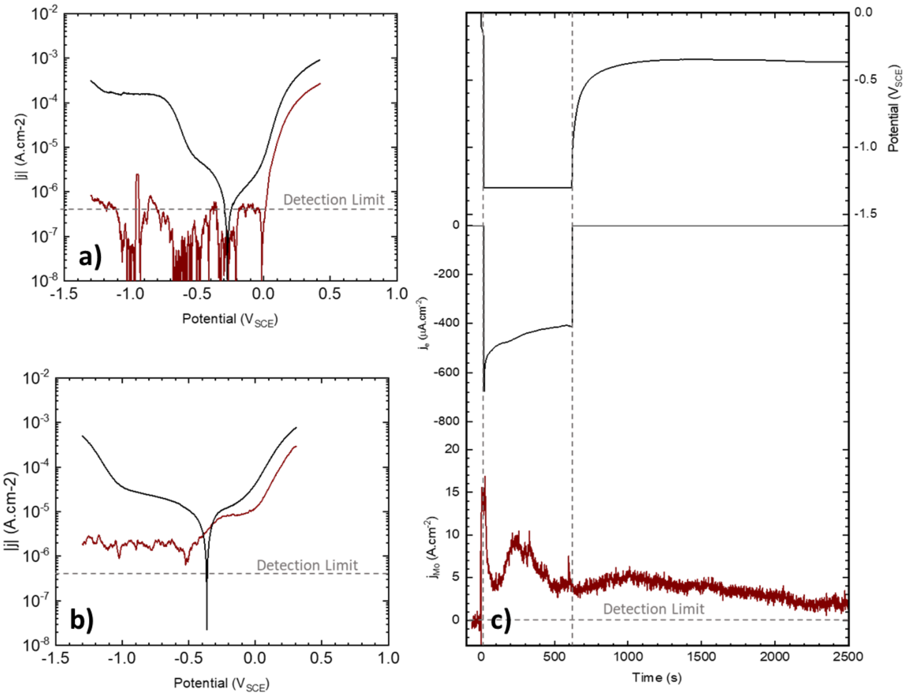

Figure 7: Equivalent current densities of in-situ elemental dissolution rates monitored via AESEC during **a)** potentiodynamic polarization of pure Mo in 0.1 M NaCl pH 4, **b)** potentiodynamic polarization of pure Mo in 0.1 M NaCl pH 10, and **c)** exposure of Mo to a -1.3 V_{SCE} potential for 600 s followed by open circuit corrosion.

3.4 Growth and Characterization of Passive Films by Impedance Spectroscopy

Figure 8 shows EIS characterization utilized to provide a more comprehensive electrochemical characterization of the air-formed solution-exposed passive films after 1800 s at OCP. All OCP values were within 80 mV of each CCA in the same environment, with no clear trends with Mo concentration. In all cases, EIS is acquired at potentials well within the passive region defined by Figure 5. In this preliminary report, the spectra for the CCAs and 316L were fit with the modified Randles circuit shown in Figure 8e with fit parameters shown in Table VI. In this model the polarization resistance (R_P) likely encompasses both charge transfer resistance and diffusional impedance. In both acidic and basic environments, R_P decreases with Mo content relative to Mo-0. Despite the high R_P values, Mo-0 has a CPE coefficient (α) below 0.8 in both pH environments, whereas the higher α values of other CCAs and 316L are indicative of more ideal capacitive behavior [65]. The corrosion resistance of the air-formed solution-exposed passive films of all CCAs are suggested to be inferior to the corrosion resistance of films formed on 316L based on lower R_P values obtained in both environments.

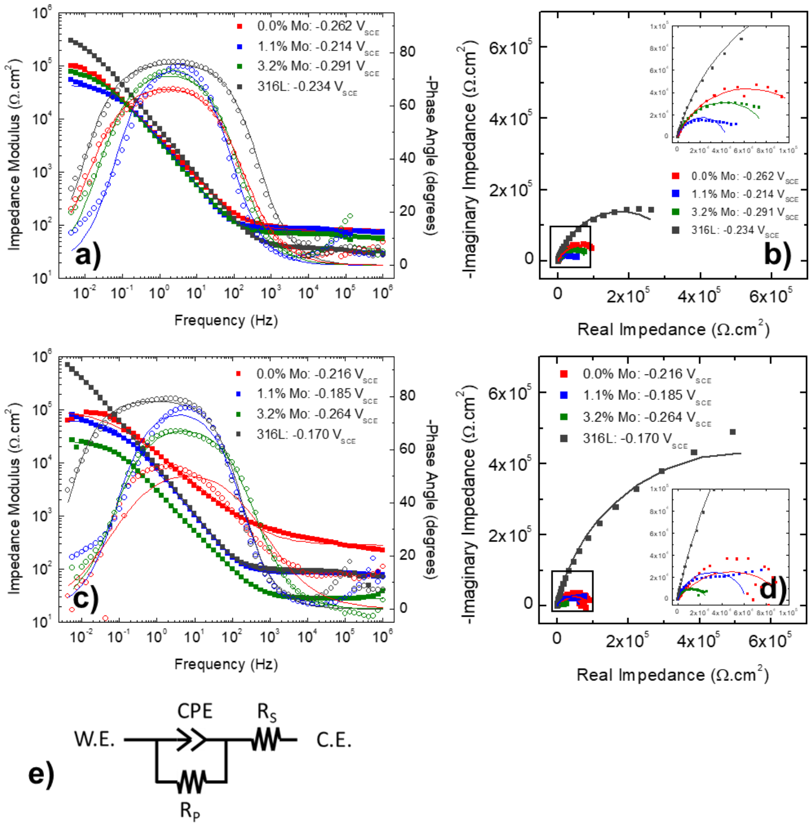

Figure 8: a,c) Bode and **b,d)** Nyquist plots obtained following 30 minutes exposure of the air-formed oxides to open circuit corrosion in $N_{2(g)}$ bubbled **a,b)** 0.1 M NaCl pH 4 and **c,d)** 0.1 M NaCl pH 10. The final OCP values and potentials at which EIS was measured are indicated in the figure legends. **e)** Equivalent circuit model utilized for EIS fits

Table VI: EIS fit parameters for the spectra shown in Figure 8 obtained in 0.1 M NaCl pH 4 and 0.1 M NaCl pH 10. Each term is defined by the Randles circuit shown in Figure 8e.

	0.1 M NaCl pH 4				**0.1 M NaCl pH 10**			
Alloy	**R_S (Ω.cm^2)**	**R_P (kΩ.cm^2)**	**Y (μS.s$^\alpha$.cm^{-2})**	**α_f**	**R_S (Ω.cm^2)**	**R_P (kΩ.cm^2)**	**Y (μS.s$^\alpha$.cm^{-2})**	**α_f**
Mo-0	81.1	126.7	55.6	0.766	282.6	96.8	19.5	0.610
Mo-1.1	80.4	43.4	51.6	0.864	82.7	61.9	28.7	0.856
Mo-3.2	63.5	82.7	59.2	0.824	28.4	26.3	75.1	0.783
316L	33.9	350.6	32.9	0.852	82.6	1039.0	23.8	0.880

During 20-day immersion in 0.1 M NaCl adjusted to pH 4, Mo-1.1 has the highest mass loss rate (Table VII). Both Mo-0 and Mo-3.2 had lower mass loss rates by over an order of magnitude, indicating there were no clear trends with Mo concentration. Figure 9 shows film breakdown is attributable to pitting, with pits frequently observed at or near second phase interfaces. Neither phase is suggested to preferentially dissolve, nor do pits appear do penetrate into either phase at significantly higher rates.

Furthermore, Figure 10 and Table VIII show both the OCP and R_P values of Mo-1.1 and Mo-3.2 decrease during long-term immersion. Decreasing OCP values suggest the passive film is not improved by the extended exposure, while both values increase during the immersion for Mo-0 and 316L, indicating growth of a more protective passive film.

Table VII: Mass loss and average area penetration rates obtained during 20-day immersion of CCAs and 316L in 0.1 M NaCl pH 4. The mass gain observed for Mo-3.2 approached the tolerance of the scale and may be interpreted as negligible.

Alloy	**Mass Loss Rate ($mg.cm^{-2}.y^{-1}$)**	**Area Average Penetration Rate ($\mu m.y^{-1}$)**
Mo-0	1.3	1.7
Mo-1.1	13.2	17.3
Mo-3.2	-0.1 (Trace)	-0.1 (Trace)
316L	0.8	1.0

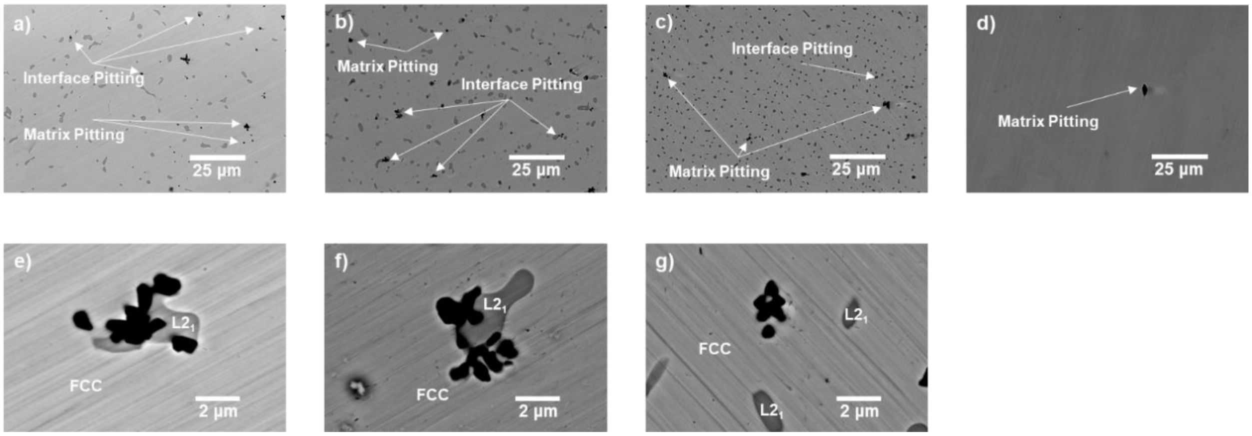

Figure 9: BSE micrographs showing representative pit morphologies for **a)** Mo-0, **b)** Mo-1.1, **c)** Mo-3.2, and **d)** 316L. High magnification micrographs show pits formed on **e)** Mo-0, **f)** Mo-1.1, and **g)** Mo-3.2 with regards to second phase morphology.

Table VIII: EIS fit parameters for the spectra shown in Figure 10 obtained following 20-day immersion in 0.1 M NaCl pH 4. Each term is defined by the Randles circuit shown in Figure 8e.

	0.1 M NaCl pH 4: Day 20			
Alloy	**R_S ($\Omega.cm^2$)**	**R_P ($k\Omega.cm^2$)**	**Y ($\mu S.s^{\alpha}.cm^{-2}$)**	**α_f**
Mo-0	72.8	1206.0	28.4	0.877
Mo-1.1	69.2	27.1	97.4	0.811
Mo-3.2	84.2	45.8	68.8	0.895
316L	71.6	1679.0	27.1	0.895

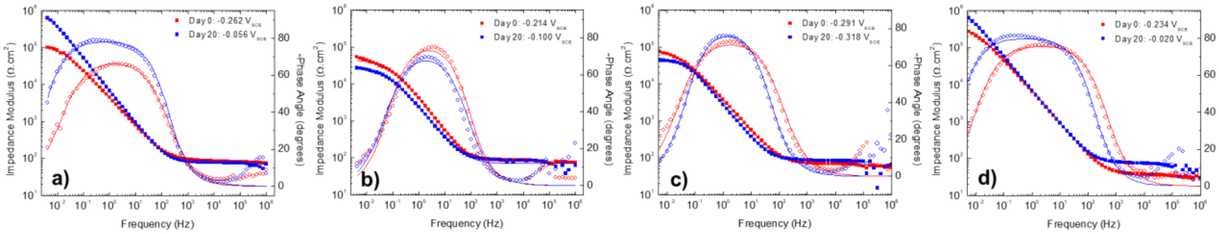

Figure 10: Bode plots following 30 minutes and 20-day exposure to open circuit corrosion in 0.1 M NaCl pH 4 of the air-formed oxides formed on **a)** Mo-0, **b)** Mo-1.1, **c)** Mo-3.2, and **d)** 316L. Spectra were fit with the equivalent circuit model shown in Figure 8e. The final OCP values and potentials at which EIS was measured are indicated in the figure legends.

A film grown in the passive region after cathodic treatment via applying a -0.2 V_{SCE} potential, indicated as part of the passive range of each CCA by initial potentiodynamic polarization (Figure 5), was also characterized. Figure 11 shows current density measurements throughout the passive film growth procedure. In pH 4 solution, the current density is generally higher in CCAs with less Mo beyond 100 s. A steady increase in the current density of Mo-0 suggests the formation of a weaker and/or dissolving passive film, although no pits or other features of localized corrosion were visible following exposure. In pH 10 solution, all current densities decrease with time and trends with Mo content are less prominent, with Mo-1.1 having the highest current density at the conclusion of the film growth procedure. Sharp decreases in current densities approaching zero occur on most alloys as anodic passivation approaches the residual oxygen reduction rate, indicating a transition from the anodic to cathodic regime. For both environments, 316L has lower current density magnitudes than all evaluated CCAs.

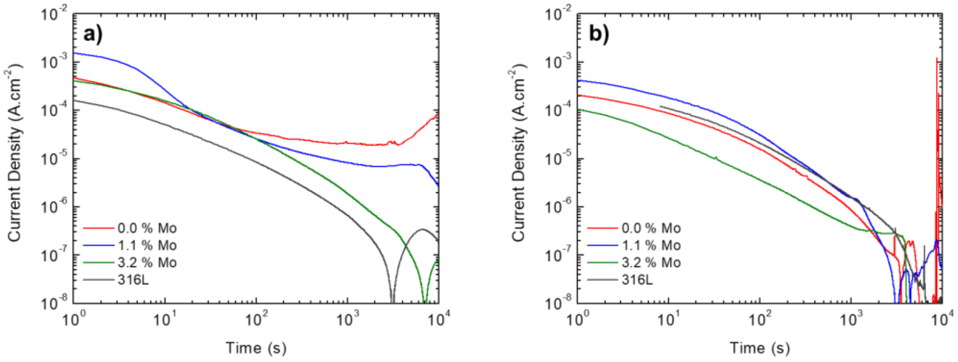

Figure 11: Current densities of CCAs and 316L during exposure to a -0.2 V_{SCE} potential in $N_{2(g)}$ bubbled **a)** 0.1 M NaCl pH 4 and **b)** 0.1 M NaCl pH 10 following cathodic reduction pre-treatment (600 s, − 1.3 V_{SCE}).

Individual elemental dissolution rates are measured during the potentiostatic film growth on Mo-3.2 via AESEC (Figure 12) in pH 4 and pH 10 solutions. Fe and Ni dissolve and followed similar trends as electron current density at pH 4 (Figure 12a), while dissolution rates of the other elements such as Al and

Ti are generally below the detection limit. In pH 10 solution (Figure 12b), Mo slightly dissolves but does not reflect trends in the electron current density, particularly past 10^3 seconds. A slight increasing trend of Al dissolution rate with time is observed at pH 10 while those of Fe, Ni, Cr and Ti are below the detection limit.

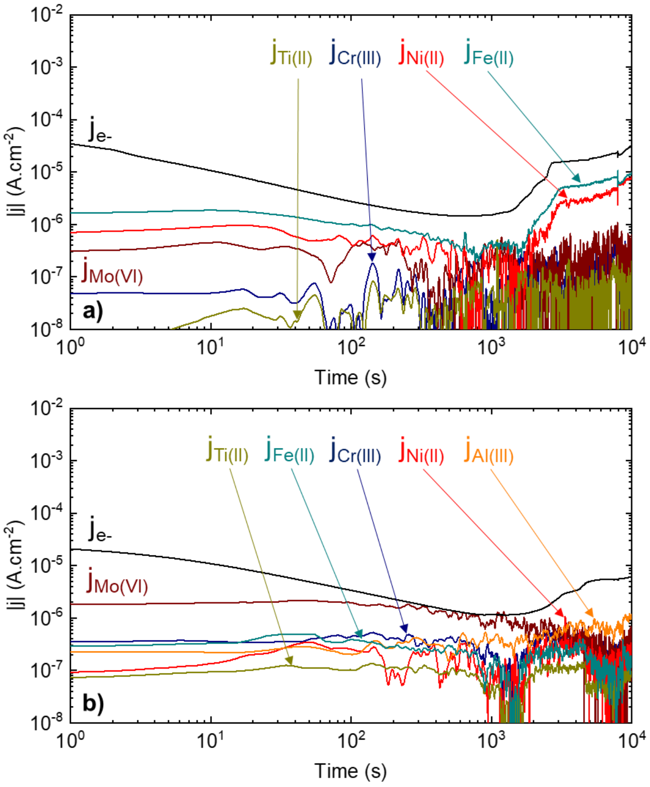

Figure 12: Equivalent current densities of in-situ elemental dissolution rates monitored via AESEC during exposure of Mo-3.2 to a -0.2 V_{SCE} potential in $N_{2(g)}$ bubbled **a)** 0.1 M NaCl pH 4 and **b)** 0.1 M NaCl pH 10. Dashed lines indicate element detection limits. Al dissolution rates are not shown in pH 4 due to high amounts of noise.

Following potentiostatic passive film growth, the films were characterized with EIS (Figure 13, Table IX) and fit with the Randles circuit described above (Figure 8e). The high current density observed during film growth (Figure 11a) is characteristic of a less corrosion resistant passive film. Unlike the case of the air-formed solution-exposed films, R_P increases with Mo content in both environments. α is above 0.85 for all alloys in both environments, indicating characteristic capacitive behaviour of the passive films. The R_P magnitude values vary less with Mo concentrations under pH 10 conditions than in pH 4 conditions, with much of the variability attributable to the low R_P of the film formed on Mo-0 in pH 4 conditions. R_P of all the CCA passive films is lower than that of 316L, regardless of Mo concentration or pH.

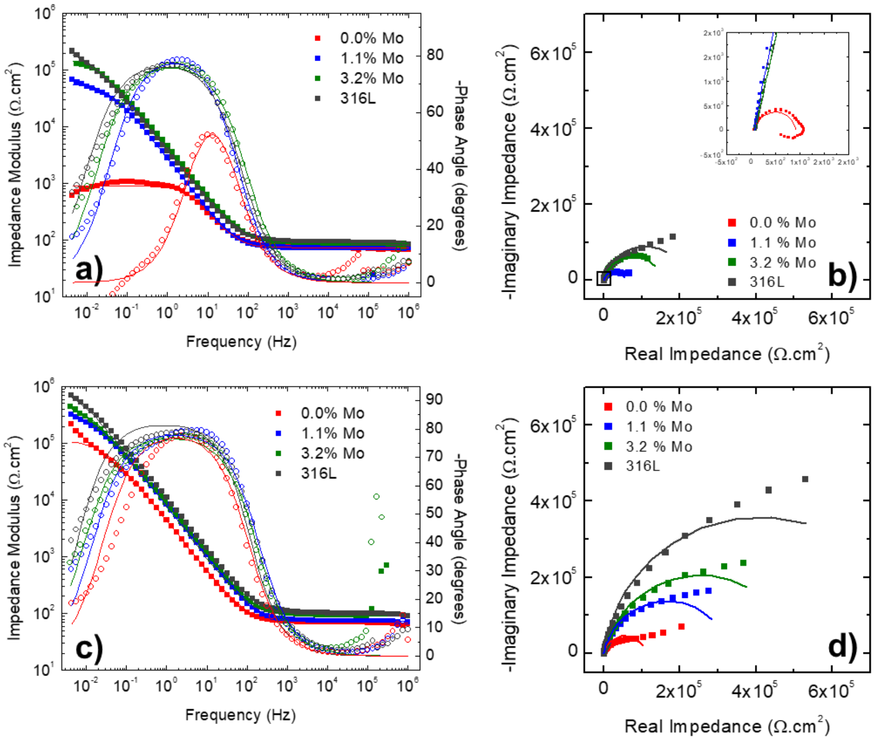

Figure 13: a,c) Bode and **b,d)** Nyquist plots obtained following cathodic reduction pre-treatment (600 s, − 1.3 V_{SCE}) and 10 ks exposure to -0.2 V_{SCE} in $N_{2(g)}$ bubbled **a,b)** 0.1 M NaCl pH 4 and **c,d)** 0.1 M NaCl pH 10. Spectra were fit with the equivalent circuit model shown in Figure 8e.

Table IX: EIS fit parameters for the spectra shown in Figure 11 obtained in 0.1 M NaCl pH 4 and 0.1 M NaCl pH 10. Each term is defined by the Randles circuit shown in Figure 7e.

	0.1 M NaCl pH 4				**0.1 M NaCl pH 10**			
Alloy	**R_S (Ω.cm^2)**	**R_P (kΩ.cm^2)**	**Y (μS.s$^\alpha$.cm^{-2})**	**α_f**	**R_S (Ω.cm^2)**	**R_P (kΩ.cm^2)**	**Y (μS.s$^\alpha$.cm^{-2})**	**α_f**
Mo-0	73.3	0.8	74.9	0.917	68.3	109.4	46.0	0.884
Mo-1.1	72.2	56.4	69.9	0.902	72.8	330.7	25.5	0.884
Mo-3.2	87.0	153.4	45.6	0.871	91.4	504.5	25.1	0.868
316L	91.4	218.7	54.5	0.871	95.5	818.0	24.1	0.918

3.5 Characterization of Passive Film Cation Fractions

XPS was utilized to characterize the passive films grown at -0.2 V_{SCE} with cation fractions of constituent elements in the passive films shown in Figure 14 and Table X. For all CCAs and growth conditions, Cr(III), Ti(IV), and (in the case of Mo-1.1 and Mo-3.2) Mo(IV)/Mo(VI) are present in the passive film at higher concentrations than their respective bulk compositions. Fe(II)/Fe(III) and Ni(II) are depleted in the passive film relative to alloy content for all cases. Al(III) is present for all CCAs, but depleted in the film compared to the bulk in the Mo-0 alloy at pH 4 and the Mo-3.2 alloy at pH 10. For all CCAs, Cr(III) is the most prominent constituent in the passive film. However, the concentration of Cr(III) in the passive film decreases both with Mo concentration and pH. Although Fe(II)/Fe(III) and Ni(II) remained depleted in the film grown on Mo-3.2 at pH 10 relative to bulk composition, the surface cation fractions increased relative to the film grown at pH 4. Such increases were compensated by decreases in Al(III), Cr(III), Mo(IV)/Mo(VI), and Ti(IV), suggesting the film more closely resembles bulk alloy composition. However, such decreases do not necessarily suggest instability of such elements in basic conditions.

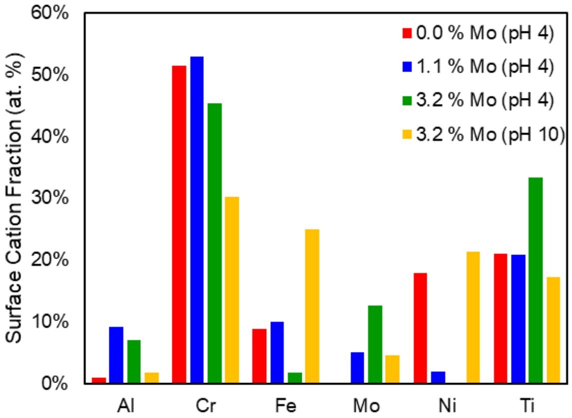

Figure 14: Surface cation fractions calculated from XPS characterization of CCA passive films formed during 10 ks exposure to -0.2 V_{SCE} in 0.1 M NaCl pH 4 and 0.1 M NaCl pH 10 following cathodic reduction pre-treatment (600 s, − 1.3 V_{SCE}).

Table X: Surface cation fractions obtained from the XPS fits shown in Figure 15. Bolded terms indicate surface cation fractions higher than the bulk alloy composition suggesting enrichment.

Alloy	**Al**	**Cr**	**Fe**	**Mo**	**Ni**	**Ti**
Mo-0 pH 4	0.9%	**51.4%**	8.9%	0.0%	17.8%	**21.0%**
Mo-1.1 pH 4	**9.2%**	**53.0%**	10.0%	**5.1%**	1.9%	**20.8%**
Mo-3.2 pH 4	**7.0%**	**45.3%**	1.7%	**12.6%**	0.0%	**33.4%**
Mo-3.2 pH 10	1.7%	**30.2%**	24.9%	**4.6%**	21.4%	**17.2%**

Figure 15 shows fit XPS spectra for constituent elements. Features characteristic of oxidized species as both hydroxides and oxides, as well as unoxidized metal are present, indicating the film is thin enough to permit observation of an attenuated signal from the bulk metal. Deconvolution of the Cr spectra suggests the presence of Cr(III) oxides, hydroxides, and that complex oxides such as possible spinels ($FeCr_2O_4$ and $NiCr_2O_4$) cannot be ruled out in the passive film. The fitting suggests formation of a Cr-Ni spinel may contribute to the stability of Ni(II) and Cr(III) in the passive film formed in the pH 10 environment, although the chemical shifts, which are determined by local interactions, are insufficient to determine long-range structure. The surface cation fraction of Ni(II) increases with a decrease in Mo

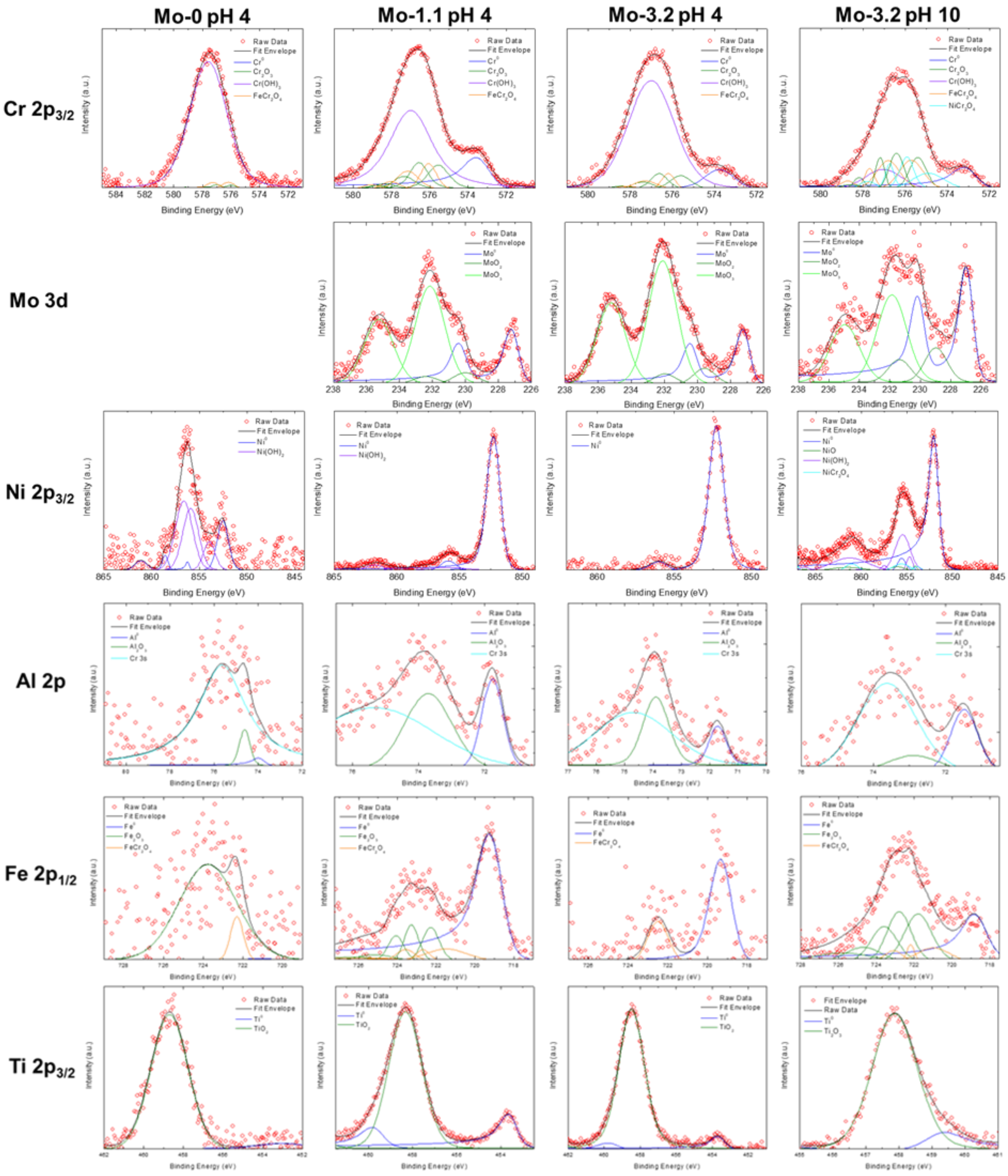

Figure 15: XPS spectra of CCA passive films formed during 10 ks exposure to -0.2 V_{SCE} in 0.1 M NaCl pH 4 and 0.1 M NaCl pH 10 following cathodic reduction pre-treatment (600 s, − 1.3 V_{SCE}). Intensities are scaled to maximum counts for each spectra as quantitative values may vary due to external factors such as surface contamination.

concentration in pH 4, with the Cr-Ni spinel no longer suggested for Mo-3.2 in pH 4. In addition to Cr(III), significant concentrations of Ti are present as Ti(IV) oxide. The Mo signal collected from the passive film of Mo-3.2 grown at pH 4 is nearly entirely attributable to the Mo(VI) valence while the film formed at pH 10 has a lower Mo surface cation fraction with a larger proportion attributable to Mo(0) and Mo(IV) valences. The 13.9 at. % surface cation fraction for Mo on the Mo-3.2 film formed at pH 4 suggests a significant role of Mo in the passivation process. Additionally, the film contains more Fe and Ni, and less overall Mo when grown in pH 10 solution than in pH 4, consistent with oxide and hydroxide thermodynamic stability. These results follow those shown by AESEC, where Fe and Ni dissolution rates were below the detection limit while Mo dissolution was observed at pH 10 (Figure 12b). At pH 4, only Fe and Ni dissolution is observed (Figure 12a), which is in agreement with the comparatively lower Fe(II)/Fe(III) and Ni(II) cation fractions in the passive film. In summary, while the films are consistently enriched in passive species predicted to be thermodynamically stable, Mo concentration plays a prominent role in altering the amount of each species.

4.0 Discussion

The selected alloys evaluate the effects of Mo additions from 0-3.2 at. % within the Al-Cr-Fe-Ni-Ti CCA systems. The alloying strategy preserves the ratios between passivating elements Al, Cr, and Ti and the composition of each of the three elements varies by less than 0.5 at. % between the CCAs (Table I). Thus, effects on corrosion resistance are attributable to Mo content. Furthermore, the Cr concentration of the investigated alloys was kept below critical thresholds for passivation in Fe-Cr (~13 at. % Cr [66]) and Ni-Cr (~12 at. % Cr [67]) alloys with Al and Ti also maintained below traditional Fe binary thresholds (~15 at. % Al [68], >47 at. % Ti [69]). Passivity below such Fe-Cr thresholds has been shown to be obtainable due to the addition of Al and Ti [7] with the optimal Al-Cr ratio informed by work in similar CCA systems [70].

The present study probes the effect of Mo alloying in the passive film (i.e., in Na_2SO_4), pit stabilization, and passive film growth in NaCl solutions at pH 4 and 10. Mo is present in the alloys mainly in the FCC matrix (Table II) and is suggested by XPS to be present in Mo(0), Mo(IV), and Mo(VI) valence states (Figure 15). Utilization of pH 4 and 10 solutions further compares the effect of Mo with different thermodynamically expected fates (solid state stability versus dissolved aqueous anions) [64]. Stable or metastable Mo oxides are suggested in the oxide at anodic potentials near pH 4 whilst at pH 10, E-pH diagrams suggest Mo to be thermodynamically stable as MoO_4^{2-} [64]. This implies that Mo may operate to inhibit pitting in its traditional function as a dissolution suppressor. However, the presence of multiple valence states introduces the possibility of aliovalent Mo doping in the passive film that can create more ionic defects which may affect passive film dissolution separate from pitting phenomena [27]. Corrosion resistant passive film formation at OCP is found to exhibit the best attributes for the solution-exposed air-formed Mo-0 passive film (Figure 8, Table VI). For instance, R_P of the Mo-0 solution-exposed air-formed oxide is higher following 20-day immersion (Figure 10a, Tables VI, VIII) and the mean i_{pass} in chloride is generally the lowest of the evaluated CCAs in this work (Figure 5, Table IV). In contrast, Mo-3.2 is suggested to be the most corrosion resistant with regards to pitting susceptibility indicated by the most positive pitting potential at pH 4 (Figure 5, Table IV).

4.1 Effect of Mo on Microstructural Partitioning and Localized Breakdown

Both the average E_{pit} and probabilistic distribution suggest improved resistance to film breakdown under acidic conditions (Figure 5b). More positive E_{rep} values for Mo-3.2 than Mo-0 were observed in both environments with less variability than changes in E_{pit}, indicating that Mo may enhance repassivation (Figures 5c, 5h). Such findings suggest that Mo plays a more prominent role in pit propagation and stability than initiation. Mo enrichment suggested by decreased dissolution rates at transpassive potentials relative to bulk composition (Figure 6) may be attributable to the local decrease in pH leading to the deposition of Mo-rich corrosion products [71]. Mo has been reported to help reform a stable passive film in mild acids after surface activation caused either by the applied cathodic potential [72] or by mechanical scratching [24]. In this case, the Mo-containing passive film may serve as a catalyst for the hydrogen evolution reaction [73] resulting in a high cathodic current density in this potential domain. High Mo valence within the passive film may add charge carriers which in turn support charge transfer reactions such as the oxygen evolution reaction [35]. For instance, Mo(IV)/(VI) doping in Cr(III) oxide leads to cation vacancies and/or excess free electrons [27].

Frequent pitting at the interface between FCC and $L2_1$ (Figure 7) is observed, identifying a microstructural feature responsible for pit initiation. This location suggests a role of grain boundaries or phase interfaces as possible contributors to the weakening of localized corrosion resistance, potentially due to the formation of defects in the passive film [74]. While increasing Mo concentration decreases pit initiation frequency in single-phase stainless steels and Ni-Cr-Mo alloys [75, 76], interface pitting may hinder the effect of Mo. Interfaces likely have less prominent effects on repassivation than initiation as the pit is grown well beyond the interface. The beneficial effects of Mo on pit repassivation (Figure 5) suggest Mo slows propagation or enhances repassivation unhindered by the interface. Furthermore, the increase in compositional partitioning in the alloy at higher Mo concentrations (Table II) may indicate localized depletion of passivating elements (e.g. Ti, Al) that may harm resistance to localized corrosion, particularly at or near the bulk metal phase interfaces (and resultant oxide film interfaces) where the film may be vulnerable to breakdown [21, 77]. Further evaluation with high resolution Auger electron spectroscopy of the variation in both bulk metal and passive film chemistry across the phase interface, including the position and local enrichment of Mo, will be discussed in a forthcoming publication. Adverse effects of partitioning may limit the otherwise beneficial effects of Mo. This is shown by lowering of E_{pit} distributions with increasing Mo concentration in basic environments, where Mo dissolution is likely and adverse microstructural effects may be more prominent (Figures 5b, 5g). Despite clear effects of Mo on microstructural partitioning, neither imaging of corroded surfaces (Figure 9) nor transpassive elemental dissolution rates (Table V) suggest preferential dissolution of either phase.

Higher concentrations of Mo in the CCA correspond to slightly increased levels of phase partitioning, where the concentration of an element in the second phase differs from that in the matrix to a greater extent than in the case of CCAs with less Mo, illustrating a secondary, but still important, effect of Mo on phase composition. The σ phase that has been previously shown to harm corrosion resistance with increasing Mo in CCAs [20, 41, 43] was not formed, likely due to the comparatively low concentration of both Cr and Mo. Mo is enriched in the FCC matrix phase, despite its prominent role as a ferritic stabilizer. Such lateral variation of Mo content in the passive film chemistry has been shown to promote selective dissolution in CoCrFeMoNi [78], but such behavior is not observed in the evaluated system (Figure 9).

Although Mo is not enriched in the $L2_1$ second phase, Al, Ni, and Ti generally increase in concentration in the second phase with increasing Mo concentrations (Table II). For example, the Ti content in the $L2_1$ phase of Mo-3.2 is over three times the Ti content in the matrix, whereas the Ti content in the $L2_1$ phase of Mo-0 is approximately twice that of the matrix. Similarly, Al concentrations in the $L2_1$ phase of Mo-0 are 2.5 times those of the matrix whereas the ratio between the same phases of Mo-3.2 is over four. This follows previous trends of Mo enrichment in phases differing from those enriched in Ti [41] and Al [40] in similar CCAs, with both elements possibly being driven away from the Mo-enriched FCC phase by the unfavorable enthalpies of mixing [79]. The enrichment of Ti and Al in phases depleted of Mo, rather than the FCC phase which is enriched Cr and Mo, may limit the ability for synergetic behavior in the passive film, particularly given high importance of Ti in the passivation process suggested by surface cation fractions (Figure 14, Table X).

The beneficial contributions of Mo must be balanced with potential effects of phase partitioning of second phase-enriched elements on localized corrosion, adding a layer of complexity to previously established trends in the single-phase Fe-Cr-Mo and Ni-Cr-Mo systems. Unlike the proposed beneficial effects of low Mn concentrations on elemental degree of partitioning, poor passivation, and overall corrosion resistance observed in a similar CCA system [18], Mo concentrations must be limited to avoid detrimental levels of partitioning. The addition of Mn or other FCC stabilizing elements could help increase the maximum allowable Mo content without harmful chemical segregation in the microstructure, but corrosion resistance may also be harmed by poor Mn passivation [80, 81]. Although Ni passivation is suppressed, low transpassive Ni dissolution rates (Table V) may suggest alternative fates such as enrichment at the metal-oxide interface [55, 82].

The effect of Mo on Ni partitioning is noteworthy as the binary enthalpy of mixing between Mo and Ni is higher than that between Mo and other system elements [79]. The unfavorable interaction between Mo and Ni may preferentially cause Ni to enrich in the Mo-depleted second phase. Unlike the case of Al and Ti, increased Mo concentration does not consistently increase the degree of Ni partitioning, although the uncharacteristically low Ni composition in the FCC phase of Mo-0 highlights uncertainty in the EDS point scans. In addition to microstructural factors, increasing Mo concentrations also reduced the concentration of $Ni(OH)_2$, following trends in the Ni-Cr-Mo system proposed by Lutton et al. [32] where Ni was also less present in the passive film due to the enhancement of other passivating elements such as Cr.

4.2 Effect of Mo on Passive Film Composition

Mo is also considered with respect to its effects on global passive film chemistry. Cr is the primary passivating species in all three CCAs and in both pH values. However, the passive film concentration varies across the three alloys. Mo is not a primary passivator in any of the evaluated CCAs, although in both Mo-containing CCAs, the passive film is enriched in Mo(IV)/Mo(VI) at the film-electrolyte interface relative to bulk composition at similar ratios (Figure 14, Table X). Notably, Mo content may be lower at film depths approaching the metal-film interface, given the tendency of Mo to enrich within outer layers of passive films formed on similar alloys [7, 27, 47, 78, 83-86]. Significant presence of Mo in the passive film is unsurprising given the thermodynamic stability of Mo oxides in a pure Mo system at pH 4 near -0.2 V_{SCE} [64]. Mo(IV)/Mo(VI) cations are still suggested to be present in the passive film, although at lower concentrations in the Mo-3.2 film formed in pH 10 solution even though Mo oxides are not thermodynamically predicted to be stable. Despite low concentration in the bulk alloy, the presence of

Mo in the alloy affects the passive film chemistry and possibly ionic defect status. As Mo concentration increases in the evaluated CCAs, Cr(III), Fe(II)/Fe(III), and Ni(II) content decrease while Al(III), Mo(VI), and Ti(VI) increase in the electrochemically formed passive films (Figure 14, Table X).

Increased Mo concentration promoted Cr(III) passivation in the Ni-Cr-Mo system explored by Lutton et al. [27, 87], particularly in Cl^- environments where Ni dissolved. In contrast, the CCAs with the highest Mo concentrations have the lowest surface cation fraction of Cr in the passive film formed in the pH 4 environment despite still being enriched relative to bulk alloy composition (Figure 14, Table X). While Ti preferentially partitions to the $L2_1$ phase, enough is still present in the FCC phase to affect global passive film chemistry. Thus, the limitation of the Cr(III) content in passive film of the CCA system may also be attributed to the high stability of Ti(IV) in the passive film. In the Ni-Cr-Mo system, Cr_2O_3 is the most stable oxide (ΔG_f° = -1050 kJ/mol) [88] whereas in the CCAs evaluated, Ti may be a preferential site for oxidation given the lower free energy of formation on a per cation basis of TiO_2 (ΔG_f° = -889 kJ/mol) [88]. Likewise, very little Al_2O_3 (ΔG_f° = -1580 kJ/mol) [88] was observed in Mo-0 while the film grown on Mo-3.2 was enriched in Al(III). Additionally, Mo-3.2 did not form any observable $Ni(OH)_2$ species in the passive film (ΔG_f° = -447 kJ/mol) [89] and had the highest combined concentration of Al(III), Cr(III), and Ti(IV) species. Thus, across both systems, Mo may be suggested to promote the presence of more stable oxide species.

Mo may affect the passive film composition by acting as an aliovalent dopant. XPS fitting (Figure 15) suggests that while oxidized Mo is dominated by Mo(VI) cations, Mo(IV) is also present. Mo(V) may have also been present given frequent observation in Ni-Cr-Mo alloys [28, 35, 87, 90], but was not identified, possibly due to overlap with other valence states. In the Ni-Cr-Mo system, Mo(IV) appears to stabilize Cr passivation while Mo(VI) cations are considered more likely to dissolve [72], however conflicting results have been suggested in $CoCrFeMnNiMo_x$ CCAs [43]. The higher valence state Mo cations may be reduced to lower valence states to locally stabilize the higher valence Ti(IV) cations relative to Cr(III) and Al(III), potentially through affecting the local stability of O vacancies [91]. During the growth of the oxide in 0.1 M NaCl pH 4 (Figure 11), the current density was lowest for Mo-3.2, suggesting slower passivation kinetics along with the well-known properties of aliovalent Mo cations [27].

A significant local enrichment of Mo(0) might support Mo acting as an non-oxidized dissolution blocker [24], whereas preservation or local enrichment of the oxidized states may favor mechanisms dependent on passivated Mo [27, 30, 31, 47]. Both valence states are suggested to be present within or near the passive film by XPS (Figure 15). However, under both Mo(0)-based mechanisms, Mo depletion in the $L2_1$ phase would limit the ability of the CCAs to resist localized corrosion within the $L2_1$ phase or at the

FCC-$L2_1$ interface and mechanisms dependent on Mo dissolution must also be considered. Mo dissolution occurred across of a range of potentials, most noticeably in the cathodic region due to the well-known stability of MoO_4^{2-} in alkaline solutions [64]. However, this was attributed to dissolution of the air-formed oxide, which has been shown to have high concentrations of Mo in similar CCAs [7]. Additionally, dissolution of air-formed oxides has yielded similar cathodic dissolution rates in the Ni-Cr-Mo system [72]. The likely proposed mechanism relating Mo dissolution to corrosion resistance is that MoO_4^{2-} ions act as an inhibitor to limit pit stability [23, 92], a possibility indicated by significant Mo dissolution being observed via AESEC (Figures 6, 12), especially in pH 10 solution. In this case, Mo does not have to originate in the $L2_1$ phase or near the interface, but can be supplied from the FCC phase and transported via comparatively more rapid liquid phase diffusion.

4.3 Comparative Effects of Mo under Acidic and Basic Conditions

Elemental dissolution trends measured with AESEC generally follow those predicted by the electrochemical stability of pure constituent elements for a given solution pH [64]. Pure Fe and Ni are predicted to dissolve at pH 4 and form insoluble species at pH 10 [64] at -0.2 V_{SCE}. E-pH diagrams have predicted stability of both Ni oxide [64] and Ni-Cr spinel [93, 94] is more favorable under basic conditions. Therefore, XPS intensity attributable to Ni-containing complex oxide and single-cation passive species significantly increased (Figure 14, Table X) while corresponding Ni dissolution rates decreased in basic conditions (Figure 12). Fe and Ni dissolve at pH 4 while they are below the detection limit at pH 10 at this potential for CCAs investigated in this work (Figures 12). Fe and Ni dissolve at a lower potentials than the other elements at both pH (Figure 6), and are depleted in the passive film at pH 4, as observed via XPS (Figure 14, Table X). Despite thermodynamic instability, limited presence of Ni and Fe in the passive films formed at pH 4 indicate metastable oxide presence and/or stability enhanced by solubility with additional cations.

Mo dissolves at much higher rates in basic solutions (Figure 11), likely due to the stability of the MoO_4^{2-} ion [64]. The increased stability of Mo oxides in acids corresponds with an increase in the surface cation fractions attributable to oxidized Mo in the Mo-3.2 film grown in pH 4 relative to when grown in pH 10 solution (Figure 14, Table X). The decreased Mo enrichment in the passive film with increasing pH follows previously established trends in 316L [95], Ni-Cr-Mo [32, 87], and the CoCrFeMoNi CCA [96]. Furthermore, Mo metal is stable at higher potentials in acids than bases [64], potentially explaining the cathodic dissolution of Mo observed in the basic environment that was not observed in the acid (Figures 6, 7).

During potentiostatic passive film growth, the current density is highest for the Mo-free sample in pH 4 solution (Figure 11a), indicating that Mo may result in an enhanced passive film formation. Alternatively, current density shows inconsistent trends with Mo concentration in pH 10 solution (Figure 11b). Potentiostatic EIS further verifies that Mo-0 had the lowest R_P at pH 4 and that of Mo-3.2 was the lowest at pH 10 (Figure 13).

Increasing Mo concentration improves pitting resistance more prominently in acidic environments (Figure 5, Table IV), similar to the case of the $Mo_{0.6}CoCrFe$ medium entropy alloy developed by Shuang et al. [97]. However, the improvement in corrosion resistance with decreasing pH observed is not present at a statistically significant level in the presently evaluated CCA series, potentially due to the lower Mo concentrations in the tested CCAs (0-3.2 at. %) than in $Mo_{0.6}CoCrFe$ (16.7 at. % Mo). The same effect is not observed with E_{rep}, where Mo resulted in higher R_P regardless of pH. Notably, the E_{rep} distribution of Mo-1.1 resembles that of Mo-3.2 in the pH 10 environment, which shows good repassivation behavior, and that of Mo-0 in pH 4, which shows poor repassivation behavior. This may indicate a lower Mo concentration is necessary for significant repassivation benefits in basic conditions.

5.0 Conclusions

Three $Al_{0.3}Cr_{0.5}Fe_2Mo_xNi_{1.5}Ti_{0.3}$ (x = 0, 0.05, 0.15) CCAs with Mo concentrations of 0, 1.1, and 3.2 at. % were synthesized and characterized to elucidate connections between microstructure and corrosion resistance with the main motivation to investigate the benefits of Mo in Cr-lean CCAs containing Al and Ti as passivators. The following conclusions were obtained:

- An FCC matrix enriched in Fe, Cr, and Mo (when added as alloying element) with $L2_1$ regions enriched in Al, Ti, and Ni was present for all CCAs. Mo is found to have indirect effects on corrosion through its impact on elemental partitioning after heat treatment at 1070 ˚C. The microstructural partitioning affects the nature of films grown on CCAs with increased Mo concentration, particularly with regards to the concentration of elements that preferentially partition to the second phase such as Ti. Such changes in element partitioning are shown to alter passive film chemistry, and thus have a significant effect on the corrosion behavior that must be accounted for within the alloy design process.
- The resistance to localized corrosion was improved with increased Mo concentration both during potentiodynamic polarization and long-term immersion, most noticeably through improvements

in the repassivation potential. Pitting often occurred at the FCC-$L2_1$ interfaces, particularly in low-Mo CCAs, but neither phase was vulnerable to selective dissolution.

- Mo also affects passivity and passive film chemistry. Decreased passive current densities and more positive repassivation potential with Mo content may suggest Mo slows corrosion reaction kinetics through solid state effects in the passive film. Species found in the passive films of CCAs with higher Mo concentration generally had more negative standard free energies, and did not appear to be limited in passivation by local enrichments in the microstructure. The overall corrosion resistance was generally worse than 316L in both acidic and basic environments, which may be attributable to the lean Cr contents compared to the high Cr content 316L as well as the microstructure containing two phases with corresponding interfaces.
- Trends in corrosion behavior with Mo content are less prominent in Al and Ti containing CCAs than single-phase alloy dependent on only Cr for passivity. The CCA design space introduces a variety of effects of alloying elements such as Mo with both metallurgical and passivity roles that have secondary effects on passivation that are not observed in single-phase or less complex alloys. Despite the presence of such effects on phase composition, Mo improves overall corrosion in the evaluated two-phase CCA series and is suggested to be beneficial for the design of corrosion resistant multi-phase CCAs.

Acknowledgements

This work was supported by the United States Office of Naval Research under grant # N00014-19-1-2420. Use of the Empyrean^{TM} Diffractometer, Quanta 650^{TM} SEM, and PHI VersaProbe III^{TM} XPS was made possible by the University of Virginia Nanomaterials Characterization Facility. The PHI VersaProbe III was procured under NSF award # 162601. Author K. Ogle and the AESEC equipment were supported by Agence Nationale de Recherche, award # ANR-20-CE08-0031 (TAPAS 2020). Kaitlyn Anderson contributed to the electrochemical characterization. S. Joseph Poon contributed to funding acquisition and sample synthesis.

References

[1] Y. Qiu, S. Thomas, M.A. Gibson, H.L. Fraser, N. Birbilis, Corrosion of high entropy alloys, npj Materials Degradation, 1 (2017) 15.

[2] J.R. Scully, S.B. Inman, A.Y. Gerard, C.D. Taylor, W. Windl, D.K. Schreiber, P. Lu, J.E. Saal, G.S. Frankel, Controlling the corrosion resistance of multi-principal element alloys, Scripta Materialia, 188 (2020) 96-101.

[3] D.B. Miracle, O.N. Senkov, A critical review of high entropy alloys and related concepts, Acta Materialia, 122 (2017) 448-511.

[4] M.-H. Tsai, J.-W. Yeh, High-Entropy Alloys: A Critical Review, Materials Research Letters, 2 (2014) 107-123.

[5] E.P. George, D. Raabe, R.O. Ritchie, High-entropy alloys, Nature Reviews Materials, 4 (2019) 515-534.

[6] R. Feng, C. Lee, M. Mathes, T.T. Zuo, S. Chen, J. Hawk, Y. Zhang, P. Liaw, Design of Light-Weight High-Entropy Alloys, Entropy, 18 (2016) 333.

[7] S.B. Inman, D. Sur, J. Han, K. Ogle, J.R. Scully, Corrosion Behavior of a Compositionally Complex Alloy Utilizing Simultaneous Al, Cr, and Ti Passivation, Corroison Science, 217 (2023) 111138.

[8] Y. Qiu, R. Liu, T. Gengenbach, O. Gharbi, S. Choudhary, S. Thomas, H.L. Fraser, N. Birbilis, Real-time dissolution of a compositionally complex alloy using inline ICP and correlation with XPS, npj Materials Degradation, 4 (2020) 7.

[9] C.P. Lee, C.C. Chang, Y.Y. Chen, J.W. Yeh, H.C. Shih, Effect of the aluminium content of AlxCrFe1.5MnNi0.5 high-entropy alloys on the corrosion behaviour in aqueous environments, Corrosion Science, 50 (2008) 2053-2060.

[10] B.-y. Li, K. Peng, A.-p. Hu, L.-p. Zhou, J.-j. Zhu, D.-y. Li, Structure and properties of FeCoNiCrCu0.5Alx high-entropy alloy, Transactions of Nonferrous Metals Society of China, 23 (2013) 735-741.

[11] Y. Qiu, S. Thomas, D. Fabijanic, A.J. Barlow, H.L. Fraser, N. Birbilis, Microstructural evolution, electrochemical and corrosion properties of AlxCoCrFeNiTiy high entropy alloys, Materials & Design, 170 (2019) 107698.

[12] Z. Tang, L. Huang, W. He, P. Liaw, Alloying and Processing Effects on the Aqueous Corrosion Behavior of High-Entropy Alloys, Entropy, 16 (2014) 895-911.

[13] D.H. Xiao, P.F. Zhou, W.Q. Wu, H.Y. Diao, M.C. Gao, M. Song, P.K. Liaw, Microstructure, mechanical and corrosion behaviors of AlCoCuFeNi-(Cr,Ti) high entropy alloys, Materials & Design, 116 (2017) 438-447.

[14] D. Yang, Y. Liu, H. Jiang, M. Liao, N. Qu, T. Han, Z. Lai, J. Zhu, A novel FeCrNiAlTi-based high entropy alloy strengthened by refined grains, Journal of Alloys and Compounds, 823 (2020) 153729.

[15] W. Guo, J. Li, M. Qi, Y. Xu, H.R. Ezatpour, Effects of heat treatment on the microstructure, mechanical properties and corrosion resistance of AlCoCrFeNiTi0.5 high-entropy alloy, Journal of Alloys and Compounds, 884 (2021) 161026.

[16] Y. Shi, L. Collins, R. Feng, C. Zhang, N. Balke, P.K. Liaw, B. Yang, Homogenization of AlxCoCrFeNi high-entropy alloys with improved corrosion resistance, Corrosion Science, 133 (2018) 120-131.

[17] D. Choudhuri, T. Alam, T. Borkar, B. Gwalani, A.S. Mantri, S.G. Srinivasan, M.A. Gibson, R. Banerjee, Formation of a Huesler-like L21 phase in a CoCrCuFeNiAlTi high-entropy alloy, Scripta Materialia, 100 (2015) 36-39.

[18] S.B. Inman, J. Han, A.Y. Gerard, J. Qi, M.A. Wischhusen, S.R. Agnew, S.J. Poon, K. Ogle, J.R. Scully, Effect of Mn Content on the Passivation and Corrosion of Al0.3Cr0.5Fe2MnxMo0.15Ni1.5Ti0.3 Compositionally Complex Face-Centered Cubic Alloys, Corrosion, 78 (2021) 32-48.

[19] K. Ishikawa, I. Ohnuma, R. Kainuma, K. Aoki, K. Ishida, Phase equilibria and stability of Heusler-type aluminides in the NiAl–Ni2AlTi–Ni2AlY (Y: V, Cr or Mn) systems, Journal of Alloys and Compounds, 367 (2004) 2-9.

[20] W. Wang, J. Wang, H. Yi, W. Qi, Q. Peng, Effect of Molybdenum Additives on Corrosion Behavior of (CoCrFeNi)(100-x)Mo(x) High-Entropy Alloys, Entropy (Basel), 20 (2018) 908.
[21] Y. Shi, L. Collins, N. Balke, P.K. Liaw, B. Yang, In-situ electrochemical-AFM study of localized corrosion of AlxCoCrFeNi high-entropy alloys in chloride solution, Applied Surface Science, 439 (2018) 533-544.
[22] M. Klimmeck, A study of the kinetics of passive layer formation on Cr-Mo alloys, Electrochimica Acta, 25 (1980) 1375-1381.
[23] K. Sugimoto, Y. Sawada, The role of molybdenum additions to austenitic stainless steels in the inhibition of pitting in acid chloride solutions, Corrosion Science, 17 (1977) 425-445.
[24] R.C. Newman, The dissolution and passivation kinetics of stainless alloys containing molybdenum—1. Coulometric studies of Fe-Cr and Fe-Cr-Mo alloys, Corrosion Science, 25 (1985) 331-339.
[25] K. Hashimoto, K. Asami, K. Teramoto, An X-ray photo-electron spectroscopic study on the role of molybdenum in increasing the corrosion resistance of ferritic stainless steels in HC1, Corrosion Science, 19 (1979) 3-14.
[26] Y. Shi, B. Yang, P.K. Liaw, Corrosion-Resistant High-Entropy Alloys: A Review, Metals, 7 (2017) 43.
[27] K. Lutton Cwalina, C.R. Demarest, A.Y. Gerard, J.R. Scully, Revisiting the effects of molybdenum and tungsten alloying on corrosion behavior of nickel-chromium alloys in aqueous corrosion, Current Opinion in Solid State and Materials Science, 23 (2019) 129-141.
[28] N. Ebrahimi, M.C. Biesinger, D.W. Shoesmith, J.J. Noël, The influence of chromium and molybdenum on the repassivation of nickel-chromium-molybdenum alloys in saline solutions, Surface and Interface Analysis, 49 (2017) 1359-1365.
[29] P.I. Marshall, G.T. Burstein, Effects of alloyed molybdenum on the kinetics of repassivation on austenitic stainless steels, Corrosion Science, 24 (1984) 463-478.
[30] J.D. Henderson, X. Li, F.P. Filice, D. Zagidulin, M.C. Biesinger, B. Kobe, D.W. Shoesmith, K. Ogle, J.J. Noël, Investigating the Role of Mo and Cr during the Activation and Passivation of Ni-Based Alloys in Acidic Chloride Solution, Journal of The Electrochemical Society, 168 (2021) 021509.
[31] G. Tranchida, F. Di Franco, M. Santamaria, Role of Molybdenum on the Electronic Properties of Passive Films on Stainless Steels, Journal of The Electrochemical Society, 167 (2020) 061506.
[32] K.L. Cwalina, H.M. Ha, N. Ott, P. Reinke, N. Birbilis, J.R. Scully, In Operando Analysis of Passive Film Growth on Ni-Cr and Ni-Cr-Mo Alloys in Chloride Solutions, Journal of The Electrochemical Society, 166 (2019) C3241-C3253.
[33] A.C. Lloyd, J.J. Noël, S. McIntyre, D.W. Shoesmith, Cr, Mo and W alloying additions in Ni and their effect on passivity, Electrochimica Acta, 49 (2004) 3015-3027.
[34] K. Gusieva, K.L. Cwalina, W.H. Blades, G. Ramalingam, J.H. Perepezko, P. Reinke, J.R. Scully, Repassivation Behavior of Individual Grain Facets on Dilute Ni–Cr and Ni–Cr–Mo Alloys in Acidified Chloride Solution, The Journal of Physical Chemistry C, 122 (2018) 19499-19513.
[35] A. Larsson, A. Grespi, G. Abbondanza, J. Eidhagen, D. Gajdek, K. Simonov, X. Yue, U. Lienert, Z. Hegedüs, A. Jeromin, T.F. Keller, M. Scardamaglia, A. Shavorskiy, L.R. Merte, J. Pan, E. Lundgren, The Oxygen Evolution Reaction Drives Passivity Breakdown for Ni–Cr–Mo Alloys, Advanced Materials, 35 (2023) 2304621.
[36] D.A. Stout, J.B. Lumsden, R.W. Staehle, An Investigation of Pitting Behavior of Iron-Molybdenum Binary Alloys, Corrosion, 35 (1979) 141-147.
[37] X. Wang, D. Mercier, S. Zanna, A. Seyeux, L. Perriere, M. Laurent-Brocq, I. Guillot, V. Maurice, P. Marcus, Effects of Chloride Ions on Passive Oxide Films Formed on Cr-Fe-Co-Ni(-Mo) Multi-Principal Element Alloy Surfaces, Journal of The Electrochemical Society, 170 (2023) 041506.
[38] Y. Liu, Y. Xie, S. Cui, Y. Yi, X. Xing, X. Wang, W. Li, Effect of Mo Element on the Mechanical Properties and Tribological Responses of CoCrFeNiMox High-Entropy Alloys, Metals, 11 (2021) 486.

[39] C. Dai, Y. Fu, Y. Pan, Y. Yin, C. Du, Z. Liu, Microstructure and mechanical properties of FeCoCrNiMo0.1 high-entropy alloy with various annealing treatments, Materials Characterization, 179 (2021) 111313.
[40] J.M. Zhu, H.M. Fu, H.F. Zhang, A.M. Wang, H. Li, Z.Q. Hu, Microstructures and compressive properties of multicomponent AlCoCrFeNiMox alloys, Materials Science and Engineering: A, 527 (2010) 6975-6979.
[41] Y.L. Chou, J.W. Yeh, H.C. Shih, The effect of molybdenum on the corrosion behaviour of the high-entropy alloys Co1.5CrFeNi1.5Ti0.5Mox in aqueous environments, Corrosion Science, 52 (2010) 2571-2581.
[42] A.A. Rodriguez, J.H. Tylczak, M.C. Gao, P.D. Jablonski, M. Detrois, M. Ziomek-Moroz, J.A. Hawk, Effect of Molybdenum on the Corrosion Behavior of High-Entropy Alloys CoCrFeNi2 and CoCrFeNi2Mo0.25 under Sodium Chloride Aqueous Conditions, Advances in Materials Science and Engineering, 2018 (2018) 3016304.
[43] X.-L. Shang, W. Zhijun, Q.-F. Wu, J.-C. Wang, J.-J. Li, J.-K. Yu, Effect of Mo Addition on Corrosion Behavior of High-Entropy Alloys CoCrFeNiMox in Aqueous Environments, Acta Metallurgica Sinica (English Letters), 32 (2018).
[44] C. Ren, K. Sun, Y.F. Jia, N.Z. Zhang, Y.D. Jia, G. Wang, Effect of Mo addition on the microstructural evolution and mechanical properties of Fe–Ni–Cr–Mn–Al–Ti high entropy alloys, Materials Science and Engineering: A, 864 (2023) 144579.
[45] Linder, Clara and Rao, Smita G. and Boyd, Robert and Greczynski, Grzegorz and Eklund, Per and Munktell, Sara and le Febvrier, Arnaud and Björk, Emma M., Effect of Mo Content on the Corrosion Resistance of CoCrFeMoxNi Thin Films in Sulfuric Acid. Available at SSRN: https://ssrn.com/abstract=4481216 or http://dx.doi.org/10.2139/ssrn.4481216.
[46] Z. Niu, Y. Wang, C. Geng, J. Xu, Y. Wang, Microstructural evolution, mechanical and corrosion behaviors of as-annealed CoCrFeNiMox (x = 0, 0.2, 0.5, 0.8, 1) high entropy alloys, Journal of Alloys and Compounds, 820 (2020) 153273.
[47] X. Wang, D. Mercier, S. Zanna, A. Seyeux, L. Perriere, M. Laurent-Brocq, I. Guillot, V. Maurice, P. Marcus, Origin of enhanced passivity of Cr–Fe–Co–Ni–Mo multi-principal element alloy surfaces, npj Materials Degradation, 7 (2023) 13.
[48] D. Sur, S.B. Inman, K.L. Anderson, J. Qi, M. Barbiari, J.R. Scully, Passivation behavior of Fe-Cr-Al-Ti alloys in sulfate containing aqueous environments, In Progress.
[49] B. Cantor, I.T.H. Chang, P. Knight, A.J.B. Vincent, Microstructural development in equiatomic multicomponent alloys, Materials Science and Engineering: A, 375-377 (2004) 213-218.
[50] C. Sun, R. Xiao, H. Li, Y. Ruan, Effects of phase selection and microsegregation on corrosion behaviors of Ti-Al-Mo alloys, Corrosion Science, 200 (2022) 110232.
[51] Y. Shi, B. Yang, X. Xie, J. Brechtl, K.A. Dahmen, P.K. Liaw, Corrosion of Al xCoCrFeNi high-entropy alloys: Al-content and potential scan-rate dependent pitting behavior, Corrosion Science, 119 (2017) 33-45.
[52] J.J. Bhattacharyya, S.B. Inman, M.A. Wischhusen, J. Qi, J. Poon, J.R. Scully, S.R. Agnew, Lightweight, Low Cost Compositionally Complex Multiphase Alloys with Optimized Strength, Ductility and Corrosion Resistance: Discovery, Design and Mechanistic Understandings, Submitted to Materials and Design, (2023).
[53] C.O.A. Olsson, D. Landolt, Passive films on stainless steels—chemistry, structure and growth, Electrochimica Acta, 48 (2003) 1093-1104.
[54] J. Qi, A.M. Cheung, S.J. Poon, High Entropy Alloys Mined From Binary Phase Diagrams, Scientific Reports, 9 (2019) 15501.

[55] A.Y. Gerard, J. Han, S.J. McDonnell, K. Ogle, E.J. Kautz, D.K. Schreiber, P. Lu, J.E. Saal, G.S. Frankel, J.R. Scully, Aqueous passivation of multi-principal element alloy Ni38Fe20Cr22Mn10Co10: Unexpected high Cr enrichment within the passive film, Acta Materialia, 198 (2020) 121-133.
[56] ASTM, Standard Guide for Applying Statistics to Analysis of Corrosion Data, in, 2010.
[57] B.A. Kehler, G.O. Ilevbare, J.R. Scully, Crevice Corrosion Stabilization and Repassivation Behavior of Alloy 625 and Alloy 22, Corrosion, 57 (2001) 1042-1065.
[58] B.A. Kehler, J.R. Scully, Role of Metastable Pitting in Crevices on Crevice Corrosion Stabilization in Alloys 625 and 22, Corrosion, 61 (2005) 665-684.
[59] K. Ogle, Atomic Emission Spectroelectrochemistry: Real-Time Rate Measurements of Dissolution, Corrosion, and Passivation, Corrosion, 75 (2019) 1398-1419.
[60] M.C. Biesinger, B.P. Payne, A.P. Grosvenor, L.W.M. Lau, A.R. Gerson, R.S.C. Smart, Resolving surface chemical states in XPS analysis of first row transition metals, oxides and hydroxides: Cr, Mn, Fe, Co and Ni, Applied Surface Science, 257 (2011) 2717-2730.
[61] M.C. Biesinger, L.W.M. Lau, A.R. Gerson, R.S.C. Smart, Resolving surface chemical states in XPS analysis of first row transition metals, oxides and hydroxides: Sc, Ti, V, Cu and Zn, Applied Surface Science, 257 (2010) 887-898.
[62] J. Baltrusaitis, B. Mendoza-Sanchez, V. Fernandez, R. Veenstra, N. Dukstiene, A. Roberts, N. Fairley, Generalized molybdenum oxide surface chemical state XPS determination via informed amorphous sample model, Applied Surface Science, 326 (2015) 151-161.
[63] A. Obrosov, R. Gulyaev, A. Zak, M. Ratzke, M. Naveed, W. Dudzinski, S. Weiß, Chemical and Morphological Characterization of Magnetron Sputtered at Different Bias Voltages Cr-Al-C Coatings, in: Materials, 2017.
[64] M. Pourbaix, Atlas of electrochemical equilibria in aqueous solutions, (1974).
[65] B. Hirschorn, M.E. Orazem, B. Tribollet, V. Vivier, I. Frateur, M. Musiani, Constant-Phase-Element Behavior Caused by Resistivity Distributions in Films: I. Theory, Journal of The Electrochemical Society, 157 (2010) C452.
[66] H.H. Uhlig, G.E. Woodside, Anodic Polarization of Passive and Non-passive Chromium–Iron Alloys, The Journal of Physical Chemistry, 57 (1953) 280-283.
[67] H.H. Uhlig, Electron configuration in alloys and passivity, Zeitschrift für Elektrochemie, Berichte der Bunsengesellschaft für physikalische Chemie, 62 (1958) 700-707.
[68] J. Peng, F. Moszner, J. Rechmann, D. Vogel, M. Palm, M. Rohwerder, Influence of Al content and pre-oxidation on the aqueous corrosion resistance of binary Fe-Al alloys in sulphuric acid, Corrosion Science, 149 (2019) 123-132.
[69] A.S. Lim, A. Atrens, ESCA studies of Fe-Ti alloys, Applied Physics A, 54 (1992) 500-507.
[70] W.H. Blades, B.W.Y. Redemann, N. Smith, D. Sur, M.S. Barbieri, Y. Xie, S. Lech, E. Anber, M.L. Teheri, C. Wolverton, T.M. McQueen, J.R. Scully, K. Seradzki, Tuning Chemical Short-range Order for Stainless Behavior at Reduced Chromium Concentrations in Multi-principal Element Alloys, (2023).
[71] J.D. Henderson, X. Li, D.W. Shoesmith, J.J. Noël, K. Ogle, Molybdenum surface enrichment and release during transpassive dissolution of Ni-based alloys, Corrosion Science, 147 (2019) 32-40.
[72] X. Li, J.D. Henderson, F.P. Filice, D. Zagidulin, M.C. Biesinger, F. Sun, B. Qian, D.W. Shoesmith, J.J. Noël, K. Ogle, The contribution of Cr and Mo to the passivation of Ni22Cr and Ni22Cr10Mo alloys in sulfuric acid, Corrosion Science, 176 (2020) 109015.
[73] S.H. Park, D.T. To, N.V. Myung, A review of nickel-molybdenum based hydrogen evolution electrocatalysts from theory to experiment, Applied Catalysis A: General, 651 (2023) 119013.
[74] P. Marcus, V. Maurice, Atomic level characterization in corrosion studies, Philosophical Transactions of the Royal Society A: Mathematical, Physical and Engineering Sciences, 375 (2017) 20160414.
[75] G.O. Ilevbare, G.T. Burstein, The role of alloyed molybdenum in the inhibition of pitting corrosion in stainless steels, Corrosion Science, 43 (2001) 485-513.

[76] B.A. Kehler, J. Scully, Role of Metastable Pitting in Crevices on Crevice Corrosion Stabilizationin Alloys 625 and 22, Corrosion, 61 (2005).
[77] P. Marcus, V. Maurice, H.H. Strehblow, Localized corrosion (pitting): A model of passivity breakdown including the role of the oxide layer nanostructure, Corrosion Science, 50 (2008) 2698-2704.
[78] Z. Wang, Z.-X. Liu, J. Jin, D.-Z. Tang, L. Zhang, Selective corrosion mechanism of CoCrFeMoNi high-entropy alloy in the transpassive region based on the passive film characterization by ToF-SIMS, Corrosion Science, 218 (2023) 111206.
[79] A. Takeuchi, A. Inoue, Classification of Bulk Metallic Glasses by Atomic Size Difference, Heat of Mixing and Period of Constituent Elements and Its Application to Characterization of the Main Alloying Element, MATERIALS TRANSACTIONS, 46 (2005) 2817-2829.
[80] H. Torbati-Sarraf, M. Shabani, P.D. Jablonski, G.J. Pataky, A. Poursaee, The influence of incorporation of Mn on the pitting corrosion performance of CrFeCoNi High Entropy Alloy at different temperatures, Materials & Design, 184 (2019) 108170.
[81] J. Yang, J. Wu, C.Y. Zhang, S.D. Zhang, B.J. Yang, W. Emori, J.Q. Wang, Effects of Mn on the electrochemical corrosion and passivation behavior of CoFeNiMnCr high-entropy alloy system in H2SO4 solution, Journal of Alloys and Compounds, 819 (2020) 152943.
[82] L. Wang, D. Mercier, S. Zanna, A. Seyeux, M. Laurent-Brocq, L. Perrière, I. Guillot, P. Marcus, Study of the surface oxides and corrosion behaviour of an equiatomic CoCrFeMnNi high entropy alloy by XPS and ToF-SIMS, Corrosion Science, 167 (2020) 108507.
[83] K.F. Quiambao, S.J. McDonnell, D.K. Schreiber, A.Y. Gerard, K.M. Freedy, P. Lu, J.E. Saal, G.S. Frankel, J.R. Scully, Passivation of a corrosion resistant high entropy alloy in non-oxidizing sulfate solutions, Acta Materialia, 164 (2019) 362-376.
[84] B. Lynch, Z. Wang, L. Ma, E.-M. Paschalidou, F. Wiame, V. Maurice, P. Marcus, Passivation-Induced Cr and Mo Enrichments of 316L Stainless Steel Surfaces and Effects of Controlled Pre-Oxidation, Journal of The Electrochemical Society, 167 (2020) 141509.
[85] Z. Wang, E.-M. Paschalidou, A. Seyeux, S. Zanna, V. Maurice, P. Marcus, Mechanisms of Cr and Mo Enrichments in the Passive Oxide Film on 316L Austenitic Stainless Steel, Frontiers in Materials, 6 (2019).
[86] J. Eidhagen, A. Larsson, A. Preobrajenski, A. Delblanc, E. Lundgren, J. Pan, Synchrotron XPS and Electrochemical Study of Aging Effect on Passive Film of Ni Alloys, Journal of The Electrochemical Society, 170 (2023) 021506.
[87] K. Lutton, J. Han, H.M. Ha, D. Sur, E. Romanovskaia, J.R. Scully, Passivation of Ni-Cr and Ni-Cr-Mo Alloys in Low and High pH Sulfate Solutions, Journal of The Electrochemical Society, 170 (2023) 021507.
[88] M.W. Chase, JANAF Thermochemical Tables, 4th Edition, Journal of Physical and Chemical Reference Data, in: NIST (Ed.), 1998.
[89] D.G. Archer, Thermodynamic Properties of Import to Environmental Processes and Remediation. II. Previous Thermodynamic Property Values for Nickel and Some of its Compounds, Journal of Physical and Chemical Reference Data, 28 (1999) 1485-1507.
[90] A. Larsson, G. D'Acunto, M. Vorobyova, G. Abbondanza, U. Lienert, Z. Hegedüs, A. Preobrajenski, L.R. Merte, J. Eidhagen, A. Delblanc, J. Pan, E. Lundgren, Thickness and composition of native oxides and near-surface regions of Ni superalloys, Journal of Alloys and Compounds, 895 (2022) 162657.
[91] V. Kumaravel, S. Rhatigan, S. Mathew, M.C. Michel, J. Bartlett, M. Nolan, S.J. Hinder, A. Gascó, C. Ruiz-Palomar, D. Hermosilla, S.C. Pillai, Mo doped TiO2: impact on oxygen vacancies, anatase phase stability and photocatalytic activity, Journal of Physics: Materials, 3 (2020) 025008.
[92] R.S. Lillard, M.P. Jurinski, J.R. Scully, Crevice Corrosion of Alloy 625 in Chlorinated ASTM Artificial Ocean Water, Corrosion, 50 (1994) 251-265.
[93] P. Lu, J.E. Saal, G.B. Olson, T. Li, O.J. Swanson, G.S. Frankel, A.Y. Gerard, K.F. Quiambao, J.R. Scully, Computational materials design of a corrosion resistant high entropy alloy for harsh environments, Scripta Materialia, 153 (2018) 19-22.

[94] K. Wang, J. Han, A.Y. Gerard, J.R. Scully, B.-C. Zhou, Potential-pH diagrams considering complex oxide solution phases for understanding aqueous corrosion of multi-principal element alloys, npj Materials Degradation, 4 (2020) 35.
[95] Z. Wang, Z.-Q. Zhou, L. Zhang, J.-Y. Hu, Z.-R. Zhang, M.-X. Lu, Effect of pH on the Electrochemical Behaviour and Passive Film Composition of 316L Stainless Steel, Acta Metallurgica Sinica (English Letters), 32 (2019) 585-598.
[96] Z. Wang, G.-H. Zhang, X.-H. Fan, J. Jin, L. Zhang, Y.-X. Du, Corrosion behavior and surface characterization of an equiatomic CoCrFeMoNi high-entropy alloy under various pH conditions, Journal of Alloys and Compounds, 900 (2022) 163432.
[97] S. Shuang, G.J. Lyu, D. Chung, X.Z. Wang, X. Gao, H.H. Mao, W.P. Li, Q.F. He, B.S. Guo, X.Y. Zhong, Y.J. Wang, Y. Yang, Unusually high corrosion resistance in MoxCrNiCo medium entropy alloy enhanced by acidity in aqueous solution, Journal of Materials Science & Technology, (2022).

Chapter 6: Variation of the Passive Film on Complex Concentrated Dual-phase $Al_{0.3}Cr_{0.5}Fe_2Mn_{0.25}Mo_{0.15}Ni_{1.5}Ti_{0.3}$ and Implications for Corrosion

This chapter was submitted to Metallurgical and Materials Transactions A with coauthors M.A. Wischhusen, J. Qi, S. J. Poon, S. R. Agnew, J.R. Scully. The manuscript is under review at the time of thesis submission.

Abstract

The passive film on a dual-phase $Al_{0.3}Cr_{0.5}Fe_2Mn_{0.25}Mo_{0.15}Ni_{1.5}Ti_{0.3}$ FCC + Heusler ($L2_1$) complex concentrated alloy formed during extended exposure to a potential in the passive range in dilute chloride solution was characterized. Each phase, with a distinct composition of passivating elements, formed unique passive films separated by a heterophase interface. High-resolution, surface sensitive characterization enabled chemical analysis of the passive film formed over individual phases. The film formed over the $L2_1$ phase had a higher concentration of Al, Ni, and Ti, while the film formed over FCC phase was of similar thickness but contained comparatively higher Cr, Fe, and Mo concentrations, consistent with the differences in bulk microstructure composition. The passive film was continuous across phase boundaries and the distribution of passivating elements (Al, Cr, and Ti) indicated both phases were independently passivated. Spatially resolved analysis of dual phases alloys with combinations of Auger electron spectroscopy and scanning transmission electron microscopy suggests the primary surface cation in passive film formed on the FCC phase was Cr and for the $L2_1$ phase was Ti. Al, Cr, and Ti were enriched in both phases within the passive film relative to their respective bulk compositions. In parallel studies, single-phase alloys with compositions representative of the FCC and $L2_1$ phases were synthesized to evaluate the corrosion behavior of each phase in isolation. The electrochemical behavior of the dual-phase alloy resembled a combination of both single-phase samples, indicating the corrosion behavior may be represented by composite theory applied to phases. However, the interphase in the dual phase was a local corrosion initiation site and may limit localized corrosion protectiveness in chloride solutions. The alloy design implications for optimization of second phase structure and morphology are discussed.

1.0 Introduction

Complex concentrated alloys (CCAs) are a broad alloy class generally defined as containing three or more constituent elements at concentrations above 5 at. % [1]. The combinations of elements and resultant interactions are not frequently seen in conventional alloys but can introduce beneficial properties such as mechanical strength [2], high fracture toughness [3], and paramagnetic or ferromagnetic behavior [4]. CCAs are additionally developed for aqueous corrosion resistance with varying degrees of success [5, 6]. Although CCAs were originally theorized to have a single-phase microstructure, with high configurational entropies contributing to the homogenous distribution of elements, the definition of the alloy class includes also alloys with dual-phase or multi-phase microstructures [7].

Many thermodynamic indicators have been historically utilized to predict single-phase stability, such as configurational entropy, enthalpy of mixing, and complex thermodynamic indicators developed in part from such values [7-9]. While such terms are useful in initial alloy design, Feng et al. [10] independently surveyed a range of single-phase and dual-phase CCAs and showed that single-phase CCAs generally satisfy criteria regarding the constituent elements' atomic radii in addition to predictive metrics developed strictly from thermodynamic indicators. Namely, CCAs with net compositionally weighted deviations of constituent element atomic radii from the average atomic radii above 4.7% (originally defined as 6.6% by Yang et al. [9]) are predicted to form multi-phase microstructures regardless of thermodynamic values. For example, the constituent elements of CoCrFeMnNi, the first CCA proposed by Cantor et al. [11], have similar atomic radii and thus the equimolar mixture was found to be single-phase. However, significant additions of Al and Ti to such CCAs, two low density elements commonly utilized for lightweight alloy design, often lead to the formation of dual-phase CCAs when a significantly larger atomic radii mismatch is exceeded [10]. Although phase stability indicators are valuable in the initial design of CCAs to alert the designer to the likelihood of dual-phase microstructures, they provide little insight into the phase volume fractions and/or compositions. Thus, it is difficult to predict properties dependent on the morphology and composition of second phase.

CCA strategies to limit corrosion resistance often rely on multiple elements simultaneously present in protective passive films that can function in several ways, such as Al, Cr, and Ti [12, 13]. Multiple elements may be present in a passive film through a range of mechanisms including layered oxides, soluble solid solution oxides [14], complex oxides with long range order, and solute trapping of non-oxidized species within the passive film [15], or a combination of the above mechanisms [16]. However, localized depletion of passivating elements limits passive film species. Notably, the formation of second phases in the CCA microstructure leads to compositional partitioning and possible concentration profiles across a multi-phase microstructure. High-temperature solutionizing treatments may be tailored for individual alloy compositions to tailor microstructural features such as present phases, phase compositions, phase morphology, and interface length [7, 17].

The increase in second phase area fraction in CCAs often improving mechanical strength [18-21], dual-phase microstructures pose significant concerns for corrosion resistance. Regions depleted in a passivating element are left susceptible to localized corrosion [5, 22-24]. For this reason, microstructural features formed due to the presence of a second phase often serve as preferential sites for localized corrosion of CCAs via mechanisms such as pit initiation at the phase interface [23, 25, 26] and preferential dissolution of one or more phases [23, 27, 28], particularly in environments that often initiate localized corrosion such as chloride. Such behavior is often enabled and/or enhanced by microgalvanic coupling [22, 29, 30]. Furthermore, the second phase area, structure, and/or composition can change the mechanism of localized corrosion, such as the transition from localized breakdown of the passive film at random locations by pitting to preferential dissolution of a Cr-depleted BCC second phase with increasing second phase area fraction as observed by Shi et al. in the $Al_xCoCrFeNi$ system [23, 31].

Wang et al. observed preferential dissolution of the FCC phase of the CoCrFeMoNi CCA, which was locally depleted in Cr and Mo due to the formation of mu and sigma phases [32]. Time of Flight Secondary Ion Mass Spectrometry (ToF-SIMS) was used to determine the composition of the passive film on both a local and global scale. Higher intensities of Cr and Mo were observed over regions suggested to be associated with the sigma phase. Additionally, depth profiling identified Cr-Mo layering phenomena specifically over the sigma phase that was not seen in the FCC matrix, further suggesting different passivation behavior. The findings provide strong evidence for lateral variation in the passive film but provide limited quantification or spatial resolution limiting the development of relationships with corrosion protectiveness.

Despite frequently observed localized corrosion in CCAs with regard to microstructural variation [5, 23, 24, 26, 31, 33-42], there has been little further study of the lateral variation of passive film chemistry and/or structure. While many studies have characterized the passive film grown on dual-phase CCAs globally, evaluation with regard to microstructure length scale is often limited as the surface characterization methods (mainly X-ray photoelectron spectroscopy) are surface sensitive but characterize an area larger the dimensions of individual phases within the microstructure, and thus lack the spatial resolution to identify the effect of, any microstructural features that may cause local variation [22, 35, 36, 43, 44]. Although there is little study of dual-phase CCA passive films on CCAs, the governing phenomena have been evaluated from similar studies on duplex stainless steels, corrosion resistant alloys with a “balanced” dual-phase microstructure with both phases containing passivating elements as in the case of many Fe-containing dual-phase CCAs.

Långberg et al. [45-47] evaluated the passive film of 25Cr-7Ni super duplex stainless steel with hard X-ray synchrotron techniques, enabling characterization of the passive film grown over individual constituent phases. A Cr- and Fe-containing passive film consisting of an outer hydroxide layer, inner oxide layer, and unoxidized Ni enrichment at the metal/oxide interface was present over both phases; however, the film formed over the ferrite phase generally had a higher Cr content, similar to the higher Cr content in the ferrite phase [45]. Cr enrichment was proposed to result from enhanced Fe dissolution occurring more prominently over the ferrite phase, leading to Cr enrichment that required higher applied potentials to dissolve [47]. No significant differences were observed in the passive film thickness between the ferrite and austenite phases; however, the film formed over (001) orientation ferrite grains was both thicker and had a higher Cr content than other ferrite phase orientations, a difference attributed to surface reactivity depending on the crystal structure of the dissolving plane [46].

Vignal et al. [48] also evaluated the chemistry of the passive film for regions formed over both the austenite and ferrite phases of 2304 duplex stainless steel. Scanning Auger electron spectroscopy and microscale XPS were utilized to compare cation fraction depth profiles over both phases, finding higher Cr/Fe ratios in the film formed above the ferrite phase. The oxide to hydroxide ratio within the film formed over austenite increased during extended aging in air; however, such changes were not observed in the regions formed over ferrite.

In addition to duplex steel passive film chemistry, local analysis of semiconductive properties has also become a topic of interest. Rahimi et al. [49] isolated the Volta potential distribution between austenite, ferrite, and intermetallic particle regions with scanning Kelvin probe force microscopy before local measurement of band gaps with scanning tunneling spectroscopy. The passive film grown over ferrite was found to be thicker than the film grown over austenitic regions. Guo et al. [50] showed increased conductivity and decreased thickness in passive film regions grown over austenite relative to those over ferrite via current sensing atomic force microscopy, but did not evaluate for corrosion behavior. The chemical composition of the passive film was also characterized, but not at a spatial resolution capable of isolating the film formed over individual phases. There is little evaluation comparing local semiconductive properties of inhomogeneous passive films to corrosion behavior.

The governing corrosion phenomena for duplex steels are dependent on the structure and area fractions of the phases present. For example, the ferrite phase dissolves at higher rates than martensite during immersion of duplex steel in 0.1 M H_2SO_4, with the polarization behavior affected by martensite area fraction [51]. Neetu et al. [52] further evaluated this effect by altering phase area fractions with differing cooling rates and quench temperatures applied to a high-C, high-Si steel. Heat treatments leading to higher area fractions of bainite (shorter continuous cooling times before isothermal holds) often corresponded with improved polarization resistance and decreased mass loss rates during immersion. Surface morphology indicated preferential dissolution of the ferrite phase during polarization. Similar preferential dissolution was observed by Ha et al. [53], where increasing ferrite concentrations introduced by heat treatment of S32101 led to decreasing pitting potentials and increased pit depth in chloride solution. Preferential dissolution was utilized by Tsai and Chen [54] to evaluate galvanic coupling between austenite and ferrite in 2205 duplex stainless steel.

Gardin et al. [55] evaluated the air-formed passive film chemistry of 2304 duplex stainless steel with X-ray photoelectron spectroscopy and time of flight secondary ion mass spectrometry. Additionally, two single-phase alloys intended to represent the austenite and ferrite phases of the duplex stainless steel were synthesized with compositions identified from computational thermodynamic modeling and similarly characterized. Surface analysis of the single-phase alloys showed more Ni and N in the passive film formed on the austenite alloy, matching trends in microstructural partitioning, whereas more Cr was present in the passive film of the single-phase ferrite alloy. The passive films of all three alloys had a higher Cr fraction in the passive film than in their respective bulk microstructure and had similar layering trends. The composition and thickness of the duplex stainless steel film more closely resembled that of the ferritic alloy than that of the austenitic alloy, despite the duplex stainless steel having roughly similar area fractions of each phase.

The existing literature body clearly shows that different phases in a multi-phase alloy may have passive films that vary in composition, structure and electrochemical properties. As such, the morphology and volume fraction of phases in the microstructure may have considerable effects on corrosion behavior. However, there is little work that evaluates such phenomena on CCAs. Many reported approaches for the design of corrosion resistant CCAs incorporate the presence of multiple passivating elements within the passive film [5, 12, 14, 16, 56]. Thus, there is a considerable need for a more thorough understanding of passivation including better assessment of the local compositions of the passive film formed over individual phases in CCAs and their effect on overall corrosion behavior. Ensuring a viable range of passivating elements which partition between phases such that a stable passive film can be formed over both phases, and second phase regions do not become preferential corrosion sites, remains a critical challenge in the design of multi-phase corrosion resistant CCAs.

This work evaluates the corrosion resistance and passive film chemistry of a dual-phase CCA, isolating the behavior of individual phases with combinations of electrochemical and surface-sensitive chemical characterization methods. Synthesis of single-phase CCAs representative of constituent phases of the dual-phase CCA, a novel method for evaluation of CCA corrosion resistance, is utilized to enable electrochemical testing of constituent phases using global methods. A variety of studies are utilized designed to develop understanding of passivity both with the effects of localized corrosion (e.g., polarization in NaCl), and without (e.g., electrochemical impedance spectroscopy, polarization in H_2SO_4). The findings are compared to electrochemical and local passive film analysis of the dual-phase CCA.

2.0 Experimental Methods

2.1 Alloy Compositions, Synthesis, and Microstructural Characterization

The compositions of three synthesized alloys are listed in Table I, including the previously studied [12, 26] $Al_{0.3}Cr_{0.5}Fe_2Mn_{0.25}Mo_{0.15}Ni_{1.5}Ti_{0.3}$ dual-phase CCA, henceforth referred to as the parent alloy, and two single-phase CCAs selected to match the compositions of the FCC and $L2_1$ constituents of the parent alloy with methods further discussed below.

Table I: Nominal compositions in atomic percent of dual-phase parent alloy and single-phase alloys. Pure elements were massed within 1% error prior to arc melting.

	Parent Alloy	Matrix (FCC)	Second Phase ($L2_1$)
Al	6.0%	3.7%	19.7%
Cr	10.0%	11.1%	1.5%
Fe	40.0%	42.5%	10.4%
Mn	5.0%	5.2%	4.0%
Mo	3.0%	3.1%	0.3%
Ni	30.0%	28.8%	44.8%
Ti	6.0%	5.6%	19.4%

CCAs were synthesized via arc-melting from pure elements (Cr > 99.2% purity, all other metals > 99.9% purity), flipped five times to ensure homogeneity, and suction cast into 1 cm diameter buttons in a water-cooled copper mold. Samples were annealed at 1070 °C, the temperature previously utilized to target the dual-phase microstructure, for five hours before quenching in water. Each sample was ground with SiC paper to a 1200 grit finish prior to electrochemical testing and polished with diamond paste to a 1 µm finish prior to microstructural and surface analysis.

The phases present in each alloy were identified via X-ray diffraction (XRD) on a PANalytical Empyrean Diffractometer^{TM} with Cu Kα x-rays (1468.7 eV) and at a scan rate of 0.15 °/sec. Microstructures were imaged via scanning electron microscopy (SEM) in backscattered electron (BSE) mode with an FEI Quanta 650^{TM}. The chemical compositions of the parent alloy were first identified via energy dispersive spectroscopy (EDS) in point scan and mapping mode, and analyzed with Oxford Instruments Aztec^{TM} software. The spot sizes for SEM and EDS were selected to ensure the probe diameter was below 10 nm, well below the size of microstructural features. EDS mapping of a representative two-phase region is shown in Figure 1. The compositions identified from point scans taken over each phase were used to develop the single-phase CCAs. The composition of the point scan of the FCC matrix of the parent alloy yielded a single-phase microstructure when synthesized into a new CCA. However, synthesis of the composition defined by the point scan obtained over the $L2_1$ phase led to the formation of a dual-phase microstructure with approximately equal area fractions of FCC and $L2_1$ phases suggested by micrograph threshold analysis. The presence of a multi-phase microstructure despite a predicted single phase microstructure was attributed to EDS spill over to the FCC phase due to the X-ray generation being possible at depths of up to 1 µm [57], which can exceed the diameters of many of the second phase particles in the parent alloy. Thus, it is likely that some characteristic emission from the FCC matrix was detected in the $L2_1$ point scan, pushing the initial composition of this phase beyond regions of single-phase stability. Therefore, a point scan of the $L2_1$ phase of the equal area fraction alloy with larger regions of $L2_1$ was selected to represent the single-phase $L2_1$ CCA shown in Table I. Point scans of the single-phase alloys, parent alloy, and equal area fraction intermediate alloy along with a micrograph of the intermediate alloy are shown in Table II and Figure 2, respectively.

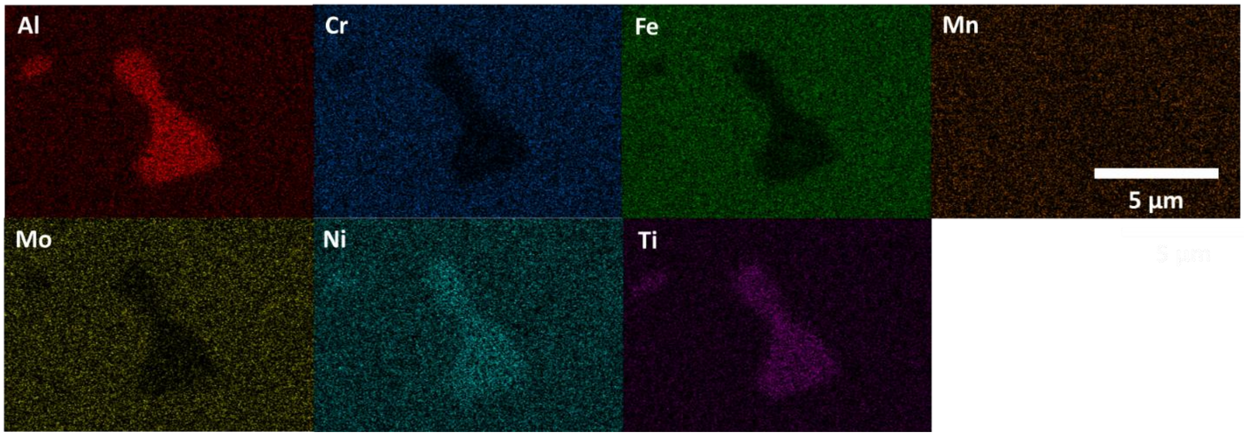

Figure 1: EDS mapping of representative two-phase region of parent alloy reproduced from [26].

Table II: EDS point scans for the parent alloy and intermediate alloy obtained from point scans of the $L2_1$ phase of the parent alloy.

Phase	Al	Cr	Fe	Mn	Mo	Ni	Ti	Area Fraction
Parent Alloy								
Matrix (FCC)	3.7	11.0	42.5	5.2	3.1	28.8	5.6	95.7 %
2nd Phase ($L2_1$)	14.3	3.5	17.1	4.2	0.9	44.1	15.8	4.3 %
Intermediate Alloy ($Al_{14.3}Cr_{3.5}Fe_{17.1}Mn_{4.2}Mo_{0.9}Ni_{44.1}Ti_{15.8}$)								
Matrix (FCC)	3.1	7.6	35.7	5.6	1.8	37.9	8.3	46.4 %
2nd Phase ($L2_1$)	19.7	1.5	10.4	4.0	0.3	44.8	19.7	53.6 %
Matrix (FCC)								
Matrix (FCC)	3.7	9.5	42.7	3.6	1.5	33.6	5.3	~100 %
Second Phase ($L2_1$)								
2nd Phase ($L2_1$)	19.9	1.3	10.0	3.4	0.1	45.1	20.3	~100 %

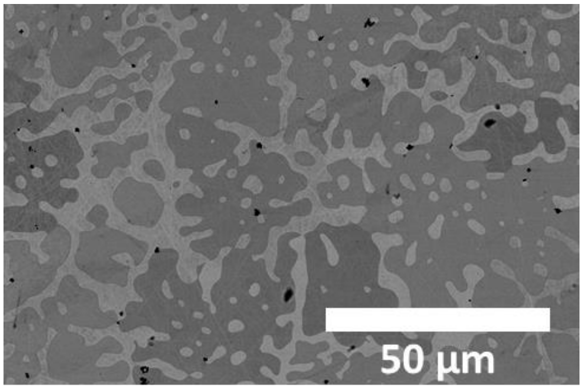

Figure 2: BSE micrograph of the intermediate alloy

2.2 Electrochemical Characterization of Corrosion Behavior

A series of electrochemical methods were selected to indicate the characteristics of the passivity and identify the relative resistance to localized corrosion behavior. All measurement were global and lack spatial resolution to characterize individual phases within the parent alloy. Electrochemical characterization of the synthesized single-phase alloys was thus used to evaluate the performance of the individual phases. A Gamry Instrument Reference 600+^{TM} potentiostat connected to a conventional three-electrode cell with the CCA sample cold-mounted in epoxy as the working electrode, a platinum mesh counter electrode, a saturated calomel reference electrode (SCE, +0.241 V vs. standard hydrogen electrode), and 0.01 M NaCl[20] (pH ~5.75) electrolyte solution was used for all electrochemical experimentation unless otherwise noted. All electrochemical experimentation was repeated threefold to ensure reproducibility. Samples were first potentiodynamically polarized using two procedures. In both cases, the scan rate was 0.5 mV/s. To evaluate the formation of the passive film, the air-formed oxide was first exposed to a -1.3 V_{SCE} treatment for 600 s before conducting cyclic polarization between -1.3 and 0.8 V_{SCE}. Additionally, the CCAs were polarized in 0.1 H_2SO_4 to evaluate the formation of the passive film in the absence of Cl^- ions capable of initiating localized breakdown. Due to excessive H_2 evolution at cathodic potentials that could form bubbles limiting conductivity, a modified procedure was used. All potentials listed below are converted from saturated mercury-mercury sulfate (-0.640 V vs. standard hydrogen electrode), the Cl^--free reference electrode that replaced the SCE for sulfate environments. The CCAs were first cathodically pre-treated with four successive potentiostatic reduction steps: a 300 s exposure to -1.0 V_{SCE}, a 3 s exposure to -1.5 V_{SCE}, a 300 s exposure to -1.0 V_{SCE}, a 60 s exposure to -1.0 V_{SCE}, and a 10 s exposure to -0.6 V_{SCE}. Then, the CCAs were polarized from 0.05 V below the stable OCP up to 0.96 V_{SCE} at a 0.5 $mV.s^{-1}$ scan rate.

Second, to characterize the solution-exposed air-formed oxide, the sample was exposed at open circuit potential (OCP) for 1800 s before conducting electrochemical impedance spectroscopy over the frequency range of 100 kHz to 1 mHz measuring 5 points/decade with a 20 mV_{RMS} AC voltage. Following EIS, the air-formed film was polarized from 0.1 V below the final OCP to 0.8 V_{SCE} followed by downward polarization from 0.8 to -1.3 V_{SCE}. Spectra were fit with Randles' circuit modified to include a constant phase element (CPE) and a bounded Warburg element. The equivalent circuit model may be

---

[20] A dilute chloride electrolyte solution at a neutral pH was selected to ensure the stable formation of a passive film over large potential range that could be evaluated prior to breakdown. An overview of the corrosion behavior of the dual-phase alloy across a range of NaCl concentrations and pH may be found elsewhere [12].

mathematically related to the impedance using the equations shown below. The impedance for the resistance components may be treated as equivalent to the magnitude of the resistors associated with solution resistance (R_S) and charge transfer resistance (R_{CT}).

$$Z_S = R_S \tag{1}$$

$$Z_{CT} = R_{CT} \tag{2}$$

The impedance of the CPE may determine from the frequency (f), CPE coefficient (α_{CPE}), and admittance (Y_{CPE}).

$$Z_{CPE} = \frac{1}{(jf)^{\alpha_{CPE}} Y_{CPE}} \tag{3}$$

Diffusional impedance is represented by a finite length Warburg component consisting of a magnitude (Y_W) and bound length (B_W).

$$Z_W = \frac{\frac{1}{Y_W}}{\sqrt{jf}} \tanh\,(B\sqrt{jf}) \tag{4}$$

Combining each subcomponent yields the net system impedance

$$Z = \frac{1}{\frac{1}{(Z_{CT} + Z_W)} + \frac{1}{Z_{CPE}}} + Z_S \tag{5}$$

Which may be further simplified

$$Z = \frac{Z_{CPE}(Z_{CT} + Z_W)}{Z_{CT} + Z_W + Z_{CT}} + Z_S \tag{6}$$

The real (Z’) and imaginary components (Z”) may be extracted as the non-imaginary and imaginary components of the equation, respectively, for the Nyquist plot as well as to calculate and fit the phase angle (Φ).

$$\Phi = \arctan\,(\frac{Z''}{Z'}) \tag{7}$$

To evaluate the formation and aging of a solution-formed passive film, a potentiostatic exposure procedure was used.[21] The samples were first exposed to -1.3 V_{SCE} for 600 s to reduce the effect of the air-formed passive film. A step increase in potential to -0.25 V_{SCE}, determined to be within the alloys’ passive ranges during potentiodynamic polarization, was then applied for 40 ks. The impedance was monitored

---

[21] For the potentiostatic exposure procedure utilized to grow a passive film, a BioLogic SP-200^{TM} potentiostat was instead utilized to decrease the timestep between current density and impedance measurements.

in-situ every 200 ms at a frequency of 5 Hz and a 20 mV_{RMS} AC voltage. Following film growth, the film was characterized with full frequency EIS at -0.25 V_{SCE} and all other parameters maintained from the air-formed oxide evaluation (100 kHz to 1 mHz, 5 points/decade, 20 mV_{RMS}). The solution-formed film was subsequently characterized with X-ray Photoelectron Spectroscopy (XPS), scanning Auger Electron Spectroscopy (AES), and scanning transmission electron microscopy (STEM) under N_2 as discussed further below.

The degree of microgalvanic coupling within the parent alloy was evaluated with zero-resistance ammetery (ZRA). The FCC single-phase CCA was used as the working electrode with the $L2_1$ single-phase CCA of equal area as the counter electrode. Open circuit potential and current of the coupled system with air-formed oxides present were monitored for 40 ks directly after mechanical grinding of each sample at both equal area ratios (0.785 cm^2) and a 10:1 FCC to $L2_1$ area ratio (0.785 to 0.0785 cm^2) selected to more accurately represent the phase volume fractions. Current densities for both area ratios were normalized relative to the area of the FCC working electrode (0.785 cm^2). The coupled potential was compared to the OCP of the parent and single-phase alloys during a 40 ks exposure air-formed oxides to open circuit corrosion in the conventional three-electrode cell.

2.3 Characterization of Surface Chemistry and Homogeneity

The chemical compositions and molecular constituents of the solution-formed oxide films were characterized with XPS. Samples were transported under $N_2(g)$ directly after the 40 ks exposure at -0.25 V_{SCE}, subsequent EIS characterization, and OCP exposure described above to a PHI VersaProbe III XPS system. Samples were exposed to lab-air for a maximum of 20 minutes at room temperature. High-resolution spectra over the Al 2p, Cr $2p_{3/2}$, Fe $2p_{1/2}$, Mn $2p_{1/2}$,[22] Mo 3d, Ni $2p_{3/2}$, and Ti $2p_{3/2}$ core spectra were obtained with Al Kα X-rays (1,486.6 eV) at a 26 eV pass energy, 100 µm spot size, and a 45° take off angle. The large spot size indicates the XPS lacks the lateral resolution to probe individual phases. Thus, the synthesized phases were treated as representative of individual phases on the local scale. Spectra were calibrated with C 1s set to 284.8 eV as a reference. Spectra were deconvoluted with KolXPD™ software with a combination of Shirly background substitutions, Doniach-Sunjic peaks for metallic features, and Voigt functions for oxidized features with characteristic peak positions, intensities, widths, and multiplet splitting from reference spectra obtained elsewhere [58-60]. The Cr 3s spectrum,

---

[22] The Fe $2p_{1/2}$ and Mn $2p_{1/2}$ spectra were selected to avoid the overlap of Ni Auger peaks in the commonly used Fe $2p_{3/2}$ and Mn $2p_{3/2}$ region. A constant binding energy shift between the deconvoluted data in the $2p_{1/2}$ series and reference spectra in the $2p_{3/2}$ series was assumed.

which overlaps the Al 2p spectrum, was fit to a single Voigt peak with the intensity defined by the total Cr $2p_{3/2}$ signal adjusted with relative sensitivity factors. Surface cation fractions (X) were obtained via total intensity (I) of the peaks fit to oxidized species for each metal (M). The total intensity was normalized via relative sensitivity factors (R) as shown below in equation 1. Elements for which surface cation fractions exceed the bulk microstructural composition for either a single-phase CCA or the parent alloy are considered enriched in the passive film [61].

$$X_M^S = \frac{\frac{I_M}{R_M}}{\Sigma \frac{I_i}{R_i}} \tag{8}$$

To evaluate the lateral variation of the passive film chemistry, the film growth procedure described above was repeated on a polished sample before transfer to a PHI 710™ Field Emission Scanning Auger Nanoprobe operating with a 10 keV, 1 nA electron beam, a beam diameter of approximately 3-5 nm, and a 0° take off angle.[23] The instrument was equipped with an SEM which facilitated the location of phases for spot probe analysis. AES spectra were obtained for five point obtained over each phase and at least 1 µm from the interface and averaged to obtain representative surface cation fractions. Additionally, qualitative analysis of surface cation fractions was measured in mapping and line-scan modes to demonstrate the changes in passive film chemistry across the FCC-$L2_1$ interface with equation 1 modified to include system specific sensitivity factors.

Finally, a cross-section of the passive film was characterized via STEM-EDS. The film growth procedure was repeated on a polished sample before transfer under $N_{2(g)}$ to a Helios UC G4™ Dual Beam Focused Ion Beam (FIB) and SEM system for cross-sectioning. The surface was deposited with a 0.4 µm protective Pt layer with a 5 keV electron beam followed by a 1.5 µm layer with the ion beam. The film cross-section was then prepared via FIB lift-out technique with a Ga^+ ion beam at an accelerating voltage of 30 keV followed by subsequent passes at 5 keV. The sample was transferred to a Thermo Fisher Scientific Themis™ 60-300 kV transmission electron microscopy system and imaged in dark-field mode operating at a 200 kV and a 350 pA beam current with probe correction, allowing for resolution as low as 0.1 nm. The bulk microstructure and passive film were mapped with STEM-EDS with a Super-X detection system over a representative area near the phase interface with three line integrals obtained to evaluate

---

[23] A 30° take off angle was instead used for qualitative mapping to improve elemental contrast.

the passive film depth profile over each phase and lateral homogeneity of the passive film across the phase interface. Compositions were obtained from intensities normalized with Velox software.

3.0 Results

3.1 Alloy Microstructure

XRD patterns shown in Figure 3 index the matrix and second phase single-phase synthesized CCAs as FCC and Heusler ($L2_1$) respectively, while peaks are present for both phases in the parent alloy XRD pattern. The presence of many peaks in the single-phase $L2_1$ CCA that were not observed in the parent alloy is attributed to the low volume fraction of the $L2_1$ phase along with possible orientation texturing. The microstructures are confirmed by BSE micrographs, as shown in Figure 4. EDS point scans listed in Table II confirm similar compositions between the synthesized single-phase CCAs and constituent phases within the parent alloy. The FCC CCA is shown to be single-phase, while the $L2_1$ single-phase CCA has small (generally less than 1 µm) regions enriched in Fe and Cr[24], whose formation may be attributed to spill-over inaccuracy from EDS measurements of the $L2_1$ phase of previous alloys, which could have incorporated signal from the FCC phase. However, given that the $L2_1$ volume fraction is much greater than that of the previously established 4.33% $L2_1$ area fraction for the parent alloy [26], the composition is assumed to be representative of the $L2_1$ behavior. The dual-phase microstructure consists of an FCC matrix with $L2_1$ features generally between 2 and 10 µm in size, well-distributed throughout the matrix. $L2_1$ regions generally have curved interfaces with the matrix; however, some, such as the case of Figure 4d, possess sharp corners and linear boundaries running in parallel with potential grain boundaries (GBs) indicated by contrast between FCC regions in the BSE micrograph.

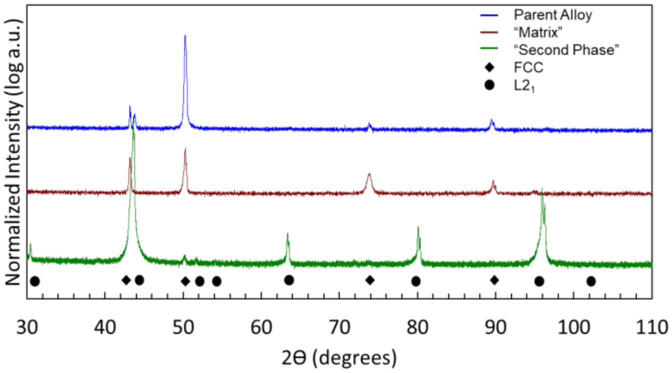

Figure 3: XRD patterns synthesized CCAs following homogenization at 1070 ˚C. Peak indexes are shown for FCC and $L2_1$ phases, with both features visible in the parent alloy.

---

[24] Fe and Cr enrichment is determined by EDS mapping (not shown); however, the feature morphology is too small to obtain reliable quantitative compositions with point scans.

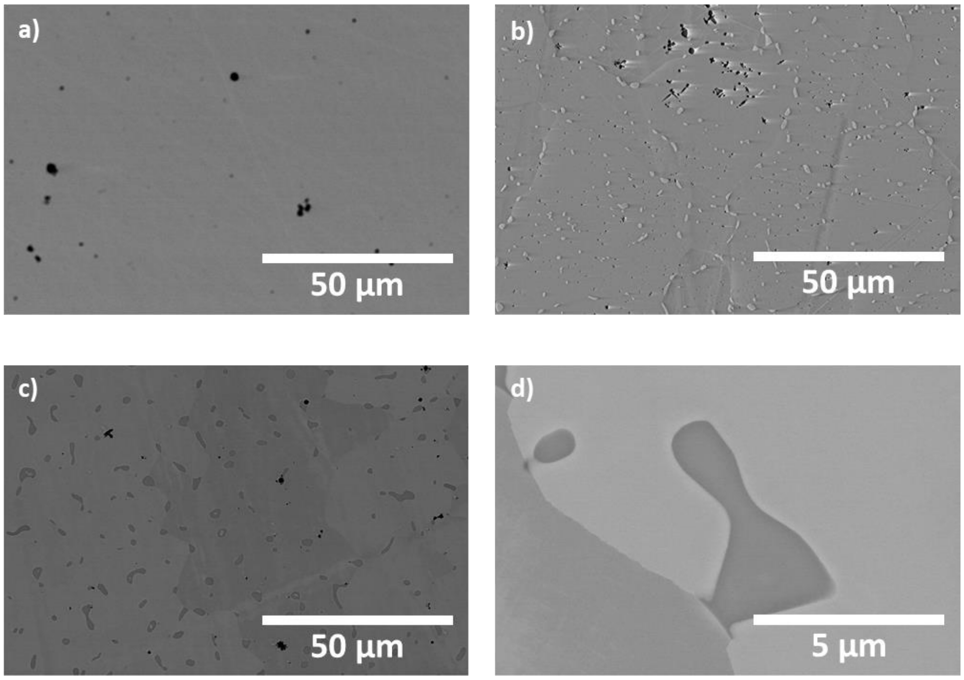

Figure 4: BSE micrographs of **a)** single-phase FCC CCA, **b)** single-phase $L2_1$ CCA, **c)** dual-phase parent alloy at low magnification, and **d)** dual-phase parent alloy at high magnification.

3.2 Corrosion Behavior of Alloys with Oxides Formed in Aqueous Solutions

E-log(i) plots comparing the corrosion behavior of the parent alloy on a global scale in 0.01 M NaCl with the single-phase CCAs are shown in Figure 5, with key values tabulated in Table III. The use of a dilute chloride solution leads to the formation of a broad passive range for all three alloys that may be characterized prior to breakdown, while the cathodic pre-treatment minimizes the effect of the air-formed oxide. Passivity of both phases is attributable to each phase having passivating elements enriched relative to the overall alloy composition (e.g., Cr in the FCC phase, Ti and Al in the $L2_1$). The corrosion potential (E_{corr}) of all three alloys is similar. Likewise, there is little variation in the passive current density (i_{pass}). For both parameters, the parent alloy resembles the values of its constituent phases. However, the lack of statistically significant variation between the alloys limits evaluation of E_{corr} and i_{pass} as a function of phase volume fraction. Pitting was the dominant breakdown mechanism for all three alloys with limited crevice corrosion near the sample-epoxy interface also observed. Pits disproportionately occurred near the FCC-$L2_1$ interface, as in the case of the micrograph shown in Figure 6. The pitting potential (E_{pit}) for the $L2_1$ phase was lower than that of the matrix phase, indicating more modest breakdown potential in $L2_1$ relative to the FCC matrix. However, the interphase boundary is the weak site. Intermittent increases in current density prior to breakdown observed for all three scans suggest metastable pitting and repassivation, with the behavior most noticeable in the matrix single-phase CCA. Notably, E_{pit} for both the parent and FCC alloys is above the range of stability for Cr_2O_3 formed on pure Cr. Enduring passivity at these potentials is attributable to stability due to the presence of Al and Ti passive species which retain a partially protective oxide [12]. The repassivation potential (E_{rep}) is defined as the potential at which the downward scan (not shown) current density is less than that of the upward scan at the same potential. As in the case of E_{pit}, E_{rep} for the L2_1 phase is lower than both the FCC and parent alloys. A negative hysteresis is present for the polarization of the air-formed oxide for the FCC CCA as stable pitting was not observed prior to the downward scan [62]. The decrease in both E_{pit} and E_{rep} for the L2_1 phase may be attributable in part to significantly lower Mo concentrations in, which has been shown elsewhere to have strong effects both of these parameters in this alloy series [33]. Both E_{pit} and E_{rep} for the parent alloy were in between the respective values for the single-phases. The parent alloy values more closely resembled those of the matrix phase, likely resulting from its higher matrix volume fraction.

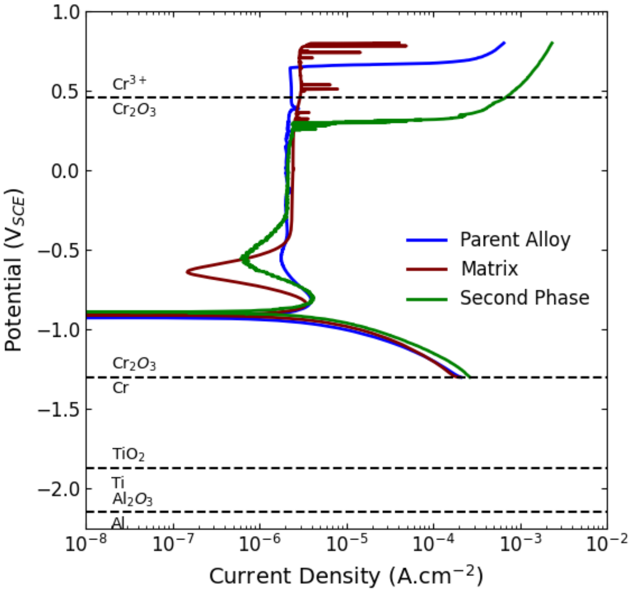

Figure 5: Potentiodynamic polarization of CCAs in 0.01 M NaCl (pH ~5.75) following cathodic pre-treatment (600 s, -1.3 V_{SCE}). Dashed lines indicate stability ranges for the oxides of passive species formed on their pure constituent elements at a pH of 5.75 predicted by Hydra Medusa software.

Table III: Selected corrosion parameters for potentiodynamic polarization in 0.01 M NaCl (pH ~5.75) shown in Fig. 5. Each term includes the mean value bounded by a one standard deviation range.

Alloy	**E_{corr} (V_{SCE})**	**E_{pit} (V_{SCE})**	**E_{rep} (V_{SCE})**	**i_{pass} ($uA.cm^{-2}$)**
Parent Alloy	-0.921 +/- 0.019	0.615 +/- 0.078	0.004 +/- 0.131	2.17 +/- 0.56
Matrix	-0.936 +/- 0.036	0.726 +/- 0.117	-0.041 +/- 0.068	2.59 +/- 1.07
Second Phase	-0.884 +/- 0.007	0.28 +/- 0.056	-0.255 +/- 0.043	2.28 +/- 0.23

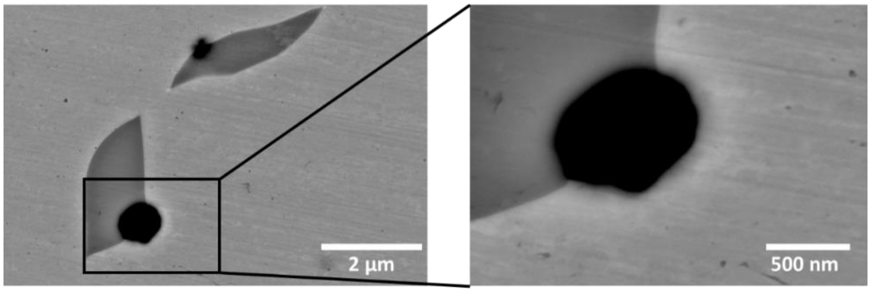

Figure 6: BSE micrograph of parent alloy with pits at FCC-$L2_1$ interface following polarization shown in Figure 4. This figure was reproduced in part from [21].

The corrosion behavior was also evaluated in 0.1 M H_2SO_4 to characterize passivity in the absence of localized corrosion-inducing Cl^- ions. E-log(i) plots are shown below in Figure 7 with tabulated parameters listed in Table IV. E_{corr} is lower for the $L2_1$ single-phase CCA than for the matrix or dual-phase CCAs. i_{pass} for the parent alloy is lower than both constituent phases, however similar values for both i_{pass} and the critical current density suggest similar rates of passive film formation and passive film strength between the three CCAs, as in the case of polarization in NaCl. i_{crit}, which has historically been used to evaluate the rates of passive film formation, shows no statistically significant differences between the CCAs.

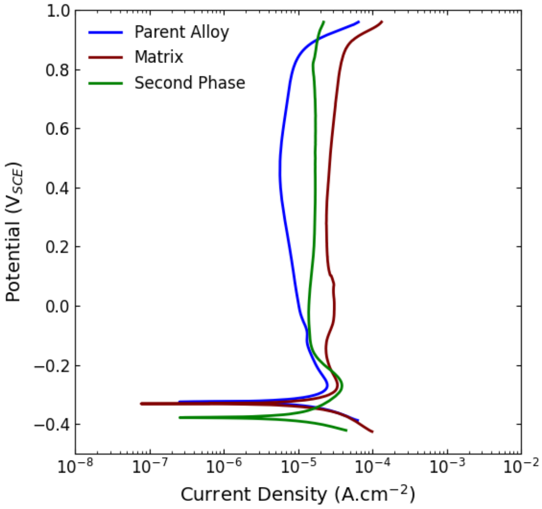

Figure 7: Potentiodynamic polarization of CCAs in 0.1 M H_2SO_4 (pH ~1) following cathodic pre-treatment.

Table IV: Selected corrosion parameters for potentiodynamic polarization in 0.1 M H_2SO_4 (pH ~1) shown in Fig. S.2. Each term includes the mean value bounded by a one standard deviation range.

Alloy	**E_{corr} (V_{SCE})**	**i_{crit} ($\mu A.cm^{-2}$)**	**i_{pass} ($\mu A.cm^{-2}$)**
Parent Alloy	-0.32 +/- 0.006	29.9 +/- 7.1	6.3 +/- 0.9
Matrix	-0.334 +/- 0.007	34 +/- 2	22.1 +/- 6.8
Second Phase	-0.365 +/- 0.023	37.9 +/- 3.5	14.1 +/- 2

3.3 Corrosion Behavior of Alloys with Native Oxides

Experiments were also conducted with the air formed oxide without the reduction step. The air-formed solution-exposed passive film was first characterized with EIS after 1800 s exposure at the film OCP in 0.01 M NaCl solution. EIS spectra of selected representative runs for each alloy are shown in Figure 8. Table V shows parameters for the fit of each spectra the equivalent circuit model shown in Figure 8c and described above. R_S and R_{CT} are attributable to the resistances attributable to the solution and passive film, respectively. The CPE is used to identify the magnitude and ideality of the capacitive behavior of the film while the Warburg component represents mass-transport-limited processes, mainly diffusion and/or migration through the passive film. All fits suggest near-ideal capacitive behavior with the α above 0.8 suggesting excellent passive films in both the single-phase and parent alloys. While the parent alloy R_{CT} is slightly lower than both phase subcomponents, the low-frequency impedance modulus data shown in Table VI, a commonly used surrogate for the polarization resistance, shows that all phases possess good passivity and that differences between the CCAs are within the range of statistical scatter. Therefore, neither constituent phase is indicated to have an inferior passive film, nor can the parent alloy with interphase boundaries be shown to be superior to or inferior to either constituent phase.

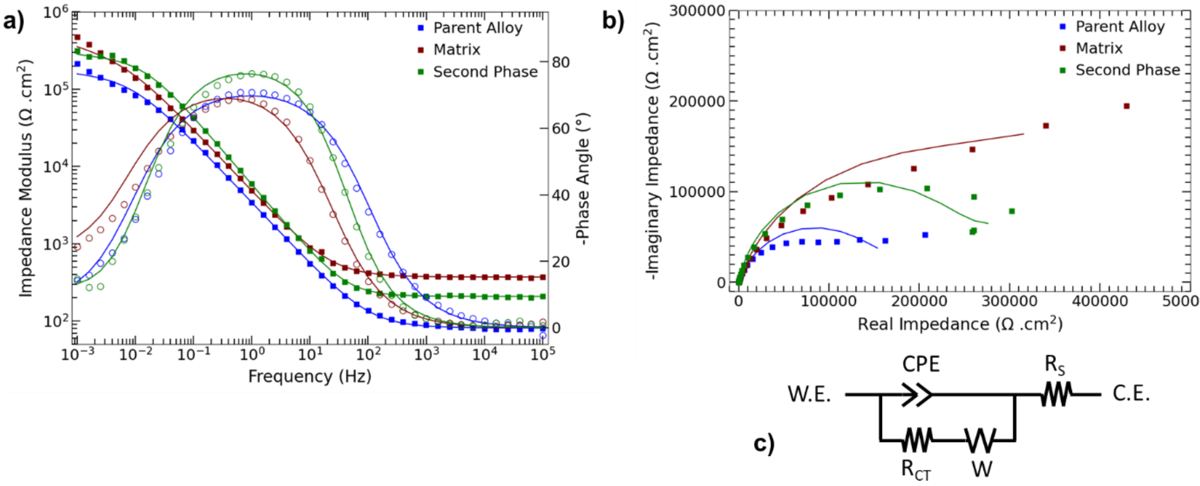

Figure 8: a) Bode and **b)** Nyquist plots of solution-exposed air-formed passive films of CCAs in 0.01 M NaCl (pH ~5.75) fit to equivalent circuit model shown in c).

Table V: EIS fit parameters for the spectra shown in Fig. 6. Each term is defined by the Randles circuit shown in Fig. 6c.

Alloy	**R_{CT} (kΩ. cm^2)**	**R_S (Ω. cm^2)**	**α_{CPE}**	**Y_{CPE} (μS.s$^{\alpha}$ .cm^{-2})**	**Y_W (μS.s$^{0.5}$ .cm^{-2})**	**B_W (s$^{0.5}$)**
Parent Alloy	158	81.3	0.802	66.9	689.4	40.3
Matrix	313	371.2	0.807	47.7	86.3	38.1
Second Phase	253	208.5	0.885	33.6	233.9	46.0

Table VI: Impedance modulus at 1 mHz for CCAs obtained during EIS of the air-formed oxide at OCP. Each value represents the sample mean and includes a one standard deviation bound.

Parent Alloy	**Matrix**	**Second Phase**
449 +/- 558	612 +/- 342	410 +/- 400

The CCAs with air-formed oxides were also characterized via polarization beginning slightly below the OCP of the films, bypassing any cathodic pre-treatment to not reduce the film. E-log(i) plots are shown in Figure 9 with key parameters identified in Table VII. The parent and matrix phase alloys had similar E_{corr} values, while E_{corr} for the L2$_1$ CCA was slightly more negative. Pitting was the dominant breakdown mechanism, with metastable pits that repassivate prior to E_{pit} also indicated for the parent and FCC alloys. However, repassivation of metastable pits was less prominent for L2$_1$ single-phase CCA. The L2$_1$ CCA also showed a less positive E_{pit}, implying inferior resistance to film breakdown. E_{pit} for the parent alloy was in between that of the two single-phase CCAs.

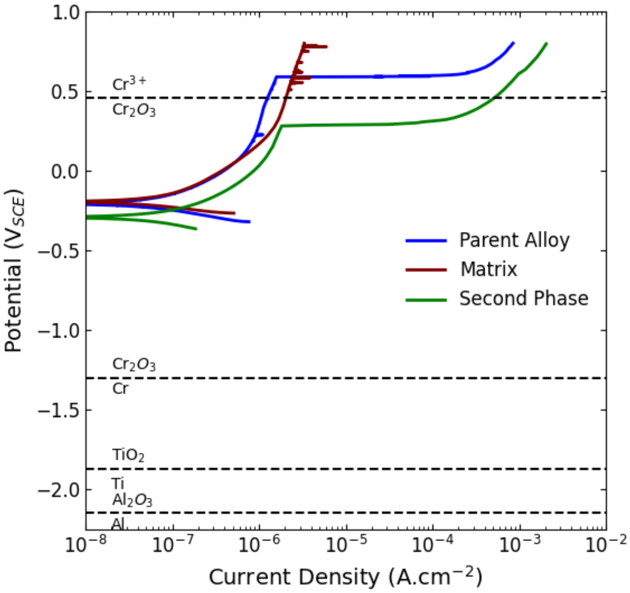

Figure 9: Potentiodynamic polarization of CCAs with air-formed oxides in 0.01 M NaCl (pH ~5.75). Dashed lines indicate stability ranges for the oxides of passive species formed on their pure constituent elements at a pH of 5.75 predicted by Hydra Medusa software.

Table VII: Selected corrosion parameters for potentiodynamic polarization in 0.01 M NaCl (pH ~5.75) shown in Fig. 7. Each term includes the mean value bounded by a one standard deviation range. Consistent stable pitting was not observed in single-phase FCC CCA with breakdown potentials often exceeding the 0.8 V_{SCE} maximum applied potential.

Alloy	**E_{corr} (V_{SCE})**	**E_{pit} (V_{SCE})**
Parent Alloy	-0.16 +/- 0.084	0.466 +/- 0.154
Matrix	-0.203 +/- 0.049	> 0.800
Second Phase	-0.300 +/- 0.098	0.303 +/- 0.174

3.4 Potentiostatic Oxide Growth and Characterization

The passive film growth kinetics during exposure to a -0.25 V_{SCE} potential, within the passive range of all three evaluated alloys, on a cathodically pre-treated (600 s, -1.3 V_{SCE}) surface for each alloy are shown in Figure 10. Current density magnitudes for each alloy decrease with time after step potentiostatic hold, while the magnitude of the imaginary component of impedance (Z”), which has been previously shown to be directly proportional to film thickness [63, 64], increases with time. For all three alloys, the current density switches from positive to negative between ~2000 and ~10000 s, indicating a change from anodic- to cathodic-dominated kinetics. Prior to the transition, all three alloys show similar film growth kinetics, consistent with similar current density measurements. The anodic current densities of the single-phase $L2_1$ CCA are the lowest, whereas they are the highest for the parent alloy. Sharp spikes the current density measurements for the single-phase $L2_1$ CCA may indicate metastable film breakdown and repassivation. Z” increases with time for all alloys, indicating and stable film growth. Changes in growth rate, such as those most visible in the step-like behavior of the single-phase $L2_1$ CCA, may indicate different metals and/or passive film layers form at different times.

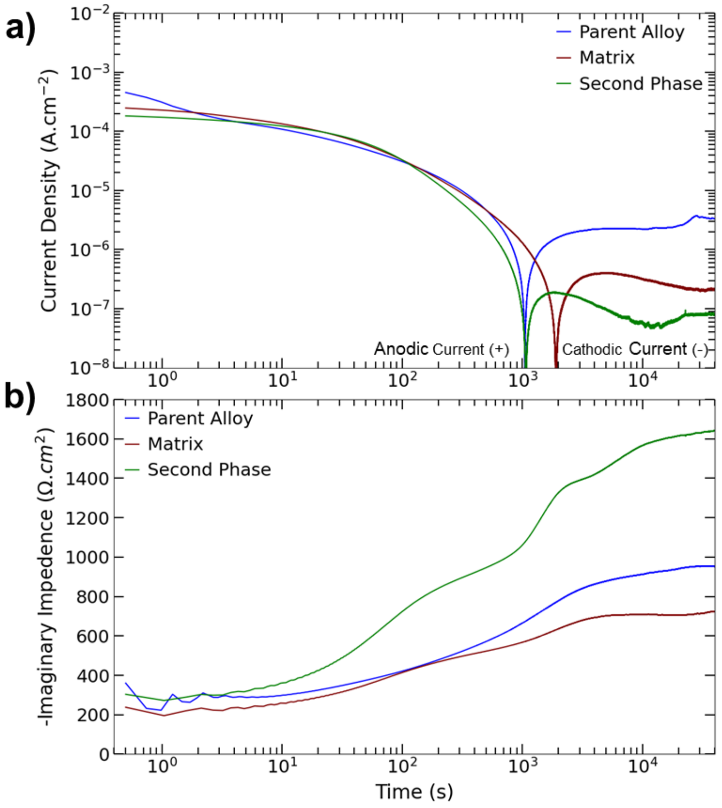

Figure 10: a) Current density and **b)** in-situ Imaginary component of impedance (5 Hz) of CCAs during potentiostatic passive film growth at -0.25 V_{SCE} in 0.01 M NaCl (pH ~ 5.75) following cathodic pre-treatment (600 s, -1.3 V_{SCE}). To minimize scatter in the data, a five point moving average is presented.

The film grown within the passive range was also characterized via EIS as shown in Figure 11. Selected representative spectra were fit to the previously described equivalent circuit model with the parameters listed in Table VIII. Similar to the case of the air-formed oxides, high α values suggest ideal capacitive behavior for all three alloys. The $L2_1$ CCA shows different time constant behavior, with the maximum phase angle magnitude obtained at a higher frequency than the other two CCAs. This may contribute to the higher Z" values during film growth and a higher impedance modulus at 5 Hz, which is shown by the phase angle plot to be firmly within the capacitive range, despite the comparatively lower R_{CT} of the single-phase $L2_1$ CCA. Low-frequency impedance data tabulated in Table IX confirms passivity of all three alloys. As in the case of the air-formed oxide, the FCC CCA has the highest mean impedance modulus, although not at a statistically significant level. This suggest both CCAs, and therefore both regions over the parent alloy, form a stable protective oxide film. Furthermore, no statistically significant differences in behavior are suggested between procedures for any of the CCAs, suggesting that the air-formed and solution-formed passive films may provide similar levels of protectiveness. Therefore, there is no strong evidence for the passivity of either phase being comparatively weaker.

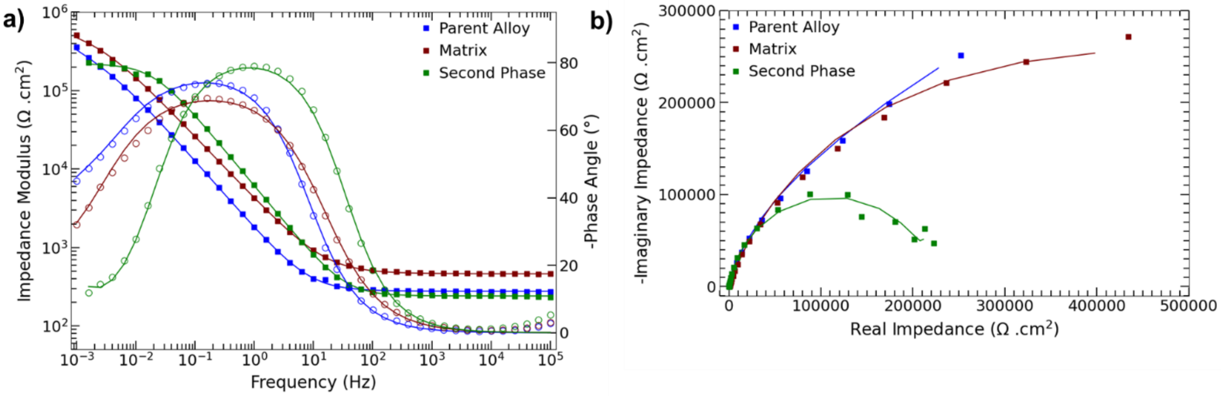

Figure 11: a) Bode and **b)** Nyquist plots of passive films of CCAs formed following potentiostatic exposure (-0.25 V_{SCE}, 40 ks) in 0.01 M NaCl (pH ~5.75) fit to equivalent circuit model shown in c).

Table VIII: EIS fit parameters for the spectra shown in Fig. 9. Each term is defined by the Randles circuit shown in Fig. 6c.

Alloy	**R_{CT} (kΩ. cm^2)**	**R_S (Ω. cm^2)**	**α_{CPE}**	**Y_{CPE} (µS.s$^{\alpha}$ .cm^{-2})**	**Y_W (µS.s$^{0.5}$ .cm^{-2})**	**B_W (s$^{0.5}$)**
Parent Alloy	270	277.3	0.861	117.4	43.1	37.9
Matrix	561	462.7	0.798	55.5	91.3	88.1
Second Phase	169	201.4	0.922	35.8	272.5	18.8

Table IX: Impedance modulus at 1 mHz for CCAs obtained during EIS of the air-formed oxide at OCP and of the solution-formed oxide following potentiostatic oxide growth (-0.25 V_{SCE}, 40 ks). Each value represents the sample mean and includes a one standard deviation bound.

Parent Alloy	**Matrix**	**Second Phase**
452 +/- 284	597 +/- 416	464 +/- 241

3.5 Galvanic Interaction of Constituent Phases

Possible galvanic interaction was evaluated utilizing ZRA. The galvanic couple potentials and net current measurements at the conclusion of a 40 ks coupling of the constituent phase alloys with air formed oxides are shown in Table X. The current densities of the coupled system following 40 ks exposure reached average values below 50 nA.cm^{-2} for both area ratios with maximum values generally below 750 nA.cm^{-2} during the exposure. Such magnitudes are well below those of i_{pass} for the parent alloy obtained during polarization (Table III). Following extended immersion, the current is generally negative for both area ratios, indicating the FCC matrix (working electrode) may be slightly cathodic or more passive to that of the L2$_1$ passive film (counter electrode). A cathodic FCC phase would suggest the galvanic couple potential following oxide exposure aging would be slightly above the OCP of the FCC phase. These results indicate negligible galvanic coupling of consequence. Furthermore, the galvanic couple potential is below E_{pit}

observed during potentiodynamic polarization of the air-formed oxides for both alloys, suggesting there is insufficient driving force for galvanic coupling-induced pitting for either phase. The coupled potential may also be compared to the OCP measurements following 40 ks solution exposure for the parent alloy shown in Table XI. Both area ratios displayed galvanic couple potentials within the statistical scatter of the final OCP measurement, possibly indicating the OCP of the parent alloy is representative of the coupling of its constituent phases.

Figure 12 shows an example plot of coupled potential and current density observed during ZRA. For the equal area ratio, the current density shows a transition from negative (preferential dissolution of the FCC CCA) to positive (preferential dissolution of the $L2_1$ CCA). Such changes in current sign occurred across multiple trials, but often occurred at different times. The decreased current magnitudes of the 10:1 area ratio, which was selected to represent the larger area fraction of the FCC phase in the parent alloy, are not statistically significant across multiple trials despite decreased exposed interface area for the $L2_1$ CCA. Across all trials for both area ratios, the coupled potential generally remains within 100 mV of -0.192 V_{SCE}, the open circuit potential of the parent alloy following 40 ks immersion of the air-formed oxide (Table XI). Changes in the coupled potential as well as the current suggest changing nature of one or both of the passive films during immersion. Although potential generally rises for the first 100 s of galvanic coupling for both area ratios, the time at which potentials begin to decrease and/or increase again are inconsistent between trials.

Table X: Coupled potential and current measurements of single-phase FCC (working electrode) and $L2_1$ (counter electrode) CCAs with air-formed oxides following 40 ks exposure in 0.01 M NaCl (pH ~ 5.75). Each term includes the mean value bounded by a one standard deviation range. Current densities are normalized to the working electrode area (0.784 cm^2).

Area Ratio	**Potential (V_{SCE})**	**Current ($nA.cm^{-2}$)**
Equal Areas	-0.217 +/- 0.052	-22.6 +/- 77.4
Larger FCC Matrix (10:1)	-0.187 +/- 0.014	-34.9 +/- 10.8

Table XI: Open circuit potentials of CCAs following 40 ks exposure of the air-formed passive film in 0.01 M NaCl (pH ~ 5.75). Each term includes the mean value bounded by a one standard deviation range.

Alloy	**OCP (V_{SCE})**
Parent Alloy	-0.192 +/- 0.085
Matrix	-0.099 +/- 0.003
Second Phase	-0.131 +/- 0.029

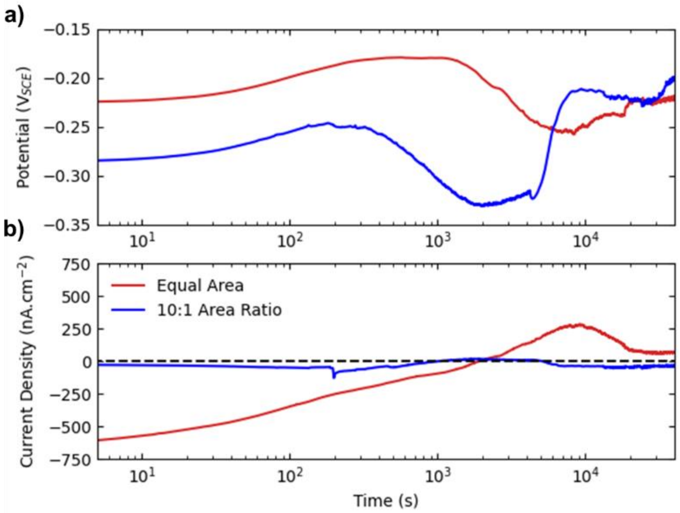

Figure 12: a) Potential and **b)** current density of galvanic couple formed between FCC and $L2_1$ single-phase CCAs with air-formed oxides in 0.01 M NaCl (pH ~ 5.75). Current densities are normalized to the working electrode area (0.784 cm^2)

3.6 Oxide Film Chemistry, Oxidation State, and Homogeneity

The passive film is suggested by XPS to contain passivated species for many constituent elements, aided by the stability of multiple passive species including Al(III), Cr(III), and Ti(IV) oxides at the -0.25 V_{SCE} potential in the ~5.75 pH environment for which the passive film was grown [65]. Figure 13 shows the deconvolutions of high resolution spectra collected over Al 2p, Cr $2p_{3/2}$, Fe $2p_{1/2}$, Ni $2p_{3/2}$, and Ti $2p_{3/2}$ core spectra into for both single-phase CCAs compared to previously obtained [12] measurements of the parent alloy. Detected surface cation fractions are reported in Table XII. The XPS spot size (100 µm) was significantly larger than the $L2_1$ regions in the parent alloy (3-5 µm) ensures the XPS spectra for the alloy cover a representative region of the microstructure and are not disproportionately characteristic of either phase. All films have high concentrations of Ti that were suggested to take the form of Ti(IV) oxide. The single-phase FCC passive film is dominated by Cr(III) signal attributable to oxide, hydroxide, and Fe-Cr spinel presence while also being enriched in Ti(IV) relative to bulk composition. The Al 2p spectra was not fit due to high noise levels with the surface cation fraction of oxidized species treated as negligible. The film formed over the $L2_1$ phase is enriched in Al(III), Cr(III), Mo(VI), and Ti(IV) relative to the bulk composition with higher Al(III) and Ti(IV) surface cation fractions and lower Cr(III) surface cation fractions than the film over the matrix phase. The decreased presence of Cr in the $L2_1$ film follows the decreased Cr composition in the bulk $L2_1$ phase. Contrastingly, the high Al(III) and Ni(II) signal in the $L2_1$ film, attributable to Al(III) oxide and Ni(II) oxide, hydroxide, and possibly Ni-Cr spinel, respectively, is likely aided by the higher concentrations of Al and Ni in the bulk $L2_1$ phase. Fe, Mn and Mo are present at low concentrations over both phases at similar magnitudes, and cannot be established as more enriched over either phase. The dual-phase CCA has both higher Ti(IV) surface cation fractions than the matrix CCA and higher Cr(III) surface cation fractions than the $L2_1$ CCA, possibly indicating enrichment of each element attributable to the higher bulk concentrations in each phase. Although Cr was indexed to low intensity of spinel in both samples, the companion metal was suggested by the Cr $2p_{3/2}$ spectra to change from Fe in films of the parent and FCC alloys to Ni in the $L2_1$ film[25]. Notably, XPS deconvolution does not provide any structural information; thus, spinel deconvolutions may merely be indicative of disordered solid solution oxide nearest-neighbor interactions as opposed to long-range ordered complex oxides [14]. Further structural characterization that would be necessary to confirm long-range ordering would require further high-intensity, hard X-ray techniques [66-68].

Table XII: Surface cation fractions obtained following potentiostatic oxide growth (-0.25 V_{SCE}, 40 ks, 0.01 M NaCl) via XPS of the dual-phase and single-phase CCAs. Bolded terms are considered enriched relative to the bulk compositions of the respective CCA shown in Table I.

Cation	Parent Alloy	Matrix	Second Phase
Al (III)	**16.9%**	0.0%	**24.1%**
Cr (III)	**15.5%**	**59.1%**	**7.5%**
Fe (II/III)	9.8%	2.5%	5.3%
Mn (II)	0.1%	0.2%	0.0%
Mo (VI)	1.9%	2.4%	0.8%
Ni (II)	1.0%	4.2%	9.2%
Ti (IV)	**54.9%**	**31.6%**	**53.1%**

Figure 14b shows AES maps characterizing the local chemical composition of the passive film formed. Distinct regions of increased Al, Ti, and Ni signal are present over the $L2_1$ phase as indicated by the secondary electron SEM micrograph. Fe and Cr are more prominent in the passive film formed over the matrix where higher bulk concentrations were present, while no conclusions were obtained regarding Mn and Mo, the two elements with the lowest compositions in the bulk alloy. Similar enrichment is present in the AES line scan (Figure 14c) with Al, Ti, and Ni enriched over the $L2_1$ phase, Fe, Cr, and Mn enriched over the FCC phase, and little Mo signal observed.

---

[25] High levels of scatter within the Fe $2p_{1/2}$ spectra makes identification of spinel species difficult, particularly in the case of the film formed over the $L2_1$ phase. Thus, proposed species are mainly suggested on the basis of the Cr $2p_{3/2}$ series. Thus, despite uncertainty in fitting the Fe $2p_{1/2}$ spectra, the replacement of $FeCr_2O_4$ with $NiCr_2O_4$ is well supported by fitting of the Cr $2p_{3/2}$ and Ni $2p_{3/2}$ spectra.

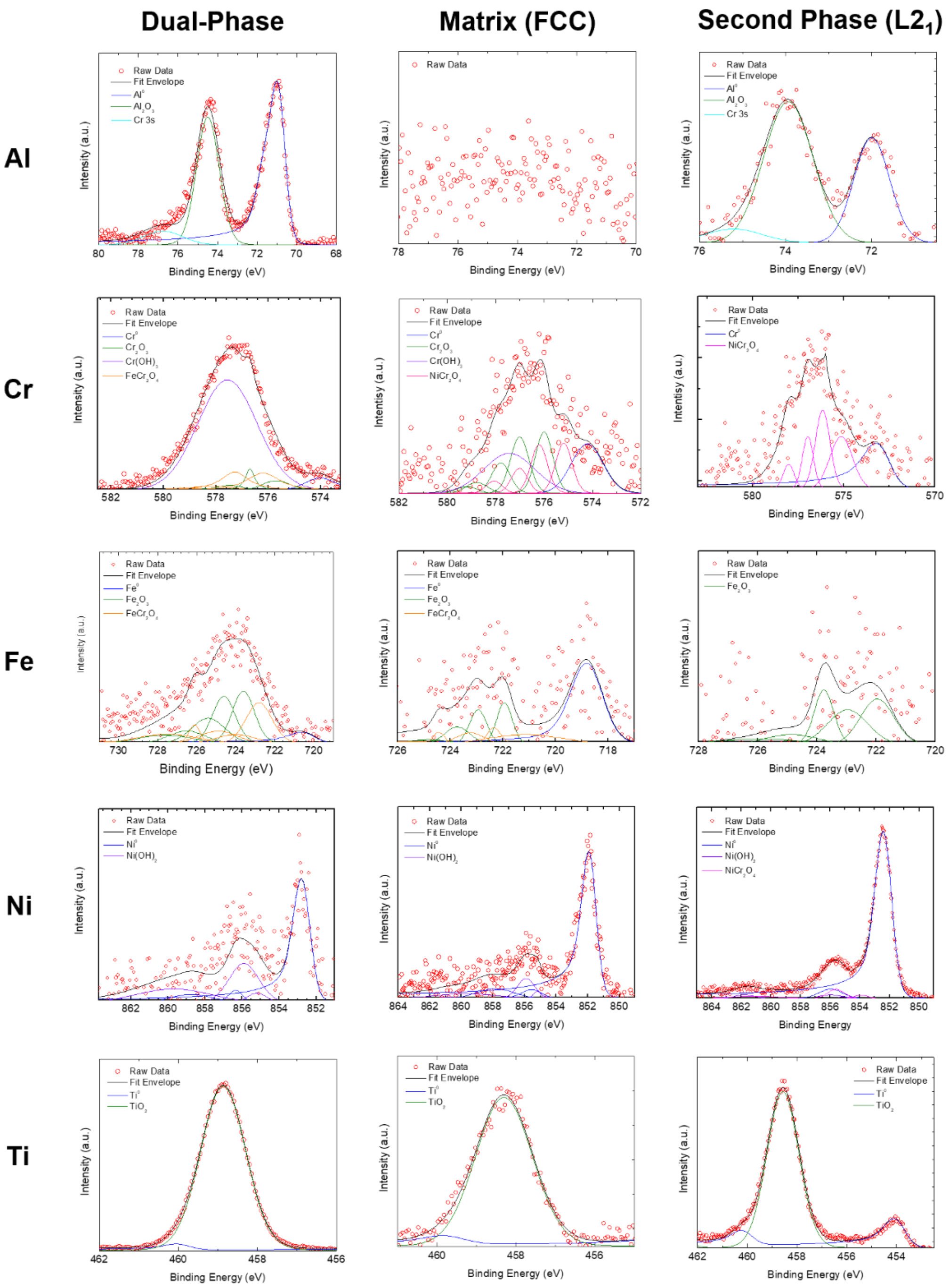

Figure 13: Selected high-resolution XPS spectra following 40 ks potentiostatic passive film growth at -0.25 V$_{SCE}$ in 0.01 M NaCl (pH ~ 5.75). Intensities are scaled to maximum counts for each spectra as quantitative values may vary due to external factors such as surface contamination.

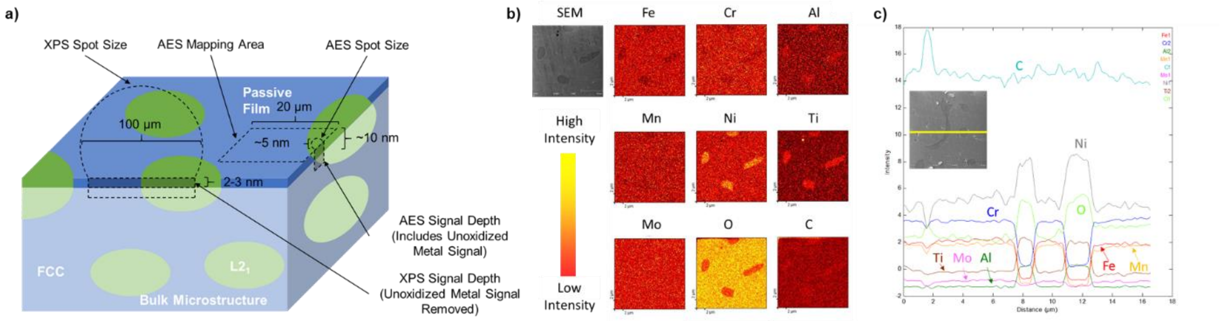

Figure 14: Auger electron spectroscopy **a)** schematic of spot size and penetration depth in comparison to XPS and microstructural morphology, **b)** elemental mapping and **c)** linescans of the dual-phase parent alloy following potentiostatic oxide grown (-0.25 V_{SCE}, 40 ks, 0.01 M NaCl).

Local passive film compositions taken over each phase are shown in Table XIII. Although both the XPS and AES point scan data indicate the film formed over the $L2_1$ phase has more Al, Ni, and Ti than that which is formed over the FCC phase, quantitative cation fractions severely differ. This may be attributable to the XPS-obtained cation fractions only presenting signals attributed to oxidized features (e.g., oxides, hydroxides, and spinels). AES point scans signal were obtained from within the photoelectron escape depth of approximately 10 nm. However, AES did not have the necessary resolution for deconvolution and thus surface cation fractions include both metallic and oxidized features. For example, the surface cation fraction for Ni is higher over both phases when measured by AES than by XPS, but this may be inflated by the high intensity of the Ni metal peak indicated by the XPS deconvolutions. Alternatively, for elements where the majority of escaped photoelectrons observed by XPS may be fit to oxidized features such as Cr and Ti, the majority of AES signal is likely attributable to passivated features.

Table XIII: Surface cation fractions obtained following potentiostatic oxide growth (-0.25 V_{SCE}, 40 ks, 0.01 M NaCl) via AES point scans over individual phases within the dual-phase CCA. Each term includes the mean value bounded by a one standard deviation range. Bolded terms are considered enriched relative to the bulk compositions of the respective CCA shown in Table I. Ni cation fractions are suggested to be inflated by signal attributable to metallic species enrichment near the metal-oxide interface.

Element	**Matrix**	**Second Phase**
Al	**10.8 +/- 1.5%**	**26.1 +/- 1.6%**
Cr	**14.7 +/- 1.1%**	**3.1 +/- 0.8%**
Fe	26.1 +/- 0.7%	6.1 +/- 0.8%
Mn	-	-
Mo	3.0 +/- 0.8%	**2.0 +/- 0.4%**
Ni	**37.2 +/- 1%**	**46.8 +/- 2.1%**
Ti	**8.2 +/- 0.7%**	15.9 +/- 0.8%

The passive film chemistry was also evaluated with the HAADF-STEM image and STEM-EDS mapping shown in Figure 15. High-angle annular dark-field (HAADF) imaging reveals an oxide layer with a thickness of 2-3 nm. Both the HAADF image and the O EDS map indicate the film thickness is fairly consistent across the FCC-$L2_1$ interface. EDS mapping shows the differing phase chemistries in both bulk microstructures. Fe and Ni show high signals in the FCC and $L2_1$ phases respectively and in the passive films grown above each phase, where a Cr-dominated passive film over the FCC phase is suggested in contrast with a Ti- and Al-dominated film formed over the $L2_1$ phase. Differences in compositional homogeneity of the passive film are confirmed by the line profile in the horizontal direction. The concentration of Al and Ti decreased when crossing the FCC-$L2_1$ interface while the concentration of Fe and Cr were higher in the film grown over the FCC phase. The changes in passive film composition occurred over a 5-10 nm lateral distance before leveling out. O concentrations were similar across both phases.

Line profiles in the perpendicular direction, from each bulk microstructure phase to the platinum deposition, illustrate the enriched elements in the passive film relative to the bulk microstructure. In the film grown over the $L2_1$ phase, Al and Ti concentrations were higher in the oxide region of the profile than in the metal region, signifying enrichment. Increasing Cr and Fe signal was also observed with the highest signal observed nearest the oxide/platinum interface, suggesting outer-layer enrichment, whereas inner-layer enrichment was suggested for Al and Ti. Ni was also shown to be present in the passive film, although at concentrations steadily decreasing with distance from the metal/oxide interface. The Ni concentration in the FCC region of the metal sharply increased near the interface but before a strong O signal was present, demonstrating enrichment in the metal near the oxide interface. In both line profiles, limited Pt signal in the outer regions of the passive film was observed but is not expected to affect comparisons between constituent element cation fractions.

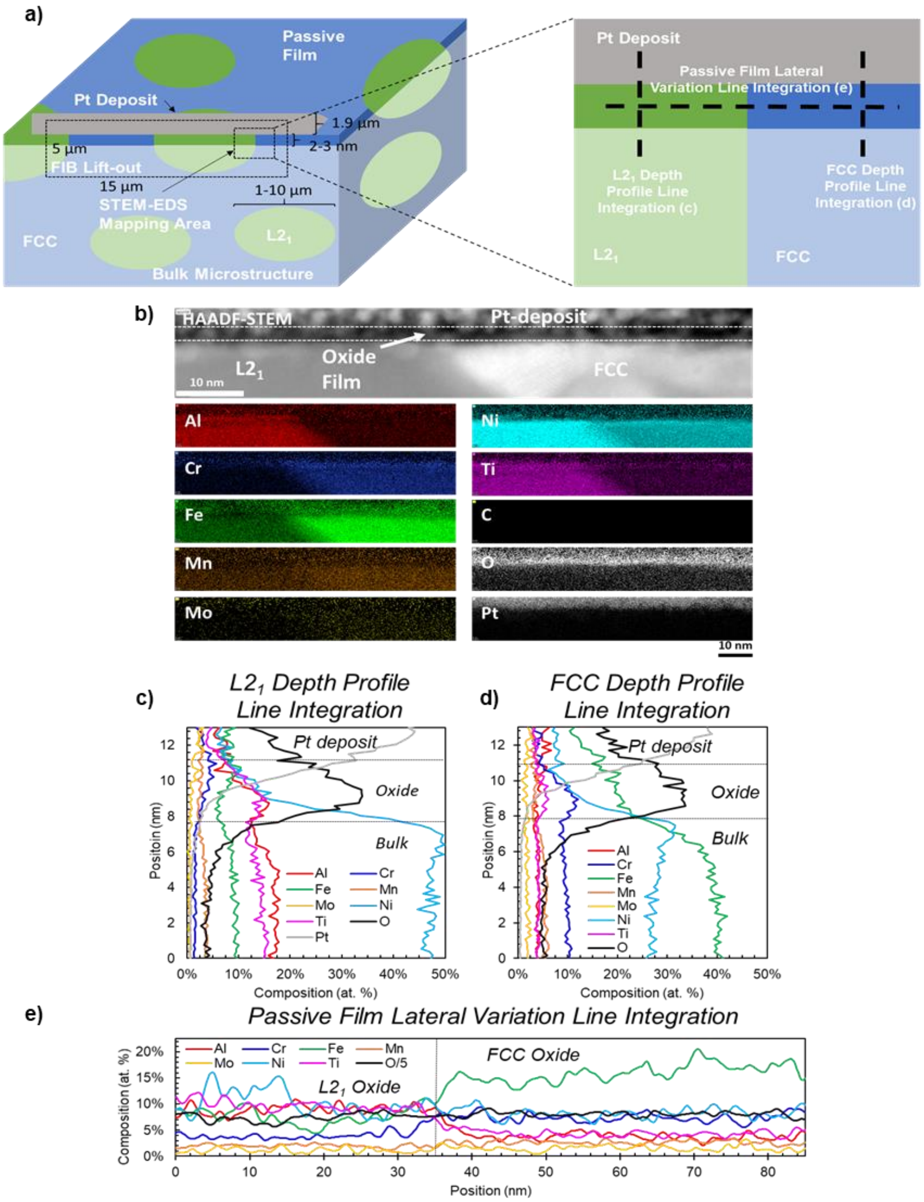

Figure 15: a) Schematic of FIB lift-out, STEM micrograph, and STEM-EDS line integrations relative to passive film and microstructural morphology. **b)** HAADF-STEM micrograph and STEM EDS mapping of phase interface of the dual-phase parent alloy following potentiostatic oxide grown (-0.25 V_{SCE}, 40 ks, 0.01 M NaCl). Quantitative line integrations are shown for the metal-oxide interfaces over the **c)** L2$_1$ second phase, **d)** FCC matrix phase, and **e)** the lateral line integration across the phase interface of the passive film.

4.0 Discussion

4.1 Thermodynamics and Kinetics Governing Passive Film Composition

Independent passive films are formed over each phase. The composition of the passive film tracks with the bulk microstructure composition over which the film was grown, as summarized in Table XIV, which follows trends previously established models for passive film chemistry from bulk composition [61]. For example, the passive film formed over the FCC phase is suggested to have higher surface cation fractions of Cr, Fe and Mo, while the film formed over the $L2_1$ phase has higher surface cation fractions of Ni, Al, and Ti (Figures 14c, 15e, Tables XII, XIII). Passive films form quickly in solution. Z", and therefore film thickness, rises rapidly for the first 100 s before reaching near-steady state values after 10 ks (Figure 10). The distinct phases within the passive film along with rapid film formation suggest surface diffusion is minor compared to cation flux perpendicular to passive film.

Table XIV: Summary of highest element in the measured composition for each single-phase CCA compared to passive film cation fractions identified via XPS following potentiostatic oxide growth (-0.25 V_{SCE}, 40 ks) in 0.01 M NaCl (pH~5.75).

Phase	**Matrix**	**Second Phase**
Bulk Alloy Dominant Elements (Table I)	Fe, Ni, Cr	Ni, Al, Ti
Passive Film Dominant Elements (Table XII)	Cr(III), Ti(IV), Fe(II)	Ti(IV), Al(III), Ni(II)

Phase composition may also be compared to traditionally established metrics for desirable passive film formation in aqueous corrosion in chloride containing environments. The matrix phase bulk Cr concentration of 10% is near the ~12 at. % limit traditionally suggested to be a minimum required for the formation of a stable Cr-dominated passive film in Fe-Cr [69] and Ni-Cr [70] alloys. This is noteworthy particularly given reports suggesting possible stabilization of Cr passive species at subcritical bulk Cr concentrations in Al- and/or Ti-containing CCAs [12, 71]. Alternatively, the bulk Cr concentration is much lower in the $L2_1$ phase (Table I) but the phase has over three times the bulk Ti concentration as the FCC matrix. Thus, the matrix bulk composition contributes to significantly higher Cr surface cation fractions in the film formed over the matrix phase (Figures 14c, 15e, Tables XII, XIII). Alternatively, the ~15 at. % limit necessary for formation of a stable Al-dominated passive film is exceeded for the $L2_1$ phase, but not for the matrix, contributing to the comparatively higher Al surface cation fractions over the $L2_1$ phase [72].

Passive film chemistry is influenced by the thermodynamic stability of oxides for each constituent species. Cr and Ti were present in the passive films of all three alloys at higher concentrations than those of each alloy's respective bulk composition, with high levels of Al also present in the dual-phase and $L2_1$ CCAs (Table XII). High levels of noise in the FCC CCA limit accurate assessment of Al concentration in the passive film, and therefore of enrichment. The stability of the passivated species is likely aided by favorable formation energies of the Al, Cr, and Ti oxide species listed in Table XV relative to other stoichiometric oxides. Similar trends are observed in the surface cation fractions obtained via AES (Table

XIII), although such values may be influenced by signal coming from unoxidized species in the bulk microstructure. Extended exposure or aging during the 40 ks film growth procedure may further promote increasing surface cation fractions of more thermodynamically favorable passive species. Gradual enrichment of the prevalent oxides may occur through preferential chemical dissolution of less stable oxides to form metal chlorides [73, 74]. Furthermore, favorable enthalpies of mixing or other beneficial interactions may contribute to Al, Cr, and Ti stability within the film [12]. Beneficial interactions with Cr and/or Al may influence the high surface cation fractions of Ti within the passive film of the matrix and parent alloy, despite comparatively lower bulk concentrations (Tables I, XII, XIII). Al, Cr, and Ti presence in the passive film is further supported by the predicted stability of their passive species from E-pH diagrams of their respective pure metals, while Fe, Mn, Mo, and Ni are predicted to exists in a dissolve state at -0.25 V_{SCE} in pH 5.75 conditions [65]. For all elements, the applied potential was well above the standard reduction potentials, indicating a sufficient driving force for passivation and/or dissolution was present. While E-pH diagrams of pure metals inform the effect of environment on passivity, stability may also be affected by interactions with other metals in the alloy, either through thermodynamic or kinetic considerations [16]. For example, despite pure Fe and Ni being suggested to dissolve, the stability of Fe and Ni in the passive film may be improved through the formation of spinel species. $NiCr_2O_4$ that is suggested to form over the $L2_1$ phase (Figure 13) has a comparable free energy of formation to pure Cr_2O_3 on both a per-atom and per-anion level (Table XV). $FeCr_2O_4$, which has a less negative free energy of formation than $NiCr_2O_4$ is instead suggested to form over the Fe-enriched FCC phase. Therefore, while free energy of formation may inform prominent chemical species in the passive film, the local composition in bulk microstructure over which the film is formed also plays a prominent effect.

Table XV: Standard free energy of formation of proposed oxide species within CCA passive films.

Species	**ΔG°_{298K} (kJ.mol^{-1})**	**Reference**
Al_2O_3	−1690.7	[75]
Cr_2O_3	−1050.0	[76]
Fe_2O_3	-742.2	[75]
Mn_2O_3	-881.1	[75]
MoO_3	-668.0	[75]
NiO	-210.54	[77]
TiO_2	−959.1	[75]
$FeCr_2O_4$	−1339.40	[76]
$NiCr_2O_4$	-1420.92	[78]

The composition of the film varies with depth over both phases. For example, the stability of Fe species may be improved by enrichment in the outer layers, where the O activity is higher, as observed in the STEM-EDS line integrations (Figures 15c, 15d) and previous sputter depth profiling [12]. Comparatively, Cr, Al, and Ti have the highest intensities at similar depths near the metal/oxide interface, The local enrichment of Ni in the bulk FCC phase near the metal/oxide interface may be influenced by the epitaxial coherency with the FCC phase may favor early Ni oxidation [79-81] before dissolution of the unstable species, leaving Ni enrichment in the metal that was not observed in the $L2_1$ phase [63, 82]. The high intensity of Ni metal near the metal/oxide interface revealed by both STEM-EDS and XPS spectral deconvolution (Figures 13, 15) indicates the AES point scans, which could not be deconvoluted to metal and oxidized valences, likely include significant signal from Ni metal that accounts for the deviation between XPS and AES obtained cation fractions (Tables XII, XIII).

4.2 Interfacial Contributions to Nature of the Passive Film

The transition between chemically distinct compositions in the passive film scale provides evidence of a heterophase interface (HI) within a passive film formed over a CCA. Compositions for each phase are suggested to be uniform beyond a transition region of less than 10 nm show no localized depletion of passivating elements was indicated near either the FCC-$L2_1$ interface of the bulk microstructure (Figure 1) or passive film phase interface (Figures 14c, 15e), limiting the risk of localized corrosion at sites hypothetically depleted in passivating elements following solutionizing heat treatments. The film thickness and limited resolution in the HAADF-STEM image (Figure 15b) prohibit characterization of the orientation and nanostructure of the oxides and subsequently the structural aspects of the FCC-$L2_1$ interface. Structural considerations may be of note given the miscibility of Fe(III) and Al(III) in corundum-like structures that likely form over the Cr(III)-enriched FCC film [14], whereas solubility, and therefore possible synergistic behavior, may be comparatively less likely in Ti(IV) oxides, which are generally suggested to be of rutile or amorphous structure with other suboxides possibly present in small amounts [83-85]. It is unclear to what degree the crystallinity of Ti(IV) oxides may affect compatibility with the corundum-like structures suggested to form over the FCC phases. Despite such limitations, the presence of a defined HI suggests the applicability of the comparatively well-established study of polycrystalline oxides [86] to explain electrochemical phenomena. For instance, oxygen vacancies, well established charge carriers under the point defect model [87], have been shown to congregate near GBs in cerium oxides and affect local electrical resistivity [88] in addition to their well-established effect on global film-formation rates [89]. Local structural changes and increased oxygen vacancy concentration may further alter the local valence of passivating cations such as Ti [90, 91], despite valence changes not being observed in the global XPS measurements (Figure 13). Such effects may be enhanced by the multi-principal cation nature of films formed over CCAs. While the effects of HIs on localized corrosion, specifically pit initiation, are unclear, the nature of the interface must be considered.

4.3 Relationship between Passivity and Localized Corrosion

Pitting is considerably more likely at phase interfaces and appears to propagate equally in all directions (Figure 6). It is difficult to determine the connection between interfacial pitting and attributes of the passive film given no significant depletion of passivating elements was observed at the interfaces with either AES or STEM-EDS (Figures 14c, 15e). Despite being slightly anodic to the FCC phase, low current density magnitude observed during galvanic coupling (Table X) and the equal growth of pits in each direction of the interface (Figure 6) suggest that the $L2_1$ phase is not subject to preferential dissolution from microgalvanic coupling. However, the consistently lower E_{pit} and E_{rep} values for the $L2_1$ CCA may imply inferior resistance to localized corrosion in the absence of galvanic coupling (Figures 5, 9, Tables III, VII). The lack of significant microgalvanic corrosion may have been aided by the similar open circuit potentials following both 1800 s (Figure 9, Table VII) and 40 ks solution exposure (Table XI). Similar values indicate a reduced driving force for microgalvanic corrosion. Additionally, passivation has been shown to decrease the current of a galvanic couple [54], indicating the ability of both phases to independently passivate may contribute to decreased influence of microgalvanic effects.

Individual phases are prone to preferential dissolution in dual-phase alloys when they are depleted in passivating elements. Passivity of both phases is further justified by similar EIS results for both the air-formed and solution-formed passive films, with neither phase having a lower low-frequency impedance at a statistically significant level (Figures 8, 11, Tables V, VI, VIII, IX). In contrast, the Al-Ni rich BCC phase is strongly depleted in Cr relative to the $Al_xCoCrFeNi$ CCA, leading to pitting and eventual preferential dissolution in chloride environments [23]. The partitioning of Cr and Ti to different phases herein in the evaluated CCA ensures passivity over both phases, and limits preferential dissolution. Additionally, unlike previously reports for duplex stainless steel [46, 50], the film is suggested to be of similar thickness on both sides of the HI (Figure 12b), which could additionally contribute to similar levels of passivity obtained over both phases.

4.4 Implications for Alloy Design

Simultaneous passivation observed over both phases verifies demonstrates that utilizing combinations of multiple phases capable of independent passivation, such as the evaluated FCC-$L2_1$ microstructure, may be utilized as a strategy for the design of multi-phase corrosion resistant CCAs.

Therefore, high-throughput methods frequently utilized to narrow a broad CCA compositional space may filter compositions to target the preset phases with both desirable structures and compositions that possess the independent ability to passivate as a method to help promote corrosion resistance [92]. Phase volume fraction in a multi-phase CCAs can be used as a tunable feature within the design process. For example, predictive measurements of mechanical properties from changing area fractions of constituent phases have also become well established within the CCA field [7, 21, 93]. However, the effect of changing phase fraction on passive film chemistry and corrosion behavior must also be considered. The surface cation fractions (Figure 13, Table XII), and by extension the corrosion behavior (Figures 5, 9), obtained for the parent alloy is generally contributed to by both constituent phases, but often not in a quantitative manner characteristic of the single-phase CCAs weighted by area fractions. This signifies that the phases may contribute both to passive film composition and corrosion behavior in a manner disproportionate to area fraction, as in the case of duplex stainless steel [55]. The findings indicate that area fraction may not be freely adjusted to tailor mechanical properties without regard to the effects on corrosion. Despite utility in identifying qualitative trends, difficulties remain in predicting corrosion behavior as a function of phase fraction with the relationship between changing second phase area fractions and overall corrosion resistance providing opportunities for future study.

The morphology of HIs in the passive film is also likely to significantly alter corrosion behavior. Grain size, and thus the morphology of GBs in the microstructure, has been shown to strongly affect the corrosion behavior of CoCrFeMnNi [94], potentially through localized thinning of the passive film [95]. Although a lack of atomic level characterization limits the analysis of GBs in the oxide film, differing passive film chemistries and polarization resistance indicate a changing oxide layer. HIs, with differing passive film chemistry on either side of the boundary, initiate more significant cation segregation than single-phase GBs; however, such segmentation may be limited by the high solubility of constituent elements aided by the high entropy nature of the passive film [96].

Ensuring the passive film possesses adequate concentrations of passivating elements over both phases is demonstrated as a viable strategy of the design of corrosion resistant CCAs [13]. While local characterization of the passive film chemistry remains inefficient, the presence of HIs at similar locations to microstructural phase interfaces (Figures 14b, 15b) ensures local passive film chemistry is affected by the local in the bulk microstructure. Thus, microstructural analysis of and/or predictive tools for volume fraction, location, and second phase regions may be useful as an initial predictive metric for dual-phase CCA passivity over each phase, allowing for targeting of compositions with global corrosion resistance.

5.0 Conclusions

The passivity and corrosion behavior of a dual-phase $Al_{0.3}Cr_{0.5}Fe_2Mn_{0.25}Mo_{0.15}Ni_{1.5}Ti_{0.3}$ CCA was characterized. Individual phases were isolated using both localized techniques on the dual-phase alloy and global techniques on single-phase CCAs of representative compositions. The following conclusions were drawn:

- The passive film over a dual-phase alloy consisted of two distinct oxides with similar thicknesses. The primary passivators in the film formed over the FCC phase was Cr(III) whilst they were Ti(IV) and Al(III) in the film formed over the $L2_1$ phase. Both phases exhibited independent abilities passivate and form protective oxides in response to external potential.
- The corrosion resistance of the dual-phase passive film was marked by corrosion attributes and properties weighted to its two constituent phase passive films. Both phases are suggested to form stable and potentially metastable passive films in NaCl at a neutral pH, with each single-phase CCA exhibiting high impedance characteristic typical of passivated protective surfaces. Passive attribute such as low passive current density and critical current density were present for each single-phase and the dual-phase CCAs at similar magnitudes.
- The dual-phase CCA breakdown potential of was in between the breakdown potentials of the FCC and $L2_1$ single-phase CCAs for both the air-formed and cathodically pre-treated surfaces. The heterophase interface in the passive film was identified as a preferential pitting sites or weak link in corrosion protectiveness compared to the oxides formed over each phase.
- Neither galvanic coupling nor dealloying corrosion was suggested to compromise the corrosion behavior of the alloy. Similar corrosion potentials may indicate a low driving force for microgalvanic coupling, potentially identifying a targetable attribute for corrosion resistance. However, the exact relationships between alloy composition, phase partitioning, and corrosion behavior require further evaluation.

Acknowledgments

This work was supported by the United States Office of Naval Research grants #N00014-23-1-2441 and #N00014-19-1-2420 under the directorship of David Shifler. Helga Heinrich operated the FIB and TEM. AES data was obtained from Surface Science Western (London, ON, Canada) by Jeffrey Henderson and Sridhar Ramamurthy. The University of Virginia Nanomaterials Characterization Facility provided FIB, SEM, TEM, XPS, and XRD facilities and technical assistance. The PHI VersaProbe III was procured under NSF award # 162601. Diego Ibarra Hoyos assisted with sample preparation. Alen Korjenic assisted with the ZRA setup and interpretation. Debashish Sur contributed to the electrochemical characterization.

References

[1] S. Gorsse, J.-P. Couzinié, D.B. Miracle, From high-entropy alloys to complex concentrated alloys, Comptes Rendus Physique, 19 (2018) 721-736.

[2] C. Varvenne, A. Luque, W.A. Curtin, Theory of strengthening in fcc high entropy alloys, Acta Materialia, 118 (2016) 164-176.

[3] B. Gludovatz, A. Hohenwarter, D. Catoor, E.H. Chang, E.P. George, R.O. Ritchie, A fracture-resistant high-entropy alloy for cryogenic applications, Science, 345 (2014) 1153-1158.

[4] M.-H. Tsai, Physical Properties of High Entropy Alloys, in: Entropy, 2013, pp. 5338-5345.

[5] Y. Qiu, S. Thomas, M.A. Gibson, H.L. Fraser, N. Birbilis, Corrosion of high entropy alloys, npj Materials Degradation, 1 (2017) 15.

[6] Y. Shi, B. Yang, P.K. Liaw, Corrosion-Resistant High-Entropy Alloys: A Review, Metals, 7 (2017) 43.

[7] D.B. Miracle, O.N. Senkov, A critical review of high entropy alloys and related concepts, Acta Materialia, 122 (2017) 448-511.

[8] D.J.M. King, S.C. Middleburgh, A.G. McGregor, M.B. Cortie, Predicting the formation and stability of single phase high-entropy alloys, Acta Materialia, 104 (2016) 172-179.

[9] X. Yang, Y. Zhang, Prediction of high-entropy stabilized solid-solution in multi-component alloys, Materials Chemistry and Physics, 132 (2012) 233-238.

[10] R. Feng, C. Lee, M. Mathes, T.T. Zuo, S. Chen, J. Hawk, Y. Zhang, P. Liaw, Design of Light-Weight High-Entropy Alloys, Entropy, 18 (2016) 333.

[11] B. Cantor, I.T.H. Chang, P. Knight, A.J.B. Vincent, Microstructural development in equiatomic multicomponent alloys, Materials Science and Engineering: A, 375-377 (2004) 213-218.

[12] S.B. Inman, D. Sur, J. Han, K. Ogle, J.R. Scully, Corrosion behavior of a compositionally complex alloy utilizing simultaneous Al, Cr, and Ti passivation, Corrosion Science, 217 (2023) 111138.

[13] S.B. Inman, J.R. Scully, Design and Discovery of Compositionally Complex Alloys (CCA) that Include High Corrosion Resistance, Corrosion, (2024) 4451.

[14] K. Wang, J. Han, A.Y. Gerard, J.R. Scully, B.-C. Zhou, Potential-pH diagrams considering complex oxide solution phases for understanding aqueous corrosion of multi-principal element alloys, npj Materials Degradation, 4 (2020) 35.

[15] X.X. Yu, A. Gulec, Q. Sherman, K.L. Cwalina, J.R. Scully, J.H. Perepezko, P.W. Voorhees, L.D. Marks, Nonequilibrium Solute Capture in Passivating Oxide Films, Physical review letters, 121 (2018) 145701.

[16] J.R. Scully, S.B. Inman, A.Y. Gerard, C.D. Taylor, W. Windl, D.K. Schreiber, P. Lu, J.E. Saal, G.S. Frankel, Controlling the corrosion resistance of multi-principal element alloys, Scripta Materialia, 188 (2020) 96-101.

[17] G.R. Aripov, V.V. Cheverikin, A.I. Bazlov, H. Mao, D.V. Louzguine-Luzgin, V.I. Polkin, S.D. Prokoshkin, The Study of Structural Changes in Homogenized High-Entropy Alloys, Physical Mesomechanics, 24 (2021) 663-673.

[18] W.-R. Wang, W.-L. Wang, S.-C. Wang, Y.-C. Tsai, C.-H. Lai, J.-W. Yeh, Effects of Al addition on the microstructure and mechanical property of AlxCoCrFeNi high-entropy alloys, Intermetallics, 26 (2012) 44-51.

[19] X.X. Liu, S.G. Ma, W.D. Song, D. Zhao, Z.H. Wang, Microstructure evolution and mechanical response of Co-free Ni2CrFeAl0.3Tix high-entropy alloys, Journal of Alloys and Compounds, 931 (2023) 167523.

[20] Z. Niu, Y. Wang, C. Geng, J. Xu, Y. Wang, Microstructural evolution, mechanical and corrosion behaviors of as-annealed CoCrFeNiMox (x = 0, 0.2, 0.5, 0.8, 1) high entropy alloys, Journal of Alloys and Compounds, 820 (2020) 153273.

[21] J.J. Bhattacharyya, S.B. Inman, M.A. Wischhusen, J. Qi, J. Poon, J.R. Scully, S.R. Agnew, Lightweight, low cost compositionally complex multiphase alloys with optimized strength, ductility and corrosion resistance: Discovery, design and mechanistic understandings, Materials & Design, 228 (2023) 111831.

[22] X.-L. Shang, Z.-J. Wang, Q.-F. Wu, J.-C. Wang, J.-J. Li, J.-K. Yu, Effect of Mo Addition on Corrosion Behavior of High-Entropy Alloys CoCrFeNiMox in Aqueous Environments, Acta Metallurgica Sinica (English Letters), 32 (2019) 41-51.

[23] Y. Shi, L. Collins, N. Balke, P.K. Liaw, B. Yang, In-situ electrochemical-AFM study of localized corrosion of AlxCoCrFeNi high-entropy alloys in chloride solution, Applied Surface Science, 439 (2018) 533-544.

[24] Z. Tang, L. Huang, W. He, P.K. Liaw, Alloying and Processing Effects on the Aqueous Corrosion Behavior of High-Entropy Alloys, in: Entropy, 2014, pp. 895-911.

[25] W. Guo, J. Li, M. Qi, Y. Xu, H.R. Ezatpour, Effects of heat treatment on the microstructure, mechanical properties and corrosion resistance of AlCoCrFeNiTi0.5 high-entropy alloy, Journal of Alloys and Compounds, 884 (2021) 161026.

[26] S.B. Inman, J. Han, A.Y. Gerard, J. Qi, M.A. Wischhusen, S.R. Agnew, S.J. Poon, K. Ogle, J.R. Scully, Effect of Mn Content on the Passivation and Corrosion of Al0.3Cr0.5Fe2MnxMo0.15Ni1.5Ti0.3 Compositionally Complex Face-Centered Cubic Alloys, Corrosion, 78 (2021) 32-48.

[27] C.-C. Yen, H.-N. Lu, M.-H. Tsai, B.-W. Wu, Y.-C. Lo, C.-C. Wang, S.-Y. Chang, S.-K. Yen, Corrosion mechanism of annealed equiatomic AlCoCrFeNi tri-phase high-entropy alloy in 0.5 M H2SO4 aerated aqueous solution, Corrosion Science, 157 (2019) 462-471.

[28] P. Cui, Z. Bao, Y. Liu, F. Zhou, Z. Lai, Y. Zhou, J. Zhu, Corrosion behavior and mechanism of dual phase Fe1.125Ni1.06CrAl high entropy alloy, Corrosion Science, 201 (2022) 110276.

[29] Y.-J. Hsu, W.-C. Chiang, J.-K. Wu, Corrosion behavior of FeCoNiCrCux high-entropy alloys in 3.5% sodium chloride solution, Materials Chemistry and Physics, 92 (2005) 112-117.

[30] Y. Fu, J. Li, H. Luo, C. Du, X. Li, Recent advances on environmental corrosion behavior and mechanism of high-entropy alloys, Journal of Materials Science & Technology, 80 (2021) 217-233.

[31] Y. Shi, B. Yang, X. Xie, J. Brechtl, K.A. Dahmen, P.K. Liaw, Corrosion of Al xCoCrFeNi high-entropy alloys: Al-content and potential scan-rate dependent pitting behavior, Corrosion Science, 119 (2017) 33-45.

[32] Z. Wang, Z.-X. Liu, J. Jin, D.-Z. Tang, L. Zhang, Selective corrosion mechanism of CoCrFeMoNi high-entropy alloy in the transpassive region based on the passive film characterization by ToF-SIMS, Corrosion Science, 218 (2023) 111206.

[33] S.B. Inman, J. Han, M.A. Wischhusen, J. Qi, S.R. Agnew, K. Ogle, J.R. Scully, Passivation and Localized Corrosion Resistance of Al0.3Cr0.5Fe2MoxNi1.5Ti0.3 Compositionally Complex Alloys: Effect of Mo Content, Corroison Science, 227 (2023) 111692.

[34] Y. Shi, L. Collins, R. Feng, C. Zhang, N. Balke, P.K. Liaw, B. Yang, Homogenization of AlxCoCrFeNi high-entropy alloys with improved corrosion resistance, Corrosion Science, 133 (2018) 120-131.

[35] S. Shuang, Q. Yu, X. Gao, Q.F. He, J.Y. Zhang, S.Q. Shi, Y. Yang, Tuning the microstructure for superb corrosion resistance in eutectic high entropy alloy, Journal of Materials Science & Technology, 109 (2022) 197-208.

[36] Q. Zhao, Z. Pan, X. Wang, H. Luo, Y. Liu, X. Li, Corrosion and passive behavior of AlxCrFeNi3−x (x = 0.6, 0.8, 1.0) eutectic high entropy alloys in chloride environment, Corrosion Science, 208 (2022) 110666.

[37] Y.L. Chou, J.W. Yeh, H.C. Shih, The effect of molybdenum on the corrosion behaviour of the high-entropy alloys Co1.5CrFeNi1.5Ti0.5Mox in aqueous environments, Corrosion Science, 52 (2010) 2571-2581.

[38] U. Martin, J. Ress, P. Pérez, P. Adeva, D.M. Bastidas, Corrosion Behavior of Al10Cr30Fe25Mn30Ti5 High-Entropy Alloy: Microstructural, Electrochemical, and Surface Analysis, in: Metals, 2022.

[39] J. Li, X. Yang, R. Zhu, Y. Zhang, Corrosion and Serration Behaviors of TiZr0.5NbCr0.5VxMoy High Entropy Alloys in Aqueous Environments, in: Metals, 2014, pp. 597-608.

[40] C.-H. Tsau, H.-P. Hsiao, T.-Y. Chien, Corrosion Behavior of CrFeCoNiV0.5 and CrFeCoNiV Alloys in 0.5 M and 1 M Sodium Chloride Solutions, in: Materials, 2023.
[41] A.V. Ayyagari, B. Gwalani, S. Muskeri, S. Mukherjee, R. Banerjee, Surface degradation mechanisms in precipitation-hardened high-entropy alloys, npj Materials Degradation, 2 (2018) 33.
[42] D.H. Xiao, P.F. Zhou, W.Q. Wu, H.Y. Diao, M.C. Gao, M. Song, P.K. Liaw, Microstructure, mechanical and corrosion behaviors of AlCoCuFeNi-(Cr,Ti) high entropy alloys, Materials & Design, 116 (2017) 438-447.
[43] K. Yamanaka, H. Shiratori, M. Mori, K. Omura, T. Fujieda, K. Kuwabara, A. Chiba, Corrosion mechanism of an equimolar AlCoCrFeNi high-entropy alloy additively manufactured by electron beam melting, npj Materials Degradation, 4 (2020) 24.
[44] W. Qi, W. Wang, X. Yang, G. Zhang, W. Ye, Y. Su, Y. Li, S. Chen, Effects of Al and Ti co-doping on the strength-ductility- corrosion resistance of CoCrFeNi-AlTi high-entropy alloys, Journal of Alloys and Compounds, 925 (2022) 166751.
[45] M. Långberg, C. Örnek, F. Zhang, J. Cheng, M. Liu, E. Grånäs, C. Wiemann, A. Gloskovskii, Y. Matveyev, S. Kulkarni, H. Noei, T.F. Keller, D. Lindell, U. Kivisäkk, E. Lundgren, A. Stierle, J. Pan, Characterization of Native Oxide and Passive Film on Austenite/Ferrite Phases of Duplex Stainless Steel Using Synchrotron HAXPEEM, Journal of The Electrochemical Society, 166 (2019) C3336.
[46] M. Långberg, F. Zhang, E. Grånäs, C. Örnek, J. Cheng, M. Liu, C. Wiemann, A. Gloskovskii, T.F. Keller, C. Schlueter, S. Kulkarni, H. Noei, D. Lindell, U. Kivisäkk, E. Lundgren, A. Stierle, J. Pan, Lateral variation of the native passive film on super duplex stainless steel resolved by synchrotron hard X-ray photoelectron emission microscopy, Corrosion Science, 174 (2020) 108841.
[47] M. Långberg, C. Örnek, J. Evertsson, G.S. Harlow, W. Linpé, L. Rullik, F. Carlà, R. Felici, E. Bettini, U. Kivisäkk, E. Lundgren, J. Pan, Redefining passivity breakdown of super duplex stainless steel by electrochemical operando synchrotron near surface X-ray analyses, npj Materials Degradation, 3 (2019) 22.
[48] V. Vignal, H. Krawiec, O. Heintz, D. Mainy, Passive properties of lean duplex stainless steels after long-term ageing in air studied using EBSD, AES, XPS and local electrochemical impedance spectroscopy, Corrosion Science, 67 (2013) 109-117.
[49] E. Rahimi, A. Rafsanjani-Abbasi, A. Davoodi, S. Hosseinpour, Characterization of the Native Passive Film on Ferrite and Austenite Phases of Sensitized 2205 Duplex Stainless Steel, Journal of The Electrochemical Society, 166 (2019) C609.
[50] L.Q. Guo, M.C. Lin, L.J. Qiao, A.A. Volinsky, Duplex stainless steel passive film electrical properties studied by in situ current sensing atomic force microscopy, Corrosion Science, 78 (2014) 55-62.
[51] K. Fushimi, K. Yanagisawa, T. Nakanishi, Y. Hasegawa, T. Kawano, M. Kimura, Microelectrochemistry of dual-phase steel corroding in 0.1M sulfuric acid, Electrochimica Acta, 114 (2013) 83-87.
[52] Neetu, P.K. Katiyar, S. Sangal, K. Mondal, Effect of various phase fraction of bainite, intercritical ferrite, retained austenite and pearlite on the corrosion behavior of multiphase steels, Corrosion Science, 178 (2021) 109043.
[53] H.-Y. Ha, T.-H. Lee, C.-G. Lee, H. Yoon, Understanding the relation between pitting corrosion resistance and phase fraction of S32101 duplex stainless steel, Corrosion Science, 149 (2019) 226-235.
[54] W.-T. Tsai, J.-R. Chen, Galvanic corrosion between the constituent phases in duplex stainless steel, Corrosion Science, 49 (2007) 3659-3668.
[55] E. Gardin, S. Zanna, A. Seyeux, A. Allion-Maurer, P. Marcus, Comparative study of the surface oxide films on lean duplex and corresponding single phase stainless steels by XPS and ToF-SIMS, Corrosion Science, 143 (2018) 403-413.
[56] S. Choudhary, Y. Qiu, S. Thomas, N. Birbilis, Element-resolved electrochemical analysis of transpassive dissolution and repassivation behavior of the multi-principal element alloy AlTiVCr, Electrochimica Acta, 362 (2020) 137104.

[57] D.C. Joy, Monte Carlo Modeling for Electron Microscopy and Microanalysis, Oxford University Press, Incorporated, New York, UNITED STATES, 1995.
[58] J. Baltrusaitis, B. Mendoza-Sanchez, V. Fernandez, R. Veenstra, N. Dukstiene, A. Roberts, N. Fairley, Generalized molybdenum oxide surface chemical state XPS determination via informed amorphous sample model, Applied Surface Science, 326 (2015) 151-161.
[59] M.C. Biesinger, L.W.M. Lau, A.R. Gerson, R.S.C. Smart, Resolving surface chemical states in XPS analysis of first row transition metals, oxides and hydroxides: Sc, Ti, V, Cu and Zn, Applied Surface Science, 257 (2010) 887-898.
[60] M.C. Biesinger, B.P. Payne, A.P. Grosvenor, L.W.M. Lau, A.R. Gerson, R.S.C. Smart, Resolving surface chemical states in XPS analysis of first row transition metals, oxides and hydroxides: Cr, Mn, Fe, Co and Ni, Applied Surface Science, 257 (2011) 2717-2730.
[61] J.E. Castle, K. Asami, A more general method for ranking the enrichment of alloying elements in passivation films, Surface and Interface Analysis, 36 (2004) 220-224.
[62] S.B. Inman, M.A. Wischhusen, J. Qi, J. Poon, S.R. Agnew, J.R. Scully, Variation of the Passive Film on Compositionally Concentrated Dual-phase $Al_{0.3}Cr_{0.5}Fe_2Mn_{0.25}Mo_{0.15}Ni_{1.5}Ti_{0.3}$ and Implications for Corrosion, Submitted to Metallurgical and Materials Transactions A, (2024).
[63] K. Lutton, K. Gusieva, N. Ott, N. Birbilis, J.R. Scully, Understanding multi-element alloy passivation in acidic solutions using operando methods, Electrochemistry Communications, 80 (2017) 44-47.
[64] B. Hirschorn, M.E. Orazem, B. Tribollet, V. Vivier, I. Frateur, M. Musiani, Determination of effective capacitance and film thickness from constant-phase-element parameters, Electrochimica Acta, 55 (2010) 6218-6227.
[65] M. Pourbaix, Atlas of Electrochemical Equilibria in Aqueous Solutions, National Association of Corrosion Engineers, 1974.
[66] F. Carrette, M.C. Lafont, L. Legras, L. Guinard, B. Pieraggi, Analysis and TEM examinations of corrosion scales grown on alloy 690 exposed to PWR environment, Materials at High Temperatures, 20 (2003) 581-591.
[67] A.J. Davenport, L.J. Oblonsky, M.P. Ryan, M.F. Toney, The Structure of the Passive Film That Forms on Iron in Aqueous Environments, Journal of The Electrochemical Society, 147 (2000) 2162.
[68] O.M. Magnussen, J. Scherer, B.M. Ocko, R.J. Behm, In Situ X-ray Scattering Study of the Passive Film on Ni(111) in Sulfuric Acid Solution, The Journal of Physical Chemistry B, 104 (2000) 1222-1226.
[69] P. King, H. Uhlig, Passivity in the iron-chromium binary alloys, The Journal of Physical Chemistry, 63 (1959) 2026-2032.
[70] H.H. Uhlig, Electron configuration in alloys and passivity, Zeitschrift für Elektrochemie, Berichte der Bunsengesellschaft für physikalische Chemie, 62 (1958) 700-707.
[71] W.H. Blades, B.W.Y. Redemann, N. Smith, D. Sur, M.S. Barbieri, Y. Xie, S. Lech, E. Anber, M.L. Taheri, C. Wolverton, T.M. McQueen, J.R. Scully, K. Sieradzki, Tuning chemical short-range order for stainless behavior at reduced chromium concentrations in multi-principal element alloys, in, 2024.
[72] J. Peng, F. Moszner, J. Rechmann, D. Vogel, M. Palm, M. Rohwerder, Influence of Al content and pre-oxidation on the aqueous corrosion resistance of binary Fe-Al alloys in sulphuric acid, Corrosion Science, 149 (2019) 123-132.
[73] K. Orson, E. Romanovskaia, A. Costine, J. Han, K. Ogle, J.R. Scully, P. Reinke, Corrosion Resistance, Composition, and Stratification of Passive Films: Ni-22Cr and Ni-22Cr-6Mo Alloys Passivated and Exposure Aged in Acidic Chloride Solutions, Journal of The Electrochemical Society, 171 (2024) 011505.
[74] K. Lutton, J. Han, H.M. Ha, D. Sur, E. Romanovskaia, J.R. Scully, Passivation of Ni-Cr and Ni-Cr-Mo Alloys in Low and High pH Sulfate Solutions, Journal of The Electrochemical Society, 170 (2023) 021507.
[75] J.D. Cox, D.D. Wagman, V.A. Medvedev, CODATA key values for thermodynamics, New York, 1984.
[76] S.E. Ziemniak, L.M. Anovitz, R.A. Castelli, W.D. Porter, Thermodynamics of Cr_2O_3, $FeCr_2O_4$, $ZnCr_2O_4$, and $CoCr_2O_4$, The Journal of Chemical Thermodynamics, 39 (2007) 1474-1492.

[77] B.S. Hemingway, Thermodynamic properties for bunsenite, NiO, magnetite, Fe3O4, and hematite, Fe2O3, with comments on selected oxygen buffer reactions, American Mineralogist, 75 (1990) 781-790.

[78] E.B. Rudnyi, E.A. Kaibicheva, L.N. Sidorov, M.T. Varshavskii, A.N. Men, (Ion + molecule) equilibrium technique applied to the determination of the activities of Cr2O3 and NiO. Standard molar Gibbs energy of formation of NiCr2O4, The Journal of Chemical Thermodynamics, 22 (1990) 623-632.

[79] H.-G. Lee, Y.-M. Lee, H.-S. Shin, C.-H. Jung, G.-W. Hong, Epitaxial deposition of NiO film on a cube-textured Ni substrate by metal-organic chemical vapor deposition, Metals and Materials, 6 (2000) 565-570.

[80] N. Kitakatsu, V. Maurice, C. Hinnen, P. Marcus, Surface hydroxylation and local structure of NiO thin films formed on Ni(111), Surface Science, 407 (1998) 36-58.

[81] L.-F. Huang, H.M. Ha, K. Lutton Cwalina, J.R. Scully, J.M. Rondinelli, Understanding Electrochemical Stabilities of Ni-Based Nanofilms from a Comparative Theory–Experiment Approach, The Journal of Physical Chemistry C, 123 (2019) 28925-28940.

[82] K.L. Cwalina, H.M. Ha, N. Ott, P. Reinke, N. Birbilis, J.R. Scully, In Operando Analysis of Passive Film Growth on Ni-Cr and Ni-Cr-Mo Alloys in Chloride Solutions, Journal of The Electrochemical Society, 166 (2019) C3241.

[83] O. Durante, C. Di Giorgio, V. Granata, J. Neilson, R. Fittipaldi, A. Vecchione, G. Carapella, F. Chiadini, R. DeSalvo, F. Dinelli, V. Fiumara, V. Pierro, I.M. Pinto, M. Principe, F. Bobba, Emergence and Evolution of Crystallization in TiO(2) Thin Films: A Structural and Morphological Study, Nanomaterials (Basel, Switzerland), 11 (2021).

[84] C.K. Dyer, J.S.L. Leach, Breakdown and Efficiency of Anodic Oxide Growth on Titanium, Journal of The Electrochemical Society, 125 (1978) 1032.

[85] M.R. Kozlowski, P.S. Tyler, W.H. Smyrl, R.T. Atanasoski, Anodic TiO2 Thin Films: Photoelectrochemical, Electrochemical, and Structural Study of Heat-Treated and Modified Films, Journal of The Electrochemical Society, 136 (1989) 442.

[86] H. Vahidi, K. Syed, H. Guo, X. Wang, J.L. Wardini, J. Martinez, W.J. Bowman, A Review of Grain Boundary and Heterointerface Characterization in Polycrystalline Oxides by (Scanning) Transmission Electron Microscopy, in: Crystals, 2021.

[87] D.D. Macdonald, The Point Defect Model for the Passive State, Journal of The Electrochemical Society, 139 (1992) 3434.

[88] P. Gao, Z. Wang, W. Fu, Z. Liao, K. Liu, W. Wang, X. Bai, E. Wang, In situ TEM studies of oxygen vacancy migration for electrically induced resistance change effect in cerium oxides, Micron, 41 (2010) 301-305.

[89] B. Roh, D.D. Macdonald, Effect of oxygen vacancies in anodic titanium oxide films on the kinetics of the oxygen electrode reaction, Russian Journal of Electrochemistry, 43 (2007) 125-135.

[90] S. Ishihara, E. Tochigi, R. Ishikawa, N. Shibata, Y. Ikuhara, Atomic structures of Ti-doped α-Al2O3 Σ13 grain boundary with a small amount of Si impurity, Journal of the American Ceramic Society, 103 (2020) 6659-6665.

[91] C. Ma, K. Chen, C. Liang, C.W. Nan, R. Ishikawa, K. More, M. Chi, Atomic-Scale Origin of the Large Grain-Boundary Resistance in Perovskite Li-Ion-Conducting Solid Electrolytes, Energy & Environmental Science, 7 (2014) 1638.

[92] D. Sur, E.F. Holcombe, W.H. Blades, E.A. Anber, D.L. Foley, B.L. DeCost, J. Liu, J. Hattrick-Simpers, K. Sieradzki, H. Joress, J.R. Scully, M.L. Taheri, An Experimental High-Throughput to High-Fidelity Study Towards Discovering Al–Cr Containing Corrosion-Resistant Compositionally Complex Alloys, High Entropy Alloys & Materials, 1 (2023) 336-353.

[93] R. Mueller, A. Rossoll, L. Weber, M.A.M. Bourke, D.C. Dunand, A. Mortensen, Tensile flow stress of ceramic particle-reinforced metal in the presence of particle cracking, Acta Materialia, 56 (2008) 4402-4416.

[94] Y. Wang, J. Jin, M. Zhang, X. Wang, P. Gong, J. Zhang, J. Liu, Effect of the grain size on the corrosion behavior of CoCrFeMnNi HEAs in a 0.5 M H2SO4 solution, Journal of Alloys and Compounds, 858 (2021) 157712.
[95] P. Marcus, V. Maurice, H.H. Strehblow, Localized corrosion (pitting): A model of passivity breakdown including the role of the oxide layer nanostructure, Corrosion Science, 50 (2008) 2698-2704.
[96] K. Syed, M. Xu, K.K. Ohtaki, D. Kok, K.K. Karandikar, O.A. Graeve, W.J. Bowman, M.L. Mecartney, Correlations of grain boundary segregation to sintering techniques in a three-phase ceramic, Materialia, 14 (2020) 100890.

Chapter 7: Conclusions

1.0 Summary

This work evaluates the microstructure, passivity, and corrosion behavior of complex concentrated alloys (CCAs) in the Al-Cr-Fe-Mn-Mo-Ni-Ti system. Benefits of CCA design arising from their multi-principal element nature, including improved distribution of passivating elements, joining of benefits from individual element additions, and the possibility of elemental synergies not observed in conventional alloys, are utilized to target improved corrosion resistance, mainly in chloride containing aqueous environments representing marine conditions. The effects of alloy composition and processing on density, cost, and mechanical properties are also considered.

Corrosion resistance is often attributed to the formation of stable protective oxide films. Films are often enriched in multiple elements relative to bulk composition, which is suggested to enhance passivity. Changing alloy composition affects the composition, and therefore, passivity, of the passive film. Furthermore, multi-phase microstructures are shown to have a multi-phase passive film form, with local composition defined by local bulk microstructure composition, with interfaces often contributing as preferential corrosion sites. For many elements, increasing concentrations may have effects on passivity that run contrary to their effects on the microstructure, and by extension, overall alloy corrosion behavior. Therefore, optimal compositions for corrosion resistance beyond simply maximizing or minimizing concentrations of certain elements may be obtained. Such trade-offs are evaluated in individual chapters in this work for four elements described further below. Finally, the nature of the multi-phase passive film is evaluated, characterized, and related to the overall design of CCAs.

In Chapter 2, the effect of Al concentration is explored. CCAs with little to no Al concentration had a single-phase microstructure, while higher Al concentrations led to the formation of $L2_1$ and $L2_1$/BCC containing microstructures. No consistent trends between metrics representing the ability of the CCA to passivate were present with Al concentration. CCAs with increasing $L2_1$ area fraction and/or the presence of a BCC phase were shown to have lower breakdown potentials with pitting frequently observed at the phase interfaces. Decreased resistance to localized corrosion was attributed in part to the lower composition of Ti in the $L2_1$ phase with increasing Al concentration. In addition to acting as a primary passivator, Ti was suggested to potentially stabilize the presence of Al species in the passive film. Thus, while Al is shown to be present in the passive film and could contribute to overall passivity in a beneficial manner, there are limits to allowable compositions before adverse microstructural effects begin to harm the resistance to localized corrosion.

The addition of and concentration optimization of Ti is explored in Chapter 3. In addition to Al, the presence of Ti in Fe-based CCAs reduces alloy density while also adding a stable passivating agent. However, as in the case of Al, excess Ti concentrations leads to the formation of undesirable second or third phases. Passive films formed for a CCA series with varying Ti concentration were enriched in Ti relative to bulk concentration. Ti concentration in the passive film did not always increase with bulk Ti concentration. Increasing bulk Ti concentrations corresponded with improved passivity evidenced by both potentiodynamic polarization and linear sweep voltammetry. Increasing Ti concentrations led to the formation of an $L2_1$ phase and, at the two highest Ti concentrations evaluated, a third Cr- and Mo-enriched phase suggested to be of Laves structure. The pitting and repassivation potentials were highest for the CCAs with moderate concentrations containing an $L2_1$ phase in the microstructure, but no Laves. Improved resistance to localized corrosion with increasing Ti concentrations was attributed to the formation of a thermodynamically stable passive film whereas the decreasing resistance to localized corrosion at high Ti concentrations was attributed to the formation of microstructural features such as phase interfaces that could act as preferential pit initiation sites. As in the case of Al, there is suggested to be an optimal Ti concentration for localized corrosion resistance. However, such a value is system specific and may be further altered by the concentration of other constituent elements.

The effect of Mn on microstructural partitioning and overall corrosion resistance was evaluated in Chapter 4. Unlike Al and Ti, Mn is a comparably less thermodynamically stable passivator and was not enriched in the passive films formed on the evaluated CCAs. Additionally, in-situ dissolution rates tracked during electrochemical testing suggests that for high-Mn CCAs, the breakdown behavior may be defined by Mn dissolution. Both passivity and resistance were suggested to decrease with Mn additions at high concentrations, however, the overall corrosion resistance increased with the addition of Mn at low concentrations relative to the Mn-free alloy. The improvement in corrosion resistance was attributed to decreased levels of partitioning for passivating elements, in particular Al and Ti, between phases. A more homogenous distribution of passivating elements was theorized to help promote the co-existence and possible synergies between the three elements, with the microstructural benefits of low Mn concentrations outweighing the negligible contributions on multi-phase CCA passivity.

While Mo is well-established as aiding resistance to localized corrosion, increasing Mo concentration increase the degree of Al and Ti partitioning in the evaluated dual-phase CCA series, having the opposite effect of Mn. Chapter 5 evaluated the proposed hypothesis that similar to increasing Mn concentration, decreasing Mo concentrations could similarly improve corrosion resistance. A series of CCAs with varying Mo concentration, all having an FCC + $L2_1$ microstructure, was evaluated for corrosion resistance. Passivity was suggested to slightly improve with decreasing Mo concentration. However, the resistance to localized corrosion was shown to detrimentally decrease in Mo-free CCAs, particular in acidic environments. Thus, while decreasing Mo concentrations may improve the homogeneity of the microstructure, they are generally not suggested to improve overall corrosion resistance. Thus, Mo addition is suggested to be beneficial in the design of corrosion-resistant CCAs with the evaluated two-phase microstructures. The effects of Mo concentration on maximum Al and/or Ti concentrations without forming a detrimental third phase remain unexplored.

Chapters 2-5 established relationships between corrosion resistance, phase composition, and the volume fraction of individual phases. However, the precise interplay between the bulk microstructure and the nature of the passive film has not been previously established for CCAs. Chapter 6 evaluates the variation in the composition of the passive film formed over different phases in the bulk microstructure. Two single-phase CCAs with compositions and structures characteristic of the constituent phases of a representative dual-phase CCA were synthesized. Both phases are suggested to independently passivate by global electrochemical and surface characterization of the single-phase CCAs and by high-resolution surface analysis of the dual-phase alloy. Two distinct phases were observed within the passive film. The film thickness was suggested to be of similar over both bulk microstructural phases. Local passive film composition was influenced by the bulk microstructure phases, with the passive film formed over the FCC phase having higher Cr concentrations and the film formed over the $L2_1$ phase having higher Al and Ti concentrations. The single phase CCAs displayed similar electrochemical behavior, with the exception of the $L2_1$ phase having a significantly lower pitting potential. The corrosion behavior of the dual-phase CCA was a mixture of the two constituent phases, with general corrosion resistance attributed to the ability of both constituent phases to independently passivate.

2.0 Future Work

The findings provide a strong basis for the incorporation of lightweight elements in the design of multi-phase CCAs. However, future work remains necessary to continue to build off the established foundations and improve the overall design process. While repeating many of the methods and procedures for new alloy systems remains a beneficial opportunity for future improvement, three suggestions that are suggested to be beneficial across many alloy systems are identified below.

Many of the evaluated passive film chemistries are suggested to have significant surface cation fractions of Al, Cr, and Ti, indicating possible coexistence. The interplay between Ti and Al is of interest given enrichment at similar depths (Chapter 2) as well as in similar areas of the passive film given their frequent enrichment in the $L2_1$ phase (Chapter 6). The increasing Al surface cation fractions for the Fe-Cr-Al-Ti and CCA series with varying Ti concentrations generally suggest that Ti may in some form stabilize the presence of Al in the passive film (Chapter 3). However, future study is necessary to establish a mechanism between the elements. Two possibilities have been proposed in this work.

First, the presence of Al in the passive film may be supported by thermodynamic factors reliant on interaction with Ti. Possibilities include both the formation of a disordered, solid-solution passive films between Al_2O_3 and Ti_2O_3 or TiO_2 as well as a long-range ordered complex oxide such as $TiAl_2O_5$. The presence of $TiAl_2O_5$ could be confirmed via diffraction methods such as glancing incident X-ray diffraction or transmission electron microscopy selected area diffraction, but experimental determination would be hindered by the thin nature of the passive film. Alternatively, computational thermodynamic modeling could predict the nature of the passive film, as has been done for previous CCAs. Such modeling could compare whether Al is predicted to dissolve in the absence or presence of Ti. Al that is predicted to not dissolve in the presence of Ti under conditions of dissolution, particularly if a complex oxide or a solid solution mixed-oxide is predicted to be stabilized by high magnitudes of the enthalpy of formation or mixing, respectively, would support proposed thermodynamic induced stability of Al species in the presence of Ti.

Alternatively, presence of Al where thermodynamic stability is not predicted may also be stabilized by kinetic factors. Mainly, a Ti-rich layer in the passive film may provide a protective layer, allowing for the presence of a metastable Al-enriched oxide layer. The possibility is further enhanced by the Al often enriching at depths slightly closer to the metal-oxide interface than Ti (Chapter 2). While atomic emission spectroelectrochemisty was used to track the time dependence of elemental dissolution rates (Chapter 4, Chapter 5), the dissolution rates of Ti-free alloys were not tracked, nor were dissolution rates of alloys in the absence of other passivators such as Cr. If metastable Al species are protected by Ti, it is expected that Al dissolution would be observed at early times in the presence of an applied potential, with decreasing dissolution rates as the electron current density decreases due to the formation of a Ti-rich passive film. The presence of Al and Ti passive species could be verified with X-ray photoelectron spectroscopy. Alternatively, continued Al dissolution would be expected in a Ti-free alloy with little to no Al passive species present due to the lack of a protective Ti-film.

Additionally, the concentration of elements selected for refinement of microstructural partitioning provide opportunities for future work. It has been shown that Mn (Chapter 4) and Mo (Chapter 5) concentrations alter the composition of passivating elements, particularly Al and Ti. The optimal Mn concentration of approximately 5 at. % was used to define compositions in CCA series that vary both Al (Chapter 2) and Ti (Chapter 3) concentrations, whereas Mo content was preserved to reduce the adverse effects of pitting (Chapter 5). However, given that compositional partitioning often informs the corrosion behavior of the CCAs, it is likely that Mn and Mo concentrations may alter the optimal Al and Ti concentrations. It is proposed that a similar CCA series with increased Mn concentrations would have higher optimal Al and Ti concentrations, and potentially improved corrosion resistance, although the degree of Mn on Al and Ti partitioning is less certain at Mn concentrations beyond 5 at. % (Chapter 4). In a similar manner, the optimal Al and Ti concentrations are predicted to decrease at higher Mo concentrations, particularly given the adverse corrosion effects of the formation of Mo-rich third phases at high Al or Ti concentrations (Chapters 2, 3). Evaluation of the optimal Al and/or Ti concentrations in CCA series with higher Mn or lower Mo concentrations could further verify effects of microstructural partitioning proposed in this work. First, the systems could be modeled with computational techniques such as the ThermoCalc or Machine Learning methods discussed in Chapter 1 to determine the degree to which Mn or Mo concentration may be altered to maximize the Al and/or Ti concentrations without the formation of a third phase. Computational work would also inform a series of CCAs that could be experimentally characterized for both microstructure and corrosion resistance. Notably, increased Mn concentrations and decreased Mo concentrations would be suggested to decrease overall corrosion resistance given the effects of Mn on dissolution rates (Chapter 4) and of Mo on pitting (Chapter 5). However, given the additional benefits of Ti on alloy density and of Al on both alloy cost and density, possibilities of increasing the concentrations of such elements provide merit for future study.

Finally, the effects of volume fraction of phases on the overall corrosion behavior independent of effects on individual phase composition remains an opportunity for future work. The passive film chemistry and lateral morphology is defined by the microstructure (Chapter 6). Therefore, a microstructure with an increasing phase fraction of a second phase can be reasonably expected to increase the volume fraction of the passive film phase that forms over such a given phase. Many studies, including this work, have evaluated the corrosion behavior of alloy series with varying phase fractions. However, the composition of individual phases in each alloy often changes, leading to changes in the composition of the phases in the passive film. To maintain composition of individual phases in the passive film, evaluation of the effect of phase volume fraction, and therefore length of heterophase interfaces, with fixed phase compositions is proposed. A CCA series has been synthesized with compositions determined as the weighted average of two single-phase CCA compositions with FCC and $L2_1$ structure. The single-phase compositions were developed from those utilized in Chapter 6, but with Mn and Mo removed to simplify the alloy space and avoid undesirable third phase formation. Compositions were weighed proportionally to a series of targeted volume fraction (0%, 5%, 20%, 50%, 80%, 95%, 100%) for the $L2_1$ phase fraction. Following homogenization, the composition of each phase in each alloy was evaluated, finding the composition of each element to generally be within 1 at. % of the targeted phase composition from the single-phase alloys.

Each CCA will be potentiodynamically polarized. It is proposed that the dual-phase CCAs will exhibit composite behavior, with corrosion properties being between the two single-phase CCAs. While some properties, such as passive current density, are expected to be directly proportional to phase volume fraction, particularly in the case of multiple phases who have differing abilities to passivate, others may differ from direct proportionality. For example, given the tendency of pitting to occur at phase interfaces (Chapter 6), it is unlikely that changes pitting potential will be directly proportional to the phase volume fraction. It is desired that such work would provide an overview of the effect of phase volume fraction on corrosion behavior in the absence of phase compositional changes. Phase volume fraction and morphology could be utilized as an input to corrosion predictive metrics as they frequently are for mechanical properties, allowing for improved evaluation of corrosion-mechanical trade-offs. Furthermore, compositions and volume fractions within the microstructure, which may be readily predictable by computational techniques such as CALPHAD. Thermomechanical processing could also be integrated to evaluate the effect of phase morphology at constant phase compositions and total volume fractions. Further incorporation of microstructural aspects into corrosion predictive metrics without synthesis and experimental evaluation could greatly improve the design efficiency and accelerate the development of the CCA field.

3.0 Conclusions

This work provides broad implications for the design of multi-phase corrosion-resistant CCAs. While the work in this study was generally limited to the Al-Cr-Fe-Mn-Mo-Ni-Ti system. It is desired that the findings may be applied to additional CCA systems in efforts to streamline and allow for effective integration of corrosion resistance into the design process. The following conclusions may be addressed:

- CCAs which contain multiple elements that are predicted to form thermodynamically stable oxides may passivate through the formation of a passive film containing multiple passivating elements. Thermodynamic stability of oxide species may be initially predicted through combinations of E-pH diagrams, Gibb's free energy of formation values, and previous experimental characterization of similar alloys. Possible synergies between passivating elements in the oxide film remain opportunities for future study both within and beyond the Al-Cr-Fe-Mn-Mo-Ni-Ti system.
- The microstructure of a CCA plays a prominent role in its corrosion resistance. The formation of undesirable phases often harms resistance to localized corrosion, regardless of the global concentration of passivating elements. Interfaces created between multiple phases are frequently shown to be preferential initiation sites for localized corrosion in chloride environments.
- Passive films formed over multi-phase material similarly consist of multiple phases with morphology defined by bulk microstructure. The local composition of the passive film, and therefore its passivity, is affected by the local composition of the bulk microstructure over which it is formed. Thus, high-throughput predictive models of alloy microstructure may be used to inform possible effects of compositional changes on corrosion behavior limiting the need for experimental characterization.
- Many elements in multi-phase CCAs have unexpected effects that may run contrary to their established roles in single-phase and/or simplified alloy systems. Evaluation of the effects of individual elements will be most accurate in the context of individual alloy systems.